Predicting the geochemical effects of SO_2 impurities during carbon storage: Batch experiments and reaction path geochemical modelling

by

Anja Birte Frank

B.Sc., Universität Trier, 2012

Thesis Submitted in Partial Fulfillment of the
Requirements for the Degree of
Master of Science

in the
Department of Earth Sciences
Faculty of Science

SIMON FRASER UNIVERSITY

Fall 2015

Approval

Name: **Anja Birte Frank**

Degree: **Master of Science**

Title of Thesis: **Predicting the geochemical effects of SO_2 impurities during carbon storage: Batch experiments and reaction path geochemical modelling**

Examining Committee:

Chair: **Dr. Shahin Dashtgard**
Associate Professor

_____

Dr. Dirk Kirste
Senior Supervisor
Assistant Professor

_____

Dr. Diana Allen
Supervisor
Professor

_____

Dr. Gregory Dipple
External Examiner
Professor, University of British Columbia

Date Defended/Approved: December 1, 2015

Abstract

The objective of this study was to improve our ability to predict CO_2-SO_2 geologic storage. SO_2 is an impurity of industrial CO_2 gas streams which is expected to intensify brine acidification resulting in enhanced mineral reaction. Short-term H_2SO_4-brine-rock experiments were combined with reaction path modelling to identify reactions and evaluate the pH and temperature dependency of reaction rates. In addition, available reactive surface area was investigated to enhance our ability to upscale to reservoir scale. Kinetically controlled reaction path models that included CO_2, SO_2 and O_2 were generated and then run at reservoir conditions for 100 y. The models predicted a rapid buffering of the SO_2 induced acidification. Compared to pure CO_2 storage the CO_2-SO_2-O_2 reservoir models resulted in enhanced carbonate reaction extents and a greater porosity increase, which have significant ramifications for the safety of the seal and the storage capacity of the storage formation.

Keywords: CO_2 storage; impurities; SO_2; geochemical modelling; upscaling

For Wolfgang Paul Schwank.

Acknowledgements

First, I would like to thank my senior supervisor, Dr. Dirk Kirste, for offering me the opportunity to work on such an interesting project. I am very grateful for the opportunities to attend conferences and workshops he provided me with. Dirk's support, patience and kindness enhanced my graduate experience significantly. I would also like to thank my supervisor, Dr. Diana Allen, for her patience and help. I am very grateful for her edits and suggestions on my thesis, which helped improve my written English. Further, I want to express my gratitude to Dr. Greg Dipple for acting as an external examiner on my committee.

I would like to acknowledge the financial assistance provided through the Australian National Low Emissions Coal Research and Development (ANLEC R&D), Australia's Cooperative Research Centre for Greenhouse Gas Technologies (CO2CRC) and the financial assistance provided by the Australian Coal Association Low Emissions Technology Limited and the Australian Government through its Cooperative Research Centre program and the Clean Energy Initiative.

Thank you to Dr. Julie Pearce, Dr. Grant Dawson and everyone else from the School of Earth Science of the University of Queensland for providing me with rock samples and data and for welcoming me in their group during my visit. I would also like to thank Dr. Ralf Haese, the Reactive Reservoir Rocks group and the CO2CRC for enabling me to visit Australia for the annual symposiums. It was a great experience working with such a remarkable group and I wish them the best for the future.

I would like to thank my grad colleagues and the staff from the Department of Earth Science of Simon Fraser University for their support and help during my Masters. A special thanks to Glenda Pauls for knowing a solution to every problem and making the impossible possible. I would also like to thank Rodney Arnold and Matt Plotnikoff for assisting me with my computer problems.

A special thanks to my friends and family for their tremendous support over the years; and to my partner, Ryan, for his never ending support and patience.

Table of Contents

List of Tables

List of Figures

List of Units

°C	Degree Celsius
cm	Centimetre
d	Day
g	Gram
h	Hour
K	Kelvin
kg	Kilogram
kJ	Kilojoule
km	Kilometre
L	Litre
m	Metre
mg	Milligram
mL	Millilitre
mm	Millimetre
mmol	Millimole
mol	Mole
Mt	Megaton
ppmv	Parts per million by volume
s	Second
vol%	Volume %
wt%	Weight %
y	Year
µm	Micrometre
µS	MicroSiemens

List of Symbols

a	Hydrogen ion activity
A_s	Mineral surface area
dia	Diameter
E_a	Activation energy
hgt	Height
k	Rate constant
K	Equilibrium constant
M	Molar concentration
n	H^+ power term
Q	Activity product
r	Reaction rate
R	Molar gas constant
T	Temperature
Γ	Pre-exponential factor for nucleation
T_0	Reference temperature (298.15 K)
a_H	Hydrogen ion activity for the acid mechanism
a_{OH}	Hydrogen ion activity for the base mechanism
n_H	H^+ power term for the acid mechanism
n_{OH}	H^+ power term for the base mechanism
$k_{25(H)}$	Rate constant at 25°C for acid mechanism
$k_{25(OH)}$	Rate constant at 25°C for base mechanism
$k_{25(nu)}$	Rate constant at 25°C for neutral mechanism
$E_{a(H)}$	Activation energy for acid mechanism
$E_{a(OH)}$	Activation energy for base mechanism
$E_{a(nu)}$	Activation energy for neutral mechanism
k_p	Precipitation rate constant
k_d	Dissolution rate constant
r_p	Precipitation rate
k_n	Nucleation rate constant set as 1 mol/s

List of Acronyms and Abbreviations

(aq)	Aqueous
(g)	Gaseous
ANLEC R&D	Australian National Low Emissions Coal Research and Development
CO2CRC	Australia's Cooperative Research Centre for Greenhouse Gas Technologies
CCS	Carbon capture and storage
CEC	Commission for Environmental Cooperation
CGSS	CO_2 Geological Srorage Solutions Pty Ltd.
e.g.	For example
EC	Electrical conductivity
EDS	Energy Dispersive Spectroscopy
GSS	Geochemist's Spreadsheet™
GWB	Geochemist's Workbench™
ICP-AES	Inductively Couple Plasma Atomic Emission Spectroscopy
ICS	Ion Chromatography System
IEA	International Energy Agency
IEAGHG	International Energy Agency Greenhouse Gas R&D Programme
IPCC	Intergovernmental Panel on Climate Change
LPNORM	Linear programming normative
Me^{2+}	Divalent metal cations
NO_x	Mono-nitrogen oxides
OECD	Organisation for Economic Co-operation and Development
QEMScan	Quantitative Evaluation of Minerals by Scanning electron microscopy
$scCO_2$	Supercritical carbon dioxide
SEM	Scanning Electron Microscopy
SFU	Simon Fraser University
SO_x	Mono-sulphur oxides
U.S. EPA	U.S. Environmental Protection Agency
UBC	University of British Columbia
XRD	X-ray Powder Diffraction
XRF	X-ray Fluorescence

Chapter 1. Introduction

The dominant cause of the observed rise in global average temperatures over the last 50 years is greenhouse gas forcing (IPCC, 2007a). Carbon dioxide (CO_2) is a major contributing greenhouse gas and the burning of fossil fuels for electricity generation is the major stationary source for CO_2. The Intergovernmental Panel on Climate Change (IPCC) suggests that carbon capture and storage (CCS) has the potential to reduce power plant emissions by more than 85% (OECD/IEA, 2006), thus helping to mitigate global warming (IPCC, 2007b). In industrial sectors like coal, steel and cement, CCS is currently the only available technology to accomplish emission reduction goals and could account for up to 20% of the needed CO_2 reduction by 2050 (OECD/IEA, 2012). Before CCS can be established on a larger scale the possible risks have to be determined to ensure that it is a safe and permanent method to store CO_2 (OECD/IEA, 2006).

The injection of CO_2 facilitates geochemical reactions by shifting thermodynamic equilibria resulting in alteration such as changed mineral assemblages (Benson and Cole, 2008). CO_2 induces brine acidification leading to acid-catalyzed dissolution of primary mineral phases and the precipitation of secondary minerals (Xu et al., 2004; Li et al., 2006; Zerai et al., 2006; Ellis et al., 2010). This might affect the aquifer permeability and porosity, changing the physical properties of the geological formation (Kaszuba et al., 2005; Kharaka et al., 2006a; Bacon et al., 2009). Previous studies of CO_2 storage include, among other approaches, geochemical (Gunter et al., 2000; Xu et al., 2004; Zerai et al., 2006) and flow and transport modelling (Pruess et al., 2004), reactive transport modelling (Knauss et al., 2005; Xu et al., 2005; Bacon et al., 2009), laboratory experiments (Kaszuba et al., 2003; Soong et al., 2004; Kaszuba et al., 2005), and pilot studies as well as demonstration sites (Kharaka et al., 2006a; Kharaka et al., 2006b; Jenkins et al., 2012).

The chemical and physical effects of CO_2 injection will vary if the injected CO_2 stream is not pure. Understanding the role of variations in composition of captured CO_2 emissions on the physical and chemical aspects of carbon storage is important to realize the safe use of CCS. Examples for impurities include air components like O_2, N_2, and Ar, as well as process dependant products such as SO_x, NO_x, and H_2 (Stanger and Wall, 2011). The primary reasons for injecting impure CO_2 include the potential to dispose of harmful co-contaminants as well as cost effectiveness (Pearce et al., 2015). The front-end processes of CCS, which include the separation of impurities, account for 75% of the total cost. Lowering the costs by allowing the injection of less pure CO_2 streams therefore results in a significant reduction of the overall costs (Knauss et al., 2005).

One of the possible impacts of impurities is the dilution of the CO_2 stream which increases the required storage volume. Other effects include the formation of strong acids leading to the lowering of the formation water pH (Ellis et al., 2010; Stanger and Wall, 2011). However, most effects of impurities are largely unknown (Crandell et al., 2010), thus further research is needed in this field to ensure the safe implementation of CCS.

This research focuses on the geochemical aspect of CO_2 storage with SO_2. SO_2 is emitted from coal fired electric power plants, the primary source of CO_2 for CCS (Ellis et al., 2010), thus it often occurs as an impurity. The addition of SO_2 is assumed to lead to an enhanced brine acidification due to the formation of strong sulphur acids (Xu et al., 2007). Previous studies on the effects of CO_2-SO_2 storage include experiments (Palandri et al., 2005a; Flaathen et al., 2010; Flaathen et al., 2011; Garcia et al., 2011; Kummerow and Spangenberg, 2011; Garcia et al., 2012; Glezakou et al., 2012; Schoonen et al., 2012) and numerical modelling studies (Knauss et al., 2005; Palandri et al., 2005a; Palandri and Kharaka, 2005b; Xu et al., 2007; Bacon et al., 2009; Crandell et al., 2010; Ellis et al., 2010; Garcia et al., 2011; Garcia et al., 2012).

This research examines the different impacts SO_2 impurities have on the chemical and physical properties of reservoir and seal rocks. The study combined laboratory experiments and numerical modelling. The experiments focused on the impact of SO_2 induced acidification and were carried out as short-term batch

experiments reacting sedimentary rocks of varying composition with acidified brine. The rock samples originated from the Western Canada Sedimentary Basin, Canada, and the Surat Basin, Australia. The latter were used to examine the effect of SO_2 storage on a potential storage site, while the former were used to investigate reaction path and reaction rate dependence associated with acidity, temperature and reactive surface area. The experimental results were then simulated in reaction path models, which helped to quantify the impact of SO_2 injection. Geochemical models of SO_2 and CO_2 injection were generated based on the reaction path and rate data determined in the experiments these addressed upscaling to reservoir scale and were run for longer time frames to investigate long term effects. This part focussed predominantly on the Surat Basin as a potential storage site, and included physical and chemical heterogeneity of the Wandoan region of the Surat Basin.

This research was carried out in affiliation with Australia's Cooperative Research Centre for Greenhouse Gas Technologies (CO2CRC), which is one of world's leading collaborative research organisations focused on carbon dioxide capture and geological storage. It was further funded by the Australian National Low Emissions Coal Research and Development (ANLEC R&D). ANLEC R&D is supported by Australian Coal Association Low Emissions Technology Limited and the Australian Government through the Clean Energy Initiative.

1.1. Carbon storage

CCS technology includes three main steps: The capture of the CO_2 from the emission source, the transport to a storage site, and the injection as a supercritical fluid into the subsurface (IPCC, 2005). Possible storage sites are deep (>800 m) saline aquifers, depleted oil or gas reservoirs, unmineable coal seams and enhanced oil or gas recovery sites (OECD/IEA, 2006) (Figure 1.1). Of these, saline aquifers are particularly suitable due to their availability, the large potential storage capacity, and the technical capability to safely inject and manage storage (Bachu, 2008; Benson and Cole, 2008).

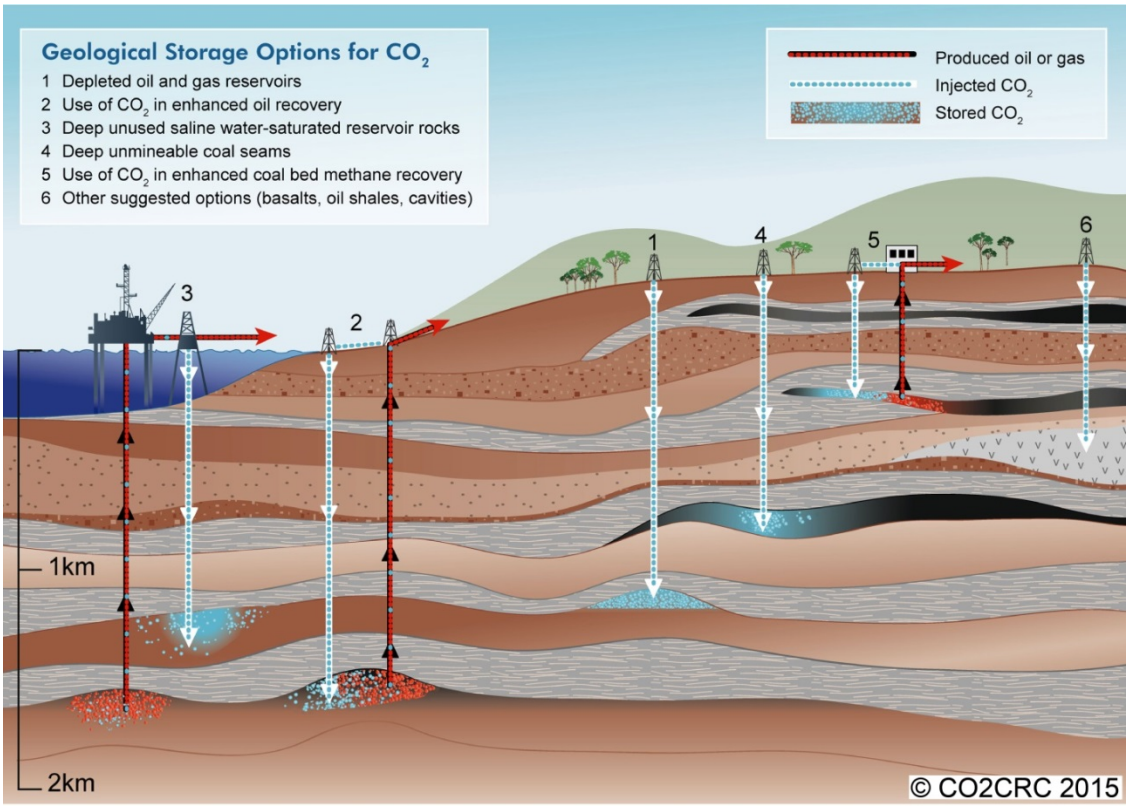

Figure 1.1 Possible storage sites for CO_2 (CO2CRC, 2015).

Under high pressure and temperature conditions, which prevail at typical injection depths, CO_2 is present as a supercritical fluid (Bachu, 2008). A supercritical fluid has the density of a liquid, but the viscosity more like that of a gas. The injected CO_2 can migrate within the storage formation and dissolve in the formation brine. The nature and scale of these processes define the interaction of CO_2 with the reservoir rock and the amount of CO_2 that can be stored for an indefinite time period (Czernichowski-Lauriol et al., 2006). The storage of CO_2 can be realized through physical or chemical mechanisms including structural/stratigraphic, residual/capillary, solution and mineral trapping (Czernichowski-Lauriol et al., 2006):

Structural/stratigraphic trapping refers to the storage of CO_2 through a physical trap. The supercritical CO_2 stays as a mobile fluid, immiscible and less dense than water, but is prevented from further upward movement through stratigraphic or structural heterogeneities. This mechanism provides the highest volumetric trapping potential in the short term (Xu et al., 2003; Xu et al., 2004). Residual/capillary trapping occurs when

residual CO_2 becomes disconnected and trapped by capillary pressure from the water in the pore spaces between the rock grains (Lu et al., 2012). Solubility trapping describes the dissolution of CO_2 in water, and mineral trapping involves the precipitation of carbonates (Czernichowski-Lauriol et al., 2006). Solubility and mineral trapping take longer periods of time than structural/stratigraphic and residual trapping, but are very desirable since they have the potential to immobilize CO_2 over longer terms increasing the safety of carbon storage (Xu et al., 2003; Xu et al., 2004; Czernichowski-Lauriol et al., 2006; Benson and Cole, 2008). Figure 1.2 summarises the order in which the different trapping mechanisms occur and their potential to store CO_2 permanently as increasing security.

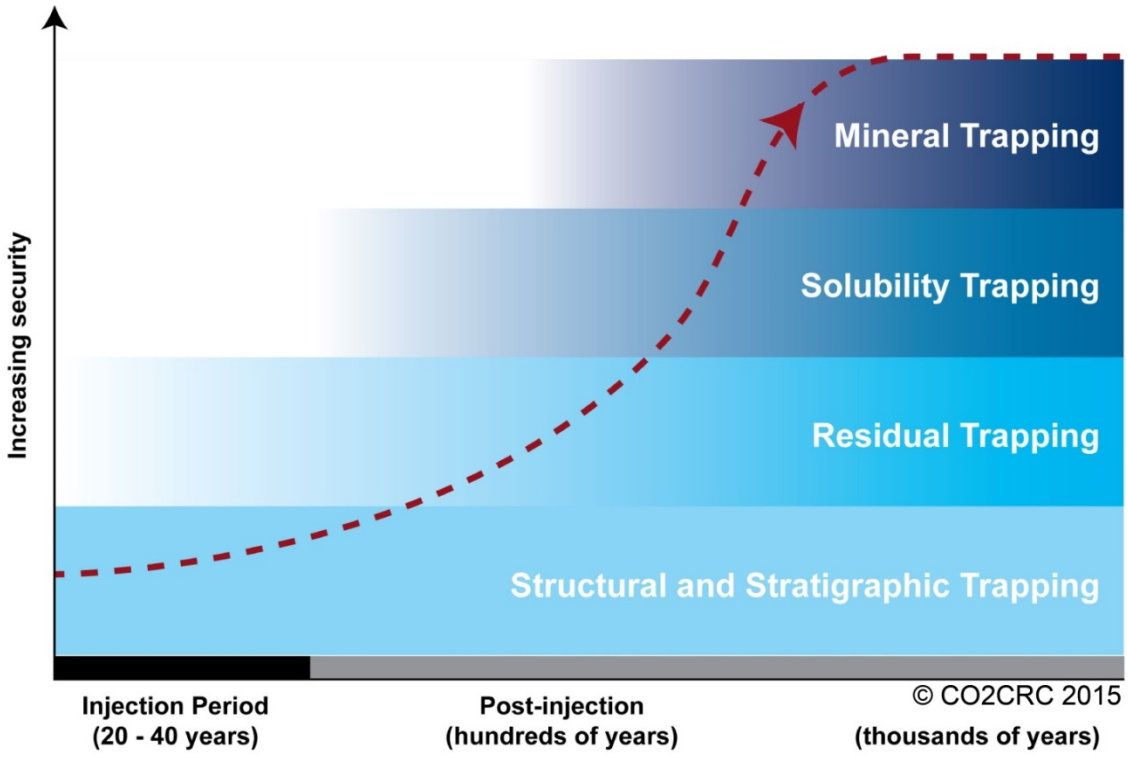

Figure 1.2 Time requirements and security of the different trapping mechanisms (CO2CRC, 2015).

Through structural/stratigraphic and residual/capillary trapping CO_2 is trapped physically. Solubility and mineral trapping, on the other hand, are chemical trapping mechanisms and will be described in further detail below.

Supercritical CO_2 ($scCO_2$) is usually less dense than water (Bachu, 2008) resulting in a phase separation with the $scCO_2$ phase on top of the formation water (Figure 1.3).

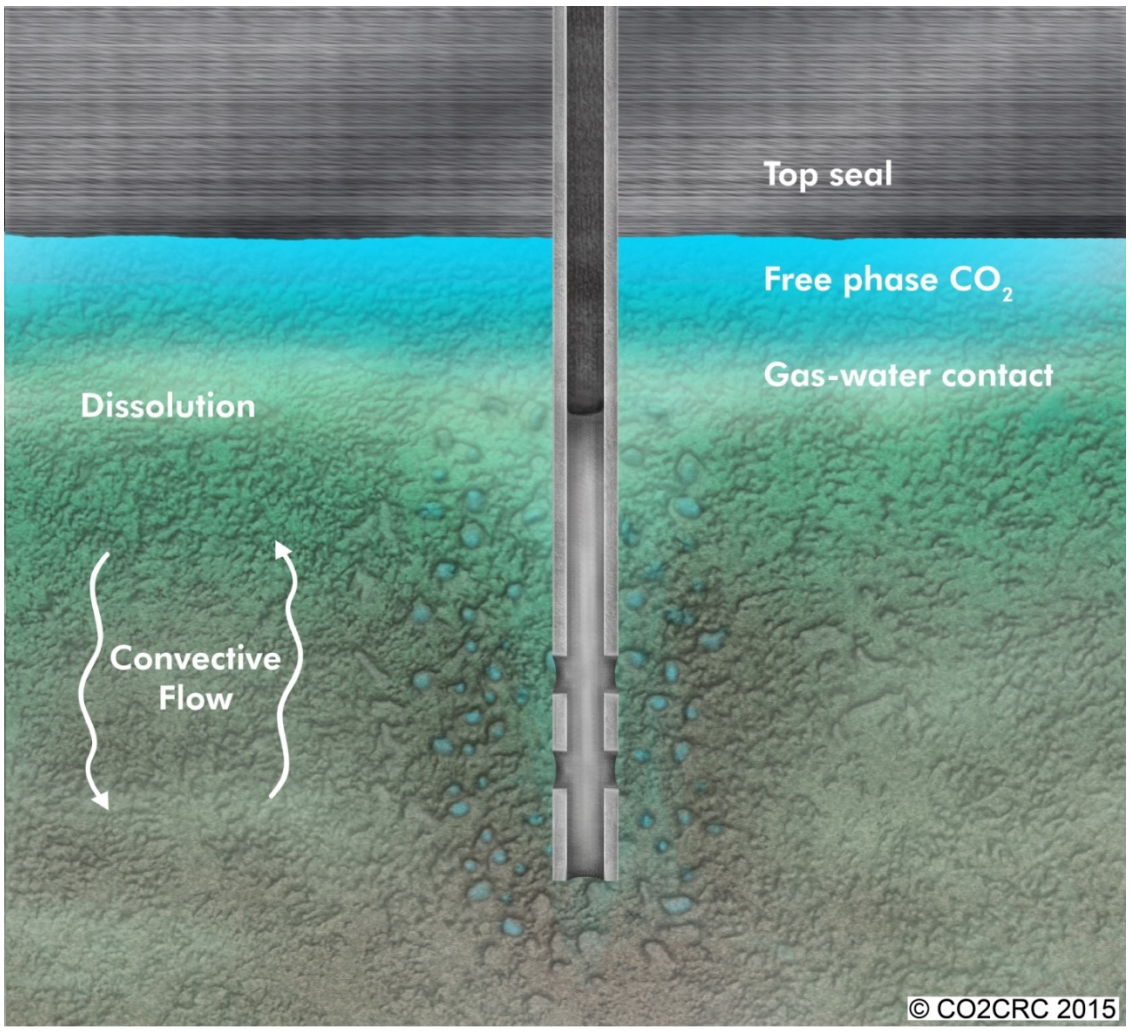

Figure 1.3 The dispersion of CO_2 in the reservoir after the injection has stopped (CO2CRC, 2015).

Dissolution trapping takes place along the gas-water contact. CO_2 dissolves in the formation water and forms weak carbonic acid (Equations 1.1; Equation 1.2), which can subsequently dissociate to form bicarbonate and carbonate ions (Equation 1.3; Equation 1.4); (Ennis-King and Paterson, 2005):

$$CO_2(g) \rightarrow CO_2(aq) \quad (1.1)$$

$$CO_2(aq) + H_2O \rightarrow H_2CO_3 \quad (1.2)$$

$$H_2CO_3 \rightarrow H^+ + HCO_3^- \quad (1.3)$$

$$HCO_3^- \rightarrow H^+ + CO_3^{2-} \quad (1.4)$$

The extent of dissolution depends on the solubility of CO_2 which varies with changing pressure, temperature and salinity (Xu et al., 2003; Xu et al., 2004; Benson and Cole, 2008) where increasing temperature and/or salinity results in decreasing solubility, while increasing pressure increases the solubility. The relatively high solubility of CO_2 affects the brine density. Through dissolution, the brine water becomes denser and starts to sink, generating convective flow and allowing the dissolved CO_2 to spread, thereby enhancing dissolution (Ennis-King and Paterson, 2005).

The brine acidification induced by reaction (Equation 1.3) leads to mineral dissolution processes (Xu et al., 2004; Li et al., 2006; Zerai et al., 2006). These can result in the release of divalent metal cations (Me^{2+}). During mineral trapping these mineral cations react with the bicarbonate, forming stable carbonate precipitates (Equation 1.5); (Xu et al., 2003; Soong et al., 2004; Xu et al., 2005):

$$HCO_3^- + Me^{2+} \rightarrow H^+ + MeCO_3 \quad (1.5)$$

The formation of calcium, magnesium and iron(II) carbonates are likely to be the main reactions contributing to the immobilization of CO_2 (Xu et al., 2004). Possible reaction products of these include calcite, dolomite, ankerite, magnesite and siderite (Soong et al., 2004).

1.2. SO_2 impurity in CO_2

SO_2 is a by-product from coal fired electric power plants and thus is often found as an impurity in CO_2 streams. In the U.S., the current regulatory environment allows for minimal SO_2 emissions, and producers are required to pay for emissions in excess of licensed amounts (U.S. EPA, 2009). Table 1.1 lists SO_2 and CO_2 emissions from the electricity generation sector in North America in 2005.

Table 1.1 SO_2 and CO_2 emissions from North American electrical power plants in 2005 (CEC, 2011).

Country	Pollutant	Emissions (tons)	Reporting Facilities
Canada	SO_2	516,695	38
	CO_2	121,299,282	72
Mexico	SO_2	1,403,015	102
	CO_2	117,737,070	102
Unites States	SO_2	9,611,608	2,724
	CO_2	2,419,514,935	2,718

It is obvious that the emitted SO_2 amounts from power plants are relatively small compared to the amount of emitted CO_2. But since SO_2 is more soluble in water than CO_2 even a small amount of it can have a significant impact on geochemical processes during storage (Ellis et al., 2010). The amount of SO_2 contamination varies with the source of the CO_2 stream (IEAGHG, 2011). It is process dependent, thus the amount of SO_2 in CO_2 streams captured pre-combustion differs from the amount in post-combustion or oxyfuel streams. Table 1.2 shows the purity of the CO_2 stream depending on the source.

Table 1.2 Possible SO_2 and SO_3 amounts in the CO_2 stream depending on its source (IEAGHG, 2011).

	Pre-combustion		Post-combustion			Oxyfuel		
	Selexol	Rectisol						
CO_2 (vol%)	97.95	99.7	99.93	99.92	99.81	85	98	99.94
SO_2 (ppmv)	-	-	10*	10*	20*	50	50	50
SO_3 (ppmv)	-	-	10*	10*	20*	20	20	20

*total concentration of SO_2 + SO_3

SO_2 impurities only occur in CO_2 streams from post-combustion capture and oxyfuel plants, and are particularly high in the latter. There are currently no existing regulations on the purity requirements of CO_2 streams, but greater than 95% is generally accepted as a limit for geological storage (Pearce et al., 2015). However, it is likely the upper limit will be defined by regulatory authorities in the process of implementing CCS on a larger scale.

After injection of a CO_2-SO_2 gas stream, the gas mixture undergoes the similar physical and chemical trapping mechanisms as those of pure CO_2 injection. While the physical trapping mechanisms are analogous to the storage of CO_2 alone, the chemical trapping mechanisms vary for SO_2. Both CO_2 and SO_2 dissolve along the gas-water contact, but due to the higher solubility of SO_2, its dissolution is favoured. This process is limited by the diffusion of SO_2 within the scCO_2 phase, and similar to CO_2, solubility is dependent on temperature, pressure and salinity (Crandell et al., 2010; Ellis et al., 2010). The solubility trapping of SO_2 can be described by three different reaction scenarios (Ellis et al., 2010): hydrolysis (Equation 1.6), oxidation (Equation 1.7) and disproportionation (Equation 1.8; Equation 1.9).

$$SO_2 + H_2O \rightarrow H_2SO_3 \quad (1.6)$$

$$SO_2 + H_2O + 0.5\ O_2 \rightarrow H_2SO_4 \quad (1.7)$$

$$SO_2 + H_2O \rightarrow 0.75\ H_2SO_4 + 0.25\ H_2S \quad (1.8)$$

$$SO_2 + H_2O \rightarrow 0.75\ H_2SO_4 + 0.25\ S^0 + 0.25\ H_2 \quad (1.9)$$

Reaction equation 1.6 shows the case of hydrolysis, which produces sulphurous acid. It occurs alone when there is no mechanism to oxidize SO_2. Under even mildly oxidizing conditions reaction 1.7 takes place. In the equation, O_2 represents all possible electron acceptors in the brine and those available in the mineral phases. The oxidation of SO_2 leads to the formation of the very strong sulphuric acid. In the last two scenarios (Equation 1.8; Equation 1.9) the sulphur in SO_2 is both oxidized and reduced, forming sulphuric acid (H_2SO_4) and hydrogen sulphide (H_2S) or elemental sulphur (S^0). Which reaction takes place and the extent depends on the given redox conditions.

The mineral trapping of SO_2 occurs through the precipitation of stable sulphur bearing mineral phases, such as gypsum, anhydrite, alunite, jarosite or pyrite (Xu et al., 2007).

The availability of data on the geochemical impact of CO_2-SO_2 storage is limited. However, both experimental and modelling studies have been conducted on the effect of

SO_2 contamination during carbon storage. Experiments were usually conducted in batch (e.g. Palandri et al., 2005a) or flow through (e.g. Schoonen et al., 2012) set ups. Existing experimental studies include investigations on the reaction of individual mineral phases or rocks with CO_2 and SO_2 and their resulting geochemistry (Palandri et al., 2005a; Garcia et al., 2011; Garcia et al., 2012; Glezakou et al., 2012; Kummerow and Spangenberg, 2011; Schoonen et al., 2012; Pearce et al., 2015), studies on dissolution and precipitation rates (Flaathen et al., 2010; Flaathen et al., 2011) and experiments on changes in sorption behaviour induced through CO_2-SO_2 storage (Sakurovs et al., 2011). The implementation of SO_2 was achieved in two ways. One is the use of an aqueous proxy for the dissolved gas, e.g. sulphate (SO_4^{-2}); (e.g. Flaathen et al., 2011). Alternatively SO_2 was introduced as a minor gas in the CO_2 stream (e.g. Palandri et al., 2005a; Pearce et al., 2015). This better represents the real case, but is harder to implement.

Geochemical modelling allows the generation of predictive simulations of storage systems and includes different model types, like thermodynamic and kinetically controlled reaction path or reactive transport models. The former uses thermodynamic data to predict brine-rock reactions by changing a system variable incrementally and calculating equilibrium at each step. Kinetically controlled reaction path models combine thermodynamic data with reaction rate data to simulate changes in brine and rock composition over time. Reactive transport modelling predicts the special and temporal distribution of changes in the chemical and physical attributes of a system, by coupling brine-rock reactions with flow and transport. Modelling studies on CO_2-SO_2 storage include: thermodynamic modelling used to constrain experimental results (Palandri et al., 2005a; Palandri and Kharaka, 2005b; Garcia et al., 2011; Garcia et al., 2012), investigations on the factors limiting the impacts of SO_2 co-storage (Crandell et al., 2010; Ellis et al., 2010), and reactive transport modelling examining the effects of CO_2-SO_2 storage on chemical and physical properties of the host rock (Knauss et al., 2005; Xu et al., 2007; Bacon et al., 2009).

1.3. Surat Basin

Part of this research focuses on rocks of the Surat Basin since it has come to be of interest as a potential carbon storage site with an estimated storage potential of 2962 Mt (CGSS, 2010). It is already a target for hydrocarbon exploration, which requires similar formation qualities in terms of porosity, permeability and thickness (Cadman et al., 1998; Bachu and Adams, 2003; Kaldi et al., 2009).

The Surat Basin is located in the east of Australia and occupies about 300,000 km^2 of central southern Queensland and central northern New South Wales (Exon, 1976) (Figure 1.4). It is part of the larger Great Artesian Basin, and is confined westward by the Nebine Ridge and eastwards by the Kumbarilla Ridge (Hodginkson et al., 2009).

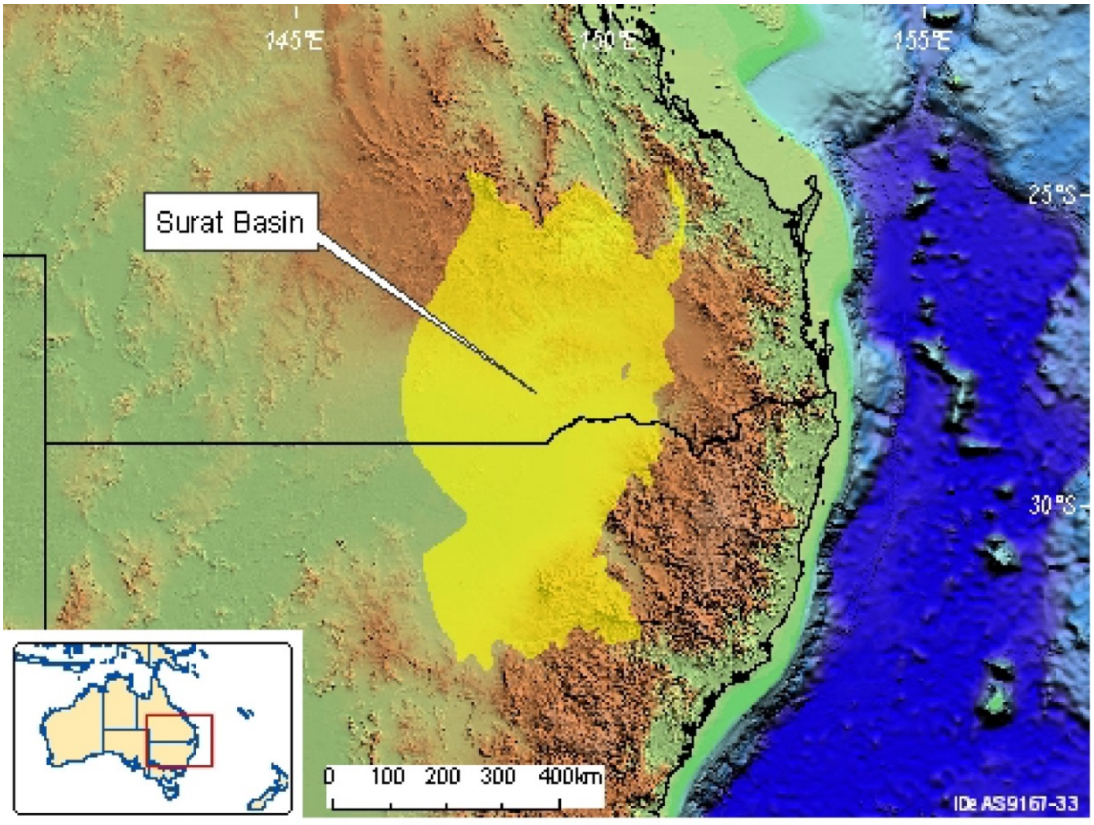

Figure 1.4 Location of the Surat Basin (Geoscience Australia, 2015).

The basin's sediments reach a thickness of up to 2,500 m and are mainly Jurassic clastic continental sedimentary rocks and Lower Cretaceous marine beds (Exon, 1976). The area of maximum deposition, the Mimosa Syncline, is the primary tectonic element in the basin and structural deformation is minor (Hoffmann et al., 2009). The sedimentary fill of the basin is characterized by a series of fining upward sedimentary cycles (Hoffmann et al., 2009). This results in a stacked sequence of reservoir/seal pairs (Hodginkson et al., 2009). The Jurassic Precipice Sandstone of the Surat Basin bears properties of a potential storage unit, while the Evergreen Formation and the Walloon Subgroup could function as regional seals, and the Hutton Sandstone units could act as secondary mixed storage and seal (Hodginkson et al., 2009).

Since this study only looks at the Precipice Sandstone, the Evergreen Formation and the Hutton Sandstone, their formation and properties are described in further detail, while the overlying formations will not be discussed.

Regional subsidence with minimal reactivation of the faulting of the Permian and Triassic led to the deposition of fluvial sandstones in the Lower Jurassic (Cadman et al., 1998). The resulting Precipice Sandstone is a laterally extensive formation which reaches a maximum thickness of 150 m in the Mimosa Syncline. It is characterized as quartz sandstone with minor siltstone and mudstone (Exon, 1976; Martin, 1977; Hoffmann et al., 2009). The Precipice Sandstone was probably deposited in a series of meandering and braided stream environments (Exon, 1976; Martin, 1977; Cadman et al., 1998; Hoffmann et al., 2009). The overlying Evergreen Formation shows characteristics of a transgressive phase forming a gradational transition from the Precipice Sandstone. Quartzose sandstones, similar to the Precipice Sandstone, are overlain by shale, siltstone and mudstone, which were probably deposited under fluvio-lacustrine to marginal marine environments during the Lower Jurassic (Exon, 1976; Martin, 1977; Cadman et al., 1998). The Evergreen Formation is up to 260 m thick and is laterally more extensive than the Precipice Sandstone (Exon, 1976; Cadman et al., 1998). Towards the end of the Lower Jurassic, the overlying Hutton Sandstone was probably deposited in a meandering river system in a fluvial floodplain environment (Exon, 1976; Hoffmann et al., 2009). The Hutton Sandstone is characterized by mica-rich, sublithic to quartzose sandstone with minor siltstone and mudstone (Exon, 1976; Martin, 1977;

Hoffmann et al., 2009). It is up to 250 m thick and laterally widespread, reaching into the Eromanga Basin to the West (Exon, 1976; Cadman et al., 1998).

In considering carbon storage, it is important to note that the relatively quartz-rich, homogeneous, laterally wide spread Precipice Sandstone and Hutton Sandstone are potentially extensive, permeable carbon storage formations. However, the more heterogeneous lithology of the Hutton Sandstone suggests that it is more reactive and, consequently, less ideal as a storage site than the Precipice Sandstone (Farquhar et al., 2013). The Evergreen Formation has the potential to act as a caprock formation due to its significant lateral extent, thickness and fine grained heterogeneous composition (Farquhar et al., 2013).

1.4. Research purpose and objectives

The purpose of this research is to improve our understanding of SO_2-brine-rock interactions under well-defined conditions and to enhance our ability to geochemically model CO_2-SO_2 storage. Given the abundance of SO_2 in emissions from coal fired plants, this kind of study is necessary to evaluate and ensure the safety of carbon storage. The research project included conducting batch experiments of different rock-brine systems under varying conditions of temperature, pH and sample particle size to investigate the effect of temperature, pH and sample particle size on reaction rates. Reaction path models were used to convert the experimental results into models simulating the geochemical processes induced by SO_2. By simulating the experiments under varying temperature and pH conditions the activation energy (E_a) and hydrogen power term (n) input were evaluated as reaction rate parameters. The experiments using different sample particle sizes investigated the effect of changing the proportion of freshly exposed reactive surface area to that contained within the pore space of the whole rock. Modelling of these experiments allowed for constraining how the reactive surface area had to be changed in order to account for the increasing proportion of whole rock pore space. This was undertaken in order to enhance our ability to upscale to reservoir scale. To simulate the long term effects of SO_2 during carbon storage, the experimental models were upscaled to reservoir scale, modified to include CO_2 and run

for 100 years. Further, reservoir models of pure CO_2 and CO_2-SO_2-O_2 storage were created to compare the effects of pure and impure CO_2 storage scenarios.

Three main objectives were addressed:

1. Experimental evaluation of SO_2-brine-rock reactions under defined conditions.
2. Evaluation of the dependence of reaction rates on different input parameters by modelling the experimental results using geochemical reaction path models.
3. Long term predictions of CO_2, CO_2-SO_2 and CO_2-SO_2-O_2 storage at reservoir scale.

1.5. Scope of work

The scope of work included the following tasks:

1. Developing an experimental set up for SO_2-brine-rock batch reactions under varying pH, sample particle size and temperature conditions
2. Preparing the batch experiments by selecting and analysing suitable rock samples and producing synthetic brine
3. Conducting the experiments, including:
    a. Temperature adjustment/monitoring
    b. Brine sampling and characterization
    c. Analysis of reacted rock samples
4. Creating GSS (Geochemist's Spreadsheet™) databases for the different experiments to better evaluate and plot the experimental results
5. Using the experimental data to develop reaction path models to:
    a. Identify geochemical reactions and participating mineral phases
    b. Investigate how varying experimental conditions influence SO_2-brine-rock reaction rates
    c. Evaluate and modify kinetic rate data for minerals specific to these experiments

6. Integrating CO_2 into the SO_2-brine-rock reaction path models and expanding those to reservoir scale and longer time frames to:
    a. Combine the effects of SO_2 with CO_2 storage
    b. Investigate long term effects of CO_2-SO_2 storage
    c. Examine the impact on a possible storage site by using physical and chemical data of the Surat Basin.

1.6. Thesis outline

This thesis has been written in chapter format and consists of a total of five chapters:

Chapter 1 provides background information on the concept of carbon capture and storage. The geochemical effect of pure CO_2 and CO_2-SO_2 injection is described, as well as the Surat Basin, a possible storage formation relevant to this research.

Chapter 2 focuses on the batch experiments conducted on SO_2-brine-rock reactions. It describes the current experimental research related to CO_2-SO_2 storage. The methodology of the experiments is explained and the results are discussed and summarized.

Chapter 3 describes the research conducted to model SO_2 storage. It explains the model set up used to convert the experimental results from chapter 2 to reaction path models. The modelling results are discussed and summarized.

Chapter 4 focuses on expanding the reaction path models from chapter 3 to model CO_2-SO_2 injection at reservoir scale and over longer terms. It explains the model set up, especially how the upscaling to reservoir conditions was done. It concludes by discussing and summarizing the modelling results.

Chapter 5 combines and summarizes the findings of this research, and gives recommendations.

Chapter 2. Experimental study on the impact of sulphuric acid on different formation assemblies under varying conditions

2.1. Introduction

CO_2 emissions from coal fired power plants are likely to include minor amounts of SO_2 (IEAGHG, 2011). While CO_2 reacts with the formation brine to form weak H_2CO_3, SO_2 reaction can result in strong acids, like H_2SO_4 (Ellis et al., 2010). Hydrolysis, oxidation and disproportionation describe the dissolution mechanisms of SO_2 in water (Crandell et al., 2010; Ellis et al., 2010). They result in the formation of sulphurous acid, sulphuric acid and sulphuric acid with hydrogen sulphide or elemental sulphur, respectively. However, modelling done by Crandell et al. (2010) and Ellis et al. (2010) suggests that SO_2 dissolution from within the $scCO_2$ plume is limited by diffusion, resulting in up to 75% of the SO_2 remaining in the gas phase. The formation of stronger acids is likely to induce enhanced mineral dissolution and precipitation (Kaszuba et al., 2005; Xu et al., 2007; Crandell et al., 2010; Ellis et al., 2010). The SO_2 induced alterations are expected to be greater near well than further away in the reservoir (Ellis et al., 2010). Reactive transport modelling of CO_2-SO_2 injection has predicted the formation of sulphuric acids around the well bore resulting in a pH of 0-1 as well as enhanced mineral dissolution and porosity (Knauss et al., 2005; Xu et al., 2007). Further, CO_2 trapping in the form of carbonates and SO_2 trapping in the form of sulphates, sulphur and minor pyrite has been predicted to occur within and outside the acidified zone. The presence of iron bearing mineral phases during CO_2-SO_2 injection is suggested to increase CO_2 mineral trapping through SO_2 induced iron reduction and siderite precipitation (Palandri et al., 2005a; Garcia et al., 2011; Garcia et al., 2012; Schoonen et al., 2012). The low brine pH induced by SO_2 impurities has been found to be buffered and neutralized, in particular in the presence of carbonates, which were

converted to sulphates (Pearce et al., 2015). Possible mineral reactions induced by H_2SO_4 acidification (Equation 2.1) are demonstrated in Equation 2.2 to Equation 2.8.

$$H_2SO_4 \rightarrow SO_4^{2-} + 2\ H^+ \quad (2.1)$$

$$Ca(CO_3) + 2\ H^+ \rightarrow Ca^{2+} + CO_2(aq) + H_2O \quad (2.2)$$

$$Ca(Fe,Mg)(CO_3)_2 + 4\ H^+ \rightarrow\ Ca^{2+} + (Fe,Mg)^{2+} + 2\ CO_2(aq) + 2\ H_2O \quad (2.3)$$

$$(Na,K)AlSi_3O_8 + 4\ H^+ \rightarrow (Na,K)^+ + Al^{3+} + 3\ SiO_2(aq) + 2\ H_2O \quad (2.4)$$

$$(Mg,Fe)_5Al(Si_3Al)O_{10}(OH)_8 + 16\ H^+ \rightarrow 5\ (Fe,Mg)^{2+} + 2\ Al^{3+} + 3\ SiO_2(aq) + 12\ H_2O \quad (2.5)$$

$$Al_2Si_2O_5(OH)_4 + 6\ H^+ \rightarrow 2\ Al^{3+} + 2\ SiO_2(aq) + 5\ H_2O \quad (2.6)$$

$$Ca^{2+} + SO_4^{2-} \rightarrow CaSO_4(s) \quad (2.7)$$

$$Ca^{2+} + SO_4^{2-} + 2\ H_2O \rightarrow CaSO_4 \cdot 2H_2O(s) \quad (2.8)$$

Equation 2.1 shows the dissociation of sulphuric acid, the product of oxidation of SO_2, which leads to an abundance of sulphate and hydrogen ions. The hydrogen ions react with different minerals resulting in their dissolution. The reaction of calcite (Equation 2.2) and ankerite (Equation 2.3) results in the release of bivalent cations, dominantly Ca, and aqueous CO_2. The released Ca reacts with the sulphate from Equation 2.1 to form anhydrite (Equation 2.7) or gypsum (Equation 2.8). The precipitation of calcium sulphates removes ions from the reaction brine, resulting in a reduction in electrical conductivity (EC). Equation 2.4 shows the acid activated reaction of feldspar, which results in the release of Na or K, Al and aqueous SiO_2. Chlorite dissolution (Equation 2.5) contributes Fe or Mg, Al and aqueous SiO_2 to the brine, while kaolinite dissolution (Equation 2.6) only results in an increase in Al and aqueous SiO_2. The ratio of released Al to SiO_2(aq) is 1:3 for feldspar, 2:3 for chlorite and 1:1 for kaolinite. The dissolution of both carbonates and silicates result in a buffering of the pH by converting H^+ to H_2O. Further, they result in a decrease in EC by converting univalent

hydrogen ions and releasing bi- or trivalent ions for which the EC probe has a different sensitivity.

Most experimental studies on CO_2 storage use pure CO_2 streams (Kaszuba et al., 2003; Bateman et al., 2005; Liu et al., 2012), which is unlikely to be achieved with the currently available capture technologies (Kather et al., 2007). The geochemical impact of CO_2-SO_2 storage, on the other hand, is less thoroughly investigated. Existing experimental studies include investigations on the reaction of individual mineral phases or rocks with CO_2-SO_2 gas and their resulting geochemistry (Palandri et al., 2005a; Garcia et al., 2011; Kummerow and Spangenberg, 2011; Garcia et al., 2012; Glezakou et al., 2012; Schoonen et al., 2012; Pearce et al., 2015), studies on mineral dissolution and precipitation (Summers et al., 2004; Flaathen et al., 2010; Flaathen et al., 2011; Wilke et al., 2012) and experiments on changes in sorption behaviour induced through CO_2-SO_2 storage (Sakurovs et al., 2011). The incorporation of SO_2 into high pressure and temperature experimental set ups was achieved in two ways. The first was the use of an aqueous proxy for the dissolved gas, e.g. sulphate (SO_4^{-2}), but was limited to the impact of elevated sulphate on reaction pathways and rates only (e.g. Flaathen et al., 2011). Alternatively SO_2 was introduced as a minor gas in the CO_2 stream (e.g. Palandri et al., 2005a; Pearce et al., 2015). The latter represents the real case better but is harder to implement.

Most experimental studies focused on the reaction of pure mineral phases with CO_2-SO_2 (Palandri et al., 2005a; Garcia et al., 2011; Garcia et al., 2012; Glezakou et al., 2012; Wilke et al., 2012). However, reaction rates derived from these experiments are likely to require modifications when describing a reservoir system, due to interactions between multiple reactions, which result in the precipitation of secondary minerals leading to coating and reduced dissolution rates of primary minerals as well as variations in porosity and permeability limiting reactive fluid access (White and Brantley, 2003).

Mineral reaction rates can be calculated as the product of the minerals reactive surface area, its reactive rate constant and the proximity to equilibrium between the mineral and the solution as shown in Equation 2.9 (Lasaga, 1995).

$$r = A_s k \left(1 - \frac{Q}{K}\right) \quad (2.9)$$

r = reaction rate

A_s = mineral surface area

k = rate constant

Q = activity product

K = equilibrium constant

The mineral specific rate constant k is usually reported at 25°C and has to be re-calculated to the actual reaction temperature. Further, the rate constant is pH dependant, which can be described by using separate rate constants and activation energies for acidic, neutral and basic mechanisms (Equation 2.10).

$$k = k_{25}^{nu}\left[\frac{-E_a^{nu}}{R}\left(\frac{1}{T} - \frac{1}{T_0}\right)\right] + k_{25}^{H}\left[\frac{-E_a^{H}}{R}\left(\frac{1}{T} - \frac{1}{T_0}\right)\right] a_H^{n_H} + k_{25}^{OH}\left[\frac{-E_a^{OH}}{R}\left(\frac{1}{T} - \frac{1}{T_0}\right)\right] a_{OH}^{n_{OH}} \quad (2.10)$$

E_a = activation energy

R = molar gas constant

T = temperature in K

T_0 = reference temperature (298.15 K)

nu = neutral mechanism

H = acid mechanism

OH = base mechanism

a = hydrogen ion activity

n = H^+ power term

This study focuses on the geochemical impact of SO_2 in the injection stream by isolating the effects of SO_2 from those of CO_2. Short term batch experiments were conducted to examine mineral reactions under SO_2 induced acidification. Oxidation was assumed to be the main mechanism of SO_2 dissolution. Hence, H_2SO_4 was used as an aqueous proxy of SO_2. The H_2SO_4-brine was reacted with different reservoir and seal rocks to identify changes in rock mineralogy and water chemistry. Sedimentary rock samples from two different locations were used. Samples from the Western Canada Sedimentary Basin were reacted at different sample particle sizes, temperature and pH conditions to evaluate the importance of reactive surface area (A_s), activation energy (E_a) and pH dependency (n) on reaction rates. The evaluation of reactive surface area impacts was of special interest to gain information on how to upscale and apply experimental results to reservoir scale. Samples originating the Surat Basin were used to examine the effect of SO_2 on a potential storage site.

2.2. Methodology

2.2.1. Material characterization and preparation

Ten rock samples were used to examine the effects of sulphuric acid on different mineralogies. Six of them (AF-01-06) originated the Western Canada Sedimentary Basin, British Columbia, Canada, and were provided by Simon Fraser University, Canada. The other four (AF-07-10) were sampled from the Chinchilla-4 core in the Surat Basin, Queensland, Australia and were provided by the University of Queensland, Australia.

The Western Canada Sedimentary Basin samples were used to investigate the effect of SO_2 induced acidification on different mineralogies at varying temperature, pH and sample particle size. They were chosen based on their mineralogical properties to investigate the behaviour of selected mineral phases. A carbonate-rich sample, two silicate-dominated samples with minor hematite and three samples with a comparatively high amount of chlorite were investigated. Carbonates were of interest due to their high

reactivity and pH buffering capacity. The silicate-rich rocks were selected to study the behaviour of less reactive mineral phases. Hematite was of importance since it had been previously proposed to trap injected CO_2-SO_2 gas mixtures geochemically (Palandri et al., 2005a; Garcia et al., 2011). Chlorite was of interest due to its high compositional variability, which results in variable reaction rates, and due to the common occurrence of chlorite in sedimentary rocks of the Surat Basin. To better understand chlorite rates several sedimentary rocks with different chlorite compositions were used. The Surat Basin samples could not be used for the parameter analysis due to a limited sample volume. They were used to determine the effect of SO_2 co-injection on a possible storage site.

The mineralogy of the Western Canada Sedimentary Basin samples was determined using Quantitative X-ray Powder Diffraction (XRD), X-ray Fluorescence (XRF), Optical Microscopy, Scanning Electron Microscopy (SEM) with Energy Dispersive Spectroscopy (EDS) and Electron Microprobe. Step-scan XRD data were collected on a Bruker D8 Focus Bragg-Brentano diffractometer at the University of British Columbia (UBC). The data were refined using Bruker Topas software for the standardless Rietveld method (Rietveld, 1969). Since this method only provides information about the quantitative composition of crystalline mineral phases, additional analyses were performed to determine the content of smectite and the presence of iron oxides and oxyhydroxides. Thin sections where prepared by Vancouver Petrographics and examined at the Petrology and Tectonics Lab at Simon Fraser University (SFU). The thin-section samples were then carbon coated at UBC to be studied using a Philips XL30 SEM with a Bruker Quantax 200 EDS and a fully-automated Cameca SX-50 Scanning Electron Microprobe. Additionally XRF data were obtained by ALS Minerals and evaluated at SFU using the linear programming normative (LPNORM) analysis code (de Caritat et al., 1994). LPNORM distributes the oxides measured using XRF to the mineral phases present determined through XRD, thin section petrology and SEM, resulting in a full chemical accounting of the major elements as mineral modal amounts. The XRD, XRF and Microprobe results are listed in Appendix A. The mineralogies of the Western Canada Sedimentary Basin samples are shown in Table 2.1.

Table 2.1 Mineralogy of the Western Canada Sedimentary Basin samples in wt%.

		AF-01	AF-02	AF-03	AF-04	AF-05	AF-06
Quartz	SiO_2	67.92	37.27	65.81	45.11	63.41	50.00
K-Feldspar	$KAlSi_3O_8$	3.25	21.22	19.68		3.60	2.20
Albite	$NaAlSi_3O_8$	1.52	25.72	0.42	30.00	14.22	2.20
Illite/ muscovite	$K(Al,Mg,Fe)_2(AlSi_3O_{10})(OH)_2$	3.00	5.00	9.00	10.40	6.00	23.40
Kaolinite	$Al_2Si_2O_5(OH)_4$	4.02	6.17	2.20	7.46	9.92	7.01
Chlorite	$(Mg,Fe)_5Al(Si_3Al)O_{10}(OH)_8$	1.86	1.93	1.20	5.47	4.90	4.50
Calcite	$CaCO_3$	11.17	0.51	0.04	1.17	0.57	0.04
Dolomite	$CaMg(CO_3)_2$	4.37					
Siderite	$FeCO_3$	0.12	0.38	0.21			2.21
Hematite	Fe_2O_3		0.80	0.58			
Pyrite	FeS_2	0.02				0.02	0.79

These data indicate that AF-01 is dominated by quartz and carbonates (calcite and dolomite) with lesser amounts of K-feldspar, albite, muscovite, kaolinite, chlorite, siderite and pyrite. The sample AF-02 contains quartz, K-feldspar and plagioclase feldspar with lesser amounts of mica, kaolinite, chlorite, calcite, siderite and hematite. The microprobe results identify the plagioclase in AF-02 as dominantly albite and the mica as muscovite. AF-03 is dominated by quartz, K-feldspar and muscovite. Small amounts of kaolinite, chlorite, albite, hematite, siderite and calcite are present as well. In sample AF-04, quartz, albite, illite and kaolinite dominate, with minor amounts of chlorite and calcite. AF-05 contains major quartz, plagioclase, and kaolinite with minor K-feldspar, mica, chlorite, calcite and pyrite. The mica was identified as illite, and plagioclase as labradorite with a Na:Ca ratio of 2:3. The caprock sample, AF-06, is dominated by quartz and illite with lesser amounts of K-feldspar, albite, kaolinite, chlorite, siderite, calcite and pyrite. Microprobe results indicated a Fe:Mg ratio of approximately 3:2 for the chlorite composition of AF-01 and AF-04, and a 1:1 ratio for AF-05. Minor amounts of Ca and Mg were detected in the siderite of AF-06.

These particular samples were selected based on mineral phases of interest. AF-01 was chosen due to its high amount of carbonates. AF-02 and AF-03 were chosen

for their abundance of silicates and the presence of hematite. AF-04, AF-05 and AF-06 were chosen because of their comparatively high volume of chlorite. AF-06 was of special interest as a shale sample with an abundance of clays.

The Surat Basin was subsampled from the Chinchilla-4 well core, which is located approximately 10 km south-south-east of Miles, Queensland. The subsamples originated from the Precipice Sandstone, Evergreen and Hutton Sandstone Formations. The mineralogy of the core had already been investigated with hyperspectral logging, XRD, QEMScan™, Optical Microscopy and SEM (Farquhar et al., 2013; Pearce et al., 2015). The results of the XRD and QEMScan analysis are listed in Appendix A. A summary of the Surat Basin sample mineralogies is shown in Table 2.2.

Table 2.2 Mineralogy of the Surat Basin samples in wt%.

		AF-07	AF-08	AF-09	AF-10
Quartz	SiO_2	94.00	35.78	43.00	50.00
K-Feldspar	$KAlSi_3O_8$	0.10	25.64	10.00	6.00
Albite	$NaAlSi_3O_8$	0.10	7.72	4.00	7.00
Illite/ muscovite	$K(Al,Mg,Fe)_2(AlSi_3O_{10})(OH)_2$	3.00	1.85	3.00	9.00
Biotite	$K(Mg,Fe)_3AlSi_3O_{10}(OH)_2$		0.39	2.00	8.00
Kaolinite	$Al_2Si_2O_5(OH)_4$	2.55	12.17	18.00	7.00
Chlorite	$(Mg,Fe)_5Al(Si_3Al)O_{10}(OH)_8$	0.20	3.69	4.00	7.00
Calcite	$CaCO_3$		0.16		
Ankerite	$Ca(Fe,Mg)(CO_3)_2$			10.00	4.00
Siderite	$FeCO_3$			4.00	
Hematite	Fe_2O_3			2.00	0.50
Unclassified			12.60		

Sample AF-07 originated from the Precipice Sandstone Formation, which is the most promising storage formation of the Surat Basin. It is dominated by quartz, with minor mica, kaolinite, feldspars and chlorite. The two caprock samples from the Evergreen Formation, AF-08 and AF-09, contain major quartz, K-feldspar, plagioclase and kaolinite with minor mica, biotite, chlorite and carbonates. The analytical results indicate that calcite is present in AF-08, while AF-09 is dominated by ankerite, siderite

and hematite. The analytical data for AF-08 show 12.6 wt% of unclassified mineral phases. AF-10 is a mineralogically reactive sandstone from the Hutton Sandstone Formation, which is also under consideration as a potential storage formation. It consists of quartz, mica, biotite and chlorite with minor K-feldspar, plagioclase, kaolinite and ankerite. The mica was identified as illite for samples AF-07, AF-08 and AF-09 and as muscovite for sample AF-10. The chlorite in all samples was determined as iron-rich (Fe:Mg = 3:1) using hyperspectral logging (Farquhar et al., 2013).

The Western Canada Sedimentary Basin samples were prepared for the experiments in three ways: cut into blocks (1.5 cm > hgt > 1 cm), crushed with a sledge hammer (dia ≤ 3 mm) and ground to powder using a mortar and pestle (dia ≤ 300 µm). The samples were reacted in these three forms under the same conditions to investigate the effect of sample particle size. Only block samples were used for the Surat Basin samples to better simulate the brine-rock interaction. For the block samples, it has to be noted that in the case of low rock permeability some of the identified mineral phases might not have been in contact with the brine.

The synthetic reaction brine was based on groundwater data from the Evergreen Formation sourced from Hodginkson et al. (2009). However, due to gaps in the water dataset, modelling had to be undertaken to generate missing data. This was done using the Spec8 and React modules of Geochemist's Workbench^{TM} (GWB) software package (Bethke and Yeakel, 2012a). Equilibrium modelling was used to evaluate the quality of the existing water data of the Evergreen Formation and to correct or estimate analytical values by assuming equilibrium with the Evergreen Formation minerals at 70°C in GWB. The resulting modelled water composition is reported in Table 2.3.

The synthetic reaction brine was mixed to largely fit the modelled water composition of the Evergreen Formation. The aluminum and iron content of the modelled brine were neglected in the synthetic brine due to their low values. Sulphuric acid was added to simulate the SO_2 in the experiment and the brine water acidification. Hence the original sulphate content of the groundwater sample was neglected as well. A total of three solutions were prepared: a baseline with no acid, a pH 3 and a pH 1.5 solution. In order to simulate the redox conditions at typical carbon storage depth, the synthetic

brine solutions were degassed if necessary. Through bubbling with nitrogen, oxygen was removed from the brine. This step was only necessary in cases in which a pH of above 3 was established. At this point iron oxides and hydroxides precipitate under oxidising conditions.

The final composition of the synthetic brine was determined at the SFU Groundwater Chemistry Laboratory. Samples of each synthetic brine were diluted 1:50 to analyse anion concentrations and 3:20 for cation analyses. The latter were further acidified with nitric acid (HNO_3^-). Anion concentrations (Cl^-, SO_4^{2-}) were determined using a Dionex ICS-3000 SP Ion Chromatography System (ICS) and major (Na, K, Ca, Mg, Fe) and minor (Al, SiO_2) element concentrations using a Horiba Jobin Yvon Ultima 2 Inductively Couple Plasma Atomic Emission Spectroscopy instrument (ICP-AES). Electrical conductivity (EC) and pH were measured using a Thermo Orion 01301MD Electrical Conductivity probe and a Thermo Orion 9107BNMD pH probe connected to a Thermo Orion 5 Star meter. The alkalinity (HCO_3) was measured only for the baseline solution by titrating a 10 mL sample with 0.1 M hydrochloric acid (HCl) using a 16900 Hach Digital Titrator. The brine properties are listed in Table 2.3.

Table 2.3 Modelled and actual synthetic brine composition in mmol/L.

	Modelled water composition	Actual water composition			
		pH 1.5 (a)	pH 1.5 (b)	pH 3	Baseline
pH	8.16	1.54	1.4	3.02	9.49
Al	$2.15x10^4$	$3.83x10^3$	$1.13Ex10^2$	$1.52x10^3$	$2.76x10^3$
Ca	0.05	0.05	0.05	0.02	0.02
Fe	$2.44x10^6$	$9.65x10^4$	$6.05x10^3$	$1.09x10^3$	$8.17x10^4$
K	0.06	0.08	0.07	0.07	0.07
Mg	0.19	0.18	0.17	0.19	0.18
Na	3.85	4.62	4.45	4.71	4.61
HCO_3	2.61				1.19
SO_4^{2-}	0.10	31.75	31.44	2.98	0.01
Cl^-	1.39	1.41	1.41	1.65	1.61
$SiO_2(aq)$	0.87	0.67	0.72	0.81	0.78

2.2.2. Experimental set up and procedure

A total of 40 batch reactor experiments (B-01 to B-40) were conducted. The Western Canada Sedimentary Basin samples were reacted under six different conditions and the Surat Basin samples only as blocks at 60ºC (Table 2.4). All samples were reacted with synthetic brine in 250 mL polypropylene-bottles for 30 days. To control the temperature conditions the samples were placed in an oven unless noted otherwise. The schematic and actual experimental set up is shown in Figure 2.1:

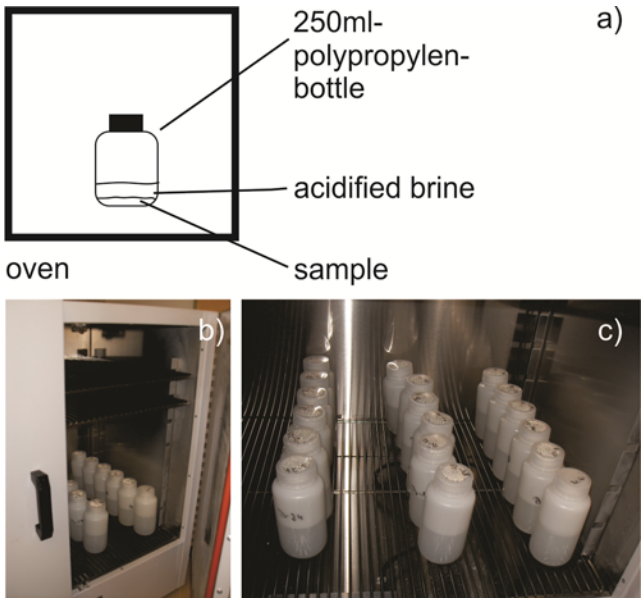

Figure 2.1 Schematic (a) and actual experimental set up (b+c).

The experimental conditions for the reaction of the Western Canada Sedimentary Basin samples were varied to investigate the effect of sample particle size, temperature and acidification. The first set of experiments (B-01 to B-06) was conducted to determine the baseline. For each Western Canada Sedimentary Basin sample, 3 g of mortared sample were reacted with 150 mL of the baseline solution at 60°C. It is important to note that these experiments were set up and sampled within a glove box. The air in the glove box was replaced with a nitrogen atmosphere to simulate reducing conditions, which prevail at a typical injection depth of about 800 m. This step was necessary to prevent iron oxides and hydroxide precipitation due to the presence of atmospheric O_2. In the experiments B-07 to B-12, 3 g of mortared sample of each Western Canada

Sedimentary Basin rock were reacted with 150 mL of the pH 1.5 solution at 60°C. The following experiments (B-13 to B-24) were reacted at the same pH and temperature conditions, but the sample particle size was varied as crushed and block. In experiments B-13 to B-19, 3 g of crushed sample was reacted with brine, while in B-18 to B-24 the rock samples were reacted as blocks. The exact weight of the block samples was determined prior to the experiment. The next set of experiments (B-25 to B-30) investigated the impact of a different starting pH by reacting 3 g of mortared sample with 150 mL of the pH 3 brine at 60°C. Like the baseline experiments, the pH 3 experiments were set up and sampled within a glove box to control the redox conditions. In experiments B-31 to B-36 the temperature effect was studied. 3 g of mortared sample for each Western Canada Sedimentary Basin sample was reacted outside the oven (~22°C) with 150 mL of the pH 1.5 solution. In the last set of experiments (B-37 to B-40), the Surat Basin samples were reacted with 100 mL of the pH 1.5 brine at 60°C. The rock samples were reacted as blocks, the exact weight of which were determined prior to the experiment. The experimental conditions for each experiment are listed in Table 2.4 and in more detail in Appendix B.

Table 2.4 Different conditions of batch reactor experiment B-01 to B-40.

	Sample origin	Sample particle size	Temperature (°C)	Starting pH
B-01-B-06	Canada	mortared	60	9.5
B-07-B-12	Canada	mortared	60	1.5
B-13-B-18	Canada	crushed	60	1.5
B-19-B-24	Canada	block	60	1.5
B-25-B-30	Canada	mortared	60	3
B-30-B-36	Canada	mortared	22	1.5
B-37-B-40	Australia	block	60	1.5

Ten to fifteen (10 to 15) 2 mL aliquots were sampled from the experimental brine over 30 days. The sampling intervals were lengthened over the course of the experiment and the exact sampling times are listed in Appendix A. To ensure fluid access to all mineral phases during the experimental time span the bottles were shaken after every sampling event. All reactions involving the pH 1.5 solution were sampled 15 times. Due to a longer settling time of the rock sample at higher pH, the number of water samples was reduced to 10 for the pH 3 and baseline experiments.

2.2.3. Analytical methods

The sampled aliquots were processed and analyzed at the SFU Groundwater Chemistry Laboratory. To remove colloids, brine aliquots were filtered using 0.45 µm Supor Membrane syringe filters. Electrical conductivity and pH were measured using a Thermo Orion 01301MD Electrical Conductivity probe and a Thermo Orion 9107BNMD pH probe connected to a Thermo Orion 5 Star meter. The brine samples were divided and diluted 1:50 and 3:20 to ensure the sample size was sufficient for analysis. Chloride (Cl^-) and sulphate (SO_4^{2-}) concentrations were determined on the 1:50 samples using a Dionex ICS-3000 SP ICS. The 3:20 samples were acidified with HNO_3^- and analyzed for sodium (Na), potassium (K), calcium (Ca), magnesium (Mg), iron (Fe), aluminum (Al) and silica (SiO_2(aq)) with a Horiba Jobin Yvon Ultima 2 ICP-AES. Both, the ICS and the ICP-AES have a 1 sigma error of ±3%. The alkalinity was measured only for the baseline solution. For alkalinity 1 mL of the 1:50 samples was diluted to 5 mL and titrated with 0.005 M HCl using a 16900 Hach Digital Titrator. The resulting water chemistry data was entered in Geochemist's Spreadsheet™ (GSS) from GWB and is listed in Appendix C. GSS was further used to calculate the saturation indices of selected mineral phases to predict their behaviour.

The reacted rock samples were mounted and carbon coated at UBC. There they were studied under a Philips XL30 SEM to verify the water chemistry results.

2.3. Results and discussion

2.3.1. Western Canada Sedimentary Basin samples

The reaction of mortared Western Canada Sedimentary Basin samples with the pH 1.5 brine at 60°C resulted in significant changes in the water chemistry. The change in the measured brine parameters was greatest over the first 2 days of experiment and flattened over the remaining 28 d. The rapid initial increase is most likely due to the presence of sample fines, which have a much larger reactive surface area compared to the coarser sample particles. The amount of change was highly dependent on the mineralogy of the sample. The greatest differences were observed for sample AF-01,

which has greater amounts of highly reactive carbonates. However, significant changes in the water composition were observed for all samples, indicating that less reactive mineral phases participated as well. Comparatively large fluctuations of up to 7.9% and 10.5% from the mean value were observed in the measured SO_4^{2-} and Cl^- concentrations, respectively. This was most likely due to errors in dilution considering that the SO_4^{2-} and Cl^- concentrations were measured at a dilution of 1:50, which magnifies errors in the sample preparation by 50. The outcomes of the experiments reacting mortared Western Canada Sedimentary Basin sample with pH 1.5 brine at 60°C are summarized in the following paragraphs.

AF-01

Over the course of the AF-01 baseline experiment, changes in the brine properties were observed (Appendix B). The greatest change was a decrease of 0.7 mmol/L for Na. The pH declined by about 0.5 over the course of the experiment. The Mg content in the brine was reduced by 0.1 mmol/L, while SO_4^{2-}, Ca, Fe, Al and K increased. The concentrations of SiO_2, HCO_3 and Cl^- as well as the EC remained fairly constant.

Of all Western Canada Sedimentary Basin samples, the reaction of AF-01 with the pH 1.5 brine at 60°C resulted in the greatest changes in solution properties (Figure 2.2). The fluid pH was buffered significantly and increased to 6, which was most likely the result of carbonate dissolution (Figure 2.2a). The EC on the other hand dropped rapidly by approximately 13000 µS/cm. This is likely due to mineral precipitation and/or pH buffering, which removes hydrogen ions from the brine. The measured amount of Na and Cl^- remained fairly stable throughout the experiment. Other ion concentrations showed significant changes. The greatest change was observed for Ca, (Figure 2.2b), likely due to the dissolution of fast reacting carbonates. The Ca concentration increased to 16 mmol/L within the first 12 hours of reaction, and subsequently dropped by 4 mmol/L to stabilize at approximately 12 mmol/L. This coupled with a decrease in SO_4^{2-} by 13 mmol/L suggests the precipitation of calcium sulphate. Due to dolomite dissolution, the Mg content increased by 5 mmol/L within the first 2 d of reaction, subsequently it stayed constant. The SiO_2, K, Fe and Al concentrations increased rapidly at the beginning of the experiment (Figure 2.2c), suggesting the dissolution of silicate phases like chlorite and K-feldspar. After about 2 d, the amount of SiO_2 in the brine started to

decrease indicating silicate precipitation. The Fe and Al content dropped rapidly after their initial increase and levelled out at ~0.002 mmol/L indicating the formation of iron and aluminium bearing mineral phases. The K content stayed fairly stable after an initial rise, which might be due to the precipitation of a K bearing mineral.

In order to identify precipitation processes explaining the decrease in EC, Ca, SO_4^{2-}, SiO_2, Al and Fe, the saturation indices of anhydrite, gypsum, alunite and smectite were calculated using GSS (Figure 2.3). Anhydrite and gypsum reached saturation and probably started to precipitate within the first 12 h of reaction (Figure 2.3a). This would account for most of the drop in EC, Ca and SO_4^{2-}. Throughout the experiment gypsum was close to saturation, while anhydrite was slightly over-saturated. This suggests that anhydrite precipitation might be preferred over gypsum precipitation; however, at 60ºC, gypsum should be preferred kinetically. Alunite reached saturation after ~1 d of reaction (Figure 2.3b) and was likely to precipitate as well, accounting to some extent for the decrease in EC, Al and SO_4^{2-}, as well as the reduced rate of increase in K. Further, smectite precipitation was identified as a potential SiO_2 and Al sink. It reached saturation after about 2 d and would result in the consumption of some Ca, Mg, K and/or Na from the brine as well. However, the rate of nucleation and precipitation of smectite may be low in this time frame. The GSS calculations did not identify a process resulting in the removal of Fe from the brine. Potential sinks of Fe are iron bearing smectite or sulphate.

The SEM analyses of the baseline samples showed an abundance of quartz, calcite and dolomite in AF-01. The SEM analyses of the reacted rock sample on the other hand did not show any calcite or dolomite, which provides evidence of the dissolution of carbonate minerals. Additionally, quartz and calcium sulphate phases were identified. The presence of calcium sulphate validates the assumption of calcium sulphate precipitation. Examples for newly formed calcium sulphate are shown in Figure 2.4.

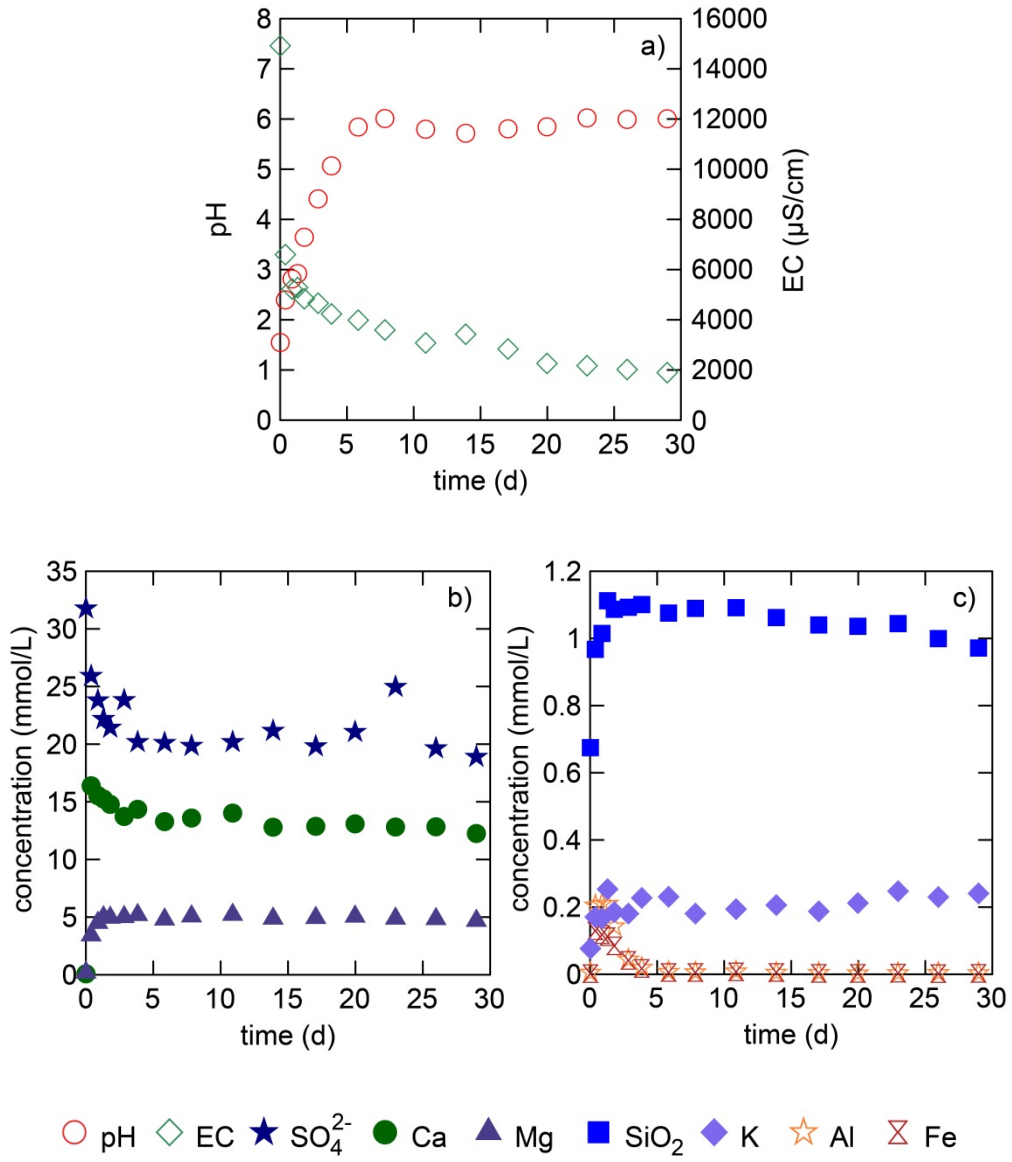

Figure 2.2 **Water chemistry for the reaction of AF-01 with pH 1.5 brine at 60°C over 30 d, showing changes in pH (a), EC (a) and, selected ions (b+c).**

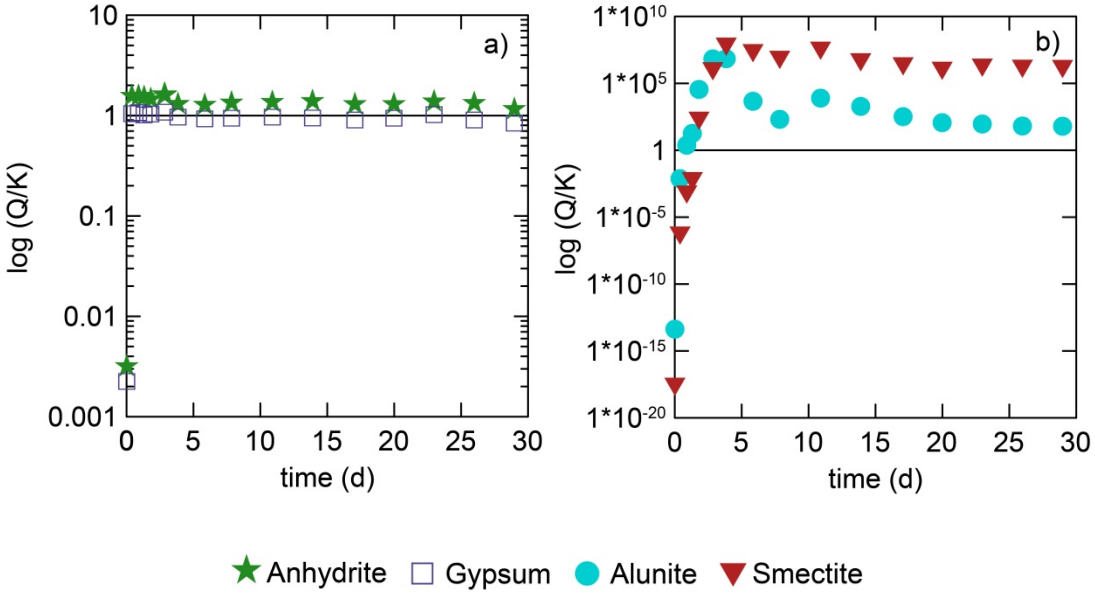

Figure 2.3 **Saturation index for anhydrite and gypsum (a) as well as alunite and smectite (b).**

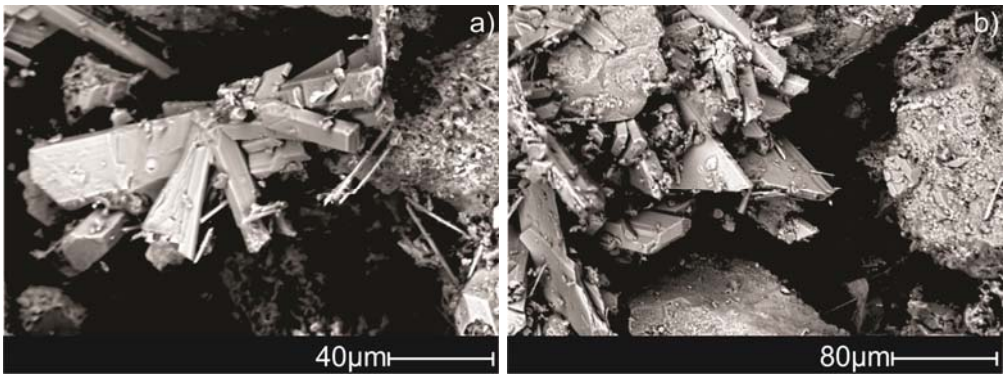

Figure 2.4 **SEM pictures of newly formed calcium sulphate mineral phases in AF-01 after the reaction with pH 1.5 brine at 60°C (a+b).**

AF-02

The baseline experiment of AF-02 showed variations in the Na concentration of up to ~0.9 mmol/L and an increase in SiO_2 of about 0.25 mmol/L (Appendix B). SO_4^{2-}, Ca, Fe, Al and K increased as well. The pH dropped by approximately 0.4 to 9.07. The Mg concentration decreased by 0.5 mmol/L. HCO_3, Cl^- and the EC showed some variations, but remained fairly constant over the course of the baseline experiment.

The reaction of AF-02 with pH 1.5 solutions at 60°C resulted in lesser change in the brine properties compared to AF-01 (Figure 2.5). Over the course of the experiment, the pH increased slightly by 0.3 (Figure 2.5a). The EC on the other hand dropped rapidly within the first day and more gradually after day 15. In total EC decreased by ~6000 µS/cm. This drop in EC is likely due to acid induced mineral dissolution, which results in a removal of hydrogen ions. The SO_4^{2-}, Na and Cl^- content stayed relatively constant over the 30 d of the experiment. Figure 2.5b and c show an increase in SiO_2, K, Mg, Ca, Fe and Al throughout the experiment. The concentration gain of these ions suggests dissolution of mineral phases like K-feldspar, muscovite and chlorite. The greatest concentration gain was observed for SiO_2 with an increase of 6.3 mmol/L. The Al content of the brine changed by 4 mmol/L and the Mg content by 2.5 mmol/L, while the rise in K and Fe was less than 1 mmol/L. A small gain in Ca suggests calcite dissolution. Both, silicate and carbonate dissolution consume hydrogen ions resulting in the slight pH increase. The ion concentrations showed no decrease over the course of the experiment, giving no evidence for mineral precipitation.

Quartz, K-feldspar, plagioclase and mica are dominant in the baseline sample of AF-02. The SEM analyses of the reacted AF-02 sample identified the same mineral phases, giving no qualitative or visual evidence for mineral reactions.

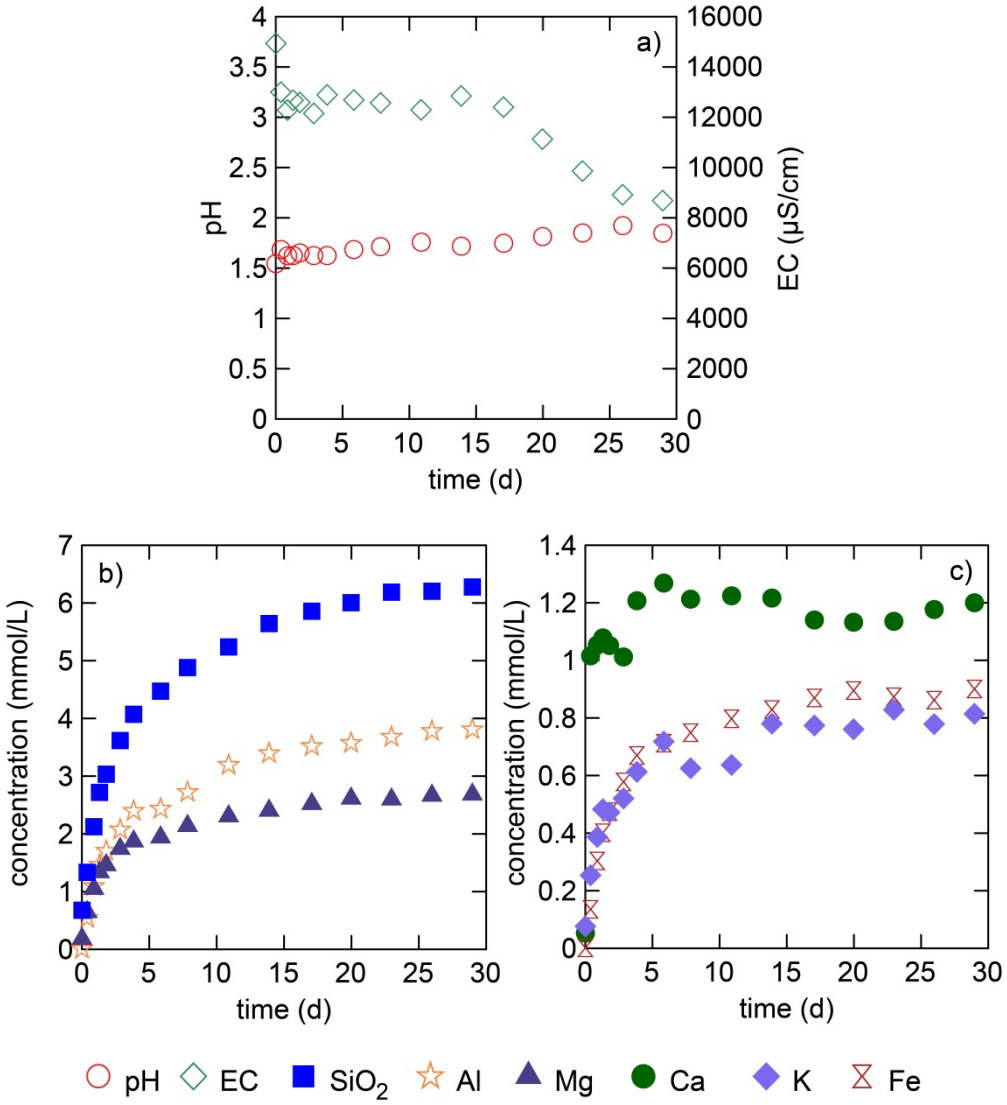

Figure 2.5 **Water chemistry for the reaction of AF-02 with pH 1.5 brine at 60°C over 30 d, showing changes in pH (a), EC (a) and, selected ions (b+c).**

AF-03

In the baseline reaction of AF-03, the pH decreased by ~0.25 (Appendix B). The greatest variation was observed for Na with a decrease of 0.5 mmol/L. HCO_3 was slightly reduced by 0.2 mmol/L, while SiO_2 showed a concentration gain of about 0.4 mmol/L.

The concentrations of Ca, Fe, Al and K increased, while Mg, Cl^- and SO_4^{2-} as well as the EC remained relatively constant.

The reaction of AF-03 with pH 1.5 solution at 60°C resulted in the least change in water chemistry of all Western Canada Sedimentary Basin samples (Figure 2.6). The pH remained constant at 1.5 over the course of the experiment (Figure 2.6a). The EC on the other hand dropped slightly at the beginning of the experiment, increased after 2 d, and dropped again after 15d. Overall the EC declined by ~3000 µS/cm, which is likely due to acid induced mineral reactions. Except for SO_4^{2-}, Cl^- and Na, the ion concentrations showed significant changes over the course of the experiment. The greatest change was observed for SiO_2 (Figure 2.6b). SiO_2 increased by ~2.5 mmol/L suggesting that silicate mineral phases dissolved. These were likely K-feldspar, muscovite and chlorite considering the gain of ~1 mmol/L in K and Al and the slight increase in Mg and Fe concentrations (Figure 2.6b, c). A small increase in Ca of about 0.1 mmol/L may be the result of dissolution of calcite. The changes in ion concentrations give no indication of mineral precipitation.

The analyses of the AF-03 baseline sample show quartz and K-feldspar as the dominant mineral phases. The SEM results of the reacted sample match the baseline results giving no evidence for mineral reaction.

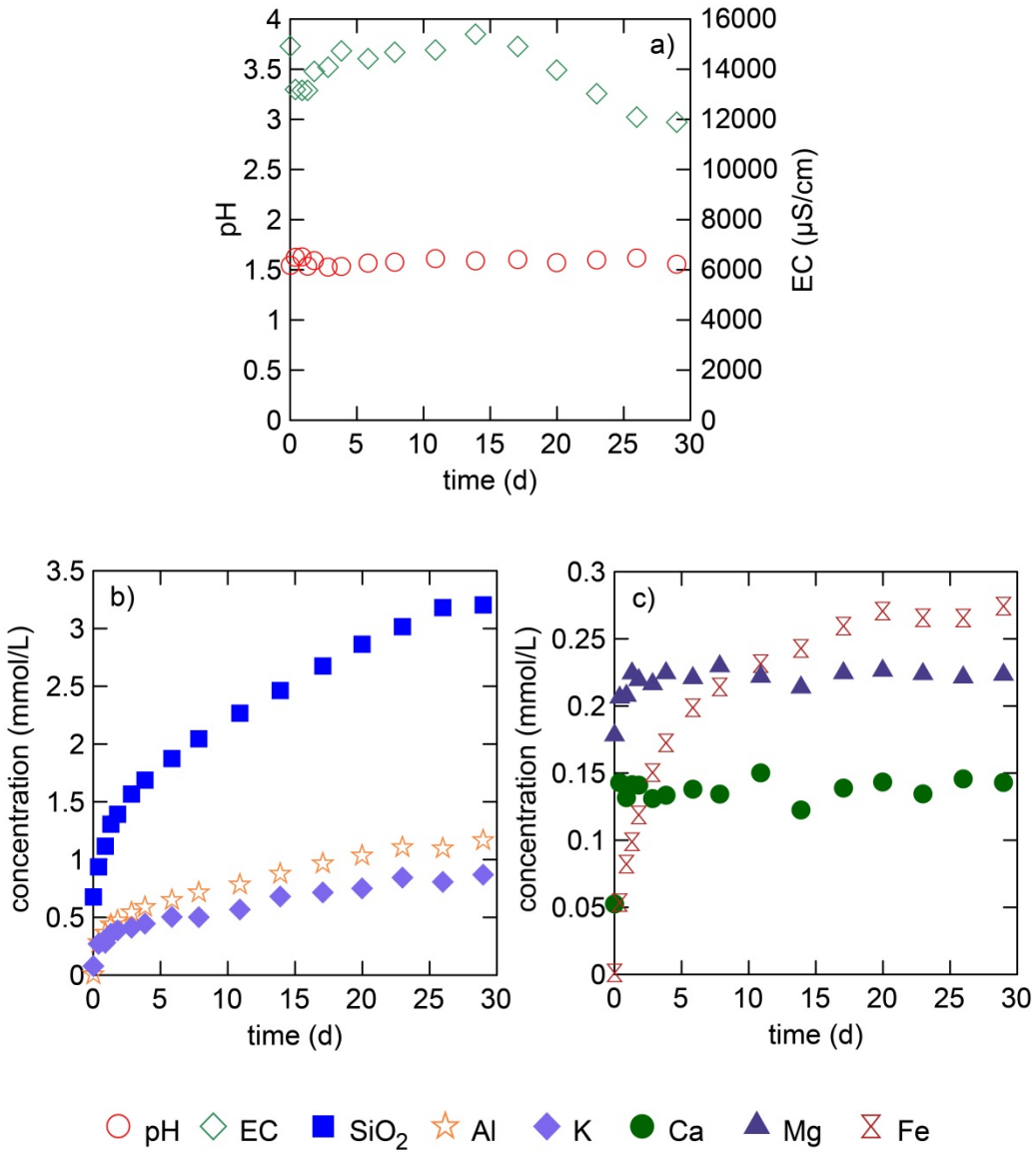

Figure 2.6 **Water chemistry for the reaction of AF-03 with pH 1.5 brine at 60°C over 30 d, showing changes in pH (a), EC (a) and, selected ions (b+c).**

AF-04

The reaction of AF-04 with the baseline solution resulted in a decrease in Na of 0.6 mmol/L and in a reduction in Mg and HCO_3 by about 0.1 mmol/L (Appendix B). The SO_4^{2-}, Ca, Fe and Al concentrations increased over the course of the baseline experiment. The concentrations of K, SiO_2 and Cl^- as well as the EC showed slight variations, but remained fairly constant. The pH declined by approximately 0.4 to 9.07.

The reaction of AF-04 with pH 1.5 brine at 60°C resulted in significant brine property changes, which are plotted in Figure 2.7. Over the course of the experiment the pH was slightly buffered likely due to mineral dissolution. The pH increased by ~0.6 to ~2.1, while the EC decreased in two steps by a total of 9000 µS/cm (Figure 2.7a). The drop in EC is likely related to the buffering in pH, which reflects the removal of hydrogen ions. Selected ion concentrations of the brine are plotted in Figure 2.7b and c. The Ca concentration increased rapidly by 2.3 mmol/L at the beginning of the experiment, indicating the dissolution of calcite. The greatest change was observed for the SiO_2, Fe and Al content with concentration increases of approximately 5 mmol/L. Further, the amount of Mg in the brine increased by 2.5 mmol/L. These changes indicate the dissolution of silicate mineral phases like chlorite. K shows a minor increase of 0.1 mmol/L probably due to illite reaction. The concentrations of SO_4^{2-}, Cl^-, and Na stayed fairly constant and are therefore not plotted. No clear evidence for mineral precipitation is suggested in the evolution of the ion concentrations.

The SEM analyses for the reacted AF-04 sample identified quartz, albite, illite and kaolinite as the dominant mineral phases. The results matched the baseline experiments giving no visual or qualitative evidence of mineral reactions.

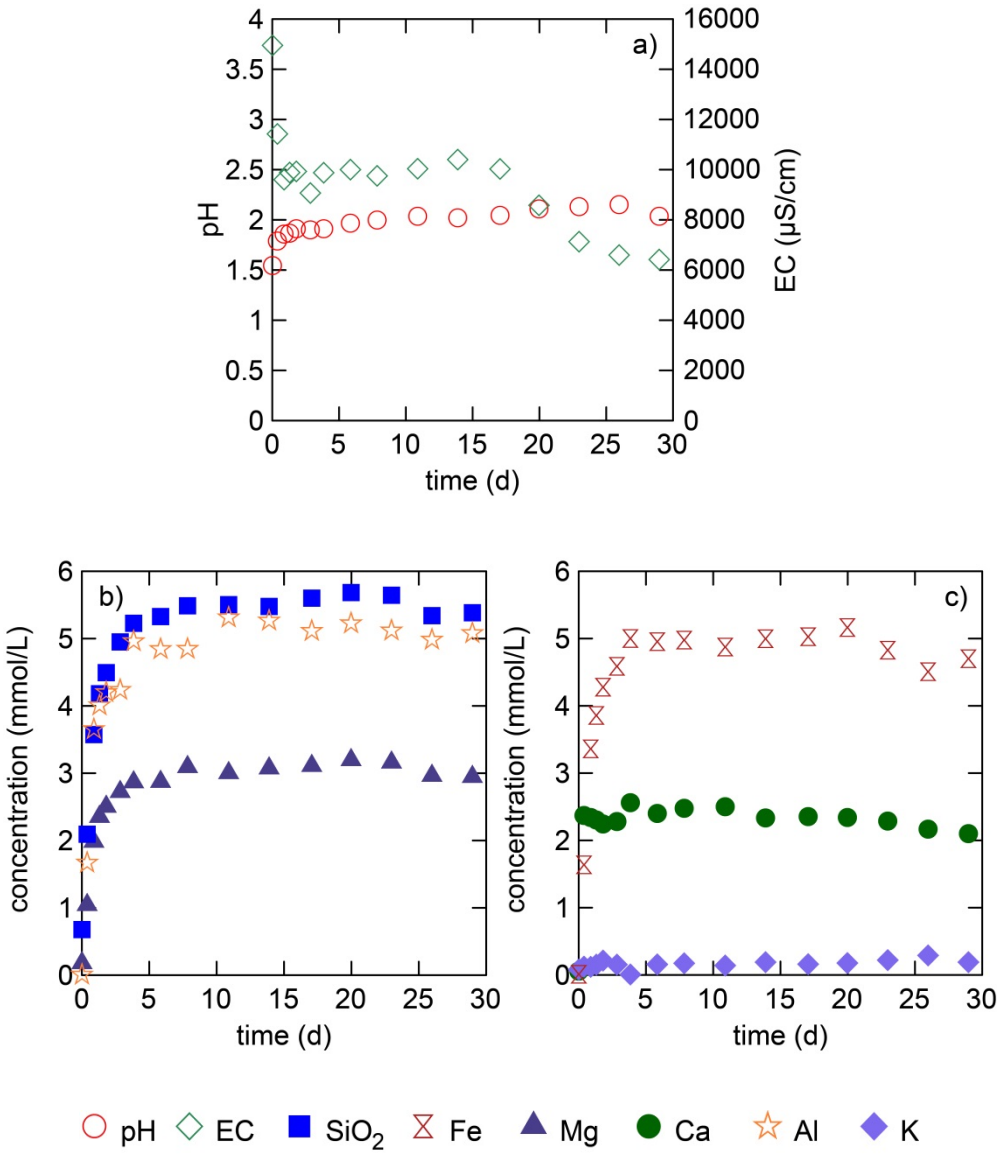

Figure 2.7 **Water chemistry for the reaction of AF-04 with pH 1.5 brine at 60°C over 30 d, showing changes in pH (a), EC (a) and, selected ions (b+c).**

AF-05

In the AF-05 baseline experiment the pH decreased by 0.7 over 30 d (Appendix B). The EC decreased slightly as well. The amount of Na in the brine varied by ~1 mmol/L and the SiO_2 content increased by 0.2 mmol/L. The Ca, Fe, Al and K concentrations increased over the course of the baseline experiment, while Mg

decreased slightly. No significant changes were observed for the other measured brine parameters.

The reaction of AF-05 with pH 1.5 brine at 60°C resulted in a slight buffering of the pH to 1.9 and a rapid decrease in the EC at the beginning of the experiment and further decrease to ~8000 µS/cm after 15 d (Figure 2.8a). The EC change is correlated to the pH increase, which describes the removal of hydrogen ions from the brine. Most ion concentrations show increasing trends throughout the experiment. The greatest concentration increases were observed for SiO_2 and Al, which increased by a total of ~5 mmol/L suggesting the dissolution of silicate phases (Figure 2.8b). These were most likely chlorite and K-feldspar considering the rise in Mg and Fe by 3 mmol/L and the slight rise in K by 0.3 mmol/L (Figure 2.8b, c). Ca increased by 0.5 mmol/L indicating calcite dissolution. The dissolution of silicate and carbonate minerals consumed hydrogen ions resulting in the pH increase. SO_4^{2-}, Cl^-, and Na on the other hand remained constant during the course of the experiment. The experimental results show no obvious indication that mineral precipitation occurred.

SEM analyses of the baseline sample showed an abundance of quartz, illite and plagioclase. The analyses of the reacted rock samples identified the same mineral phases, giving no qualitative or visual evidence for mineral reaction.

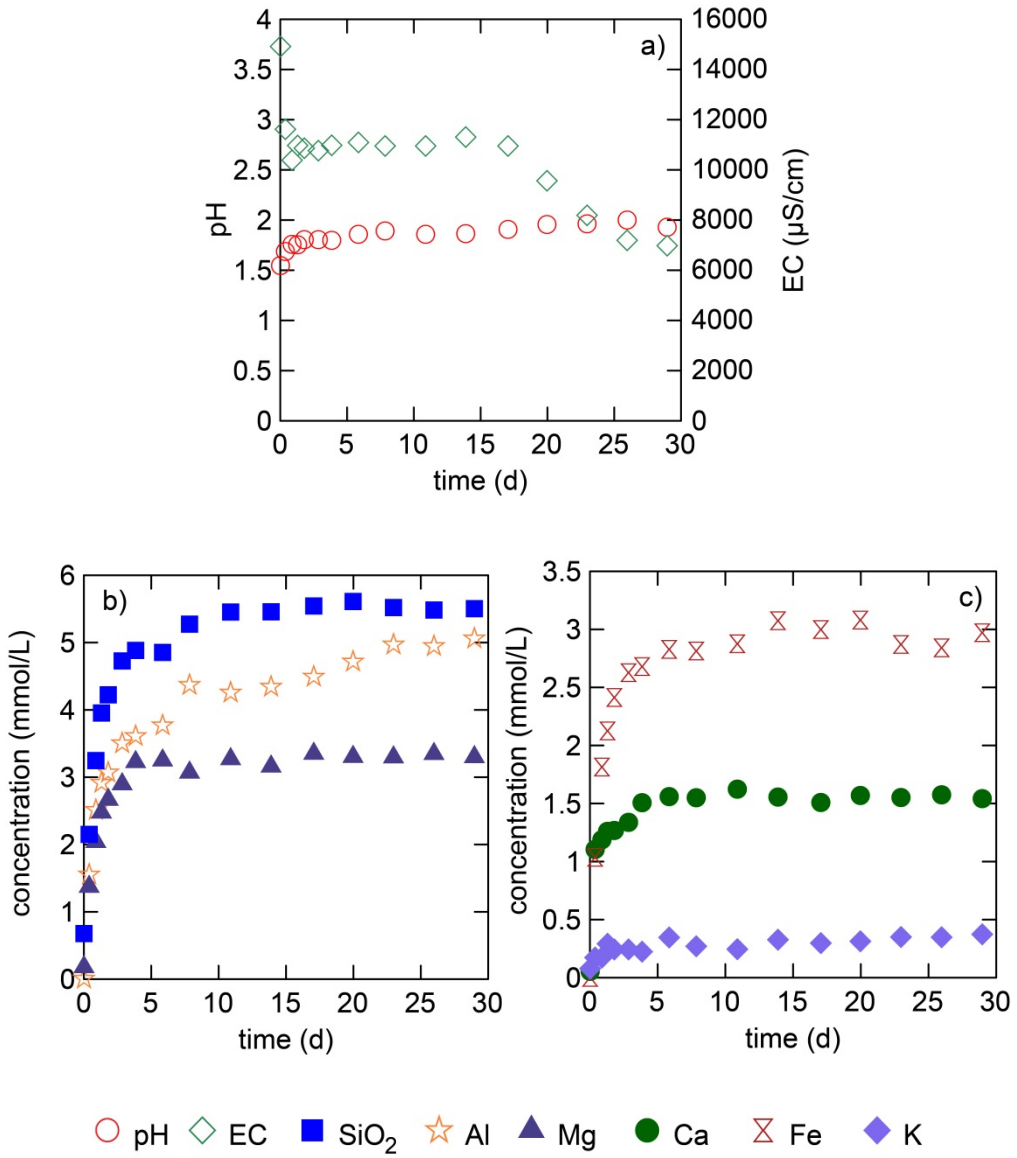

Figure 2.8 **Water chemistry for the reaction of AF-05 with pH 1.5 brine at 60°C over 30 d, showing changes in pH (a), EC (a) and, selected ions (b+c).**

AF-06

Of all baseline experiments the reaction of AF-06 showed the greatest change in brine composition (Appendix B). The pH dropped by more than 1 and the EC increased by ~140 µS/cm. The concentration of Na showed the greatest variation between 4.5 mmol/L and 6 mmol/L. Over a 30 d period the amount of SiO_2 in the brine dropped rapidly by 0.5 mmol/L and the amount of Mg by about 0.15 mmol/L. Further a steep

increase of 0.8 mmol/L was observed for the SO_4^{2-} content, while the remaining brine properties showed only minor changes.

The reaction of AF-06 with pH 1.5 solution at 60°C resulted in water chemistry changes plotted in Figure 2.9. The pH increased to ~2 and was accompanied by a total drop in EC of ~7000 µS/cm (Figure 2.9a). Most ions present in the brine increased in concentration throughout the experiment, except for SO_4^{2-} and Cl^-, which remained fairly stable. Na increased rapidly at the beginning and dropped to about 6.5 mmol/L at the end of the experiment (Figure 2.9b). These variations are slightly higher, but still similar to the ones observed in the baseline experiment of AF-06 and are therefore likely negligible. The concentration of Fe showed the greatest change with an increase of approximately 5 mmol/L, which was likely due to siderite and chlorite dissolution. Calcite possibly reacted as well resulting in an increase in Ca of 1 mmol/L (Figure 2.9c). The SiO_2 and Al contents both increased by 4.5 mmol/L, while the Mg content increased by about half that amount. Combined with an increase in K of 0.5 mmol/L, these changes suggest the dissolution of K-feldspar and chlorite. The changes in ion concentrations give no clear evidence for mineral precipitation.

The SEM analyses of the AF-06 baseline sample identified quartz and illite as the dominant mineral phases. The SEM results of the reacted sample match these observations giving no evidence for mineral reactions.

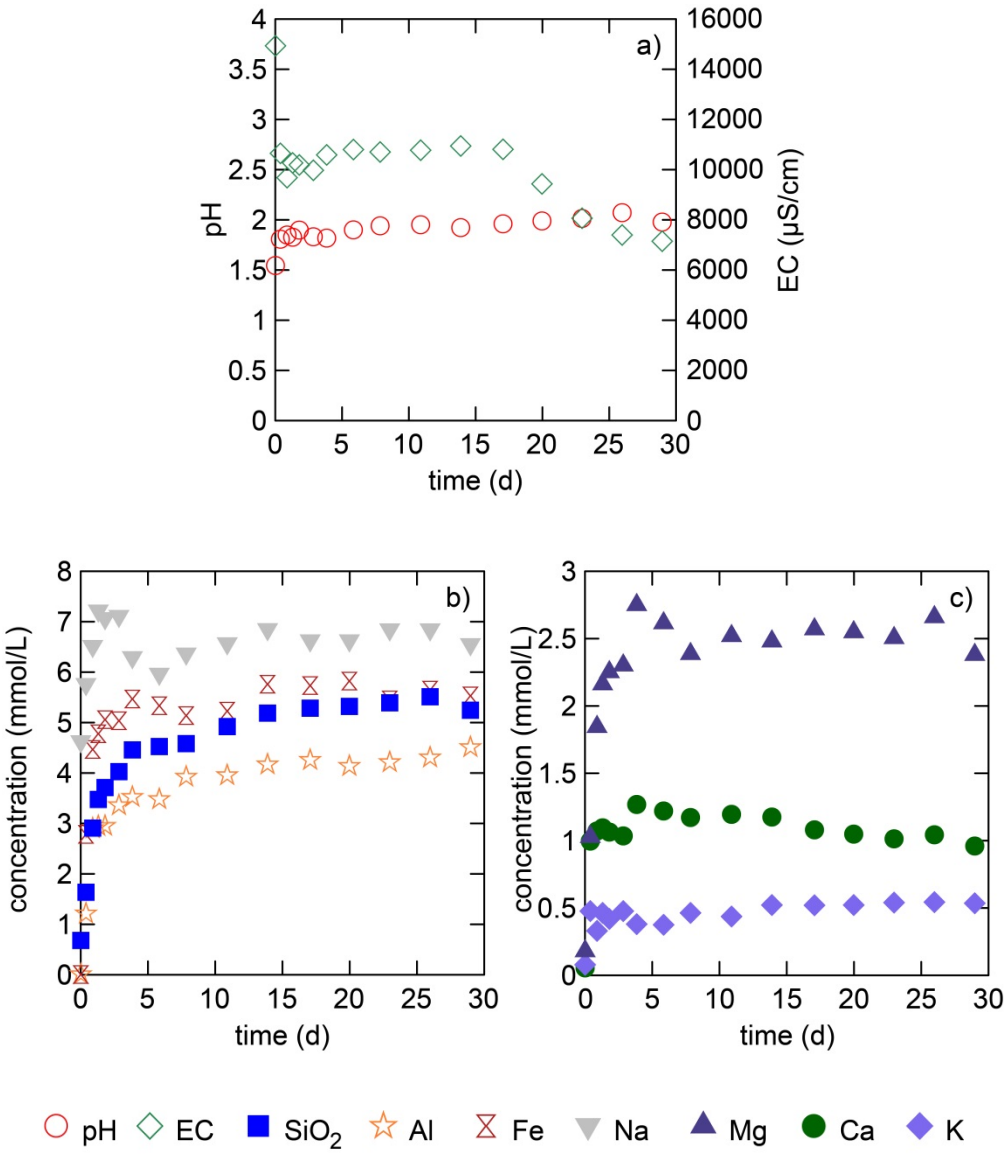

Figure 2.9 **Water chemistry for the reaction of AF-06 with pH 1.5 brine at 60°C over 30 d, showing changes in pH (a), EC (a) and, selected ions (b+c).**

Discussion

The reaction of the Western Canada Sedimentary Basin samples showed that the effect of SO_2 induced acidification on a brine-rock system is strongly dependent on the rock mineralogy. Carbonate minerals are highly reactive and dissolve rapidly, resulting in a pH buffering. The extent of those carbonate dissolution reactions depends on the kind and amount of carbonate present. Calcite has the highest reaction rate,

followed by dolomite. Siderite and ankerite react the slowest of all carbonates, but their reaction rate is still significantly greater than silicate mineral reaction rates. Silicate mineral phases participate in H_2SO_4-brine-rock reactions as well. The Western Canada Sedimentary Basin sample experiments indicate the dissolution of chlorite, illite, muscovite and K-feldspar. However, unlike the dissolution of calcite and dolomite, silicate mineral dissolution could not be proven by comparing SEM analysis of pre- and post-reaction rock samples. The AF-01 experiment showed a potential for SO_2 trapping in the form of calcium sulphate precipitation, which is important for permanent and safe storage of SO_2.

2.3.2. Parameter analysis

To investigate the effect of selected parameters on the reaction path and reaction rate, the Western Canada Sedimentary Basin samples were reacted under different sample particle size, temperature and pH conditions. The first parameter investigated was sample particle size. The Western Canada Sedimentary Basin samples were reacted in mortared, crushed and block form to evaluate the role of available reactive surface area. This is important since actual storage systems are rock-dominated with limited fluid access, while the batch experimental set up is water-dominated with nearly unlimited fluid access. Hence, in order to better understand accessible reactive surface areas in a storage system limiting factors need to be assessed under controlled experimental conditions. The second parameter investigated was temperature. By reacting mortared Western Canada Sedimentary Basin samples at two different temperatures (22°C and 60°C) the temperature dependence of the mineral reactions was investigated. This enables the evaluation of the activation energy input as a reaction rate parameter in the rate equations for the different mineral phases. This is particularly important for mineral phases with variable composition and origins, such as chlorite, for which the majority of kinetic rate data comes from chlorite of metamorphic or hydrothermal origin (e.g. Lowson et al., 2007) and focuses on the slightly less aluminous end members clinochlore and daphnite (Holland et al., 1998). The final parameter studied was pH. The dependence of reaction rates on pH was examined by using pH 1.5 and pH 3 brine in the experimental set up. This was done for two reasons: 1) to evaluate the H^+ power term input as a reaction rate parameter in the rate equations and 2) to

investigate spatial variations in the type and extent of reactions expected in a storage site. The pH 1.5 brine simulates near injection well conditions, where the injected supercritical fluid occupies most of the pore space, while the pH 3 brine represents conditions further away from the injector where SO_2 concentrations in the plume are expected to be lower. The experimental results of the parameter analysis are summarized for AF-01, AF-03 and AF-06 of the Western Canada Sedimentary Basin in the following paragraphs. These samples were selected due to their mineralogical properties. AF-01 was chosen to investigate the reaction behaviour of carbonates; AF-02 to investigate the reactivity of silicate minerals, and AF-06 to investigate chlorite and clay reactions.

Sample particle size

The reaction of the Western Canada Sedimentary Basin samples in mortared, crushed and block form resulted in different outcomes. It is important to note that in order to compare the experimental outcomes the results of the block reactions had to be scaled down to 3 g of rock sample to match the mortared and crushed experiments. The results show that while the mortared and crushed reactions often resulted in similar changes, a significant difference was observed for the block experiments. Overall the data identify an increasing reaction rate with decreasing sample particle size. This is of significance since it points out that experimental results using mortared samples are likely to overestimate the reaction rates for an actual reservoir because the accessible reactive surface area is overestimated.

AF-01

The experimental results of the AF-01 reaction changed significantly depending on whether the rock sample was in mortared, crushed or block form. Figure 2.10 shows the change in pH, EC and selected ion and element concentrations for each of the three particle sizes. The changes in Mg, Ca and SO_4^{2-} were very similar for the crushed and mortared AF-01 samples (Figure 2.1f, g, i). SO_4^{2-} decreased in the mortared and crushed experiment by 13 mmol/L, while little to no change was observed in the block reaction. Ca increased rapidly in the mortared and crushed experiment, followed by a slow decrease. The block sample reaction on the other hand resulted in a steep, but

comparatively slower Ca concentration increase in the initial 5 d. The amount of Ca in the brine flattened out at about 10 mmol/L, which was ~2 mmol/L lower than the final amount in the crushed and mortared experiment. The Mg content rose steeply at the beginning of all three sample particle size experiments and eventually flattened out. The change in Mg was less rapid in the block reaction and the total increase was about 2 mmol/L lower compared to the mortared and crushed experiment. These differences in the experimental outcomes indicate that less carbonate dissolved and less calcium sulphate precipitated in the block experiment most likely due to limited fluid access to the cementing carbonates. The decreased carbonate reaction amount with increased sample particle size resulted in less pH buffering. The pH change declined from 4.5 in the mortared sample to 2.2 in the crushed sample to 0.8 in the block sample (Figure 2.10a). The EC appears to be negatively correlated to the pH. The EC decreased by ~13000 µS/cm in the mortared experiment, by ~11000 µS/cm in the crushed experiment, and by ~9000 µS/cm in the block experiment (Figure 2.10b).

In the mortared experiment SiO_2, Al and Fe showed a rapid increase over the first 2 d, followed by a decreasing trend (Figure 2.10c, d, e). Al and Fe showed a similar behaviour in the crushed experiment, but the initial increases were about 0.15 mmol/L and 0.1 mmol/L higher, respectively, and the subsequent decreases were slower than in the mortared reaction. The block sample showed a slower Al and Fe gain. However, both concentrations reached maximal concentrations, similar to the ones of the mortared reaction. While the Al concentration flattened out between 0.3 mmol/L and 0.35 mmol/L in the block experiment, the Fe started to decrease after about 15 d of reaction. Unlike the mortared sample, the SiO_2 concentration of the crushed and block experiment showed no decreasing trend after the initial increase and remained fairly constant at ~1.4 mmol/L. The different outcomes for SiO_2 and Al indicate a reduction in the amount of silicate precipitation from the crushed to the mortared to the block experiment, which was likely due to the lower pH. The decrease in Fe concentration in all three sample particle size experiments suggests that an iron bearing mineral phase precipitated. Combined with the constant SiO_2 increase and low pH of the block experiment the Fe decrease is most likely not due to the formation of an iron silicate, iron oxide or iron hydroxide, suggesting the precipitation of an iron sulphate. The change in K was similar for all three sample particle sizes (Figure 2.10h). However, a slight reduction in the K

change was observed from the crushed to the mortared to the block experiment, indicating slightly different dissolution patterns for potassium-bearing mineral phases, like K-feldspar.

The SEM analysis did not detect any calcite or dolomite in the crushed and mortared samples, nor on the surface of the block sample where they were clearly present pre-reaction. Instead newly precipitated calcium sulphate phases were found in all three sample particle size experiments. While these were very abundant and clearly formed in the crushed and mortared experiments, the block experiment mainly showed crystallization on the surface of other mineral phases (Figure 2.11).

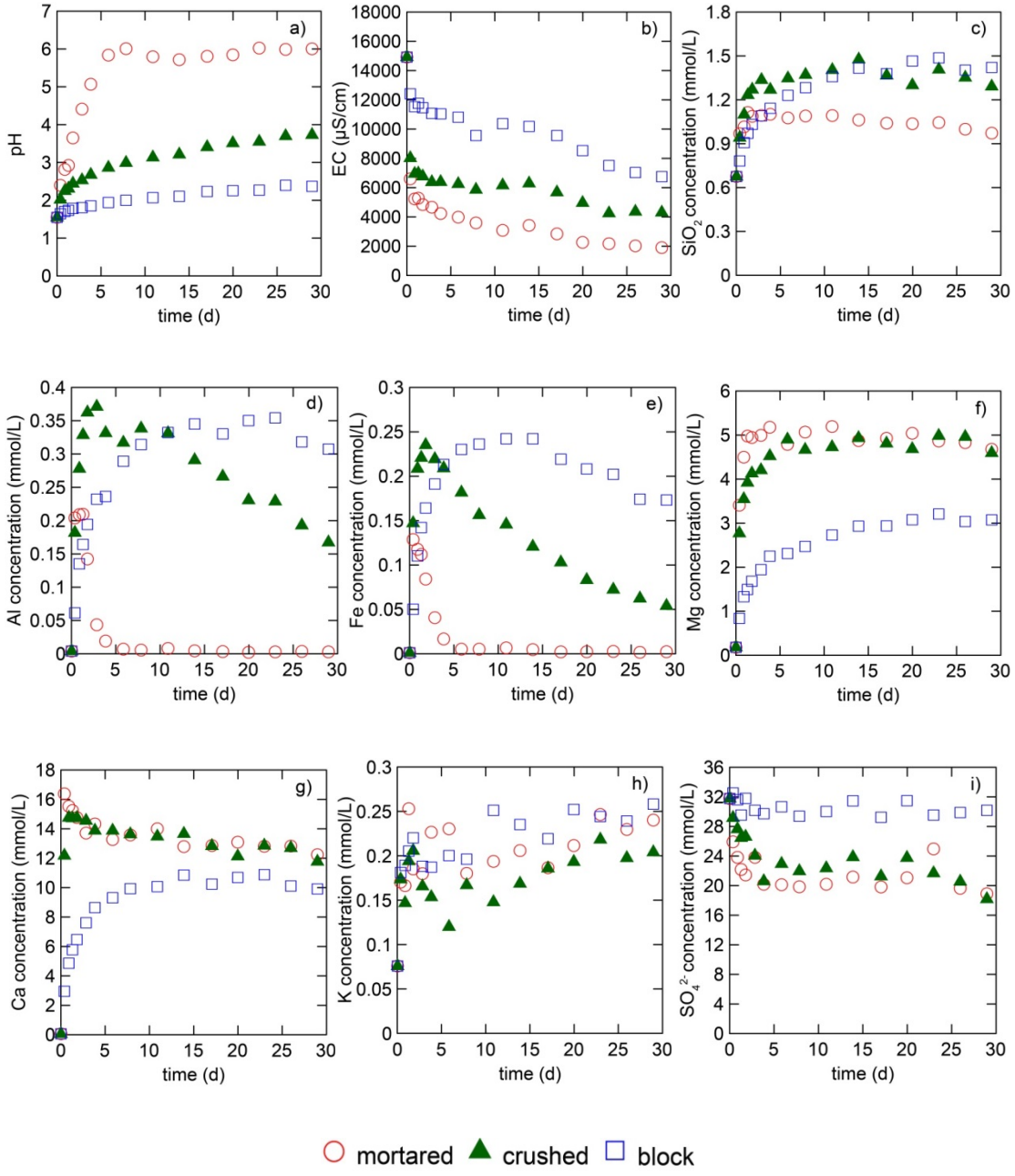

Figure 2.10 **Experimental brine pH (a), EC (b), SiO_2 (c), Al (d), Fe (e), Mg (f), Ca (g), K (h) and SO_4^{2-} (i) concentration of AF-01 reaction at different sample particle sizes.**

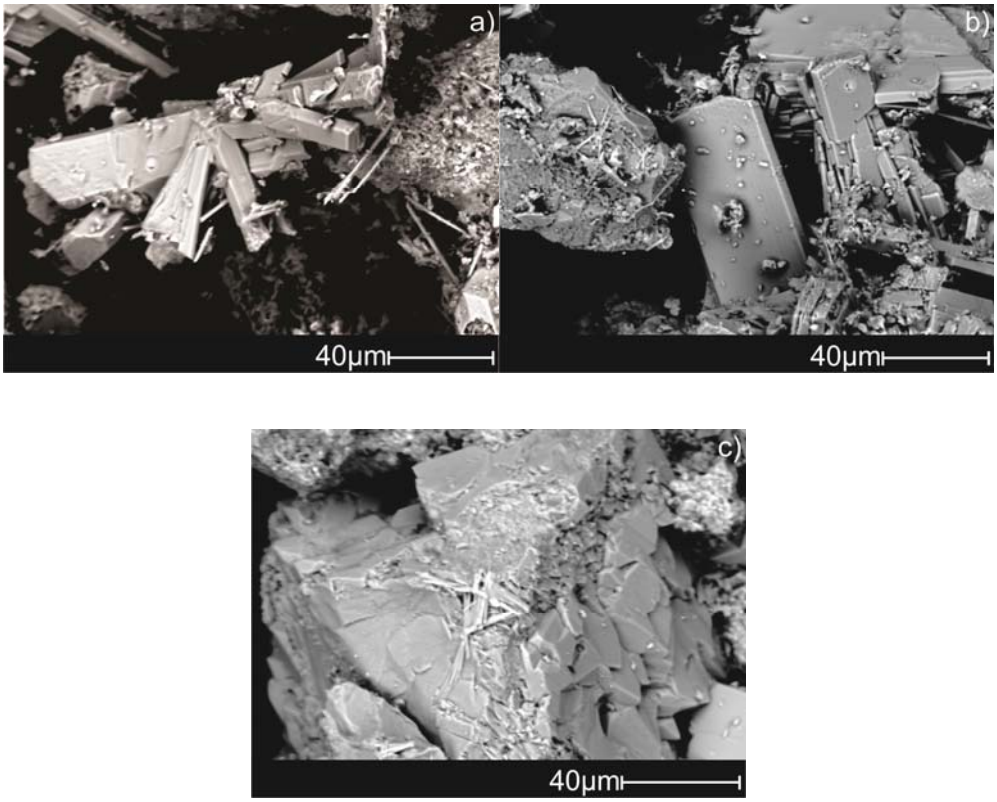

Figure 2.11 Precipitated calcium sulphate in the reaction of mortared (a), crushed (b) and block (c) AF-01.

AF-03

The sample particle size experiments of AF-03 resulted in significantly different reaction extents (Figure 2.12). The evolution in pH and EC coincided for all three sample particle size experiments of A-03 (Figure 2.12a, b). SiO_2 constantly increased in all three experiments (Figure 2.12c); however, the increase in concentration in the mortared experiment was about 1 mmol/L greater than in the crushed and about 2 mmol/L greater than in the block reaction. The increase in Al was about half in the crushed and about six times less in the block experiment compared to the mortared experiment (Figure 2.12d). The reduced changes in SiO_2 and Al suggest a reduction in silicate reaction extent with increased sample particle size, due to less reactive surface area exposure. The Fe and K contents followed the same trend as SiO_2 and Al with less change with increasing sample particle size (Figure 2.12e, h). The change in Mg was very similar in all three experiments (Figure 2.12f); however, a slight reduction in reaction extent from the mortared sample to the crushed sample to the block sample is observed. The different

experimental outcomes for K, Fe and Mg might be due to slower K-feldspar, chlorite and siderite reaction extents at greater sample particle size. The evolution of Ca shows a slower initial increase with increased sample particle size (Figure 2.12g), suggesting that the dissolution of Ca-bearing minerals, most likely calcite, was slowed down due to a reduction in accessible reactive surface area. However, the total change of Ca is very similar in all three reactions, indicating that the reactive brine completely infiltrated the pore space resulting in the same amounts of calcite dissolution.

All three reacted rock samples of the sample particle size experiment are dominated by quartz and K-feldspar, which corresponds to the observations of the baseline experiment. Hence, no qualitative or visual evidence for mineral reactions were found.

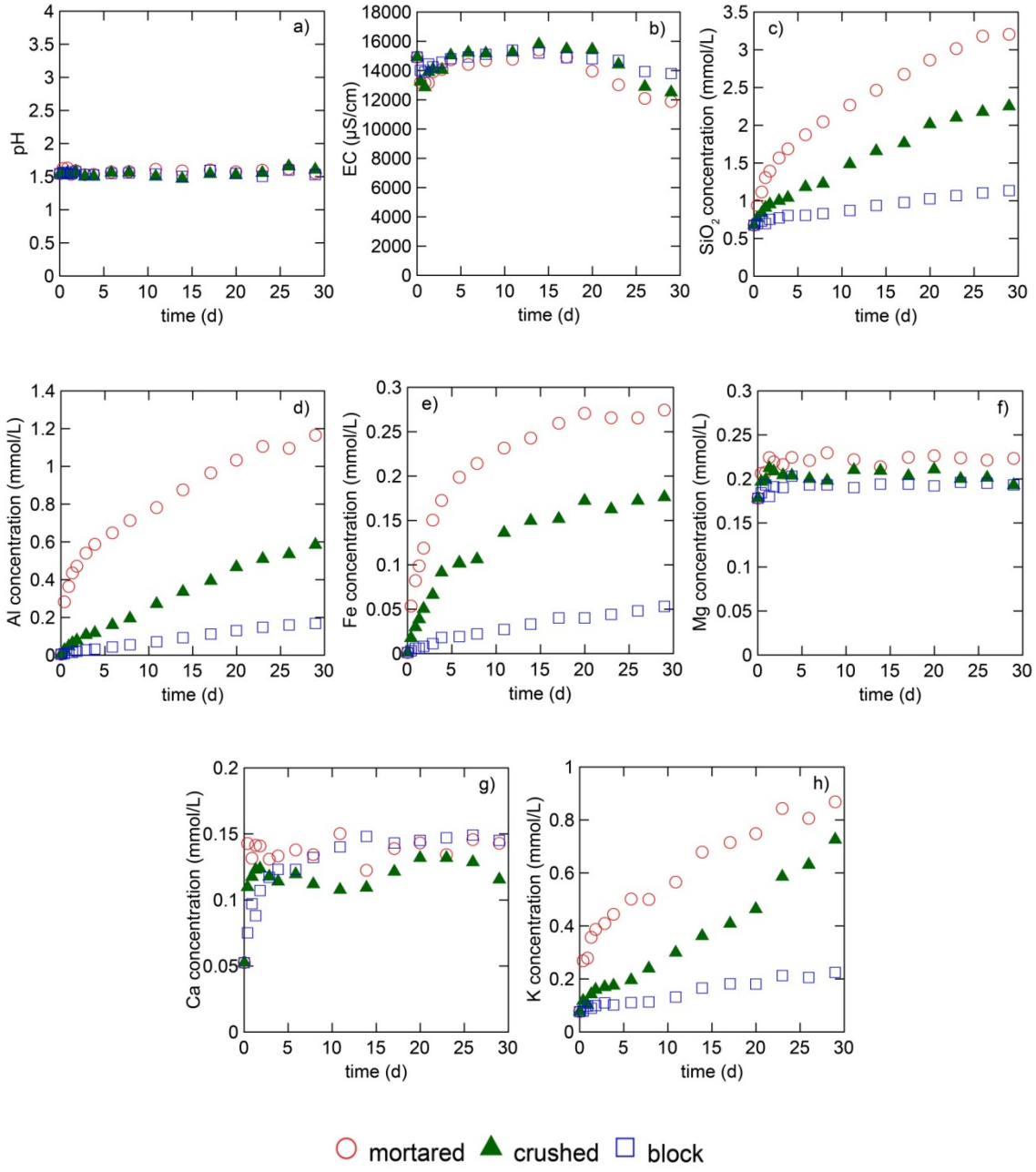

Figure 2.12 Experimental brine pH (a), EC (b), SiO_2 (c), Al (d), Fe (e), Mg (f), Ca (g) and K (h) concentration of AF-03 reaction at different sample particle sizes.

AF-06

The experiments reacting AF-06 at different sample particle sizes gave similar results for the mortared and crushed samples, but significant differences for the block sample. Important to note is that the block sample of AF-06 fell apart early in the

experiment due to the swelling of clay. Hence, the changes of the block reaction might be overestimated. Selected brine parameters are plotted in Figure 2.13. The evolution in pH of all three sample particle size experiments of AF-06 coincide (Figure 2.13a). The EC on the other hand dropped by ~3000 µS/cm less in the block experiment compared to the mortared and crushed experiment (Figure 2.13b). This suggests that less acid induced mineral reaction happened in the block experiment resulting in a lower consumption of hydrogen ions. The reaction of AF-06 as a mortared and as a crushed sample resulted in very similar changes for the ion concentrations as well. The block experiment on the other hand showed only about half the increase in SiO_2, Al and K (Figure 2.13c, d, h). This indicates less silicate dissolution due to the decreased reactive surface area access. For the Fe and Mg concentrations the change in the block sample was about one fifth lower compared to the other sample particle sizes (Figure 2.13e, f). This was less than expected and most likely due to an increased accessibility to siderite and chlorite after the disintegration of the block sample. In accordance with this, the initial increase in Ca was slower for the block experiment, but the total change was very similar to the crushed and mortared experiment (Figure 2.13g), likely due to better calcite accessibility after the disintegration of the rock sample.

The SEM analyses of the reacted samples showed an abundance of quartz and illite in all three sample particle size experiments. This matches the baseline experiment.

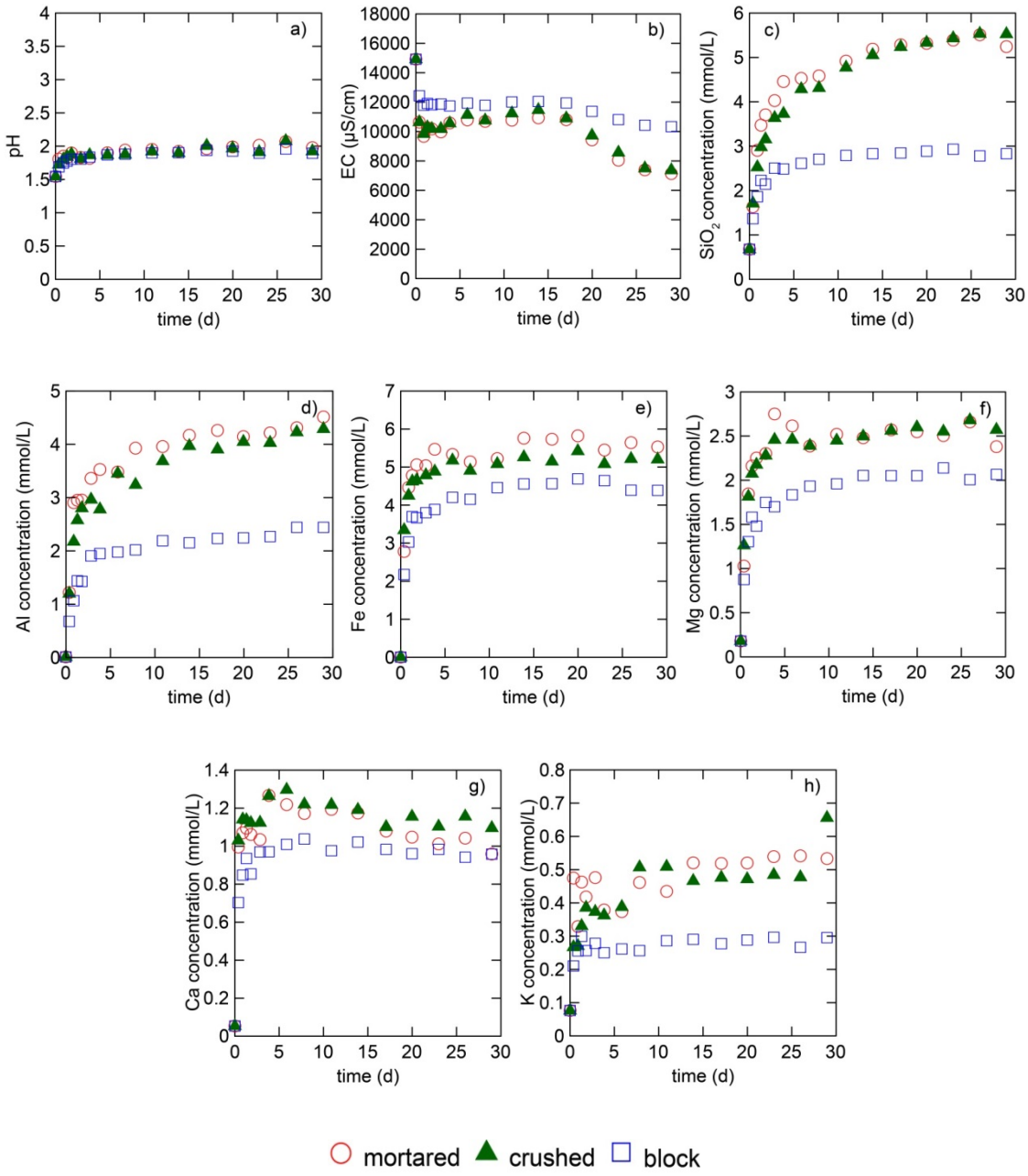

Figure 2.13 Experimental brine pH (a), EC (b), SiO_2 (c), Al (d), Fe (e), Mg (f), Ca (g) and K (h) concentration of AF-06 reaction at different sample particle sizes.

Temperature

The Western Canada Sedimentary Basin sample experiments under two temperature conditions resulted in different outcomes. The reaction rates were often

significantly lower at 22°C compared to 60°C. Silicate mineral reactions in particular were sensitive to changes in temperature. The different experimental outcomes at different temperatures outline the importance of activation energy input as a reaction rate parameter.

AF-01

The experimental outcomes for AF-01 at 22°C and 60°C showed some significant differences. The change in pH, EC and selected ion and element concentrations are plotted in Figure 2.14. The concentrations of Mg, Ca and SO_4^{2-} showed very similar trends at both temperatures (Figure 2.14f, g, i). SO_4^{2-} decreased in both experiments by a total of 13 mmol/L, while Mg increased rapidly by about 5 mmol/L. The maximum Ca content of the brine was ~2 mmol/L higher in the low temperature reaction, but both reactions showed the same development and end at a similar final value. The slightly higher initial increase in Ca at 22°C is likely due to the retrograde solubility of carbonates, which results in more calcite or dolomite reaction at lower temperatures. However, the extent of carbonate dissolution and sulphate precipitation appears to be very similar at both temperatures. This was likely the cause of similar pH buffering extents in both experiments. The final pH is only about 0.6 lower in the 22°C reaction compared to the 60°C reaction (Figure 2.14a). The initial decrease in EC was by ~2000 µS/cm greater at 22°C (Figure 2.14b). However, the evolution in EC was almost identical at both temperatures and the total change less than 1000 µS/cm different indicating similar reaction extents at both temperatures.

The SiO_2, Al and Fe content of the brine showed an increase at both temperatures within the first 2 d, which was followed by a decreasing trend (Figure 2.14c, d, e). However, the total gain in SiO_2 was about four times higher at 60°C. The initial rise in Al at 22°C was less than half of the increase observed in the high temperature experiment. A subsequent drop in Al resulted in a final concentration of 0.003 mmol/L in the high temperature experiment and 0.01 mmol/L at 22°C. The different experimental outcomes for SiO_2 and Al at varied temperatures outlines the temperature dependence of silicate reaction and the importance of an activation energy input in the calculation of mineral reactions. The initial Fe increase at 22°C was only about two thirds of the increase at 60°C and the subsequent drop in Fe resulted in a final

concentration of 0.002 mmol/L at 60°C and 0.004 mmol/L at 22°C. The evolution of K was almost identical at both temperatures (Figure 2.14h). The initial K increase was slower at a lower temperature, but the total gain in concentration was ~0.2 mmol/L at both temperatures.

Unlike in the baseline rock sample, the SEM analysis detected no calcite or dolomite in either rock sample. Instead newly precipitated calcium sulphate phases were found to be abundant and clearly formed (Figure 2.15).

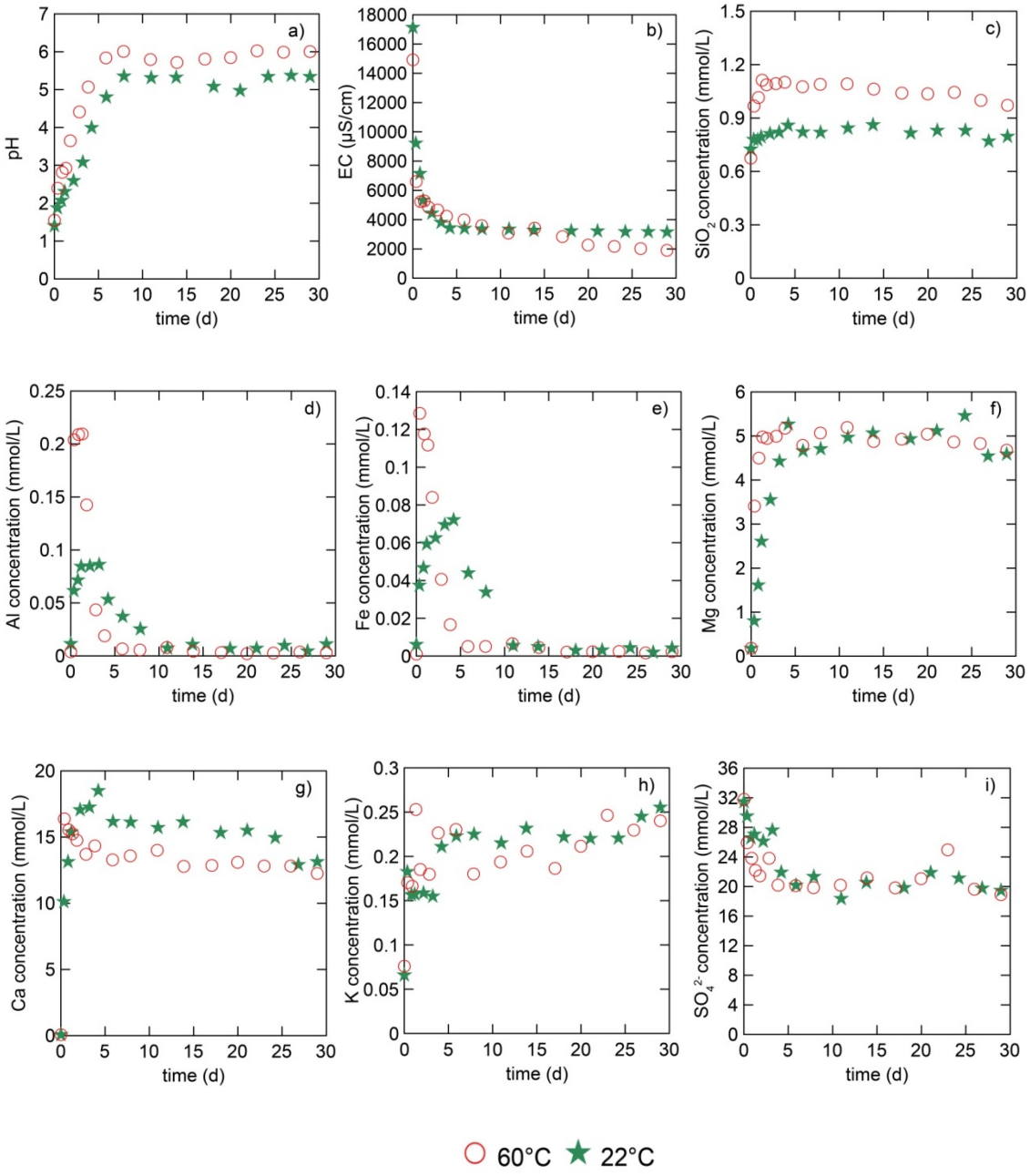

Figure 2.14 Experimental brine pH (a), EC (b), SiO_2 (c), Al (d), Fe (e), Mg (f), Ca (g), K (h) and SO_4^{2-} (i) concentration of AF-01 reaction at 22°C and 60°C.

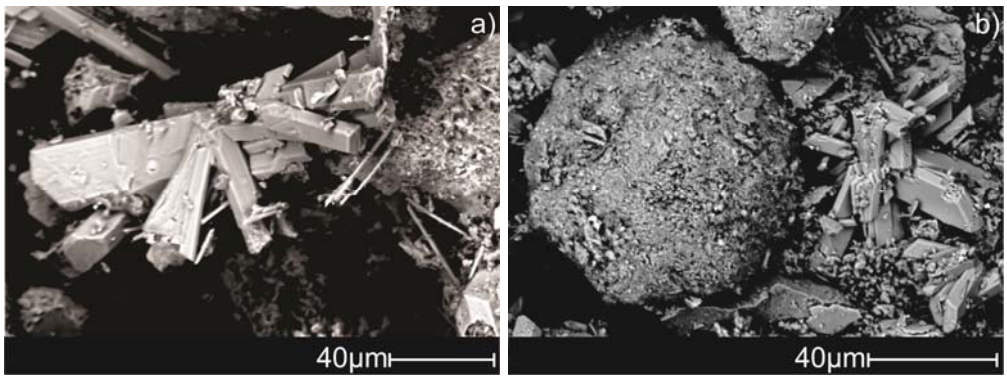

Figure 2.15 Precipitated calcium sulphate in the reaction of AF-01 at 22°C (b) and 60°C (a).

AF-03

The reaction of AF-03 at 22°C and 60°C resulted in significantly different experimental outcomes. The changes in pH, EC, and selected element concentrations at both temperatures are plotted in Figure 2.16. The evolution in pH was very similar in both temperature experiments (Figure 2.16a). However, the reaction at 22°C took place at a marginally lower pH. The difference in pH is reflected in the EC, which is 2000 µS/cm higher at 22°C than at 60°C (Figure 2.16b). The increase in SiO_2 was about 5 times higher in the 60°C experiment compared to the 22°C experiment (Figure 2.16c). For Al, the concentration gain was 4 times higher in the high temperature reaction (Figure 2.16d). Further, the changes in Fe and K were about three times higher, and the Mg was twice as high at 60°C compared to 22°C (Figure 2.16e, h, f). The smaller change in SiO_2, Al, K, Fe and Mg at 22°C is likely due to less K-feldspar, chlorite and siderite dissolution and emphasizes the importance of activation energy in the calculation of reaction rates. The Ca concentration change is almost identical at both temperatures (Figure 2.16g), suggesting that about the same amount of Ca-bearing minerals dissolved.

The SEM analyses of the reacted rock samples showed no significant difference between the two temperature experiments. Both samples showed an abundance of quartz and K-feldspar, which matches the observations of the baseline experiment giving no obvious indication for mineral reaction.

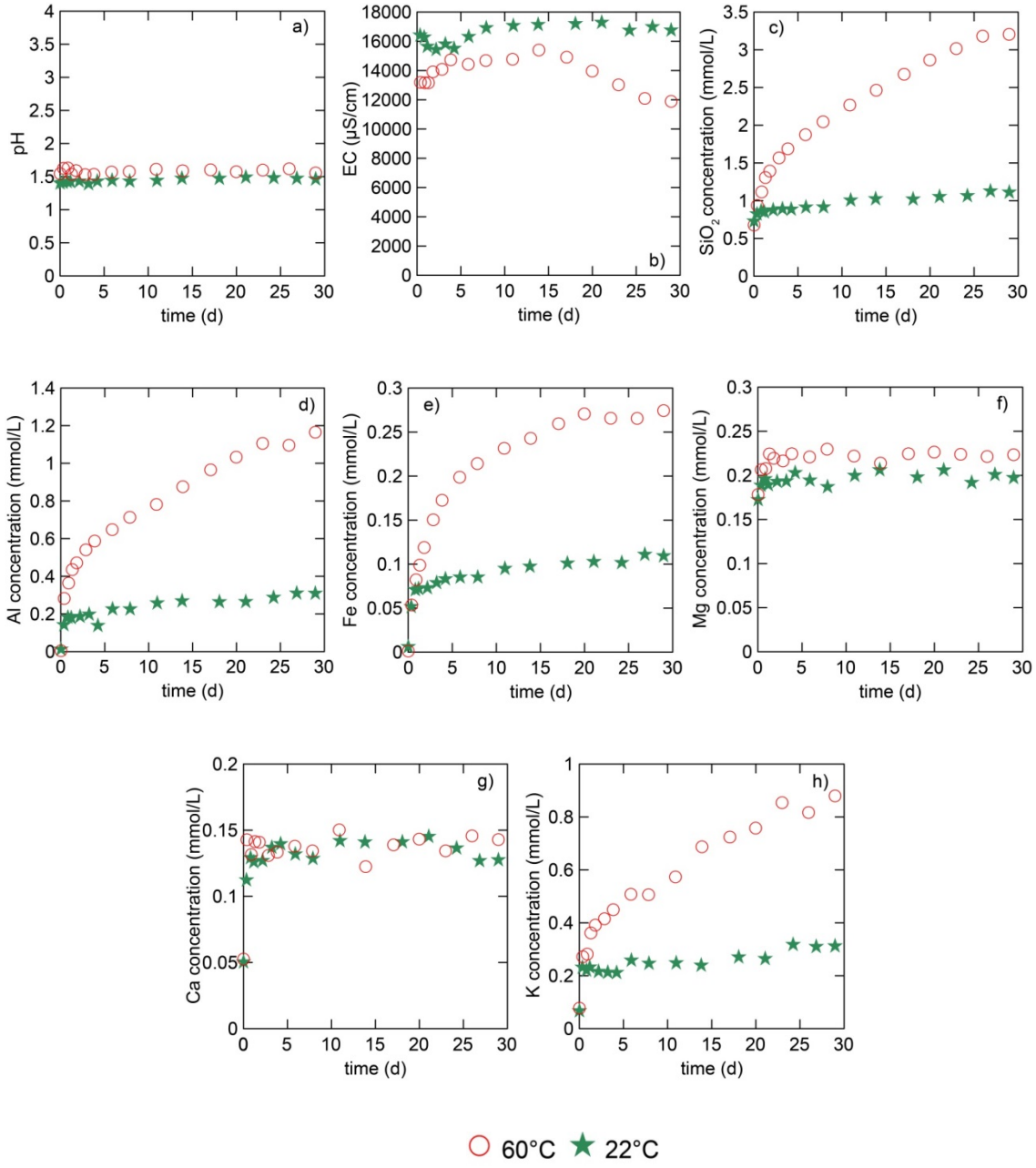

Figure 2.16 Experimental brine pH (a), EC (b), SiO_2 (c), Al (d), Fe (e), Mg (f), Ca (g) and K (h) concentration of AF-03 reaction at 22°C and 60°C.

AF-06

The experiments reacting AF-06 at 22°C and 60°C showed a significant reduction in reaction extent at lower temperature (Figure 2.17). The pH buffering extent was slightly higher in the high temperature experiment of AF-06 than at 22°C (Figure

2.7a). This is reflected in a higher decrease in EC of about 2000 µS/cm at 60°C (Figure 2.7b). The change in SiO_2 was about half as great in the low temperature experiment compared to the 60°C experiment (Figure 2.7c). The Al increase at 22°C was about two thirds of the increase at 60°C (Figure 2.7d). The reduced slope of SiO_2 and Al reflects the temperature dependence of silicate mineral reactions and the importance of activation energy input as a reaction rate parameter. The change in K was slightly lower in the low temperature experiment (Figure 2.7h), likely due to less K-feldspar reaction. The increase in Fe was only about 1 mmol/L lower at 22°C reaction compared to 60°C (Figure 2.7e). The Mg content in the brine showed a final difference of 0.5 mmol/L between the two temperature experiments (Figure 2.7f). The smaller differences between both experiments for Fe and Mg are most likely due to the fact that besides silicate reactions, retrograde carbonate dissolution contributes to their concentration. The evolution of Ca was very similar in both temperatures experiments (Figure 2.7g), likely due to the retrograde solubility of calcite.

The reacted samples of the temperature experiments were both dominated by quartz and illite, which corresponds to the baseline experiment. Hence, no qualitative or visual evidence for mineral reactions was found.

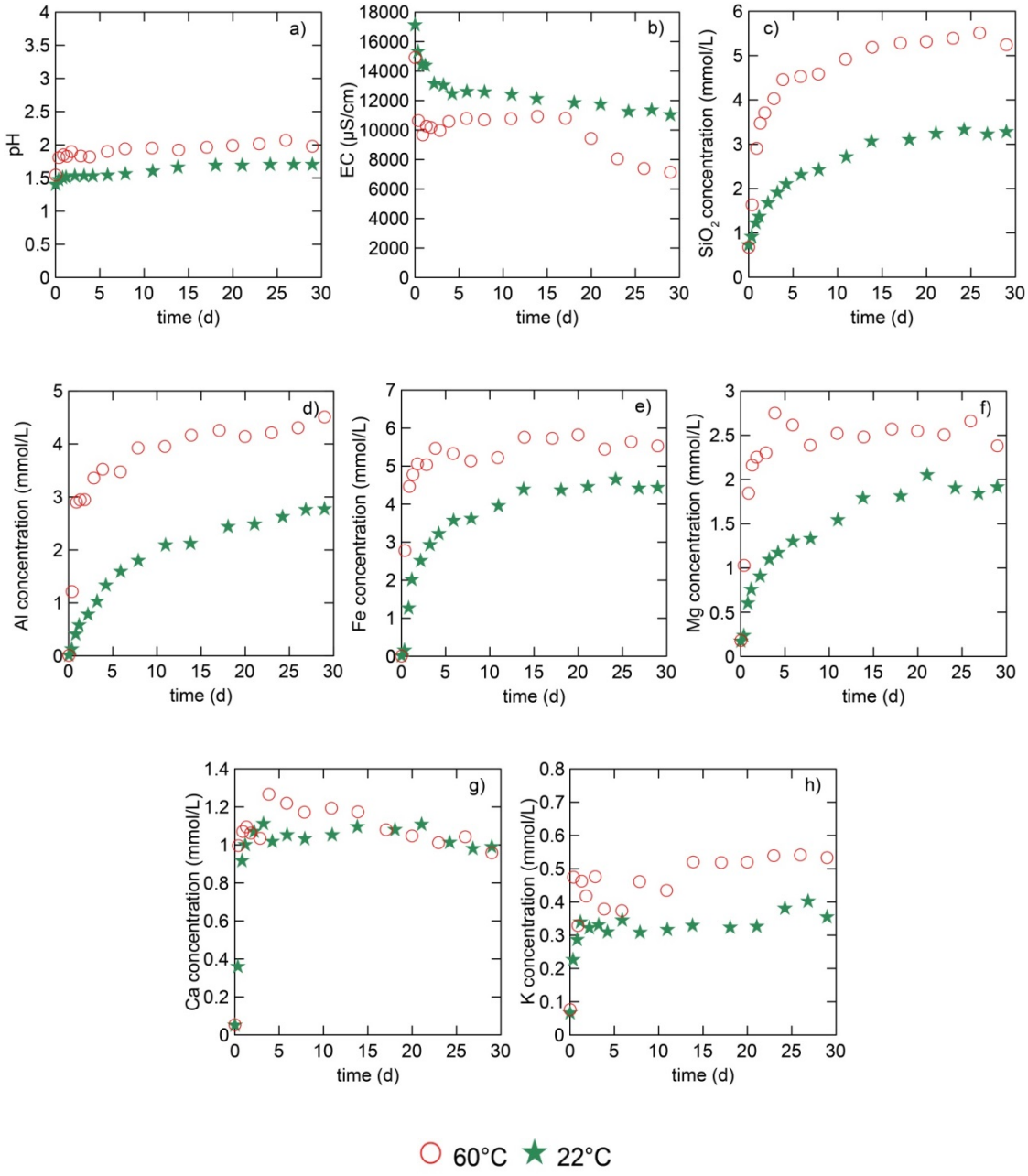

Figure 2.17 Experimental brine pH (a), EC (b), SiO_2 (c), Al (d), Fe (e), Mg (f), Ca (g) and K (h) concentration of AF-06 reaction at 22°C and 60°C.

Starting pH

The reaction of the Western Canada Sedimentary Basin samples at the two different starting pH values resulted in significantly different outcomes. The reaction extent of the pH 3 experiments was found to be lower than the reaction extent of the pH

1.5 experiments. Both silicate and carbonate mineral reactions showed a sensitivity towards changes in pH. This highlights the importance of the H^+ power term input as a reaction rate parameter.

AF-01

The reaction of AF-01 with pH 1.5 brine resulted in a significantly different outcome than reaction with pH 3 brine. The changes in pH, EC and selected ion and element concentrations are plotted for both experiments in Figure 2.18. pH buffering of about 5 orders of magnitude is observed for both experiments (Figure 2.18a). However, since pH is a logarithmic measure the total buffering capacity was higher in the low pH experiment. Interesting to note is that the final pH of the pH 3 experiment was close to the baseline value. The rapid initial pH buffering resulted in both experiments in pH conditions at which the pH rate dependency is diminished. However, while the pH 3 experiment reached these conditions within the first hours of reaction, the pH 1.5 reaction was pH dependant for about 4 d. Due to the lower H_2SO_4 acidification of the pH 3 brine, the SO_4^{2-} content was one eighth of the pH 1.5 brine (Figure 2.18i). While SO_4^{2-} decreased significantly in the pH 1.5 experiment, it remained fairly stable in the pH 3 reaction. This indicates that no sulphate phases precipitated in the pH 3 experiment. The lower initial acidification also resulted in a 15 times lower EC in the pH 3 experiment (Figure 2.18b). Like SO_4^{2-}, the EC decreased significantly in the low pH experiment, but stayed relatively constant in the pH 3 experiment.

The Ca content increased by about 1 mmol/L in the pH 3 experiment, which was significantly lower when compared to the maximum increase of ~16 mmol/L in the low pH reaction (Figure 2.18g). The change in Mg showed a rapid increase at low pH, but decreased marginally at pH 3 (Figure 2.18f). The trends in Ca and Mg suggest high carbonate reaction rates at pH 1.5 and some calcite, but no dolomite dissolution at pH 3. No significant increase or decrease was observed for the amount of SiO_2, Al and Fe for the pH 3 experiment (Figure 2.18c, d, e). This stands in contrast to a rapid initial rise and subsequent decline in SiO_2, Al and Fe concentrations observed at pH 1.5. The constant SiO_2 and Al concentrations in the pH 3 experiment suggest that little to no silicate dissolution or precipitation took place. The increase in K was about 0.1 mmol/L lower at pH 3 than at pH 1.5 (Figure 2.18h), indicating a reduction in K-feldspar dissolution.

The SEM analysis of the pH 3 sample identified quartz, calcite and dolomite as the dominant mineral phases, which matches the results of the baseline experiment. Hence, no significant change in the mineral composition was observed. This stands in contrast to the pH 1.5 experiment, in which existing carbonate phases were replaced by calcium sulphate. The discrepancy between both pH experiments highlights the importance of pH dependence when calculating reaction rates.

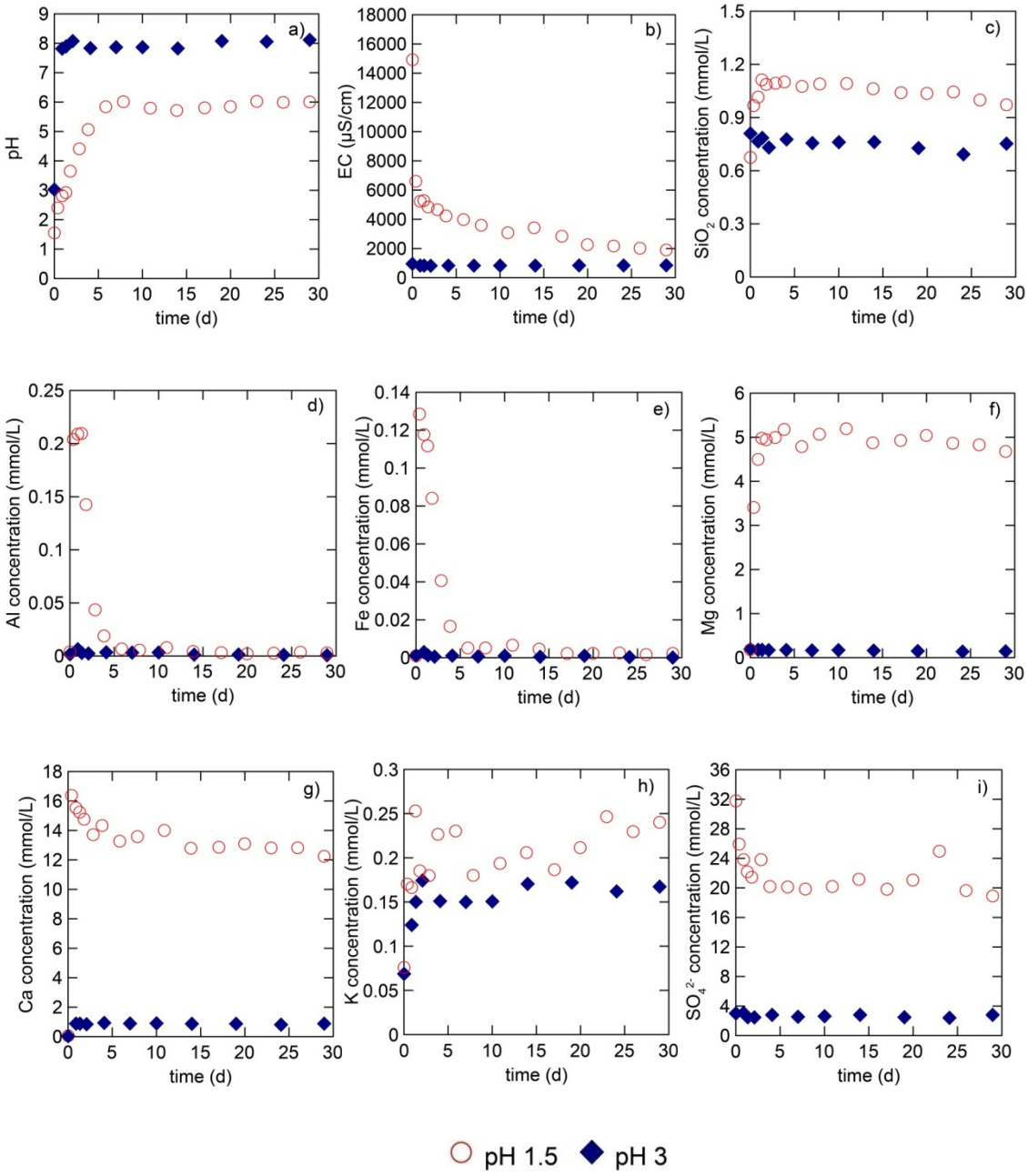

Figure 2.18 Experimental brine pH (a), EC (b), SiO_2 (c), Al (d), Fe (e), Mg (f), Ca (g), K (h) and SO_4^{2-} (i) concentration of AF-01 reaction with pH 1.5 and pH 3 brine.

AF-03

The experiments of AF-03 with pH 1.5 and pH 3 solution resulted in different experimental outcomes (Figure 2.19). The pH 3 experiment of AF-03 resulted in a

buffering of the pH to 3.5, while no significant pH increase was observed at pH 1.5 (Figure 2.19a). However, since pH is a logarithmic measurement, a minimal change at pH 1.5 could describe the same change in hydrogen ions as the buffering extent observed at pH 3. Due to the lower brine acidification in the pH 3 experiment, the EC is 15 times lower compared to the pH 1.5 experiment (Figure 2.19b). The EC decreases over the course of the pH 1.5 reaction, but stayed fairly constant in the pH 3 reaction suggesting lower mineral reaction extents at pH 3.

The increases in SiO_2 and Al concentrations were over 10 times greater in the pH 1.5 experiment compared to the pH 3 reaction (Figure 2.19c, d), highlighting the importance of pH dependency input when calculating silicate reaction rates. The changes in Fe and K are about 10 times higher in the low pH reaction as well (Figure 2.19e, h). Compared to the evolution of SiO_2, Al and K, the increase in Fe concentration was steeper at the beginning and flattened out towards the end of the experiment. This suggests a second source for Fe besides silicate minerals, which is most likely siderite. Mg showed no significant increase in concentration at pH 3, while it increased marginally at pH 1.5 (Figure 2.19f). The rise in Ca was more than halved in the pH 3 experiment compared to the pH 1.5 experiment (Figure 2.19g), highlighting the importance of pH dependency input when calculating carbonate reaction rates.

The reacted rock samples of the pH experiments are both dominated by quartz and K-feldspar, which matches the observations of the baseline experiment.

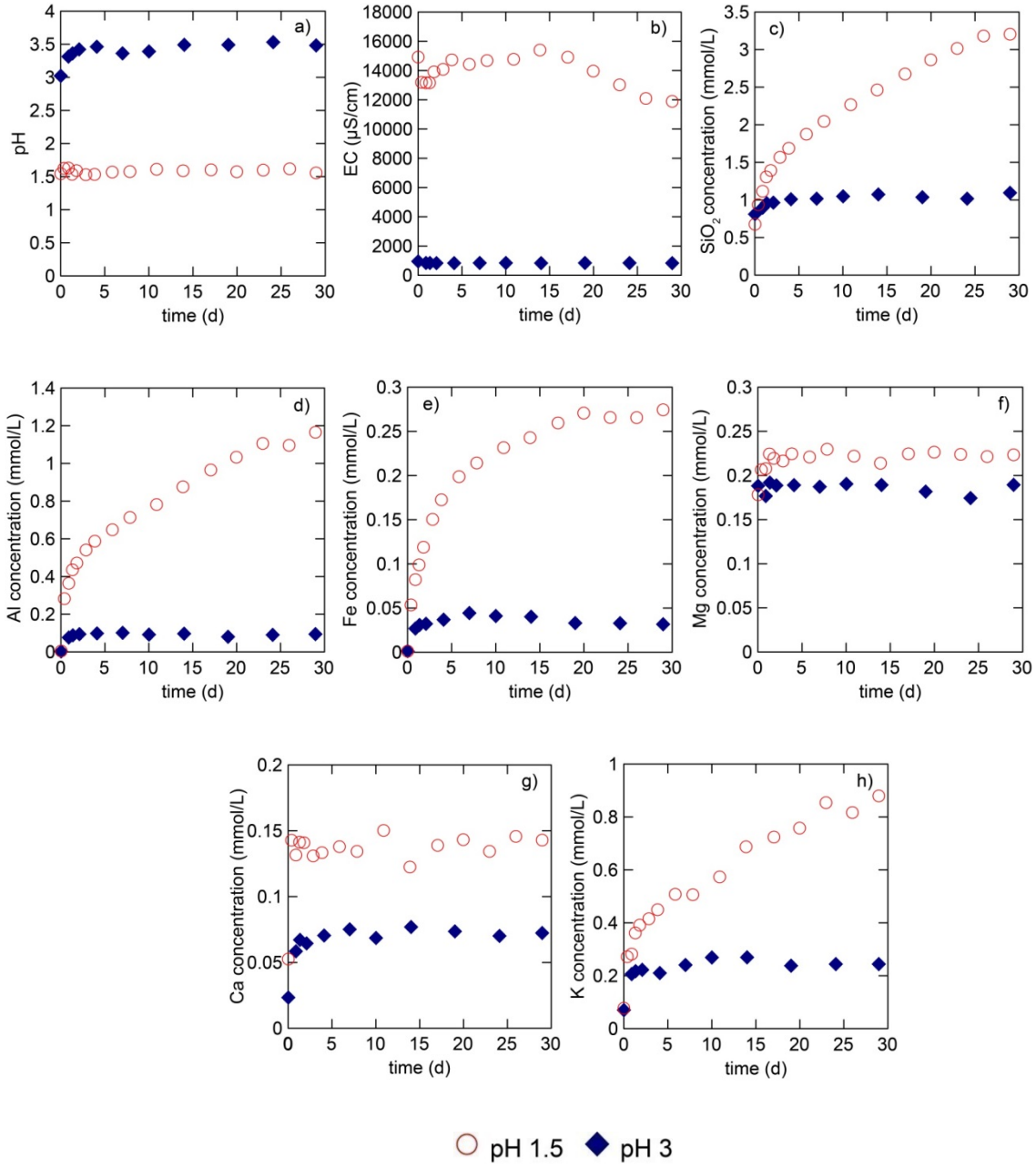

Figure 2.19 Experimental brine pH (a), EC (b), SiO_2 (c), Al (d), Fe (e), Mg (f), Ca (g) and K (h) concentration of AF-03 reaction with pH 1.5 and pH 3 brine.

AF-06

The reaction of AF-06 with pH 1.5 brine resulted in a significantly different outcome than the reaction with pH 3 brine. Figure 2.20 shows the change in pH, EC and selected element concentrations over the course of the experiment. The reaction of AF-

06 at pH 3 resulted in a rapid buffering of the pH to values at which the pH dependency of reaction rates is diminished (Figure 2.20a). At pH 1.5 on the other hand only a slight buffering of the pH was observed. Due to the lower acidification at pH 3, the EC was 15 times lower than at pH 1.5 (Figure 2.20b). The EC dropped significantly in the low pH experiment, while it remained fairly constant at pH 3, indicating greater reaction extents at pH 1.5. SiO_2 increased in concentration by approximately 4 mmol/L in the pH 1.5 experiment, while it decreased by a little less than 0.5 mmol/L in the pH 3 experiment (Figure 2.20c). This suggests that silicate mineral dissolution dominated at pH 1.5, while precipitation reactions dominated at pH 3. Al and Fe increased rapidly to values around 5 mmol/L in the low pH experiment (Figure 2.20d, e). However, in the pH 3 reaction both concentrations stayed fairly constant at $9x10^{-4}$ mmol/L and $1x10^{-4}$ mmol/L, respectively. The Mg content dropped slightly within the first 2 d of the pH 3 experiment and rose again over the following time period (Figure 2.20f). The initial decline in Mg matched the baseline experiment and must therefore represent the same process. At pH 1.5 the initial increase in SiO_2 and Al is less steep than the initial increase in Fe and Mg, suggesting that the latter is not entirely due to silicate reaction. Another source of Fe and Mg is likely carbonate dissolution. At pH 3 the total change in Ca was reduced by a factor of 5 and the total change in K to about half of the change observed at pH 1.5 (Figure 2.20g, h). The smaller changes in ion concentration at pH 3 highlight the importance of pH dependency input when calculating reaction rates.

The reacted samples of the pH experiments were both dominated by quartz and illite, which matches the baseline experiment giving no obvious evidence for mineral reaction.

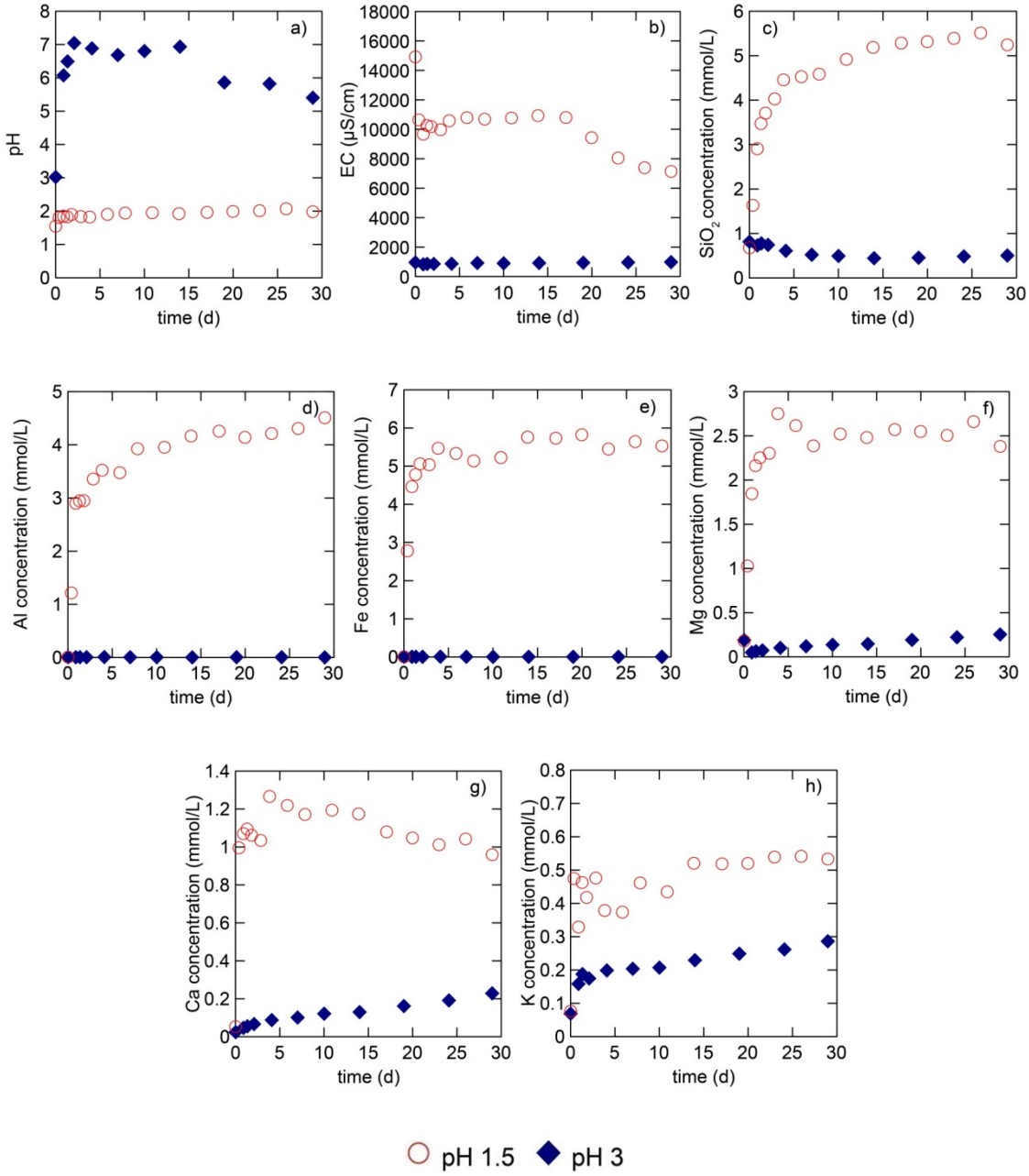

Figure 2.20 Experimental brine pH (a), EC (b), SiO_2 (c), Al (d), Fe (e), Mg (f), Ca (g) and K (h) concentration of AF-06 reaction with pH 1.5 and pH 3 brine.

Discussion

The parameter analysis of the Western Canada Sedimentary Basin samples identified significant differences in the experimental outcome with varied sample particle size, temperature and starting pH. The comparison of sample particle size shows

a positive relationship between reduction in reaction extent, and increasing particle size. Very similar experimental outcomes for the crushed and mortared samples indicate that the brine infiltrated the full available pore space of the crushed sample. For the block samples a complete infiltration was assumed as well, since their reactions resulted in a total Ca change similar to those observed in the crushed and mortared experiments. The similar change in Ca indicates that about the same amount of Ca-bearing minerals reacted in all three sample particle size experiments, which is only likely if pore access was complete, especially since the major Ca source was cementing calcite. The reduction in reaction extent with increased sample particle size demonstrates that experimental batch reactions overestimate reaction rates occurring in an actual storage reservoir. This needs to be considered carefully when estimating the effect of SO_2 storage based on experimental data.

The temperature experiments showed an obvious reduction of silicate mineral dissolution with lower temperature. The reaction extent of carbonate minerals on the other hand was similar at both temperatures due to their retrograde solubility, which makes them less soluble with increasing temperatures. This highlights the importance of activation energy data when predicting reaction rates. However, most available reaction rate data are based on experiments on pure igneous or metamorphic mineral phases, not on physically and chemically weathered and then deposited and lithified rocks. Therefore, the reaction rate data are unlikely to reflect accurate mineral reaction rates for sedimentary rocks, which are used in this study.

The pH experiments show a significant reduction of mineral reaction with increased pH, indicating a pH dependency for both silicate and carbonate minerals. The effect of SO_2 injection, therefore, can be expected to be highest at the injection well where the greatest acidification occurs. Further away from the injection well less mineral dissolution will occur and the pH is likely to be buffered to its original value.

2.3.3. Surat Basin samples

The reaction of the block Surat Basin samples with pH 1.5 brine at 60°C resulted in significant changes in the water chemistry after 30 d. The reaction extent was greatest

during the first 2 d and leveled out over the following 28 d of experiment, probably due to the presence of sample fines and exposed fresh surfaces on the block. The changes in brine composition are strongly dependant on the rock mineralogy. The Precipice Sandstone sample was least reactive, while the Hutton Sandstone had the greatest change in brine composition. The two Evergreen samples were almost as reactive as the Hutton Sandstone, with AF-08 being slightly more reactive than AF-09. Large fluctuations in concentrations were observed for the SO_4^{2-} and Cl^- concentrations likely due to the high dilution of 1:50 during the measurements. The SO_4^{2-}, varied by up to 4% from the mean value, while the Cl^- concentration varied by up to 25%. The experimental outcomes of the Surat Basin reaction with pH 1.5 brine at 60°C are summarized in the following paragraphs.

AF-07

Figure 2.21 shows the measured changes in water chemistry for the reaction of the Precipice Formation sample (AF-07) with pH 1.5 brine at 60°C. The rock sample was the least reactive Surat Basin sample and therefore the changes were small. The measured pH was constant at 1.4, while the EC varied between ~11000 µS/cm and 14500 µS/cm (Figure 2.21a). The ion concentrations of the brine mostly increased during the experiment, except for SO_4^{2-}, Cl^- and Na, which remained fairly stable. The greatest change was for SiO_2 which increased in concentration by approximately 0.6 mmol/L, followed by Al with an increase in concentration of 0.3 mmol/L (Figure 2.21b), indicating the dissolution of silicate mineral phases. K and Fe increased by ~0.15 mmol/L, while Mg and Ca increased marginally by ~0.05 mmol/L (Figure 2.21b, c). The changes in ion concentrations suggest that silicate mineral phases like illite, K-feldspar and chlorite dissolved. However, the initial increases in Fe, Mg and Ca were more rapid than the initial increase in SiO_2 and Al, suggesting an additional source for the former. Further, the Precipice Sandstone Formation had no source mineral identified in the mineralogy that can account for the increase in Ca. This indicates the presence of an undetected amount of carbonate minerals like ankerite. No indication for mineral precipitation was observed.

The SEM analysis of the reacted rock sample showed an abundance of quartz with lesser kaolinite and K-feldspar. Since these minerals were also present in the pre-reaction sample the SEM results gave no evidence of mineral reaction.

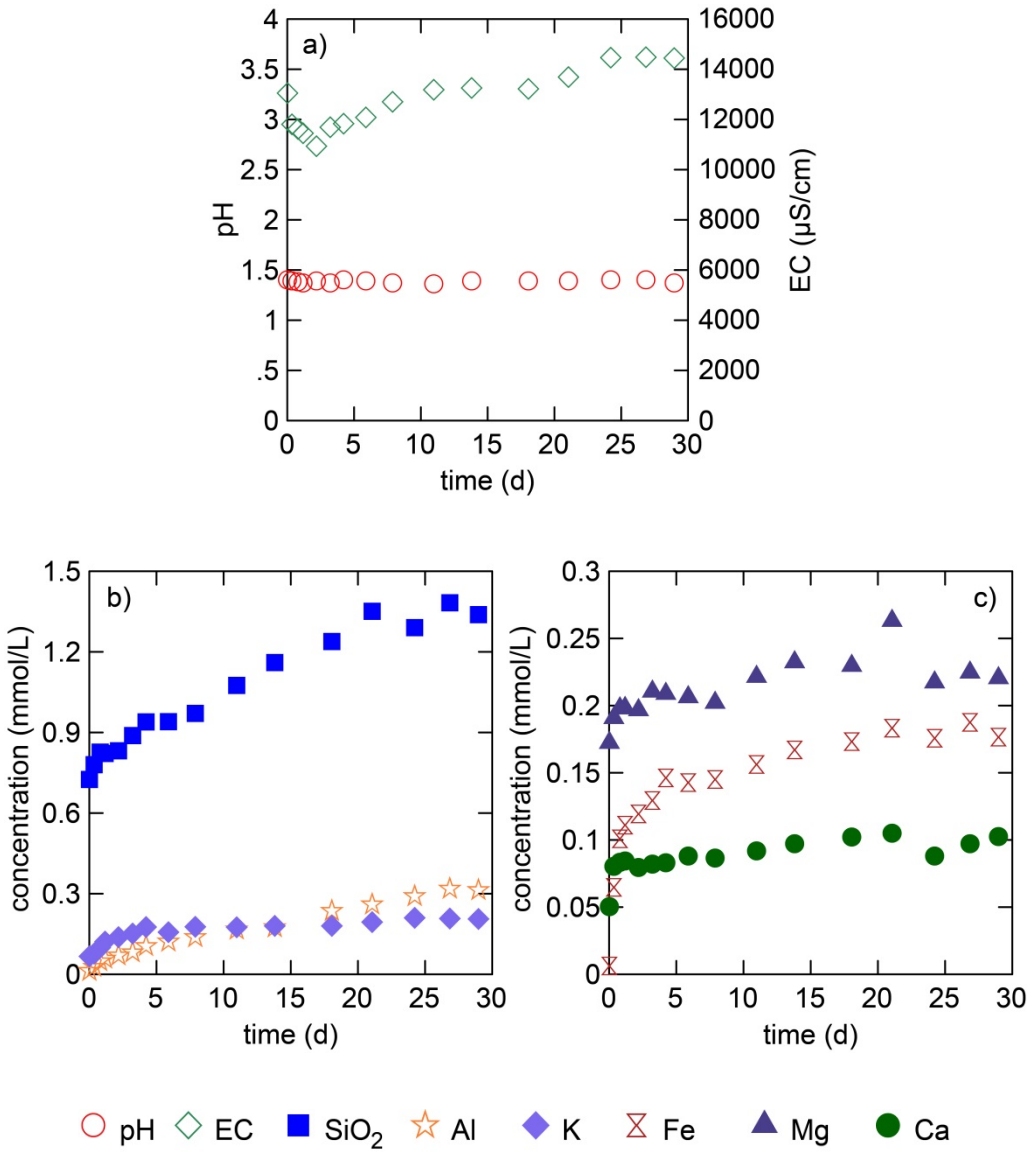

Figure 2.21 **Water chemistry for the reaction of AF-07 with pH 1.5 brine at 60°C over 30 d, showing changes in pH (a), EC (a) and, selected ions (b+c).**

AF-08

The reaction of the Evergreen Formation sample, AF-08, with pH 1.5 brine at 60°C resulted in a significant change in brine composition (Figure 2.22). pH buffering was observed resulting in an increase in pH to approximately 1.9 (Figure 2.22a). The EC decreased to 8000 µS/cm in the first to 2 d, where it remained constant over the rest of the experiment. The drop in EC likely reflects the pH buffering reaction, which removes hydrogen ions from the brine. Most ion concentrations increased, except for SO_4^{2-} and Cl^-, which remained fairly constant over the course of the experiment. SiO_2, Al, Fe and Ca had the greatest increases with increases in concentration of ~4 mmol/L (Figure 2.22b, c). This suggests the dissolution of silicate and carbonate phases. The Mg and Na content gained about ~2 mmol/L, while K increased by ~0.7 mmol/L. The rise in ion concentrations indicates that mineral phases like calcite, chlorite, K-feldspar, illite and albite dissolved, while no evidence for precipitation was recognized. The amount of calcite in sample AF-08 is not sufficient to account for the total change in Ca. About 36 mg of calcite would need to dissolve to result in the observed Ca increase. The 0.16 wt% of calcite in sample AF-08 equals only 3 mg, indicating that the unclassified mineral phases of this sample are likely to include other carbonate minerals.

The SEM analysis of the reacted AF-08 sample identified quartz, kaolinite, K-feldspar and albite as the main mineral phases. This matches the analysis of the unreacted rock sample giving no evidence for mineral reactions.

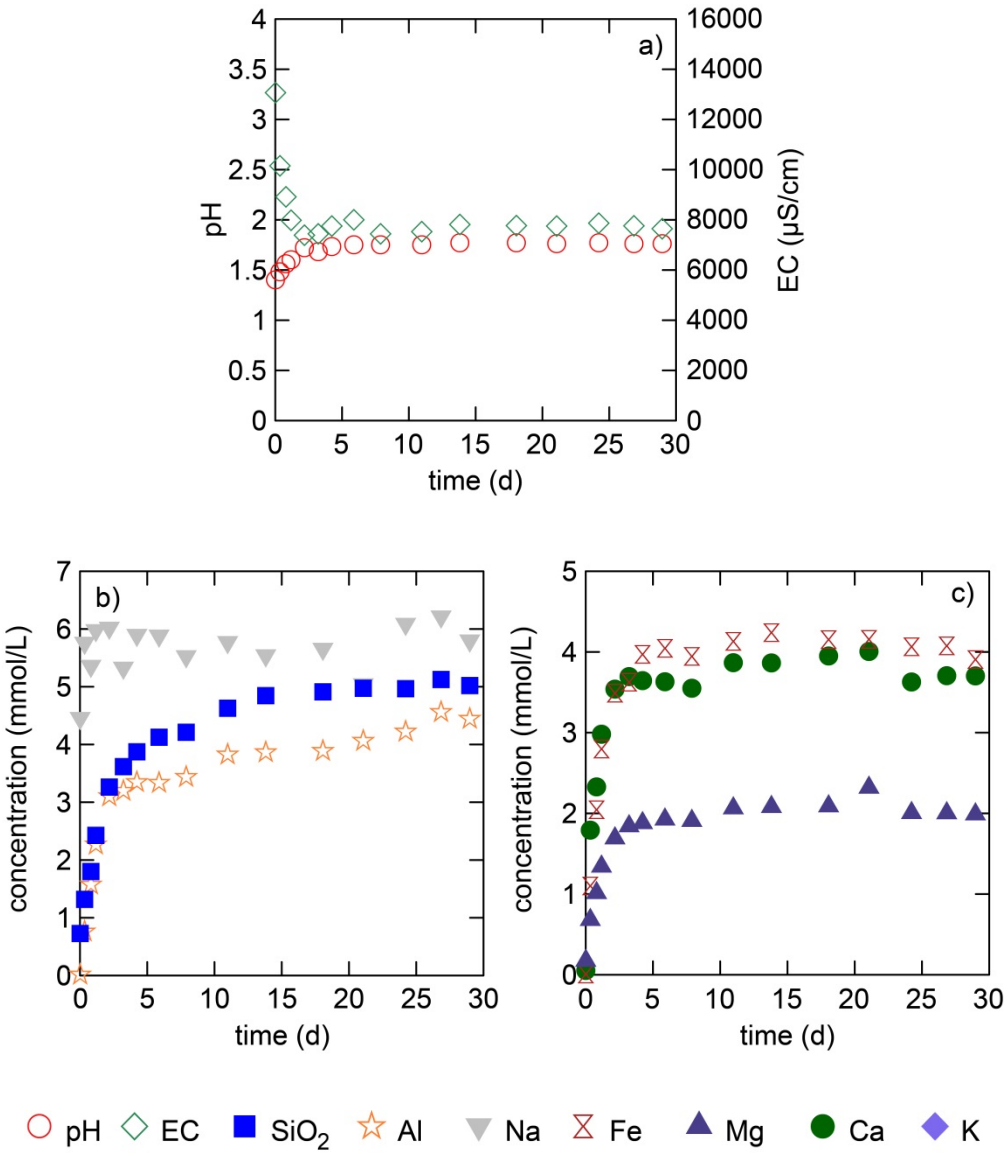

Figure 2.22 Water chemistry for the reaction of AF-08 with pH 1.5 brine at 60°C over 30 d, showing changes in pH (a), EC (a) and, selected ions (b+c).

AF-09

The second Evergreen Formation sample, AF-09, showed a smaller reaction extent compared to AF-08 at pH 1.5 and 60°C (Figure 2.23). The pH increased by approximately 0.2, while the EC decreased by ~3300 µS/cm (Figure 2.23a), likely due to the removal of hydrogen ions. The amount of SO_4^{2-} and Cl^- in the reaction brine remained constant throughout the experiment. The greatest increases in concentration

were observed for SiO_2, Al and Fe, which reached values of approximately 4 mmol/L at the end of the experiment (Figure 2.23b, c), probably due to silicate mineral dissolution. However, the initial Fe increase is steeper than the increase of SiO_2 and Al suggesting more than one Fe source. K and Ca had the lowest change, while Mg and Na increased by about 1.5 mmol/L. Like Fe, Mg and Ca increased rapidly in the beginning of the experiment suggesting carbonate dissolution. Hence, a combination of silicate (e.g. K-feldspar and albite) and carbonate dissolution (e.g. ankerite) are likely to account for the changes in ion concentrations. No evidence for mineral precipitation was observed.

The SEM analysis of the reacted AF-09 sample showed an abundance of quartz, kaolinite and K-feldspar, which was also found in the unreacted sample. In contrast to the pre-reaction mineralogy, there was a lack of carbonates on the surface of the reacted AF-09, which confirms that ankerite and siderite dissolved throughout the experiment.

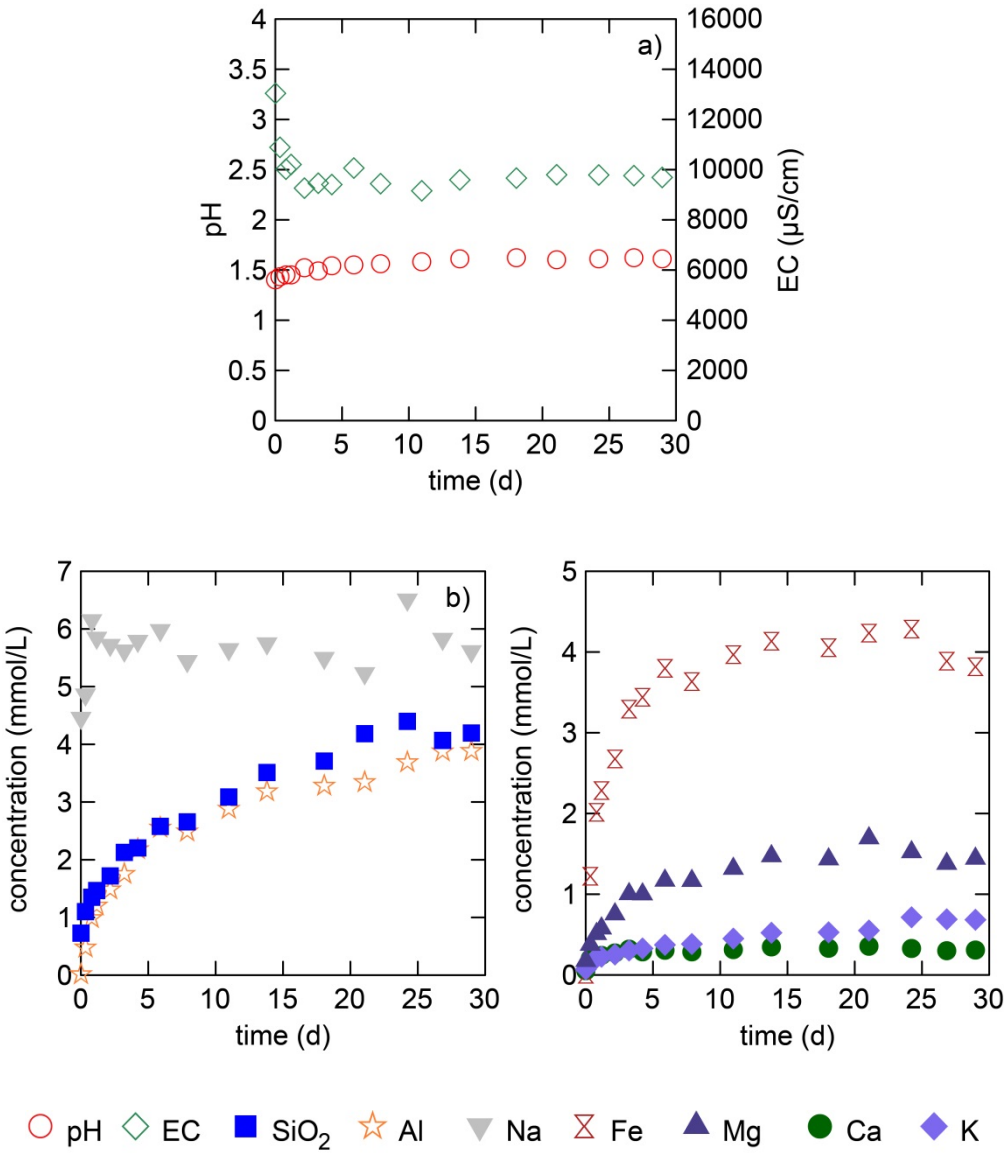

Figure 2.23 Water chemistry for the reaction of AF-09 with pH 1.5 brine at 60°C over 30 d, showing changes in pH (a), EC (a) and, selected ions (b+c).

AF-10

The reaction of the Hutton Formation sample, AF-10, with pH 1.5 brine at 60°C resulted in significant changes in the brine composition (Figure 2.24). Of all of the Surat Basin samples, the Hutton Formation sample appeared to be most reactive. The pH was buffered to 2 (Figure 2.24a), likely resulting in the observed drop in EC from 13000 µS/cm to 6000 µS/cm through the removal of hydrogen ions. Most ion concentrations

increased over the course of the experiment, except for SO_4^{2-}, Cl^- and Na, which remained fairly constant. The greatest change was for Fe with a concentration increase of ~9 mmol/L (Figure 2.24b), which is most likely due to a combination of ankerite and chlorite dissolution. The amount of Al and SiO_2 in the reaction brine increased by 5 mmol/L and 4 mmol/L, respectively. This suggests that silicate phases dissolved. The rise in Mg was about 2 mmol/L, while K and Ca increased by less than four times that amount (Figure 2.24c). The initial increase in Fe and Mg is steeper than the initial increase in SiO_2 and Al, indicating that the former is not entirely due to silicate dissolution. The additional Fe and Mg concentrations in the brine are likely due to carbonate dissolution, which also accounts for the small increase in Ca. The increase in ion concentrations indicates that mineral phases like ankerite, muscovite, K-feldspar, chlorite and biotite dissolved. Mineral precipitation processes could not be identified through the changes.

The SEM analysis showed an abundance of silicate minerals like quartz, kaolinite, muscovite, albite and K-feldspar, which were also present in the unreacted rock. However, no major chlorite, biotite or ankerite were found on the surface of the reacted AF-10 sample indicating these were dissolved.

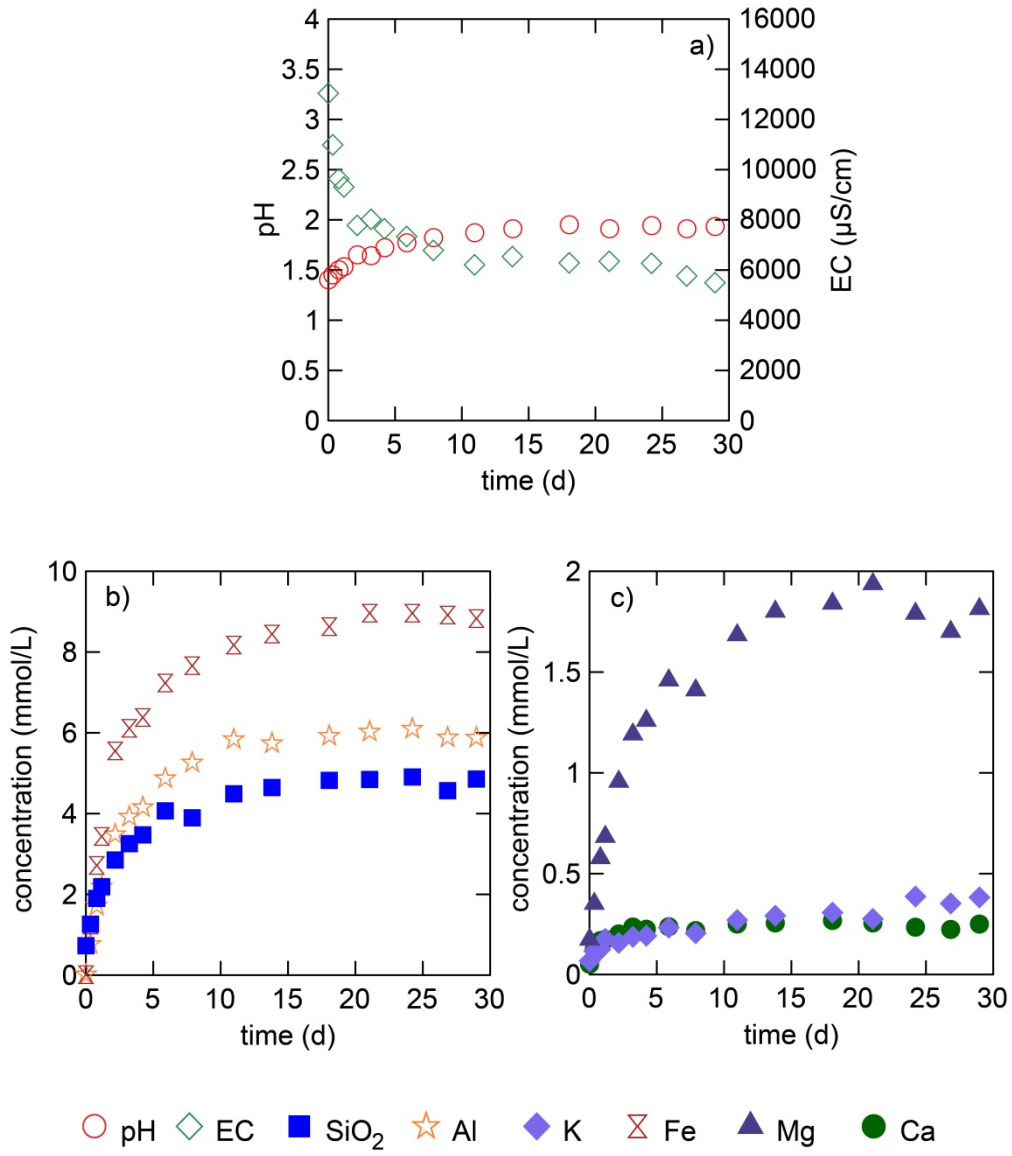

Figure 2.24 Water chemistry for the reaction of AF-10 with pH 1.5 brine at 60°C over 30 d, showing changes in pH (a), EC (a) and, selected ions (b+c).

Discussion

The Surat Basin sample experiments showed that an injection of SO_2 results in different outcomes for the Surat Basin formations, which is due to variations in mineralogy. The Precipice Formation is a very promising injection site due to its comparatively unreactive homogeneous mineralogy, which lacks carbonates and is dominated by quartz. There was very little change in brine composition even at pH 1.5.

SO_2 injection is likely to result in the dissolution of mineral phases, like illite, K-feldspar and chlorite, which is likely to increase the porosity of the formation. This is of interest since it has the potential of enlarging the available storage space. The short time period of the experiments showed no indication of mineral trapping for SO_2; mineral trapping is the safest way to store injected gases. The overlaying Evergreen Formation functions as a stratigraphic trap for gas injected into the Precipice Sandstone Formation. The reaction of the Evergreen Formation samples shows greater changes in brine composition compared to the Precipice Formation. Hence, mineral reactions are likely to occur along the Precipice-Evergreen (aquifer-caprock) border. Carbonate minerals present in the Evergreen Formation have the potential to buffer the pH significantly. Siderite, ankerite, chlorite, illite, K-feldspar and albite are likely to dissolve post SO_2 injection, possibly resulting in an increase in porosity and permeability. This is of concern since it affects the sealing properties of the caprock formation. However, the experimental results only represent short term effects of SO_2 injection and give no information about long term porosity and permeability change. The Hutton Sandstone Formation is also considered as a potential storage formation. Its reaction shows the greatest change in brine properties. Like the Evergreen Formation, it has the potential to buffer the pH of the formation water through carbonate dissolution. Furthermore, SO_2 injection is likely to result in the dissolution of silicate minerals, like muscovite, K-feldspar, chlorite and biotite. Hence, the Hutton Formation's porosity is likely to increase thereby enlarging potential storage space. Like the Precipice Sandstone Formation, the Hutton Sandstone Formation shows no evidence for SO_2 mineral trapping over the short time frame of the experiment.

2.4. Conclusion and recommendation

2.4.1. Western Canada Sedimentary Basin samples

The outcome of the Western Canada Sedimentary Basin experiments was strongly dependent on the sample mineralogy. The experimental data indicated rapid carbonate dissolution, which buffered the pH. Calcite, in particular, dissolved to a great extent, which could be proven by comparing pre- and post-reaction rock samples. One

sample showed a potential for SO_2 trapping, since calcite was replaced by a calcium sulphate precipitate. Silicate mineral phases participated in the H_2SO_4-brine-rock reactions as well, but at slower reaction rates. However, no visual evidence of silicate dissolution or precipitation was found using SEM analysis.

The experiments at different sample particle sizes identified a reduction in reaction extent with increasing sample particle size. A full infiltration of the crushed and block samples was assumed since they resulted in a similar release of Ca from the mineral phase as the mortared samples, which is only possible if full pore access is accomplished. The lower reaction extent at greater sample particle size demonstrates that experimental results overestimate the reaction rates occurring in a natural system, which is of importance when using experimental data to predict SO_2 storage at reservoir scale.

The lower temperature experiments resulted in a significant reduction in silicate reaction, while the reaction extent of carbonate minerals was similar at both temperatures. The pH experiments on the other hand showed a significant reduction of silicate and carbonate reaction with increased pH. This highlights the importance of activation energy and pH dependency data when predicting reaction rates.

The results of the Western Canada Sedimentary Basin experiments give qualitative evidence on which mineral phases are likely to react and on how different mineral reactions depend on the investigated parameters. Since no quantitative values could be obtained through the experiments, additional measures have to be taken in order to identify all mineral phases participating in the H_2SO_4-brine-rock reaction and quantify the amount of reacting mineral phases that dissolve or precipitate. Further, activation energy and pH dependency values of different mineral phases as well as the influence of accessible reactive surface area need to be evaluated to quantify the effect of the investigated parameters. Chapter 3 addresses these issues by combining the experimental data with reaction path models and quantifying the change in mineral composition under the different experimental conditions.

2.4.2. Surat Basin samples

The outcome of the Surat Basin experiments was highly dependent on the mineralogy. The reaction of the Precipice Formation sample resulted in very little change in brine composition due to a lack of reactive mineral phases. The dissolution of silicate mineral phases is likely to increase the porosity of the Precipice Sandstone Formation, which would be beneficial for its injectivity and storage capacity. The Evergreen Formation experiments resulted in a greater change in brine composition than the Precipice Formation experiment, indicating a greater change in mineralogy. The carbonate minerals preset in the Evergreen Formation have the potential to buffer the SO_2 induced acidification. The dissolution of Carbonate and silicate minerals is likely to increase the porosity of the Evergreen Formation, which has significant ramifications for its sealing properties. The Hutton Sandstone experiment showed the greatest change in brine properties, indicating a high amount of dissolution. Like the Evergreen Formation, the Hutton Sandstone has the potential to buffer the SO_2 induced acidification through carbonate dissolution. The combined dissolution of carbonate and silicate minerals is likely to increase the porosity of the Hutton Sandstone increasing its potential storage capacity. None of the Surat Basin sample experiments showed any potential for trapping SO_2 in the mineral phase over the course of the experiment.

The Surat Basin samples experiments provide qualitative information on which mineral phases are likely to react post SO_2 injection, as well as possible porosity and permeability changes. To evaluate the potential of the Surat Basin as a storage site, further investigations are necessary in order to quantify the change in mineral composition for the different formations and evaluate the porosity and permeability changes induced by SO_2 injection. This will provide a framework to assess the safety of the Evergreen Formation as a potential caprock and the possibility of permanent SO_2 storage for the Precipice and Hutton Formation. Chapter 3 approaches this problem by combining the experimental results with reaction path modelling to quantify the change in mineral composition for each Surat Basin sample.

Chapter 3. Modelling short term H_2SO_4-brine-rock reaction experiments under varying conditions

3.1. Introduction

SO_2 is a common impurity in CO_2 gas streams from coal fired power plants. While CO_2 dissolves in water to form weak carbonic acid, SO_2 reacts to form sulphurous acid and sulphuric acid leading to enhanced brine acidification and mineral reaction (Kaszuba et al., 2005; Xu et al., 2007; Ellis et al., 2010). However, SO_2 dissolution from within the $scCO_2$ plume can be controlled by diffusion, which could limit the extent of SO_2 induced acidification (Ellis et al., 2010). In previous studies, the low brine pH induced by CO_2-SO_2 injection was found to be buffered by the mineral dissolution reactions; in particular, carbonates played a significant role (Pearce et al., 2015). Reactive transport modelling studies on CO_2-SO_2 storage predict a reduction in brine pH to 0-1 and enhanced mineral dissolution and porosity around the injection well (Knauss et al., 2005; Xu et al., 2007). Further, the precipitation of carbonates, sulphates, sulphur and minor pyrite is predicted to trap CO_2 and SO_2 within and outside the acidified zone (Knauss et al., 2005; Xu et al., 2007). CO_2 mineral trapping is likely to increase in the presence of SO_2 when iron bearing minerals are present due to SO_2 induced iron reduction and siderite precipitation (Palandri et al., 2005a; Garcia et al., 2011; Garcia et al., 2012; Schoonen et al., 2012).

Experiments give qualitative information on mineral reactions, brine composition changes and possible porosity and permeability changes. Geochemical models, coupling kinetically controlled reaction path models to experimental observations, are useful tools to quantify experimental results (Gaus et al., 2008). Modelling studies on the impacts of pure and impure CO_2 injection on whole rocks or reservoirs have been published, but most of them do not successfully validate their findings with experimental

data. A large number of modelling studies on pure CO_2 storage are available. They include reaction path modelling (Gunter et al., 2000; Pruess et al., 2004; Xu et al., 2004; Allen et al., 2005; Zerai et al., 2006; André et al., 2007; Gherardi et al., 2007; Gaus et al., 2008; Cantucci et al., 2009) as well as reactive transport modelling (Gaus et al., 2005; Knauss et al., 2005; Xu et al., 2005; Bacon et al., 2009). The body of knowledge on modelling CO_2 storage with SO_2 on the other hand is limited. Studies include thermodynamic modelling used to constrain experimental results (Palandri et al., 2005a; Palandri and Kharaka, 2005b; Garcia et al., 2011; Garcia et al., 2012), investigations on the factors limiting the impacts of SO_2 storage (Crandell et al., 2010; Ellis et al., 2010) and reactive transport modelling examining the effects of CO_2-SO_2 on chemical and physical properties of the host rock (Knauss et al., 2005; Xu et al., 2007; Bacon et al., 2009).

This study uses kinetically controlled reaction path modelling to simulate the experiments described in chapter 2. The reactions of the Western Canada Sedimentary Basin samples under varied pH and temperature conditions were modelled to evaluate activation energy and hydrogen power term as input parameters for reaction rate calculations. By modelling the different sample particle size experiments mineral reactive surface data was produced and evaluated to enable upscaling of experimental results to reservoir scale. Furthermore, SO_2 induced mineral reactions were identified and quantified for the Western Canada Sedimentary Basin and Surat Basin sample experiments.

3.2. Methodology

Kinetically controlled reaction path models were used to model the experimental results of H_2SO_4-brine-rock reactions described in chapter 2. This was undertaken using the React module of the Geochemist's Workbench^{TM} (GWB) Release 9.0 software package (Bethke and Yeakel, 2012a; Bethke and Yeakel, 2012b) with a modified version of the thermo.com.V8.R6 database as the thermodynamic database for minerals, gases and aqueous species (Delany and Lundeen, 1989). Kinetically controlled reaction path modelling uses kinetic rate data to simulate changes in mineral content and brine composition with time. This is achieved by calculating the changing mineral and fluid

composition through dissolving under-saturated or precipitating over-saturated mineral phases at predefined reaction rates. The reaction rate equation is based on the transition state theory (TST) and calculates mineral reaction rates by combining the mineral's reactive surface area, the reaction rate constant and the proximity to equilibrium between the mineral and the solution as shown in Equation 3.1 (Lasaga, 1995).

$$r = A_s k_d \left(1 - \frac{Q}{K}\right) \tag{3.1}$$

r = reaction rate

A_s = mineral reactive surface area

k_d = dissolution rate constant

Q = activity product

K = equilibrium constant

A more complex form of Equation 3.1 is required to take the effects of inhibiting or catalysing species into account (in this case related to the pH) and for temperatures other than 25°C (Equation 3.2).

$$k_d = k_{25}^{nu}\left[\frac{-E_a^{nu}}{R}\left(\frac{1}{T} - \frac{1}{T_0}\right)\right] + k_{25}^{H}\left[\frac{-E_a^{H}}{R}\left(\frac{1}{T} - \frac{1}{T_0}\right)\right] a_H^{n_H} + k_{25}^{OH}\left[\frac{-E_a^{OH}}{R}\left(\frac{1}{T} - \frac{1}{T_0}\right)\right] a_{OH}^{n_{OH}} \tag{3.2}$$

E_a = activation energy

R = molar gas constant

T = temperature in K

T_0 = reference temperature (298.15 K)

nu = neutral mechanism

H = acid mechanism

OH = base mechanism

a = hydrogen ion activity

n = H^+ power term

In this study, mineral specific reaction rate scripts, which were read by the React code of GWB, were used. The scripts incorporated the temperature and the pH dependence of mineral dissolution rates by using different rate constants and activation energies for acidic, neutral and basic mechanisms (Equation 3.2).

Commonly, mineral precipitation rates are poorly constrained and therefore are estimated by using the TST equations describing the dissolution rate and allowing precipitation when the saturation index exceeds 0. If the mineral is present in the system then the reactive surface area, defined by the mineral amount, is used. If a mineral is not present then either a value is assigned for the nucleation site density or an initial volume ratio relative to the volume of solids is used (Bethke and Yeakel, 2012b). This study combined and modified the classical nucleation theory and the non-linear portion of the Burton-Cabrera-Frank (BCF) crystal growth theory to calculate mineral precipitation rates as described in Pham et al. (2011) and Hellevang et al. (2013a) (Equation 3.3).

$$r_p = A_s k_p \left(\frac{Q}{K} - 1\right)^2 - k_n exp\left\{-\Gamma \left[1/\left(T^{3/2} \ln\left(\frac{Q}{K}\right)\right)\right]^2\right\} \quad (3.3)$$

k_p = precipitation rate constant

k_n = nucleation rate constant set as 1 mol/s

Γ = pre-exponential factor for nucleation

The nucleation and precipitation rate equation was included in the reaction rate scripts read by the React module and the required data were taken from Pham et al. (2011) (Table 3.1). The thermodynamic and kinetic rate data required to model

geochemical reactions were taken from different sources (Plummer et al., 1987; Palandri and Kharaka, 2004; Golubev et al., 2009; Smith et al., 2013) and modified to fit the experimental data (Table 3.1).

Table 3.1 Kinetic rate parameters for mineral phases used in the reaction path modelling; the dissolution rate constant at 25°C (k_{25}) and activation energy (E_a) for the acidic (H) and neutral (nu) dissolution mechanism, the H^+ power term (n), the precipitation rate constant (k_p) calculated from the dissolution rate constant (k_d) and the pre-exponential factor for nucleation (Γ).

	$k_{25(H)}$ (mol/m²s)	$E_{a(H)}$ (kJ/mol)	n	$k_{25(nu)}$ (mol/m²s)	$E_{a(nu)}$ (kJ/mol)	k_p	Γ
Chalcedony				$1.7x10^{-13}$	68.7	k_d	$2x10^{10}$
K-Feldspar	$8.7x10^{-11}$	40	0.4-0.5	$3.89x10^{-13}$	38	k_d	$2x10^{10}$
Albite	$6.9x10^{-11}$	55	0.457	$2.75x10^{-13}$	69.8	k_d	$2x10^{10}$
Illite	$1.4x10^{-12}$	22	0.37-0.45	$8.91x10^{-16}$	14	k_d	$2x10^{10}$
Muscovite	$1.4x10^{-12}$	22	0.37	$2.82x10^{-14}$	22	k_d	$2x10^{10}$
Biotite	$1.45x10^{-10}$	22	0.525	$2.82x10^{-13}$	22	k_d	$2x10^{10}$
Kaolinite	$4.9x10^{-12}$	60-65.9	0.7-0.777	$6.61x10^{-14}$	22.2	$k_d/10$	$2x10^{10}$
Chlorite	$1.2x10^{-10}$	15-40	0.7-0.8	$1.00x10^{-13}$	94.3	k_d	$2x10^{10}$
Calcite	0.501	14.4	1	$1.55x10^{-06}$	23.5	k_d	$1x10^{10}$
Dolomite	$6.46x10^{-04}$	36.1	0.7	$2.95x10^{-08}$	52.2	$k_d/100$	$3x10^{10}$
Ankerite	$1.79x10^{-04}$	32-48	0.75-0.8	$1.80x10^{-07}$	43	$k_d/100$	$3x10^{10}$
Siderite	$1.79x10^{-04}$	48	0.75	$1.80x10^{-07}$	48	$k_d/100$	$3x10^{10}$

Thermodynamic and kinetic rate data for stoichiometric mineral phases are generally available in literature (e.g. Palandri and Kharaka, 2004). If the exact composition of non-stoichiometric minerals is measurable, thermodynamic data can be calculated. Alternatively end-members or surrogates can be used. In this study, phlogopite ($KAlMg_3Si_3O_{10}(OH)_2$) was substituted for biotite, K-Mg illite ($K_{0.6}Mg_{0.25}Al_{1.8}Al_{0.5}Si_{3.5}O_{10}(OH)_2$) was substituted for illite and beidellite ($(Na;K;Ca_{0.5}Mg_{0.5})_{0.33}Al_{2.33}Si_{3.67}O_{10}(OH)_2$), and nontronite were substituted ($(Na;K;Ca_{0.5}Mg_{0.5})_{0.33}Fe_2Al_{0.33}Si_{3.67}O_{10}(OH)_2$) for smectite.

Solid solution mixing models were used to create the initial mineral input of plagioclase, chlorite and ankerite. Their thermodynamic properties were calculated using the methods described in Davidson (1994), Holland et al. (1998) and Arnorssen and Stefansson (1999). The plagioclase present in the Surat Basin samples was previously identified as albite and the chlorite composition as iron-rich using hyperspectral logging (Farquhar et al., 2013). Microprobe data on the composition of plagioclase were available for samples AF-02, AF-04 and AF-05 (Appendix A). The plagioclase in AF-01, AF-03 and AF-06 was set to albite in accordance with the XRD results. Microprobe measurements on the exact chlorite composition were only available for sample AF-01, AF-04 and AF-05. For the samples AF-02, AF-03 and AF-06 the chlorite composition had to be approximated. For sample AF-02 and AF-03 magnesium-rich chlorite was assumed since the observed increase in Fe over the course of the experiment was rather low and likely dominated by siderite dissolution. A Fe:Mg ratio of 1:3 was chosen for AF-02 and 1:9 for AF-03. Chlorite present in sample AF-06 was assumed to be iron-rich according to the observed changes in concentration. A Fe:Mg ratio of 3:1 was chosen to fit the experimental data. Siderite and calcite present in AF-06 were summarized as ankerite ($CaFe_{0.5}Mg_{0.5}(CO_3)_2$) to account for the minor amounts of Ca and Mg detected by the microprobe. This solution underestimates the observed increase in Fe slightly, but otherwise provided the best fit for the experimental data. Ankerite present in the Surat Basin samples was defined as a more iron-rich ankerite ($CaFe_{0.7}Mg_{0.3}(CO_3)_2$) according to values used by Pearce et al. (2015). A summary of the ion ratios used in the models for plagioclase, chlorite and ankerite composition is shown in Table 3.2.

Table 3.2 Ion ratio of chlorite, plagioclase and ankerite in the Western Canada Sedimentary Basin and Surat Basin samples.

	Western Canada Sedimentary Basin samples						Surat Basin samples
	AF-01	AF-02	AF-03	AF-04	AF-05	AF-06	AF-07 - AF-10
Chlorite (Fe:Mg)	60:40	25:75	10:90	65:35	50:50	75:25	75:25
Plagioclase (Na:Ca)	100:0	100:0	100:0	100:0	40:60	100:0	100:0
Ankerite (Ca:Fe:Mg)						50:25:25	50:35:15

Aside from AF-09, the Surat Basin samples did not contain the appropriate mineralogy to account for the observed changes in Ca and Fe. The rapid changes in Ca and Fe indicated that the most likely mineral phases containing them were carbonates. Hence, ankerite or siderite was added to the input mineralogy (Table 3.3). 1 wt% ankerite was added to the mineralogy of AF-07 to account for the slight increase in Ca observed in the reaction of AF-07. For the mineralogy of sample AF-08 only QEMScan data were available, which in comparison to the XRD results underestimated the amounts of carbonates significantly (Appendix A). Hence, the 12.6 wt% of unclassified material was set as ankerite to account for the rapid increase in Ca and Fe. The mineralogy of AF-10 was altered to include 5 wt% of siderite to account for the rapid initial increase of Fe in the AF-10 reaction. The added amounts of carbonates are not necessarily meant to reflect the actual amount, but the presence of carbonates in sufficient quantity to account for the experimental water chemistry.

At temperatures below 80-90°C, quartz precipitation is limited, which means it is unlikely to constrain silica activity (Abercrombie et al., 1994).Therefore, this study uses chalcedony over quartz to better model compositional conditions beneficial to the stability of silica-rich mineral phases. Thermodynamic data for amorphous silica were taken from the literature and used to model chalcedony reactions (Palandri and Kharaka, 2004).

During the short period of the experiment the initial modelling results showed no reaction of hematite or pyrite. Therefore, these minerals were not included in the final models to lower computing times.

Table 3.3 Revised mineralogy of Surat Basin samples in wt%.

	AF-07	AF-08	AF-09	AF-10
Chalcedony	94.00	35.78	43.00	50.00
K-Feldspar	0.10	25.64	10.00	6.00
Albite	0.10	7.72	4.00	7.00
Illite	3.00	1.85	3.00	
Muscovite				9.00
Biotite		0.39	2.00	8.00
Kaolinite	2.55	12.17	18.00	7.00
Chlorite	0.20	3.69	4.00	7.00
Calcite		0.16		
Ankerite	1.00	12.60	10.00	4.00
Siderite			4.00	5.0

The mineral input was determined in grams (g) using the exact sample weight for every experiment (Appendix A) and the mineralogy data of the rock samples (Table 2.1; Table 3.3). H_2O was defined as the solvent and set to 0.15 free kg (150 mL) for the Western Canada Sedimentary Basin and 0.1 free kg (100 mL) for the Surat Basin experiments. The input was based on the measured synthetic brine composition of each experiment (Table 2.3). Since no alkalinity value was available for the low pH solutions, the HCO_3 concentration of the baseline experiment was used in the initial model input. To account for the uncertainty associated with that solution, a charge balance was applied to HCO_3. Further, SO_2(aq) was swapped for SO_4^{2-}, CO_2 for H^+ and O_2(g) for O_2(aq). The amount of H_2SO_4 added to the brine controlled the pH. Since the measured pH value is likely more reliable than the SO_4^{2-} concentration obtained from a 1:50 dilution, the concentration of SO_2(aq) was set to fit the starting pH. Values of 31 mmol/L and 37 mmol/L SO_2(aq) were chosen to simulate the pH 1.5 brine and a value of 2.1 mmol/L to achieve a pH of 3. O_2(g) and CO_2 were set to their atmospheric fugacity of 0.21 and 0.0004. For the pH 3 experiments, the O_2 fugacity was reduced by two orders of magnitude to account for the nitrogen atmosphere in the glovebox. This step was deemed unnecessary for CO_2 due to its already low concentration. The fugacity of both gases was fixed over the 30 d modelling period since the batch system was opened on a

regular basis for sampling. The simulation temperature was set to 60°C for all models, except the low temperature experiment models, which were modelled at 22°C.

The simulation covered the 30 days of the experiment and was undertaken in two time steps. The model had to be separated into two time steps to account for sample fines, which were created through cutting, crushing and mortaring the different rock samples. Compared to the rock sample itself the sample fines had significantly greater reactive surface areas resulting in enhanced reaction rates at the beginning of the experiment. To model the reaction rates of the sample fines, the first two days of reaction were modelled with mineral reactive surface areas up to $5x10^6$ cm^2/g. After the first two days of reaction the reaction rates decreased significantly suggesting complete dissolution of the sample fine. The mineral and brine composition output of the two-day model was used to set up the second time step, which simulated the reaction of the rock sample without the influence of sample fines. Hence, the reactive surface areas used in the second time step are likely to represent the available reactive surface area of the different mineral phases better. The initial reactive surface areas were reduced by one order of magnitude for silicates and by a factor between 0 and 30 for carbonates to model the subsequent 28 d. The scaling factor for the carbonates had to be adjusted depending on the carbonate phase and rock sample due to the high sensitivity of carbonate reaction rates on reactive surface area. The mineral reactive surface area was considered the only variable in the model and was adjusted to achieve the best degree of fit to the experimental data. The reactive surface area of a mineral is controlled by selective sites and is highly variable considering the effects of surface coating, grain to grain contacts, grain edges, faces on minerals with a tabular morphology, and channelling of the reactive fluid flow (Sonnenthal and Spycher, 2000; Li et al., 2006; Zhu et al., 2006). To simplify the model, the silicate minerals were assigned groups with one surface area depending on grain size observations with SEM and thin sections. Chalcedony, albite and K-feldspar were grouped as major framework minerals and assigned lower reactive surface areas than the group of clay minerals, which consisted of illite, muscovite, biotite, kaolinite and chlorite. The carbonate minerals on the other hand were assigned unique values. The reactive surface areas applied in the second model step are listed in Table 3.4 and in more detail in Appendix E.

Table 3.4 Range of assigned reactive surface area for mineral phases in cm^2/g.

	Western Canada Sedimentary Basin samples			Surat Basin samples
	Mortared	**Crushed**	**Block**	**Block**
Chalcedony; albite; K-feldspar;	800-8000	500-8000	100-1000	2000-5000
Illite; muscovite; biotite*; chlorite; kaolinite	$1x10^4$-$5x10^5$	$1x10^4$-$5x10^5$	$0.5x10^4$-$3x10^5$	$5x10^4$-$1x10^5$
Calcite	0.05-2	0.05-1	0.003-0.1	0.01
Dolomite	5	1	0.2	
Ankerite	0.1	0.1	0.1	0.007-0.02
Siderite	0.25-0.5	0.25-0.5	0.1-0.2	0.1

*biotite was treated like a framework mineral for AF-10

3.3. Results and discussion

3.3.1. Temperature and initial pH

The first step of the modelling was to evaluate the temperature and pH dependence of the reaction rates against the published values. The activation energy and/or the power term for H^+ activity had to be adjusted for selected mineral phases to fit the experimental data at different temperatures or pH values. The kinetic rate data sourced from literature (Plummer et al., 1987; Palandri and Kharaka, 2004; Golubev et al., 2009; Smith et al., 2013) were used to first determine whether the activation energies for the different dissolution reactions were appropriate, and second to establish whether the pH dependence was correct. The model reactive surface areas were adjusted for the low temperature experiments until the models matched the experimental results. Running the same models at a higher temperature allowed for the identification of unsuitable activation energies when the model output did not match the experimental data of the higher temperature experiments. The activation energy for any reaction that resulted in mismatch was then iteratively adjusted until the models and experimental results coincided. The same process was undertaken for the experiments at different pH values. The resultant activation energies and power terms were then used in all of the subsequent modelling.

Temperature

The activation energies applied in the reactive rate scripts were taken from literature sources. The data for chalcedony, albite, K-feldspar, kaolinite and muscovite are from Palandri and Kharaka (2004); the data for chlorite are from Palandri and Kharaka (2004) and Smith et al. (2013); the data for calcite and dolomite are from Plummer et al. (1987); and the data for siderite are from Golubev et al. (2009) (Table 3.5). The activation energy for ankerite was set to the literature values for siderite, and for illite to the values for muscovite. However, the literature rate data were not sufficient to model the reactions of the Western Canada Sedimentary Basin samples at different temperatures and had to be modified for selected minerals (Table 3.5). This is due to the fact that most available literature data on mineral reaction rates are based on experiments with igneous or metamorphic rock sourced single-mineral phases, which are likely to behave differently to sedimentary rock mineral mixtures.

Table 3.5 Adjusted activation energies applied to model the Western Canada Sedimentary Basin experiments at different temperatures compared to literature values (Golubev et al. 2009; Palandri and Kharaka, 2004; Plummer et al. 1987; Smith et al., 2013); n.c. indicates no adjustment was made from published values.

	Ea (kJ/mol)	
	Literature	**Adjusted**
Chalcedony	68.7	n.c.
K-Feldspar	51.7	40[all]
Albite	65	55[all]
Illite	22	n.c.
Muscovite	22	n.c.
Kaolinite	65.9	60[AF-01, AF-04, AF-05]
Chlorite	25.1-88	15-40[all]
Calcite	14.4	n.c.
Dolomite	36.1	n.c.
Ankerite	48-61	48[AF-06]
Siderite	48-61	48[all]

Chlorite required the greatest adjustments due to its compositional variability (Appendix D). The literature data indicated lower activation energies for Mg-rich chlorite

(Smith et al., 2013) compared to Fe-rich chlorite (Palandri and Kharaka, 2004). The same trend was observed for the applied modelling values. To model the reaction of chlorite with 90% Mg, an activation energy of 15 kJ/mol was used. At the other end of the spectrum, an activation energy of 40 kJ/mol was required to simulate the reaction of chlorite with 75% Fe. The K-feldspar and albite activation energies described in Palandri and Kharaka (2004) were found to be ~10 kJ/mol too high to model the Western Canada Sedimentary Basin experimental data; however, the values are well within the range reported for feldspar dissolution (Blum and Stillings, 1995). The literature value of kaolinite provided a good enough fit, but was decreased by 6 kJ/mol for the AF-01, AF-04 and AF-05 model to improve the results. The activation energy used to model the reaction of siderite was found to be at the lower end of the literature values described in Golubev et al. (2009). The ankerite in AF-06 reacted similarly to siderite, which is reasonable since it was used to model a mixture of impure siderite and calcite. Hence, the activation energy used to simulate the reaction was maintained at the siderite value.

Initial pH

The reaction rate scripts used pH dependency values, which were taken from literature sources. The data for albite, K-feldspar, kaolinite and muscovite are from Palandri and Kharaka (2004); the data for chlorite are from Palandri and Kharaka (2004) and Smith et al. (2013); the data for calcite and dolomite are from Plummer et al. (1987); and the data for siderite are from Golubev et al. (2009) (Table 3.6). Ankerite was set to the literature values for siderite, and illite to the values for muscovite. However, the literature rate data were not sufficient to model the reaction of the Western Canada Sedimentary Basin samples at different acidity levels, for the same reasons as the activation energies. The literature data and the modified values used to model the Western Canada Sedimentary Basin sample reactions at pH 1.5 and 3 are listed in Table 3.6. All of the modified values fall within the range of published values for these mineral phases.

Table 3.6 Adjusted power for H^+ applied to model the Western Canada Sedimentary Basin experiments at different stating pH compared to literature values (Golubev et al. 2009; Palandri and Kharaka, 2004; Plummer et al. 1987; Smith et al., 2013); n.c. indicates no adjustment was made from published values.

	n	
	Literature	**Adjusted**
K-Feldspar	0.5	0.4^{all}
Albite	0.457	n.c.
Illite	0.37	$0.45^{AF\text{-}01, AF\text{-}04, AF\text{-}05}$
Muscovite	0.37	n.c.
Kaolinite	0.777	$0.7^{AF\text{-}01, AF\text{-}04, AF\text{-}05}$
Chlorite	0.49	$0.7\text{-}0.8^{all}$
Calcite	1	n.c.
Dolomite	0.5	$0.7^{AF\text{-}01}$
Ankerite	0.75	n.c.
Siderite	0.75	n.c.

The H^+ power term for chlorite required the largest adjustment. The modelling of the experimental data showed that chlorite reaction rates are more sensitive to low acidic conditions than suggested by the literature. The hydrogen power term used by the models was between 0.7 and 0.8. Similar values have been reported in previous publications on chlorite rates (e.g. Hamer et al., 2003). The pH dependency of chlorite reaction rates showed no obvious connection to the compositional variability of chlorite. The model also resulted in a higher hydrogen power term for dolomite, which coincides to the high solubility of carbonates at low pH. K-feldspar was found to be slightly less sensitive to changes in pH compared to published data. The literature values describing the pH dependency of kaolinite and illite resulted in a decent fit of the experimental data. The values were only adjusted in selected cases to slightly improve the results.

Discussion

By modelling the Western Canada Sedimentary Basin experiments at different temperatures and starting pH values, kinetic rate data for selected mineral phases were evaluated. The activation energy and H^+ power terms found in different literature sources were not always sufficient to model the experimental data. This indicates that kinetic rate

data commonly derived from experiments on single-phase, igneous/metamorphic minerals do not always match the behaviour of multi-mineral, sedimentary rocks made up of physically and chemically weathered minerals, both transported and authigenic. This is especially true for compositionally variable minerals, like chlorite, which had a wide range in activation energies (Table 3.5). Chlorite also displayed a greater pH dependency than indicated in the majority of the literature (Table 3.6). The same was found for dolomite and siderite.

3.3.2. Western Canada Sedimentary Basin Samples

The GWB models of the Western Canada Sedimentary Basin samples fit the observed brine changes reasonably well. Carbonates and chlorite were identified as the most reactive mineral phases. Of the carbonates, calcite reacted the fastest and to the greatest extent, followed by dolomite, then siderite and ankerite. Chlorite reactivity was especially high when no or only little siderite was present, likely due to the lower iron content of the brine. The simulations also predicted feldspar, mica and kaolinite dissolution, but to a lesser extent. Chalcedony, smectite and sulphates (e.g. gypsum) were identified as the main precipitating phases. The two-step modelling approach resulted in an abrupt change in reaction rates, which did not always fit the experimental results perfectly. However, it was deemed a good enough fit and was determined that and this study refrained from further refinement to keep the model easily applicable.. The outcome of the models simulating the reaction of the mortared Western Canada Sedimentary Basin samples with pH 1.5 brine at 60°C are summarized in the following paragraphs.

AF-01

The fit of the model to the brine changes of the experiment of AF-01 with pH 1.5 brine at 60°C is shown in Figure 3.1. The rapid initial increase in pH and the Ca, Mg and Fe concentrations was modelled by carbonate dissolution (Figure 3.1a, b, c; Table 3.7). Of all carbonates, calcite showed the greatest reaction extent and decreased by 0.32 g. Dolomite reacted quickly as well with 3.63 wt% dissolved, while only 0.02 wt% of siderite dissolved. The model accounted for the early decrease in SO_4^{2-}, Ca, Fe and Al by precipitating sulphate minerals. Due to an abundance of Ca, gypsum ($Ca(SO_4)\cdot 2H_2O$)

precipitation dominated with the formation of nearly 0.3 g. Jarosite ($KFe_3(OH)_6(SO_4)_2$) and alunite ($KAl_3(OH)_6(SO_4)_2$) were predicted to precipitate as well, but to a lesser extent. According to the model, gypsum and jarosite reached saturation and started to precipitate within the first 20 minutes of the experiment. The assumption of immediate precipitation at saturation agrees with the change in SO_4^{2-} and Ca, and therefore is applicable to gypsum. However, the early formation of jarosite underestimated the brine Fe and K content, so jarosite is likely better represented with a kinetic control on precipitation.

In the model, alunite reached saturation after ~28 h and started to precipitate, which fit the observed decrease in Al concentration. The model calculated the initial increase in SiO_2 and Al through chlorite and feldspar dissolution. Chlorite also contributed to the Fe and Mg concentration in the brine. Chlorite had the greatest reaction extent of all silicate minerals, decreasing by 0.17 wt%. Almost 2 mg of both albite and K-feldspar dissolved, resulting in a slight increase in Na and K. The effect of albite reaction on the Na concentration could not be distinguished due to the high initial Na concentration. Besides chlorite and feldspars, muscovite and kaolinite dissolution contributed to the SiO_2 and Al contents, but to a much lesser extent. The decrease in SiO_2 after about 4 d of reaction was modelled by assuming saturation and precipitation of calcium-rich smectite.

Chalcedony was over-saturated over the 30 d of reaction and 0.5 mg precipitated. The modelled change in SiO_2 concentration over the first 2 d matched the experiment but the later amounts were slightly underestimated. A similar pattern was observed for the change in pH where the model fit the data for the first 2 d of experiment, but was subsequently underestimated, and then after ~7 d the model overestimated the H^+ activity. These observations are likely due to the drastic drop in reactive surface area between the first and second time step. By underestimating the pH for ~5 d the model likely overestimated the amount of acid catalyzed dissolution. However, due to the rapid carbonate dissolution within the first 2 d of reaction the pH was already buffered to a value at which the influence of pH on reaction rates is significantly reduced. Hence, the deviation of the model from the experimental pH likely resulted in a neglectable error for mineral reaction rates.

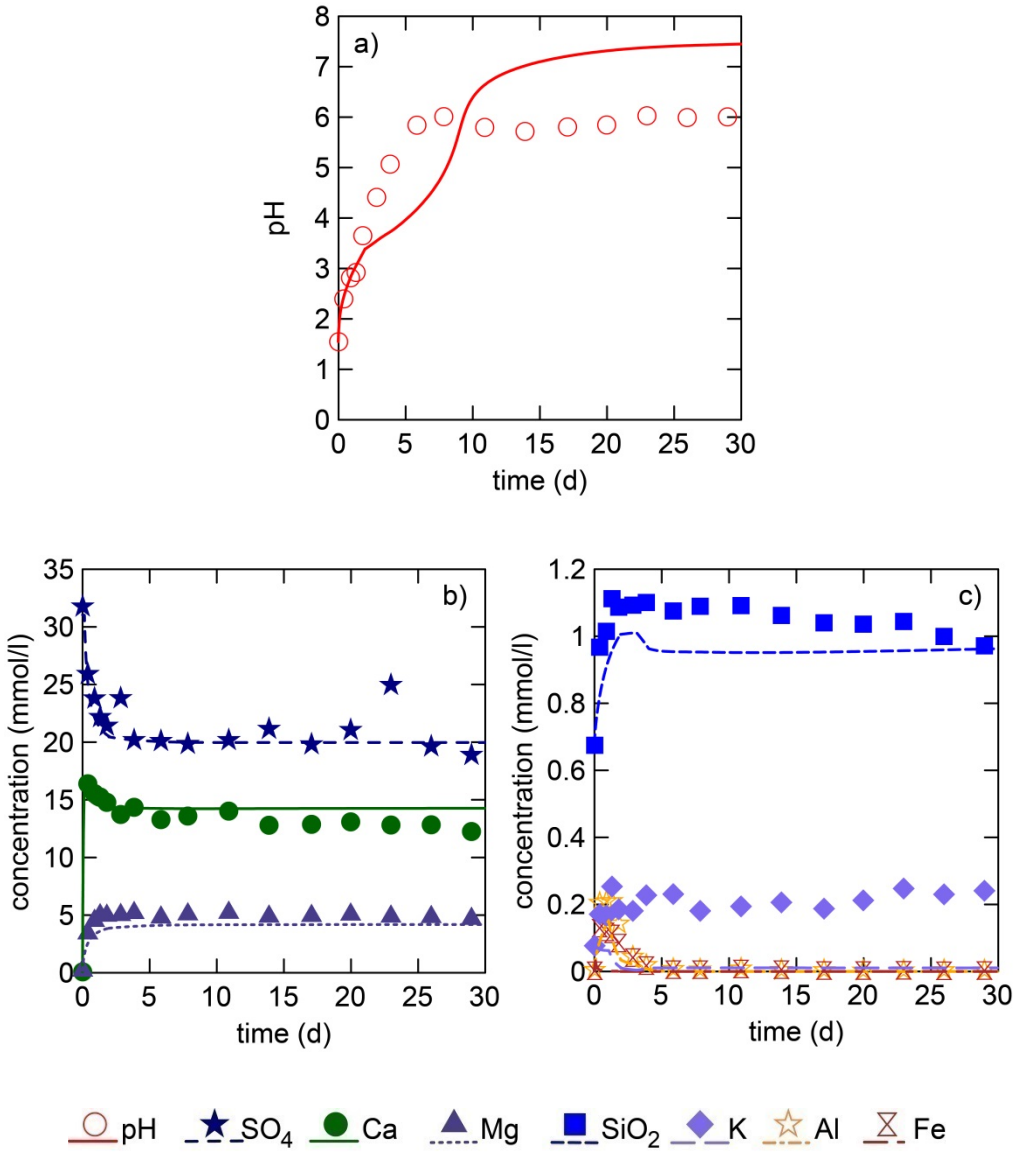

Figure 3.1 **Modelled (lines) and observed (symbols) change in brine properties for the reaction of AF-01 with pH 1.5 brine at 60°C over 30 d; the modelled SO_4 concentration gives the elemental sulphur concentration, while the observed values are ion concentrations.**

Table 3.7 Modelled extent of mineral dissolution (-) and precipitation (+) in g and change in mineralogy in wt% for the reaction of AF-01 with pH 1.5 brine at 60°C over 30 d.

	Δ g	Δ wt%
Chalcedony	4.80×10^{-4}	0.02
K-Feldspar	-1.81×10^{-3}	-0.06
Albite	-1.96×10^{-3}	-0.07
Muscovite	-4.49×10^{-4}	-0.01
Kaolinite	-4.73×10^{-4}	-0.02
Chlorite	-0.01	-0.17
Calcite	-0.32	-10.72
Dolomite	-0.11	-3.63
Siderite	-5.24×10^{-4}	-0.02
Gypsum	0.28	9.44
Alunite	3.38×10^{-3}	0.11
Jarosite	4.70×10^{-3}	0.16
Smectite	2.01×10^{-3}	0.07

AF-02

The brine properties of the reaction of AF-02 with pH 1.5 brine at 60°C were well represented by the model (Figure 3.2). The model accounted for the rise in pH by reacting carbonate minerals (Figure 3.2a; Table 3.8). The rapid increase in Ca was the result of dissolving 0.51 wt% calcite very early in the experiment (Figure 3.2c). The final Ca concentration was slightly underestimated by the model, which is probably due to some undetected Ca content in the other carbonate minerals. Siderite decreased by 0.17 wt% and contributed to the quick rise in Fe. Another Fe source was chlorite, which decreased by ~40 mg adding to the Mg, Al and SiO_2 content of the brine (Figure 3.2b). The model underestimated the change in Mg, which might be due to a slightly different Mg:Fe ratio of the chlorite compared to the modelled chlorite composition or undetected Mg content in the carbonates. The increase in SiO_2 and Al was modelled through not only chlorite, but also K-feldspar and kaolinite dissolution; 40 mg of albite, 30 mg of K-feldspar and 20 mg of kaolinite went into solution. Muscovite dissolved as well, but the reaction extent was about one order of magnitude lower. The reaction of K-feldspar and muscovite simulated the change in K well, while albite dissolution contributed to the Na

content of the brine. However, due to the high initial amount of Na, the effect of albite dissolution was insignificant over the short term of the experiment.

According to the model, chalcedony was over-saturated throughout the experiment and precipitated about 20 mg, thereby reducing the total increase in SiO_2. The initial increase and final values of SiO_2, Al, Fe and K were fit very well by the model. However, the change in SiO_2 was overestimated during the first 5 d of experiment, while the Al, Fe and K increase was underestimated over the majority of the second time step. This is likely due to the significant decrease (at least 1 order of magnitude) in reactive surface area of the model between the time intervals required for modelling the initial fine particle dissolution (2 d) and the later portion of the experiment.

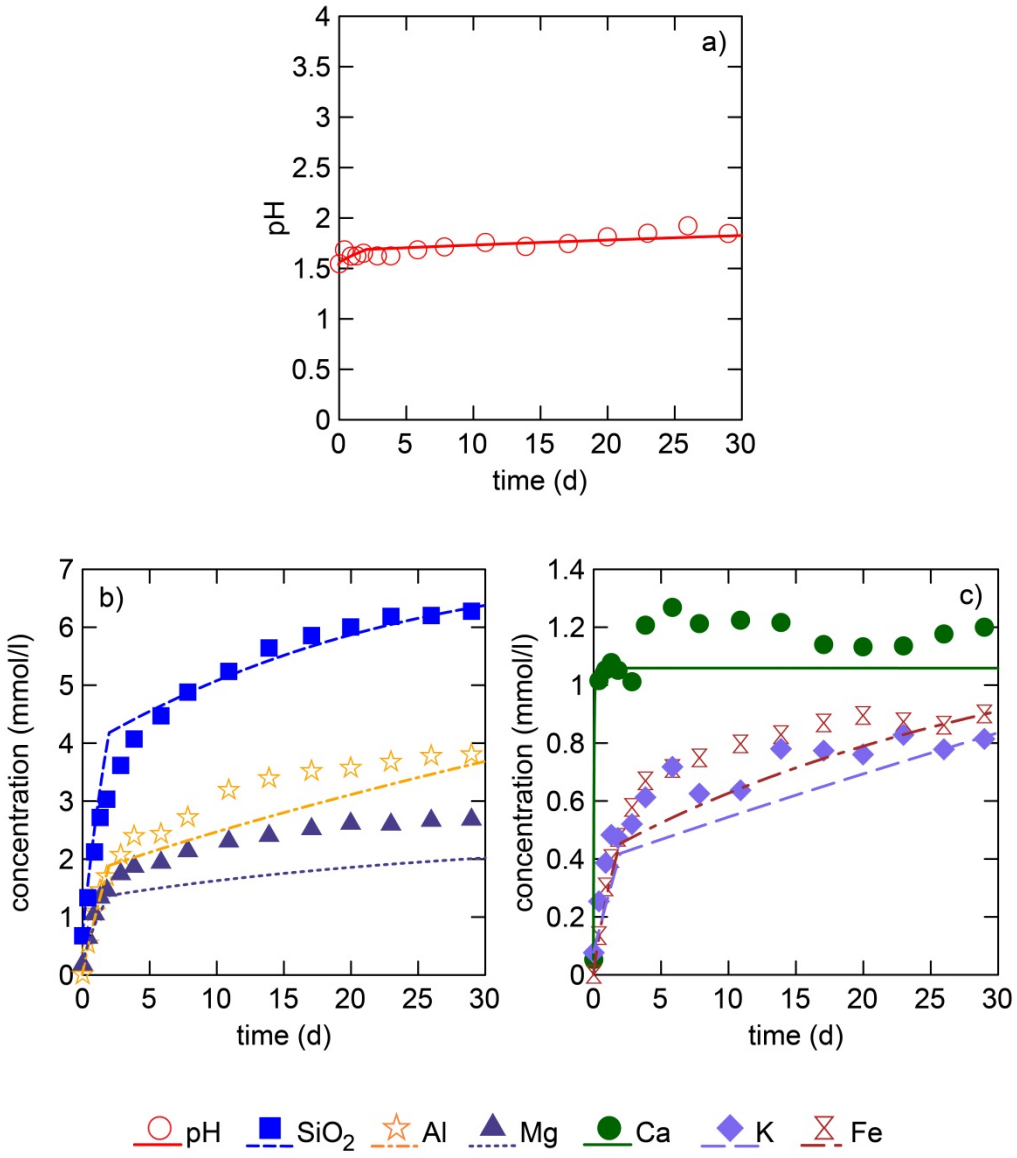

Figure 3.2 **Modelled (lines) and observed (symbols) change in brine properties for the reaction of AF-02 with pH 1.5 brine at 60°C over 30 d.**

Table 3.8 Modelled extent of mineral dissolution (-) and precipitation (+) in g and change in mineralogy in wt% for the reaction of AF-02 with pH 1.5 brine at 60°C over 30 d.

	Δ g	Δ wt%
Chalcedony	0.02	0.57
K-Feldspar	-0.03	-0.97
Albite	-0.04	-1.35
Muscovite	-4.53×10^{-3}	-0.15
Kaolinite	-0.02	-0.51
Chlorite	-0.04	-1.48
Calcite	-0.02	-0.51
Siderite	-0.01	-0.17

AF-03

The results of modelling the reaction of AF-03 with pH 1.5 brine at 60°C are shown in Figure 3.3. The gain in SiO_2 and Al was modelled predominantly by assuming K-feldspar dissolution (Figure 3.3b; Table 3.9). Over 30 d the model reacted 40 mg of K-feldspar, which reproduced the increase in K concentration. Furthermore, albite, chlorite, kaolinite and muscovite dissolution was calculated to contribute to the SiO_2 and Al concentrations. Albite and chlorite both decreased by ~1.3 mg, muscovite by ~0.5 mg and kaolinite by ~0.35 mg. The reaction of chlorite also added to the concentration of Mg and Fe in the brine (Figure 3.3c). Due to its low iron content, chlorite played a minor role in the Fe increase in the brine. The initial gain in Fe was modelled by reacting 0.15 wt% of the siderite. The model further predicted a decrease in calcite by 0.04 wt%, which accounted for the rapid increase in Ca. Like the experiment, the model showed almost no pH increase over the 30 d modelling period (Figure 3.3a) reflecting the low abundance of reactive carbonate mineral phases in this rock.

The model predicted chalcedony over-saturation and precipitation, which reduced the change in SiO_2. The model fit the change in K and Mg well; however, both SiO_2 and Al were underestimated after the 30 d modelling period. The difference between the experimental and modelled Al values is fairly low. This might be due to the model using minerals that have a slightly different composition than the ones present in the actual rock sample. Initially the model overestimated the increase in SiO_2, but by day 10, the

change was underestimated. This was likely the result of the abrupt decrease in reactive surface area between the first and second modelling step. Another explanation might be that the model overestimated the amount of chalcedony precipitation over the 30 d.

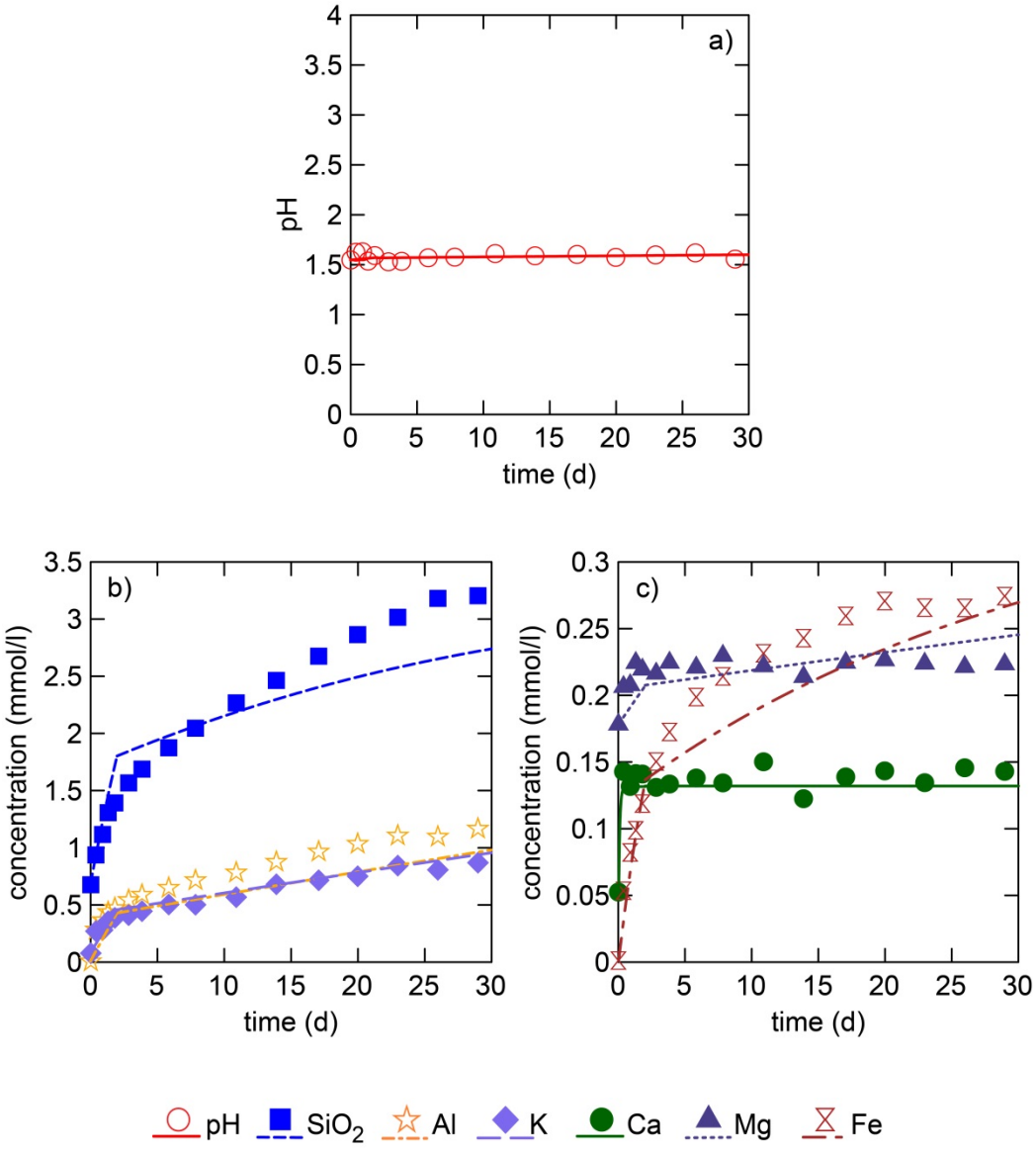

Figure 3.3 **Modelled (lines) and observed (symbols) change in brine properties for the reaction of AF-03 with pH 1.5 brine at 60°C over 30 d.**

Table 3.9 Modelled extent of mineral dissolution (-) and precipitation (+) in g and change in mineralogy in wt% for the reaction of AF-03 with pH 1.5 brine at 60°C over 30 d.

	Δ g	Δ wt%
Chalcedony	0.01	0.22
K-Feldspar	-0.04	-1.23
Albite	-1.29×10^{-3}	-0.04
Muscovite	-5.20×10^{-4}	-0.02
Kaolinite	-3.51×10^{-4}	-0.01
Chlorite	-1.29×10^{-3}	-0.04
Calcite	-1.20×10^{-3}	-0.04
Siderite	-4.60×10^{-3}	-0.15

AF-04

The modelled and experimental results of the AF-04 reaction at pH 1.5 and 60°C are presented in Figure 3.4. The initial rapid increase in Ca was modelled by dissolution of 1.17 wt% calcite at the beginning of the simulation (Figure 3.4c; Table 3.10). The reaction of calcite accounted for the initial increase in pH (Figure 3.4 a); according to the model the later pH rise was due to chlorite dissolution. The reaction of 0.16 g of chlorite also fit the increases in SiO_2, Fe, Mg and Al (Figure 3.4b, c). Both the pH and SiO_2 concentrations were slightly overestimated, indicating that the extent of chlorite reaction was overestimated by the model. Hence, the rise in Fe and Mg might partially be due to Fe-Mg carbonates unaccounted for in the mineralogy. Albite and illite were predicted to decrease by 10 mg and kaolinite by 30 mg, contributing to the increase in SiO_2 and Al, although the impact would be small relative to the chlorite contribution. With the reaction of illite the model accounted for the minimal increase in K. The total change in SiO_2 was overestimated by the model, while Al was underestimated for the majority of the modelling period. This was likely due to the model using silicate solid solutions or end members which have a different composition than the minerals in the actual rock sample. It could also indicate that the model underestimated the role of precipitation within the 30 d modelling period. Only chalcedony was modelled as over-saturated and formed ~10 mg.

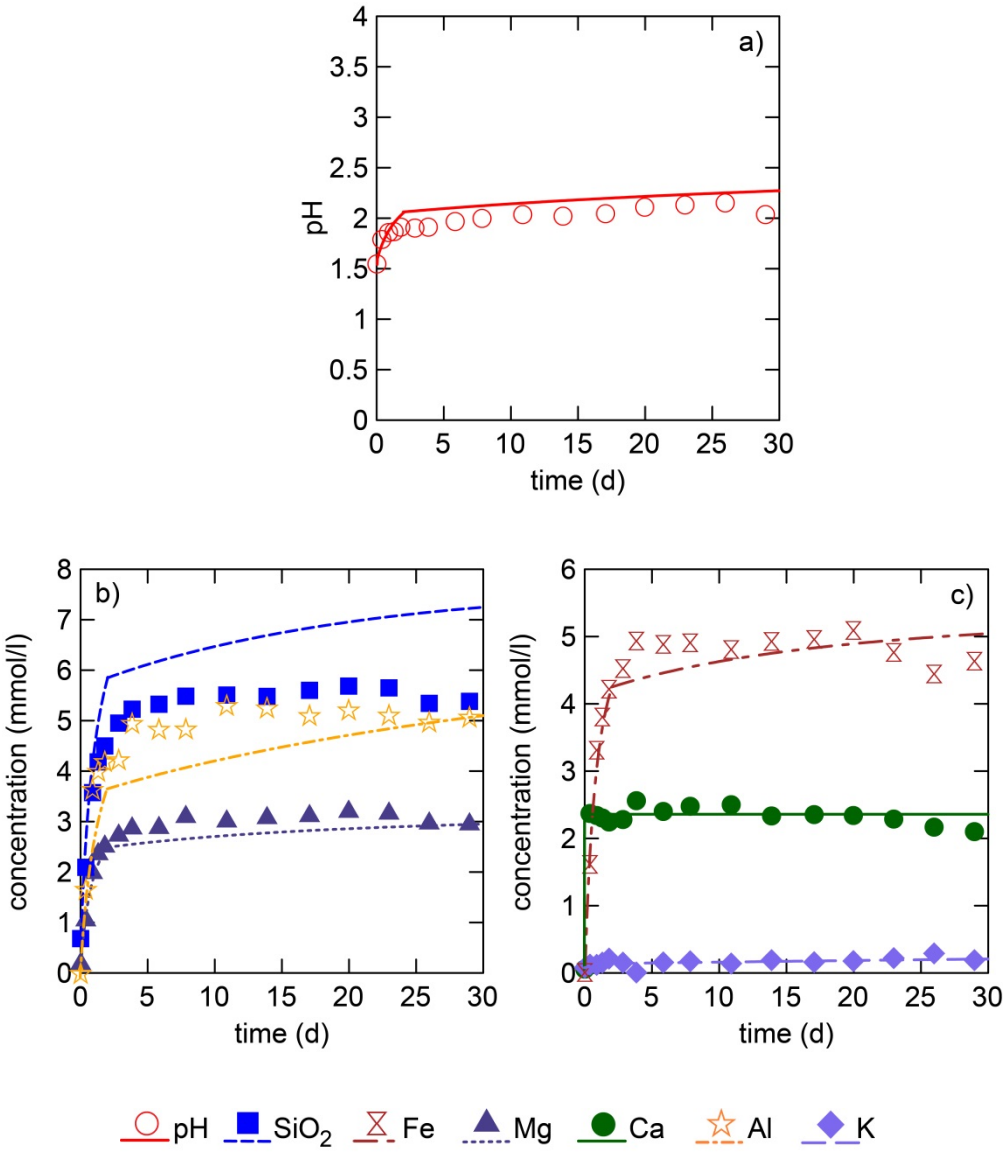

Figure 3.4 **Modelled (lines) and observed (symbols) change in brine properties for the reaction of AF-04 with pH 1.5 brine at 60°C over 30 d.**

Table 3.10 Modelled extent of mineral dissolution (-) and precipitation (+) in g and change in mineralogy in wt% for the reaction of AF-04 with pH 1.5 brine at 60°C over 30 d.

	Δ g	Δ wt%
Chalcedony	0.01	0.24
Albite	-0.01	-0.23
Illite	-0.01	-0.43
Kaolinite	-0.03	-0.92
Chlorite	-0.16	-5.19
Calcite	-0.04	-1.17

AF-05

Figure 3.5 shows the experimental and modelling results of the reaction of AF-05 with the pH 1.5 brine at 60°C. The model fit the quick initial increase in Ca and pH through a decrease in calcite by 0.57 wt% (Figure 3.5a, c; Table 3.11). The slower rise in Ca over the rest of the 30 d modelling period was realised by reacting ~20 mg of labradorite. The more gradual increase in pH was calculated to be through dissolution of 0.13 g of chlorite resulting in the majority of the increases in SiO_2, Fe, Mg and Al (Figure 3.5a, b, c). The remaining changes in SiO_2 and Al were modelled by dissolving labradorite, K-feldspar, illite and kaolinite. The reaction of ~5 mg of K-feldspar and ~10 mg of illite fit the increase in K well.

The decrease in SiO_2 was modelled by allowing chalcedony precipitation following over-saturation in the early part of the experiment. Approximately 40 mg of chalcedony formed over the 30 d modelling period. However, this underestimated the change in SiO_2 indicating an overestimation of chalcedony precipitation. The modelled change in pH, Al, Mg and Fe on the other hand slightly overestimated the experimental increase. This suggests that less chlorite reacted than was modelled. Potential alternative sources of Fe and Mg are undetected impurities or carbonates.

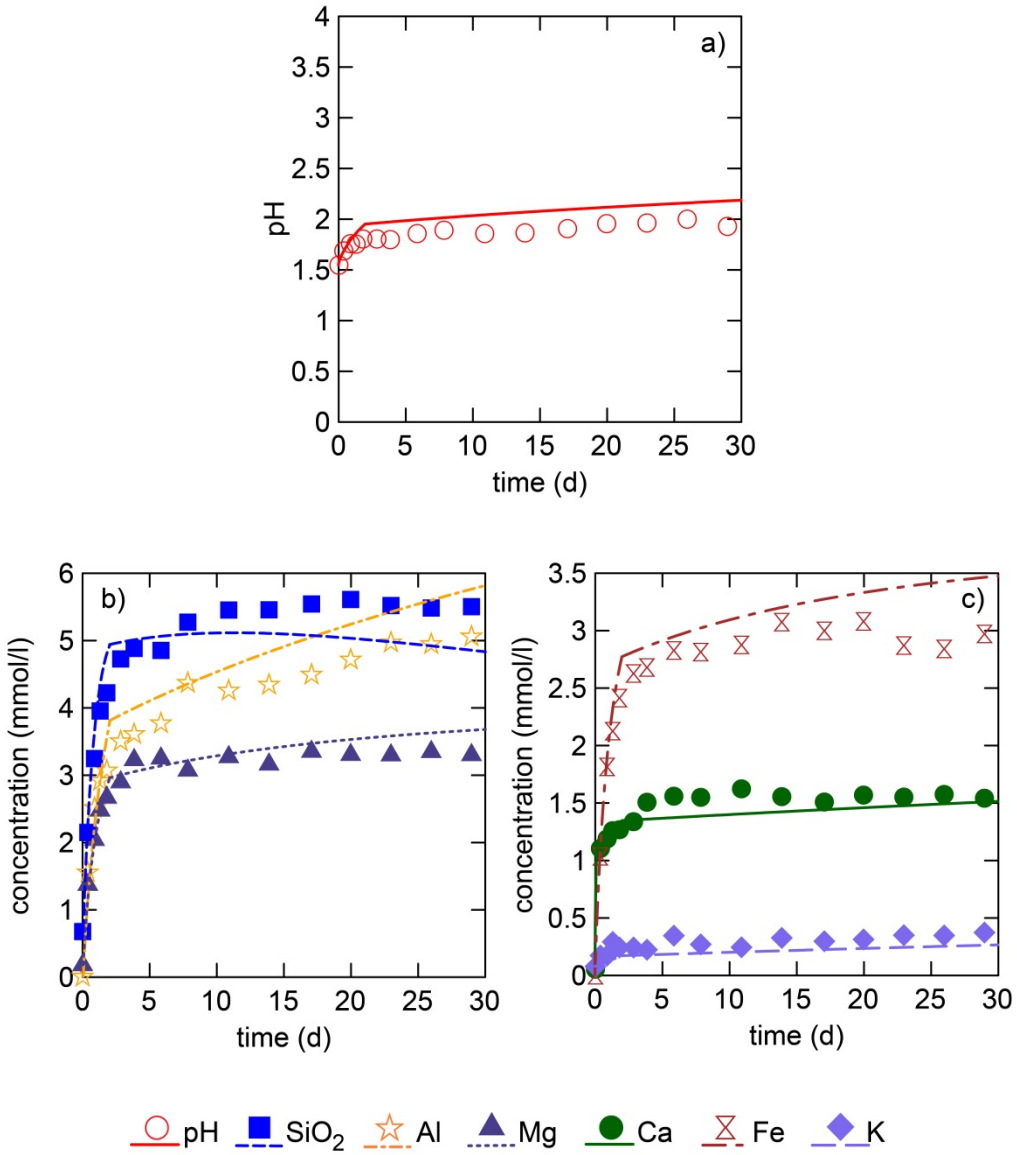

Figure 3.5 **Modelled (lines) and observed (symbols) change in brine properties for the reaction of AF-05 with pH 1.5 brine at 60°C over 30 d.**

Table 3.11 Modelled extent of mineral dissolution (-) and precipitation (+) in g and change in mineralogy in wt% for the reaction of AF-05 with pH 1.5 brine at 60°C over 30 d.

	Δ g	Δ wt%
Chalcedony	0.04	1.18
K-Feldspar	-4.95×10^{-3}	-0.17
Albite	-0.02	-0.76
Illite	-0.01	-0.21
Kaolinite	-0.04	-1.17
Chlorite	-0.13	-4.47
Calcite	-0.02	-0.57

AF-06

The model output and experimental data of the reaction of AF-06 with pH 1.5 brine at 60°C are shown in Figure 3.6. The model predicted 40 mg of ankerite dissolution to simulate the rapid initial increase in pH, Ca, Fe and Mg (Figure 3.6a, b, c; Table 3.12). The experimental data for Ca was matched by the model for the first ~10 d, but showed a slight decrease after that, which was not captured by the model. This might have been due to precipitation of a Ca-bearing mineral not included in the model. The reaction of almost 3.99 wt% chlorite contributed to the increase in pH, Mg and Fe as well as SiO_2 and Al. The total gain in SiO_2 and Al was simulated by including not only chlorite, but also feldspar, kaolinite and illite dissolution. The concentration change in Al was matched by the first modelling step, but was slightly overestimated towards the end of the modelling period. This suggests the precipitation of an Al-bearing mineral, which was captured by the model. With the reaction of illite and K-feldspar, the model predicted the K increase in the experiment well. The extent of albite dissolution, however, was not sufficient to simulate the rise in Na, but baseline experiments indicated an increase in Na unrelated to the acid reaction. The additional Na in the brine may have originated from drilling fluid residues.

Chalcedony super-saturation and precipitation was modelled to occur, which reduced the total increase in SiO_2. The initial increase in Fe and Mg were underestimated by the model. This was likely due to an underestimation of the extent of

the carbonate dissolution reaction as well as a mismatch with the stoichiometry of the carbonate minerals rather than being related to chlorite dissolution.

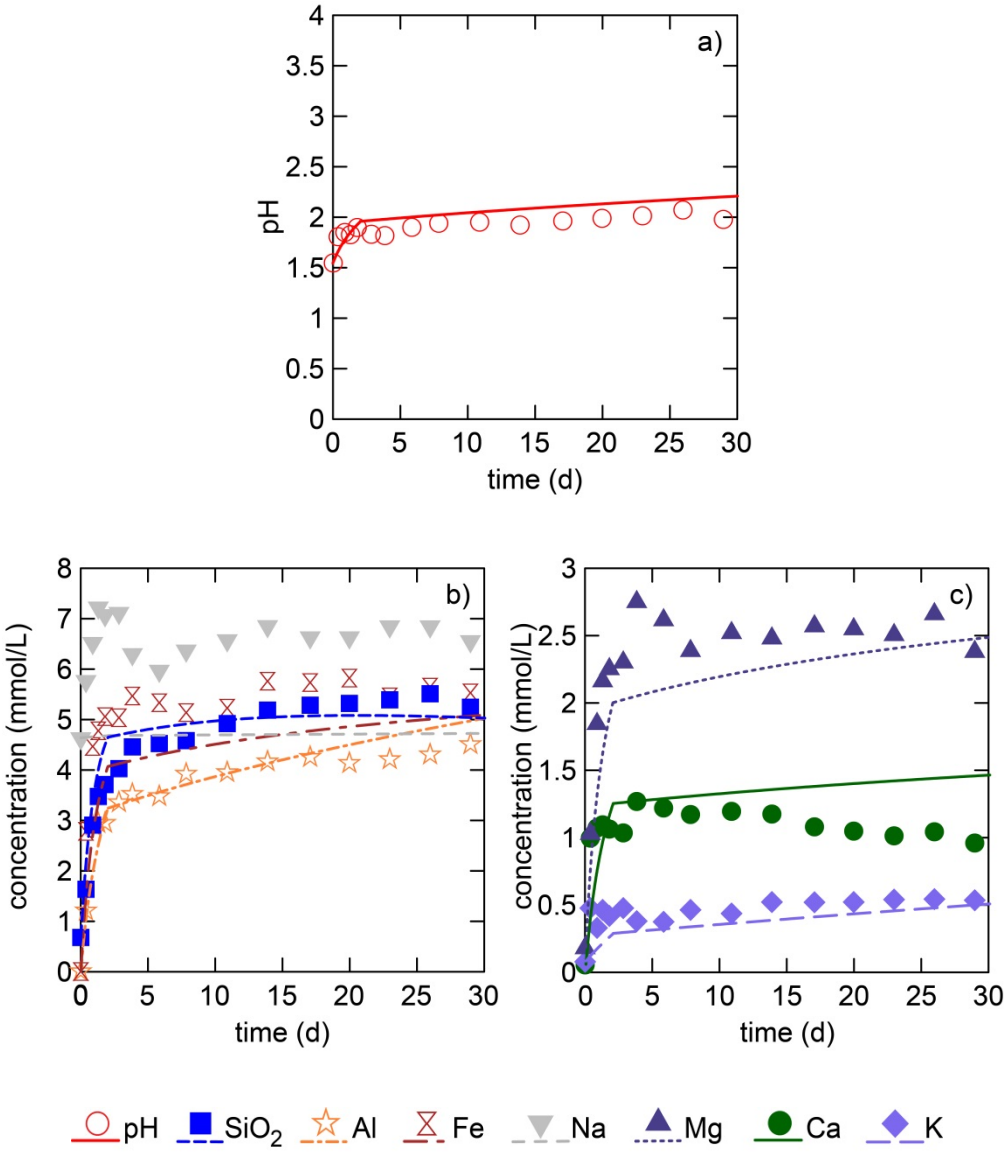

Figure 3.6 Modelled (lines) and observed (symbols) change in brine properties for the reaction of AF-06 with pH 1.5 brine at 60°C over 30 d

Table 3.12 Modelled extent of mineral dissolution (-) and precipitation (+) in g and change in mineralogy in wt% for the reaction of AF-06 with pH 1.5 brine at 60°C over 30 d.

	Δ g	Δ wt%
Chalcedony	0.03	0.87
K-Feldspar	-3.04×10^{-3}	-0.10
Albite	-3.44×10^{-3}	-0.11
Illite	-0.03	-1.13
Kaolinite	-0.02	-0.77
Chlorite	-0.12	-3.99
Ankerite	-0.04	-1.42

Discussion

The reaction path models of the Western Canada Sedimentary Basin sample reactions identified mineral reactions induced by SO_2 injection and quantified their reaction extent. Carbonates and chlorite were the most reactive mineral phases and dominant pH buffers, even when only minor amounts were present. Of the carbonates, calcite showed the highest reactivity and dissolved rapidly in all Western Canada Sedimentary Basin samples. This was followed by dolomite. The reaction extent of siderite varied depending on the sample mineralogy, whereby when lower amounts of the other carbonates were present, more siderite reacted due to less pH buffering. Ankerite behaved very similarly to siderite. Carbonate reactivity was characterized as rapid and extensive, especially when compared to the silicates. The presence of Ca containing carbonates in particular was important since if sufficient carbonate dissolved, gypsum precipitation occurred. This would potentially have implications on the porosity and permeability of the reservoir or seal.

While the carbonates reacted relatively quickly, the silicate reactions were slower and could be discerned in the experimental data by the more gradual increase in the SiO_2, Al and the associated cations. The extent of silicate reaction was especially low in sample AF-01, which was characterized by high amounts of carbonates and displayed the greatest amount of pH buffering. The quick carbonate reaction resulted in significant pH increase and less acid induced silicate reaction. On the other hand, sample AF-03,

which was dominated by silicates, showed little silicate reaction as well, likely due to the low amounts of reactive silicate phases like chlorite.

Chlorite was identified as the most reactive silicate mineral. Its reaction extent was highly dependent on the mineralogy. It was least reactive in samples with siderite, probably as the result of the relatively high Fe content in solution. This would have increased the saturation index of chlorite thereby creating less thermodynamic drive for reaction. Kaolinite dissolution showed a similar behaviour to chlorite. Feldspars and micas went into solution as well, but their reaction extent was generally low. Chalcedony was commonly over-saturated due to the silicate dissolution reactions and formed in all simulations. While this may not be considered physically as likely as gypsum precipitation, during dissolution leaving behind a silica-rich leached layer is observed in natural systems (e.g. Zhu et al., 2006) and may be considered the equivalent of SiO_2 precipitation (Zhu and Lu, 2009).

Other precipitating phases identified by the GWB model were gypsum, alunite, jarosite and smectite. The possibility of sulphate precipitation is of interest, since it acts as a permanent trap for injected SO_2. Further, it is important to note that no kinetic constraints had to be applied to model gypsum precipitation. Pyrite and hematite did not react over the simulation time and were therefore disregarded.

3.3.3. Sample particle size

To model the reaction of the Western Canada Sedimentary Basin Samples at different sample particle size the applied reactive surface areas had to be modified significantly. While the reactive surface areas used to model the mortared and crushed experiment were often similar, a significant reduction in reactive surface area was necessary to model the block experiment. The mineral reactions under different conditions of particle size are summarized for sample AF-01, AF-03 and AF-06, which investigate the reactivity of carbonates, silicates and shale samples, respectively.

AF-01

The model resulted in significantly different mineral reaction extents for AF-01 depending on whether the rock sample was in mortared, crushed or block form (Table 3.13; Table 3.14). The reactive surface area of calcite was halved between the mortared simulation and the crushed simulation. To model the block reaction the reactive surface area was further decreased by a factor of ten, which resulted in 8.34 wt% less dissolution compared to the crushed experiment. The dolomite reactive surface area was decreased by a factor of 25 between the mortared and block experiment, which resulted in a reduction in dissolution of about 1.75 wt%.

Calcite and dolomite dissolution resulted in the over-saturation of gypsum due to the release of Ca into the brine. Gypsum was modelled to precipitate in all three sample particle size simulations. However, due to the lower calcite and dolomite reaction in the block model, less Ca was available, resulting in 5.78 wt% less gypsum precipitation compared to the mortared simulation.

The siderite reactive surface area was decreased by a factor of 2.5 between the mortared and the block model, which resulted in half the amount of siderite dissolution. Although the initial reactive surface area of the clay minerals was halved to model the block experiment, the chlorite and kaolinite dissolution extent was similar in the mortared and in the block model. In the crushed sample simulation, on the other hand, chlorite and kaolinite showed a decrease in reaction compared to the mortared model, although both used the same reactive surface area for the clay mineral. Muscovite showed a similar reaction extent in the mortared and crushed model, but dissolved less in the block model. K-feldspar and albite dissolution decreased between the mortared and crushed model despite both models using the same reactive surface areas. The block model used a reactive surface area 8 times smaller than the other two models, which resulted in 0.05 wt% less K-feldspar and 0.06 wt% less albite dissolution. Chalcedony was over-saturated and formed in all three simulations. However, the precipitation extent of chalcedony decreased from the mortared to the crushed to the block model. Ca-rich smectite reached saturation and started to precipitate in the mortared and crushed model. More smectite formed in the crushed model likely due to a higher Ca availability, since less gypsum formed in this model. Only the mortared model predicted the

formation of alunite. In contrast, Jarosite precipitated in all three simulations. The reaction extent of jarosite decreased from the mortared to the crushed to the block model, likely because of fewer ions being available due to less mineral reaction.

Table 3.13 Reactive surface areas (cm^2/g) applied to model the reaction of AF-01 at different sample particle sizes.

	Mortared	Crushed	Block
Chalcedony; albite; K-feldspar	8000	8000	1000
Illite; muscovite; kaolinite; chlorite	$1x10^5$	$1 x10^5$	$0.5 x10^5$
Calcite	0.1	0.05	0.005
Dolomite	5	1	0.2
Siderite	0.5	0.5	0.2

Table 3.14 Modelled dissolution (-) and precipitation (+) extent for AF-01 mineral phases in wt% for the sample particle size experiments of AF-01.

	Mortared	Crushed	Block
Chalcedony	0.02	0.01	$2.82x10^{-3}$
K-Feldspar	-0.06	-0.05	-0.01
Albite	-0.07	-0.03	-0.01
Muscovite	-0.01	-0.01	$-4.62x10^{-3}$
Kaolinite	-0.02	$-1.2x10^{-3}$	-0.02
Chlorite	-0.17	-0.14	-0.16
Calcite	-10.72	-3.67	-2.38
Dolomite	-3.63	-1.41	-0.94
Siderite	-0.02	-0.01	-0.01
Gypsum	9.44	3.70	1.83
Alunite	0.11		
Jarosite	0.16	0.12	0.07
Smectite	0.07	0.10	

AF-03

The simulation of the mortared, crushed and block reaction of AF-03 resulted in significantly different mineral reaction extents (Table 3.15; Table 3.16). The reactive surface area of calcite was the same for all three simulations. However, the calcite reaction extent was about 0.03 wt% higher in the mortared model compared to the crushed and block models. Still, since no adjustment in carbonate reactive surface area between the different sample size experiments was necessary, the reactive brine likely infiltrated the rock sample completely in all three experiments. Due to the low amount of calcite in AF-03 and the high reactivity of calcite this resulted in complete exposure and fast dissolution of calcite for all sample particle sizes. In contrast, siderite dissolution decreased with increasing sample particle size. In total the reactive surface area had to be reduced to a fifth of the initial value used in the mortared model and the smaller reactive surface area resulted in four times less siderite dissolution in the block simulation. This would suggest that there is a difference in the habit of the 2 carbonate minerals and that fluid access was reduced for the siderite.

All silicate minerals showed a reduction in extent of reaction between the mortared and the block model as well. The reactive surface area used for the framework silicates was more than halved to model the crushed reaction, and was divided by almost nine to model the block reaction. The reaction extent of both feldspars decreased significantly from the mortared to the block simulation. Chalcedony precipitation decreased from 0.22 wt% in the mortared model to 1.28×10^{-3} wt% in the block model. Due to decreased silicate mineral dissolution, the brine was less over-saturated with respect to chalcedony resulting in slower crystal growth rates. The clay minerals reaction extent was halved between the crushed and the mortared simulation, despite both models using the same reactive surface area. To model the block experiment, the initial reactive surface area of the clay minerals was halved, which resulted in a further decrease in reaction extent.

Table 3.15 Reactive surface areas (cm^2/g) applied to model the reaction of AF-03 at different sample particle sizes.

	Mortared	Crushed	Block
Chalcedony; albite; K-feldspar	7000	3000	800
Illite; muscovite; kaolinite; chlorite	$1x10^4$	$1x10^4$	5000
Calcite	0.1	0.1	0.1
Siderite	0.5	0.25	0.1

Table 3.16 Modelled dissolution (-) and precipitation (+) extent for AF-03 mineral phases in wt% for the sample particle size experiments of AF-03.

	Mortared	Crushed	Block
Chalcedony	0.22	0.01	$1.28x10^{-3}$
K-Feldspar	-1.23	-0.21	-0.06
Albite	-0.04	-0.01	$-2.00x10^{-3}$
Muscovite	-0.02	-0.01	$-3.10x10^{-3}$
Kaolinite	-0.01	$-4.57x10^{-3}$	$-2.33x10^{-3}$
Chlorite	-0.04	-0.02	-0.01
Calcite	-0.04	-0.01	-0.01
Siderite	-0.15	-0.03	-0.01

AF-06

The model resulted in significantly different mineral reaction extents for sample AF-06 depending on whether the rock sample was in mortared, crushed or block form (Table 3.187, Table 3.18). The different sample particle size models all used the same reactive surface area for ankerite, indicating a complete exposure of ankerite to the reactive brine. This is likely due to the fact that the block sample of AF-06 disintegrated early into the experiment. Despite the same reactive surface area being used, the reaction extent of ankerite decreased with increasing sample size. The mortared model dissolved 1.42 wt% of the present ankerite, while only 0.29 wt% reacted in the crushed model and 0.23 wt% in the block model. The extent of reaction of the framework silicates showed a significant decrease with increasing sample particle size. The reactive surface

area of the clay minerals was the same for the mortared and the crushed experiment, but was reduced to 60% of its original value in the block simulation. As a result, the dissolution extent of chlorite was reduced by a total of 3.02 wt%. Kaolinite reaction decreased by 0.65 wt% and illite by 0.86 wt%. For the framework silicates, the reactive surface area applied in the mortared model was divided by five to model the crushed experiment and by ten to simulate the block reaction. The modelled dissolution extent of both feldspars decreased by one order of magnitude between the block and the crushed model and was reduced by a factor of 3 between the crushed and the block model. Chalcedony was calculated as over-saturated and precipitated in all three simulations. However, due to less silicate dissolution in the crushed and block model, these simulations had less SiO_2 available in the brine resulting in significantly less chalcedony precipitation. The block model calculated 0.8 wt% less chalcedony precipitation than the mortared model. Besides chalcedony, 0.23 wt% of Mg-rich smectite was modelled to precipitate in the block simulation.

Table 3.17 Reactive surface areas (cm^2/g) applied to model the reaction of AF-06 at different sample particle sizes.

	Mortared	Crushed	Block
Chalcedony; albite; K-feldspar	5000	1000	500
Illite; muscovite; kaolinite; chlorite	$4x10^5$	$4x10^5$	$3x10^5$
Ankerite	0.1	0.1	0.1

Table 3.18 Modelled dissolution (-) and precipitation (+) extent for AF-06 mineral phases in wt% for the sample particle size experiments of AF-06.

	Mortared	Crushed	Block
Chalcedony	0.87	0.09	0.07
K-Feldspar	-0.10	-0.01	-3.35×10^{-3}
Albite	-0.11	-0.01	-3.66×10^{-3}
Illite	-1.13	-0.42	-0.27
Kaolinite	-0.77	-0.31	-0.12
Chlorite	-3.99	-1.27	-0.97
Ankerite	-1.42	-0.29	-0.23
Smectite			0.23

Discussion

The applied reactive surface areas used to model the experiments had to be modified significantly depending on which rock sample was used and at what sample particle size they were reacted at (Table 3.19). The variations in reactive surface area between rock samples of the same sample particle size were likely due to factors like, grain size, surface coating and grain to grain contacts, which were different for each sample. The variations in reactive surface area for the same rock samples but at different sample particle size were likely due to more grain to grain contacts and limited fluid access with increased sample particle size. As a general observation, between the mortared and the block sample experiments, the reactive surface area of the framework silicates was reduced by nearly an order of magnitude and the reactive surface area of the clay silicates was halved. Carbonate minerals in particular required significant adjustments in reactive surface area due to their pore filling habit, which limits exposed surface area. The change in carbonate reactive surface area was dependent on the type of carbonate. While calcite, siderite and dolomite reactive surface areas were decreased by over one order of magnitude between the mortared and the block experiments, the reactive surface area for ankerite remained constant in all three reactions. This result is likely biased due to the fact that ankerite was only present in the shale sample of the Western Canada Sedimentary Basin. Its block and crushed samples disintegrated early into the experiment, resulting in a greater reactive surface area for ankerite. So these results may not be representative for ankerite.

The applied reactive surface areas are associated with some uncertainties, which depend largely on the mineral type. The uncertainties in reactive surface area were evaluated for the different mineral phases by testing the tolerance of the model to changes in reactive surface area. For that the reactive surface areas of the different carbonate minerals and silicate mineral groups were gradually increased/decreased to determine at which reactive surface area no fit could be achieved with the experimental data. The uncertainties associated with the carbonate reactive surface areas were generally lower than the uncertainties associated with the silicate minerals. Due to the high reactivity of calcite, the uncertaintiy associated with the calcite reactive surface area was less than ±5% of the original calcite reactive surface area, since even the slightest change in reactive surface area resulted in a mismatch to the experimental data. The dolomite, ankerite and siderite reactive surface areas were less affected by changes than the calcite reactive surface area resulting in an uncertainty of less than ±10%. The reactive surface areas of the group of framework silicate minerals showed a mismatch to the experimental data when changed by up to ±15%. The biggest uncertainty was associated to the clay mineral surface areas, whichcould be varied by up to ±20% of the original surface area and still capture the major trends of the experimental data. Further, the grouping of silicate mineral reactive surface areas resulted in uncertainties, since the minerals in one group are unlikely to have exactly the same reactive surface area. However, the resulting error was assumed to be low, since the different silicate minerals assigned to one group are likely to have similar reactive surface area exposures due to their similar grain sizes.

The silicate reactive surface areas used to model the experiments are significantly greater compared to literature values from Xu et al. (2005) (Table 3.19). Xu et al. 2005 calculated mineral surface areas by assuming that the framework of the rock was made up of a cubic array of truncated spheres. Further, the calculated geometric surface areas of selected clay minerals were increased to account for edges in these sheet silicate minerals (Xu et a., 2005). In a final step Xu et al. (2005) reduced the calculated mineral surface areas by one order of magnitude to account for factors limiting fluid access in a rock dominated reservoir system (Xu et al., 2005). The values applied in this study on the other hand describe a water dominated experimental system where a proportion of the exposed surface area of the blocks was fresh cut surfaces.

This explains the difference in silicate reactive surface area between the empirical and literature data. The carbonate reactive surface areas on the other hand were significantly smaller than the upscaled literature values. This is likely due to their pore filling habit that limits fluid access. It is important to note that the reactive surface area values used by Xu et al. (2005) are only an approximation of an actual reservoir system and contain a large amount of uncertainty, since they were based on a theoretical calculation instead of measured values. However, calculations by Hellevang and Aargaard (2013b) show that especially for low porosity rocks the BET measured surface area may be orders of magnitude greater than the geometric surface area calculated using pore throat geometry, which supports the use of geometrically calculated reactive surface areas, like the ones used by Xu et al. (2005), as a better approximation of reservoir conditions and indicates that upscaling from the laboratory used values requires significant reduction to describe whole rock surface areas. The significant differences in reactive surface area between the different sample particle size experiments point to the importance of upscaling when trying to apply experimental results to an actual geological formation. Further, the different scaling factors used for the different mineral phases suggest that upscaling is not uniform, but needs to be adjusted depending on the mineral phase.

Table 3.19 Range of reactive surface areas (cm^2/g) applied to model the different Western Canada Sedimentary Basin experiments at different sample particle sizes compared to literature values (Xu et al., 2005).

	Western Canada Sedimentary Basin samples			Literature
	Mortared	Crushed	Block	Upscaled
Chalcedony; albite; K-feldspar;	800-8000	500-8000	100-1000	9.8
Illite; muscovite; chlorite; kaolinite	$1x10^4$-$5x10^5$	$1x10^4$-$5x10^5$	5000-$3x10^5$	9.8-151.6
Calcite	0.05-2	0.05-1	0.003-0.1	9.8
Dolomite	5	1	0.2	9.8
Ankerite	0.1	0.1	0.1	9.8
Siderite	0.25-0.5	0.25-0.5	0.1-0.025	9.8

3.3.4. Surat Basin Samples

The Surat Basin models identified carbonates, chlorite and biotite as fast reacting mineral phases. K-Feldspar, mica and kaolinite reacted as well, but at lower rates. The only precipitating phase identified in the Surat Basin experiments was chalcedony, which was over-saturated in all of the simulations. The modelling approach with two time steps resulted in a drastic drop in reaction rate between the first and second time step. A more gradual approach would probably provide a better fit. This study refrained from this step to save computing time and to keep the model simple and easily applicable. The model outcome of the simulation reacting the Surat Basin samples with pH 1.5 brine at 60°C are summarized in the following paragraphs.

AF-07

The modelled and experimental results of the Precipice Sandstone experiment at pH 1.5 and 60°C are shown in Figure 3.7. The model required dissolution of ankerite to model the gain in Ca (Figure 3.7 c; Table 3.20). Ankerite dissolution also contributed to the Mg and Fe concentration in the brine. However, the dominant process used to model the gain in Mg and Fe was chlorite dissolution. Chlorite, kaolinite, illite and K-feldspar dissolution combined resulted in the increases in SiO_2 and Al (Figure 3.7 b). The final amount of SiO_2 was underestimated by the model, while the Al concentration was overestimated. While the precipitation of chalcedony did remove some dissolved SiO_2, the total was not sufficient to account for the discrepancy. This indicates that the chosen aluminosilicate mineral stoichiometries might not fit the actual mineral phases perfectly. Another reason for the deviation may result from an underestimation of K-feldspar dissolution and overestimation of illite and kaolinite dissolution. The model dissolved less K-feldspar than illite, to account for the rise in K in the brine; however, the total amount of K in the brine was underestimated. The relative Al:Si ratio decreases from kaolinite to illite to K-feldspar and this, combined with the difference in the experiment Al:Si ratio, suggests an underestimation of K-feldspar dissolution. However, increasing the K-feldspar reaction rate in the model resulted in K-feldspar saturation and precipitation leaving the modelled fit the best possible.

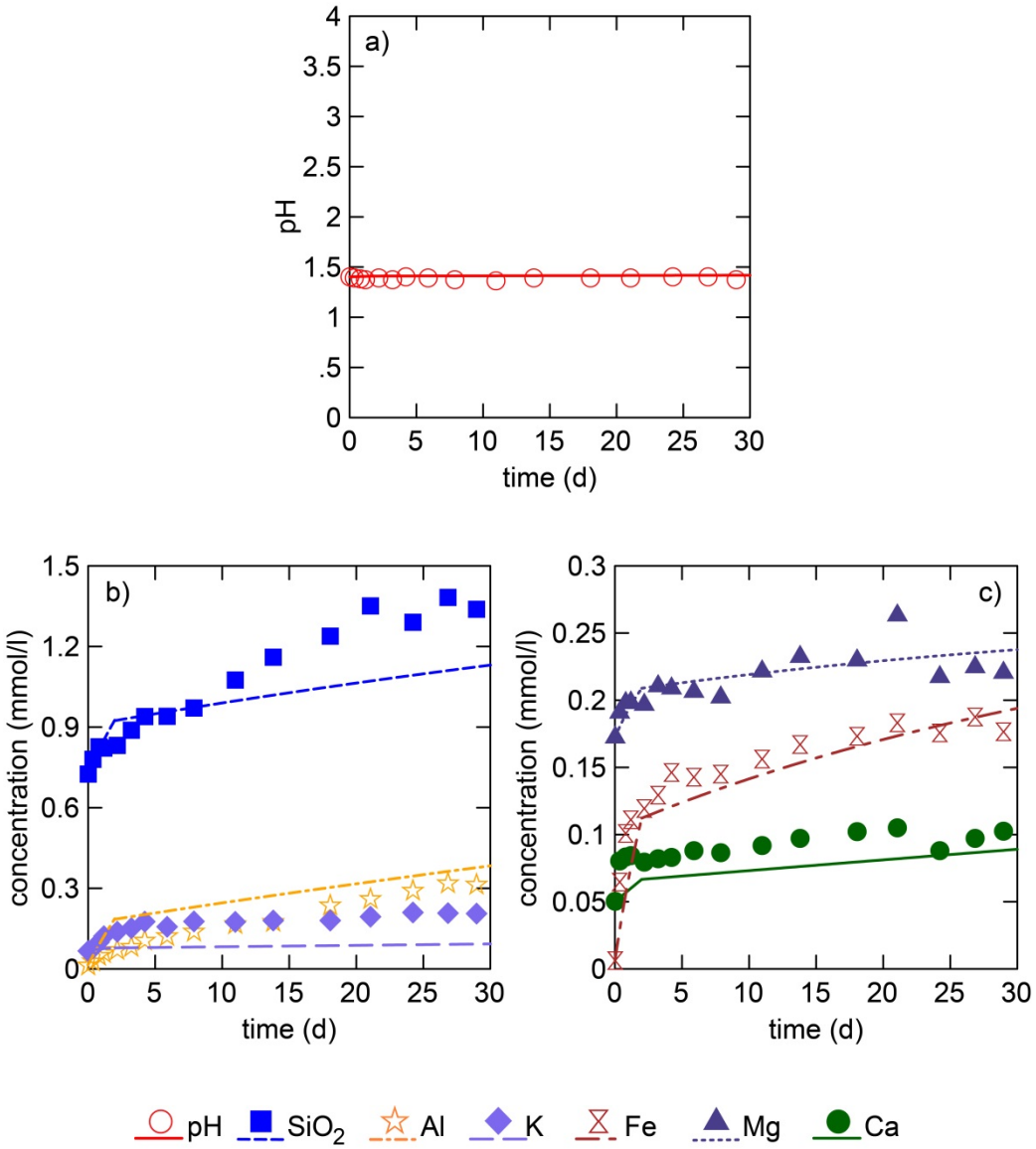

Figure 3.7 **Modelled (lines) and observed (symbols) change in brine properties for the reaction of AF-07 with pH 1.5 brine at 60°C over 30 d.**

Table 3.20 Modelled extent of mineral dissolution (-) and precipitation (+) in g and change in mineralogy in wt% for the reaction of AF-07 with pH 1.5 brine at 60°C over 30 d.

	Δ g	Δ wt%
Chalcedony	1.00×10^{-4}	0.01
K-Feldspar	-4.78×10^{-5}	-2.95×10^{-3}
Albite	-5.70×10^{-5}	-3.52×10^{-3}
Illite	-8.90×10^{-4}	-0.06
Kaolinite	-2.81×10^{-3}	-0.17
Chlorite	-2.40×10^{-3}	-0.15
Ankerite	-8.18×10^{-4}	-0.05

AF-08

The fit between the first Evergreen Formation sample experiment with pH 1.5 brine at 60°C and the reaction path model is shown in Figure 3.8. The model predicted calcite and ankerite dissolution to account for the initial increase in Ca and pH (Figure 3.9a, c; Table 3.21). 0.26 wt% of calcite and 4.14 wt% of ankerite dissolved over the modelling period with the majority dissolving in the first few days. 1.93 wt% chlorite and 0.2 wt% biotite dissolved, contributing, along with ankerite, to the Fe and Mg concentration of the brine. In addition to chlorite and biotite, feldspar, illite and kaolinite dissolution resulted in the increase of SiO_2 and Al in the brine (Figure 3.9b). The model reacted 20 mg of K-feldspar to account for the majority of K in the brine. The reaction of 10 mg of albite contributed some amount of Na to the brine. However, albite reaction was not sufficient to account for the total increase in Na. A potential source for the unaccounted Na might be drilling fluid residues. Some SiO_2 precipitation (~10 mg of chalcedony) was predicted. While the increase in SiO_2 was reasonably well predicted by the model, the change in Al was underestimated. This is likely due to the relatively high (12.6 wt%) content of unresolved (low crystallinity and/or organic) material in the QEMScan. This material was assigned as ankerite to simulate the presence of ankerite in a sufficient quantity to simulate the change in water chemistry. However, it may have included amorphous gibbsite and/or kaolinite of low crystallinity as well, which, when dissolving would contribute to the high Al. The model was deemed sufficient nevertheless, since it fit most of the experimental data, identifying the dominant reactions.

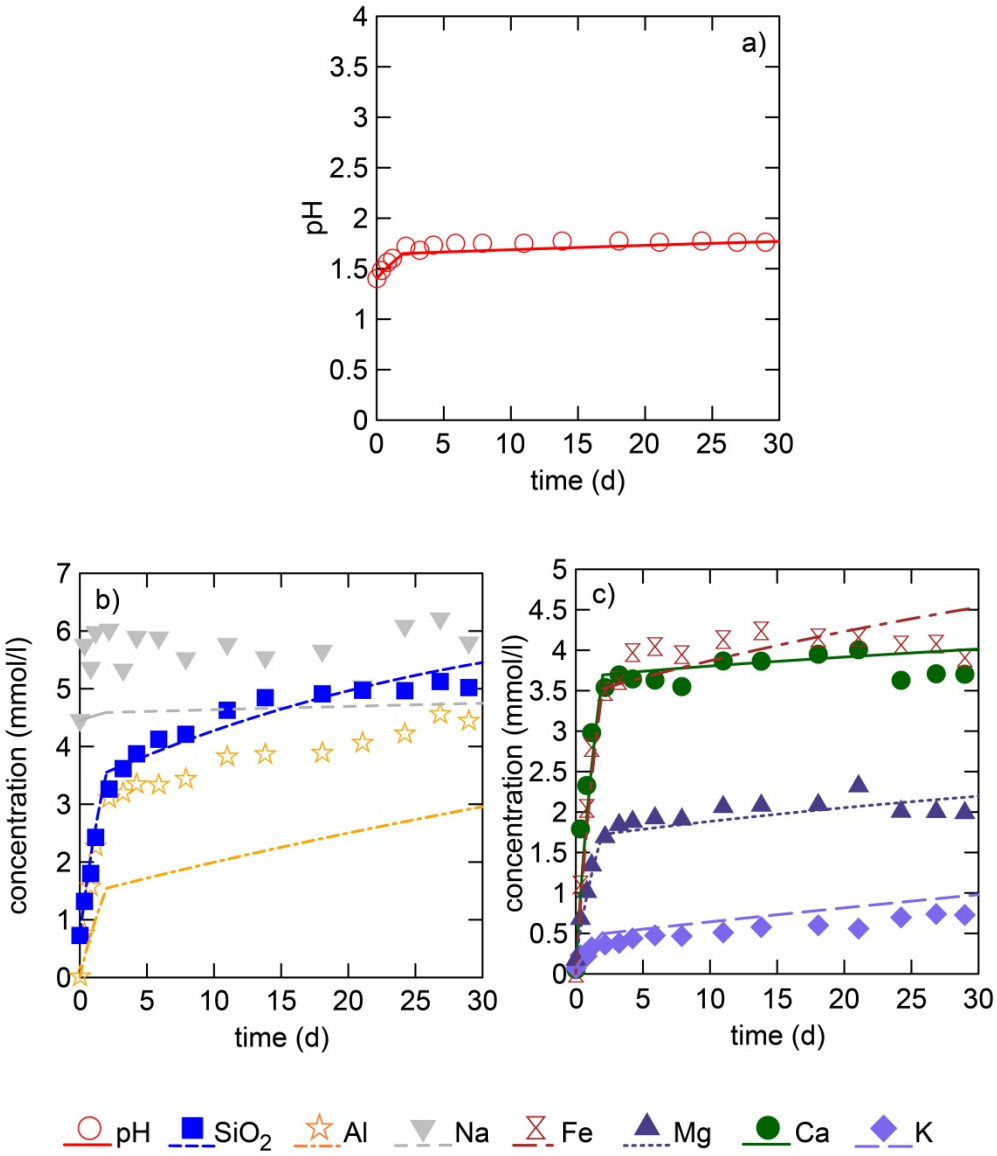

Figure 3.8 **Modelled (lines) and observed (symbols) change in brine properties for the reaction of AF-08 with pH 1.5 brine at 60°C over 30 d.**

Table 3.21 Modelled extent of mineral dissolution (-) and precipitation (+) in g and change in mineralogy in wt% for the reaction of AF-08 with pH 1.5 brine at 60°C over 30 d.

	Δ g	Δ wt%
Chalcedony	0.01	0.38
K-Feldspar	-0.02	-1.24
Albite	-0.01	-0.43
Illite	-1.93×10^{-4}	-0.01
Biotite	-3.74×10^{-3}	-0.20
Kaolinite	-0.01	-0.46
Chlorite	-0.04	-1.93
Calcite	-3.00×10^{-3}	-0.16
Ankerite	-0.08	-4.14

AF-09

Figure 3.9 shows the experimental and modelling results of the reaction of the second Evergreen Formation sample with the pH 1.5 brine at 60°C. The model fit the rapid increase in Ca, Fe and Mg and initial pH increase by dissolving ankerite and siderite (Figure 3.9a, c; Table 3.22). As another source of Fe and Mg, the model dissolved 2.68 wt% of chlorite and 0.54 wt% of biotite. While the Ca and Mg content were well matched, Fe was slightly underestimated at the beginning of the modelling period and overestimated towards the end. This is likely due to the two-step modelling approach with one order of magnitude lower reactive surface areas in the 2nd step. The increase in SiO_2 and Al in the brine (Figure 3.9b) was modelled by assuming chlorite, feldspar, illite, biotite and kaolinite dissolution, but was dominated by chlorite dissolution. The total gain in SiO_2 was lowered slightly by the precipitation of chalcedony. The model calculated chalcedony over-saturation throughout the modelling period and precipitated ~3.5 mg. The increase in SiO_2 was initially overestimated, but the total change was well matched. The increase in Al on the other hand was underestimated throughout the modelling period. The deviation in SiO_2 concentration, like the deviation in Fe, may be due to the abrupt reduction in reactive surface area between the first and second modelling step. The SiO_2 and Al concentrations are very similar suggesting a kaolinite- or berthierine- like mineral phase dissolution dominating. It is probable that a low crystallinity mineral phase that would have a higher rate constant than kaolinite was

present. However, attempts to match the experiment data using higher rates of kaolinite dissolution were not successful in capturing the trend.

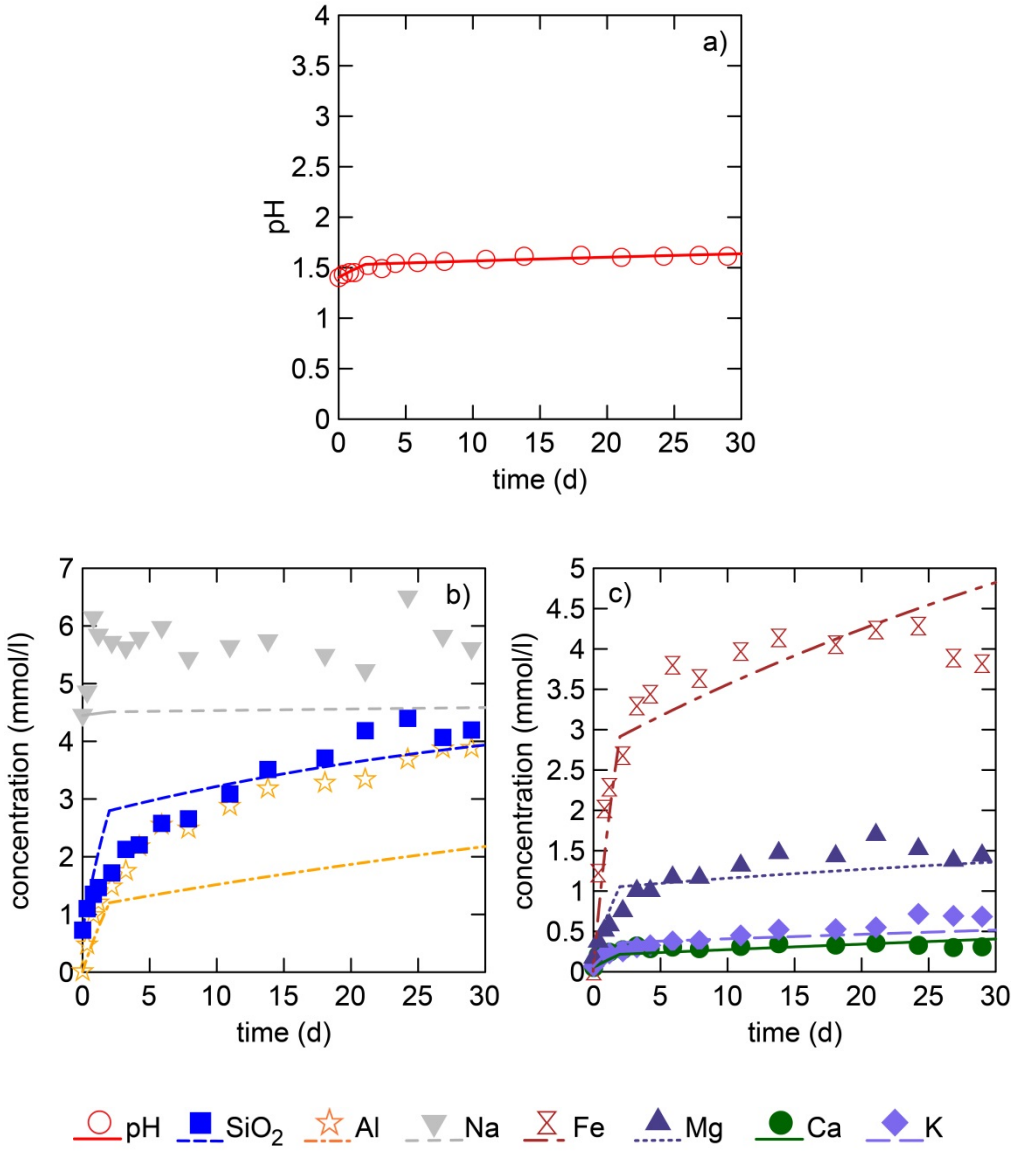

Figure 3.9 Modelled (lines) and observed (symbols) change in brine properties for the reaction of AF-09 with pH 1.5 brine at 60°C over 30 d.

Table 3.22 Modelled extent of mineral dissolution (-) and precipitation (+) in g and change in mineralogy in wt% for the reaction of AF-09 with pH 1.5 brine at 60°C over 30 d.

	Δ g	Δ wt%
Chalcedony	4.46×10^{-3}	0.34
K-Feldspar	-0.01	-0.66
Albite	-4.07×10^{-3}	-0.31
Illite	-4.64×10^{-4}	-0.04
Biotite	-0.01	-0.54
Kaolinite	-0.01	-0.71
Chlorite	-0.04	-2.68
Ankerite	-0.01	-0.42
Siderite	-0.02	-1.87

AF-10

The resulting brine composition for the reaction of the Hutton Sandstone with pH 1.5 brine at 60°C were well simulated by the model (Figure 3.10). The rapid initial increases in Ca, Mg and Fe were modelled through siderite and ankerite dissolution (Figure 3.10b, c; Table 3.23). Chlorite dissolution also contributed to the increase in Fe and Mg. The dissolution of ankerite, siderite and chlorite accounted for most of the increase in pH (Figure 3.10a). The reaction of K-feldspar, albite, muscovite, biotite and kaolinite, combined with the dissolution of chlorite, accounted for the increase in SiO_2 and Al; however, chlorite dissolution dominated. Chalcedony was calculated as over-saturated and 10 mg was precipitated reducing the increase in SiO_2. The total increase in SiO_2 was fit fairly well, while the Al concentration was underestimated throughout the modelling period. Like in the Evergreen experiments, this is probably due to stoichiometric uncertainties and given the relatively large amount of chlorite dissolution simulated, it is likely the chlorite composition was inaccurate. The reaction of 10 mg of albite contributed to the total amount of Na in the brine as well, but the effect of albite reaction was insignificant, due to the high baseline concentration of Na.

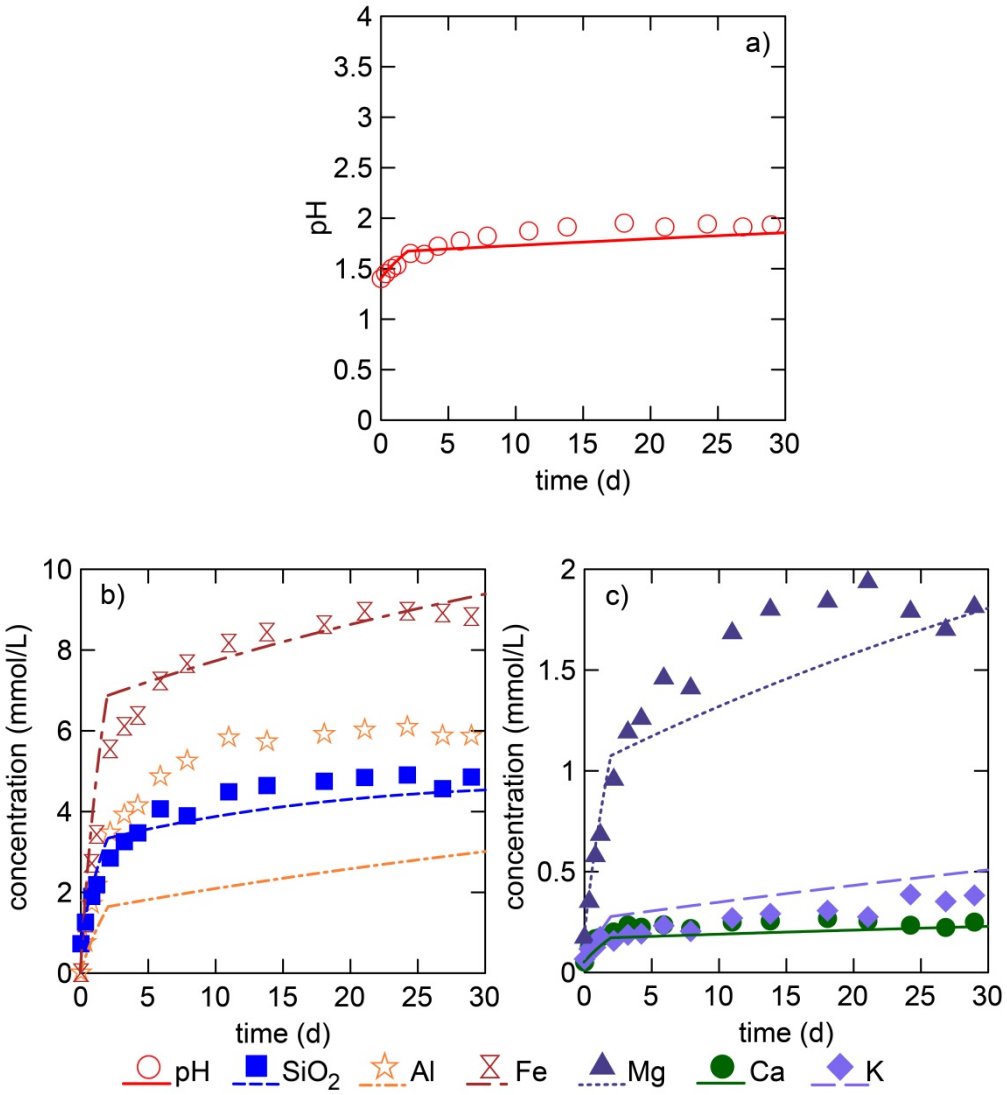

Figure 3.10 **Modelled (lines) and observed (symbols) change in brine properties for the reaction of AF-10 with pH 1.5 brine at 60°C over 30 d.**

Table 3.23 Modelled extent of mineral dissolution (-) and precipitation (+) in g and change in mineralogy in wt% for the reaction of AF-09 with pH 1.5 brine at 60° over 30 d.

	Δ g	Δ wt%
Chalcedony	0.01	0.39
K-Feldspar	-0.01	-0.28
Albite	-0.01	-0.38
Muscovite	-1.73×10^{-3}	-0.07
Biotite	-0.01	-0.27
Kaolinite	-0.01	-0.23
Chlorite	-0.06	-2.49
Ankerite	-3.72×10^{-3}	-0.15
Siderite	-0.07	-2.83

Discussion

The Surat Basin samples provided the opportunity to determine which mineral phases participated in the H_2SO_4-brine-rock reaction and to what extent for a location that is considered as a potential injection site of CO_2 captured from a coal fired power plant. Except for hematite, all mineral phases present reacted. Carbonates and chlorite were identified as the most reactive mineral phases in the Surat Basin samples. Except for chalcedony, all participating mineral phases dissolved indicating potential porosity and permeability increases. However, the total amount of mineral reaction varied depending on the sample. The Precipice Sandstone, a potential storage formation, was dominated by comparatively unreactive silicates and showed very little change. The most reactive minerals were ankerite, chlorite and kaolinite. In total, the sample mass decreased only by about 7.5 mg, which is less than 0.5% of the original sample weight. There was no evidence of SO_2 trapping, since the model did not predict any sulphate mineral saturation and precipitation.

The Evergreen Formation, which overlays the Precipice Sandstone and acts as the regional seal, was the most reactive. The models show that both Evergreen Formation sample experiments are characterized by carbonate and chlorite dissolution. Sample AF-08 was slightly more reactive than AF-09, which decreased by 8% and 7% in sample mass, respectively. This is of importance, since a long term reduction in mass

could increase the porosity and permeability of the Evergreen Formation, affecting its sealing properties. However, the results derived from short term experiments are likely to overestimate the reaction rates of a storage formation. In particular, the high water to rock ratio of the experiments resulted in conditions that are unlikely to occur in the seal, where low porosity and permeability restrict fluid access. Further upscaling and long term analysis might result in no significant porosity or permeability changes.

The Hutton Sandstone is also considered as a potential storage formation, but unlike the Precipice Sandstone it is characterized by a fairly reactive mineralogy. The Hutton Sandstone reactions were dominated by carbonate, chlorite and biotite dissolution. The Hutton block sample decreased by 0.16 g in mass, which equals about 6% of the original sample weight. Like the Precipice Sandstone, the model predicted no SO_2 trapping over the simulation period. However, both potential storage formations are characterized by dissolution, which might lead to an increase in porosity and storage volume.

The Surat Basin models predicted the same mineral reactions for the Surat Basin formations as experimental models done by Farquhar et al. (2015) and Pearce et al. (2015) on CO_2-water-rock and CO_2-SO_2-water rock reactions, respectively. Both studies reacted samples from the Surat Basin in a static batch reactor at 60°C and 12 MPa with a fresh water brine for a duration of 16 days. A system of valve tubes was used to add pure CO_2 gas (Farquhar et al., 2015) and CO_2 gas containing 0.16% SO_2 (Pearce et al., 2015) and to extract up to five fluid samples for analysis. In both scenarios carbonates were identified as rapidly dissolving mineral phases, while silicate minerals followed a more gradual dissolution trend confirming the observations of this study. The main difference between the outcomes of the two experiments is the extent of acid induced reaction, which was significantly greater in Pearce et al. (2015). Hence, the approach of a controlled pH used in this study is likely a sufficient solution to simulate CO_2 injection. The use of H_2SO_4 as an aqueous proxy for SO_2 in this study was considered a major uncertainty of this study, since the formation of sulphuric acid is controlled by the presence of oxidants in the system. However, the precipitation of gypsum/anhydrite observed in a Hutton Sandstone sample of Pearce et al. (2015) confirms the formation of

sulphuric acid, rendering the use of H_2SO_4 a good approach to model SO_2 injection in the Surat Basin.

While the experiments by Pearce et al. (2015) were conducted under a controlled pressure of 12 MPa to simulate reservoir conditions, this study used no pressure controls. However, the resulting mineral reactions and reaction extents were very similar suggesting that pressure plays a minor role in controlling SO_2 induced geochemical reactions. The use of pressure controlled vessels and the use of gas over an aqueous proxy require costly equipment, which was avoided in this study with similar results. Further, by avoiding a pressurized system with a system of valves, sampling of the reactive brine was simplified. The sampling intervals could be chosen freely; therefore, the greater number of samples taken during the experiments provided tighter constraints on the mineral reactions and their amounts.

3.4. Conclusions and recommendations

3.4.1. Western Canada Sedimentary Basin samples

The Western Canada Sedimentary Basin experimental models at different temperature and pH revealed variability in kinetic rate data for stoichiometrically variable minerals, like chloride and ankerite. Further, the activation energy and H^+ power terms found in different literature sources are often derived from experiments with igneous or metamorphic rock sourced single-mineral phases and perhaps are not sufficient to describe the reaction of authigenic sedimentary mineral phases like chlorite.

The geochemical reactions induced by SO_2 simulated acidification were strongly dependent on the mineralogy of the Western Canada Sedimentary Basin samples. The reaction path models quantified the mineral reactions, identifying carbonates and chlorite as the most reactive mineral phases and the greatest pH buffers. Carbonate minerals dissolved rapidly at the beginning of the modelling period, while silicate minerals dissolved more gradual. As precipitating phases, the models identified chalcedony, smectite and sulphate phases, such as gypsum and jarosite.

The Western Canada Sedimentary Basin experimental models at different sample particle sizes required different reactive surface areas to model the reaction of the individual mineral phases/groups. Small changes in the sample particle size from mortared to crushed to block resulted in a significant reduction in accessible reactive surface area. A comparison of the empirical reactive surface areas to literature values showed that carbonate minerals in particular required significant scaling due to their pore filling habit, which limits exposed surface area.

The GWB models simulating the Western Canada Sedimentary Basin experiments identified H_2SO_4 induced mineral reactions and quantified their reaction extent. They produced kinetic rate data, enabling the simulation of mineral reactions at different temperature and acidity levels. Further, they outlined the importance of upscaling between changes in sample particle size. However, since the models only describe short term effects of SO_2 addition in a water dominated experimental system additional steps are required to investigate the long term effects of CO_2-SO_2 storage. Chapter 4 addresses this issue by combining the effects of SO_2 impurities with CO_2 storage at reservoir scale and quantifying the change in mineral composition.

3.4.2. Surat Basin samples

The kinetically controlled geochemical reaction path models of the Surat Basin rock experiments allowed the identification and quantification of mineral reactions in low pH conditions typical of SO_2 co-injection. The geochemical reactions were strongly dependent on the mineralogy of the samples. Like for the Western Canada Sedimentary Basin samples, carbonates and chlorites were identified as the most reactive mineral phases. Carbonates rapidly dissolved at the beginning of the experiments, while silicate reactions were significantly slower. The Precipice Sandstone Formation mineralogy included very little reactive mineral phases, and therefore showed very little change during the experiments. The Evergreen Formation and Hutton Sandstone Formation on the other hand included greater amounts of reactive mineral phases and displayed significantly higher reaction extent. The more extensive dissolution of carbonates and chlorite resulted in greater ion concentrations in the brine and significant pH buffering. Further, the H_2SO_4-brine-rock reaction resulted in a loss in sample weight of up to 8%,

which is likely to increase porosity and permeability resulting in significant ramifications for seal safety and storage capacity. Hence the mineralogy may impact the safety of a caprock and the storage capacity of a reservoir formation. However, the sample particle size experiments emphasized that experimental results are likely to overestimate mineral reaction rates and with that the loss in sample weight.

The GWB models simulating the Surat Basin experiments identified the different mineral phases participating in H_2SO_4-brine-rock reactions and quantified dissolution and precipitation processes. They predict an increase in porosity and permeability and no SO_2 trapping over the short time frame of the experiment. However, the models only describe short term effects of SO_2 addition in a water dominated experimental system. To evaluate the potential of the Surat Basin as a CO_2-SO_2 storage site, further investigations are necessary in order to assess the sealing properties of the Evergreen Formation and the storage capacity of the Hutton and Precipice Sandstone. Chapter 4 addresses this problem by combining SO_2 and O_2 impurities with CO_2 storage at reservoir scale and quantifying the change in mineral composition and with that the change in porosity over a time period of 100 years.

Chapter 4. Modelling the geochemical impact of CO_2-SO_2 storage in different formation assemblies

4.1. Introduction

Captured emissions from coal fired power plants are dominated by CO_2 but may contain low concentrations of reactive impurities like SO_2. While CO_2 dissolves to form weak carbonic acid, SO_2 reacts to form sulphurous acid, sulphuric acid and/or hydrogen sulfide depending on the redox conditions (Ellis et al., 2010). Hence, the geological storage of CO_2-SO_2 gas mixtures is likely to result in greater brine acidification compared to pure CO_2 storage. This could result in enhanced mineral dissolution and precipitation affecting critical reservoir properties, like porosity and permeability (Kaszuba et al., 2005; Xu et al., 2007; Crandell et al., 2010; Ellis et al., 2010; Kummerow et al., 2007). The effect of SO_2 induced mineral reactions is expected to be greatest close to the injection well (Ellis et al., 2010). Reactive transport modelling conducted by Knauss et al. (2005) and Xu et al. (2007) confirmed this by predicting the formation of sulphuric acid close to the injection well resulting in a brine pH near unity. The simulations indicated an increase in porosity in the acidified zone due to mineral dissolution. Outside the acidified zone, carbonate and sulfate precipitation resulted in a decrease in porosity. However, modelling done by Crandell et al. (2010) and Ellis et al. (2010) suggests that previous modelling studies overestimated SO_2 induced acidification, since SO_2 dissolution from within the $scCO_2$ plume is diffusion limited. Further, Pearce et al. (2015) found that the low brine pH induced by SO_2 can be buffered and neutralized by the formation mineralogy, in particular carbonates, which were converted to sulphates if sufficient calcium was present.

Most studies on carbon storage have focused on pure CO_2 injection (e.g. Pruess et al., 2004; Xu et al., 2004; Gaus et al., 2008), with very few addressing the potential

risks SO_2 induced acidification can have on critical reservoir properties. The available data on CO_2-SO_2 storage is limited. Existing studies include experimental (Summers et al., 2004; Flaathen et al., 2010; Flaathen et al., 2011; Kummerow and Spangenberg, 2011; Sakurovs et al., 2011; Glezakou et al., 2012; Schoonen et al., 2012; Wilke et al., 2012), modelling (Knauss et al., 2005; Palandri et al., 2005b; Xu et al., 2007; Bacon et al., 2009; Crandell et al., 2010; Ellis et al., 2010), as well as combined experimental and modelling approaches (Palandri et al., 2005a; Garcia et al., 2011; Garcia et al., 2012; Pearce et al, 2015). However, none of these studies has converted short term experimental and modelling data into long term storage predictions.

Predictive models are a useful tool for evaluating the safety of CO_2-SO_2 storage. However, data derived from short term experiments and models are unlikely to represent the CO_2-SO_2 impact in an actual reservoir. They often focus on single mineral phase reactions in a water dominated system using powdered samples to accelerate reactions. Reservoir systems on the other hand are rock dominated systems comprised of multiple mineral phases. In this setting, reaction rates are highly dependent on exposed mineral reactive surface area. However, mineral reactive surface area in rocks is difficult to quantify, especially since brine-mineral reactions occur primarily on selected sites of the available mineral surface area (White, 1995; Gaus et al., 2005; Xu et al., 2005; Brantley et al., 2008; Gaus et al. 2008). Moreover, the reactive surface area is constrained by factors like coating, grain to grain contacts, and fluid flow channelling (Sonnenthal et al., 2000; Li et al., 2006; Zhu et al., 2006). Mineral surface areas can be estimated geometrically or using the Brunauer Emmett and Teller (B.E.T.) method (Brantley et al., 2008). However, it has been suggested that the available reactive surface area is between one and three orders of magnitude smaller than the calculated mineral surface area (Lasaga, 1995; White, 1995) and that it varies over several orders of magnitude during reaction (Brantley et al, 2008; Scislewski et al., 2010). Hence, upscaling is required in order to translate short term experimental and modeling data into long term simulations of real systems.

Perhaps just as importantly, CO_2 industrial gas streams are likely to contain other impurities (Stanger and Wall, 2011). Of special interest is O_2, which can be present in amounts of up to 5 vol% (IEAGHG, 2011). The injection of O_2 will turn the redox

conditions of a storage formation from reducing to oxidising, and therefore is likely to result in mineral reactions similar to acid mine drainage. The injection of CO_2-SO_2-O_2 gas mixtures is likely to result in a complete oxidation of SO_2, maximizing the formation of sulphuric acid (Pearce et al., 2015). Experiments conducted by Wilke et al. (2012) showed more extensively corroded mineral surfaces as well as enhanced cation mobilization in CO_2-SO_2 experiments that included residual air, than in pure CO_2-SO_2 experiments. It is clear that the captured CO_2 streams will contain impurities, and in order to understand how these impurities might impact the reservoir and seal systems, simulations that include O_2, as well as the highly reactive SO_2, in the injection stream need to be conducted.

This chapter focuses on the long term effects of CO_2-SO_2 storage at reservoir conditions. The experimental models described in chapter 3 were upscaled to reservoir scale and 100 y duration. CO_2 was included in the models to combine the effect of SO_2 with CO_2 storage. The Western Canada Sedimentary Basin models were used to investigate the importance of upscaling differences at reservoir scale, by scaling and comparing the reactive surface area data from the mortared and the block experiments. For the Surat Basin formations, three different scenarios were modelled: CO_2, CO_2-SO_2 and CO_2-SO_2-O_2 injection. The first two scenarios were used to quantify the difference between pure CO_2 storage and CO_2-SO_2 storage, while the latter scenario was used to evaluate the effect of injecting an oxidant into a reducing environment.

4.2. Methodology

Kinetically controlled reaction path models were used to evaluate the longer term effects of CO_2-SO_2 storage at reservoir scale. For this, the short term models in Chapter 3 simulating H_2SO_4-brine-rock reactions were modified to include pure CO_2, CO_2-SO_2 and CO_2-SO_2-O_2 using the React module of the Geochemist's Workbench^{TM} V.9 software package with the modified version of the thermo.com.V8.R6 database and the GWB kinetic rate scripts (Bethke, 2012a; Bethke, 2012b). The kinetic rate data input was expanded to include hematite and pyrite (Palandri and Kharaka, 2004; Pham et al., 2011) (Table 4.1). The precipitation rate constant of K-feldspar was changed from the

dissolution rate constant to one hundredth of the dissolution rate constant to inhibit K-feldspar precipitation, which is unlikely at the simulation temperature of 60°C.

Table 4.1 Kinetic rate parameters for mineral phases used in the reaction path modelling; the dissolution rate constant at 25°C (k_{25}) and activation energy (E_a) for the acidic (H) and neutral (nu) dissolution mechanism, the H^+ power term (n), the precipitation rate constant (k_p) calculated from the dissolution rate constant (k_d) and the pre-exponential factor for nucleation (Γ).

	$k_{25(H)}$ (mol/m²s)	$E_{a(H)}$ (kJ/mol)	n	$k_{25(nu)}$ (mol/m²s)	$E_{a(nu)}$ (kJ/mol)	k_p	Γ
Chalcedony				$1.7X10^{-13}$	68.7	k_d	$2x10^{10}$
K-Feldspar	$8.71x10^{-11}$	40	0.4-0.5	$3.89x10^{-13}$	38	$k_d/100$	$2x10^{10}$
Albite	$6.92x10^{-11}$	55	0.457	$2.75x10^{-13}$	69.8	k_d	$2x10^{10}$
Illite	$1.41x10^{-12}$	22	0.37-0.45	$8.91x10^{-16}$	14	k_d	$2x10^{10}$
Muscovite	$1.41x10^{-12}$	22	0.37	$2.82x10^{-14}$	22	k_d	$2x10^{10}$
Biotite	$1.45x10^{-10}$	22	0.525	$2.82x10^{-13}$	22	k_d	$2x10^{10}$
Kaolinite	$4.9x10^{-12}$	60-65.9	0.7-0.777	$6.61x10^{-14}$	22.2	$k_d/10$	$2x10^{10}$
Chlorite	$1.23x10^{-10}$	15-40	0.7-0.8	$1.00x10^{-13}$	94.3	k_d	$2x10^{10}$
Calcite	0.501	14.4	1	$1.55x10^{-06}$	23.5	k_d	$1x10^{10}$
Dolomite	$6.46x10^{-04}$	36.1	0.7	$2.95x10^{-08}$	52.2	$k_d/100$	$3x10^{10}$
Ankerite	$1.79x10^{-04}$	32-48	0.75-0.8	$1.80x10^{-07}$	43	$k_d/100$	$3x10^{10}$
Siderite	$1.79x10^{-04}$	48	0.75-0.9	$1.80x10^{-07}$	43	$k_d/100$	$3x10^{10}$
Hematite	$4.07x10^{-10}$	66.2	1	$2.51x10^{-15}$	66.2	k_d	$1x10^{10}$
Pyrite	$3.02x10^{-08}$	56.9	0.5	$2.82x10^{-05}$	56.9	k_d	$2x10^{10}$

The mineral input was recalculated to cm^3 for 1 kg of H_2O based on the mineralogy data of the samples (Table 2.1; Table 3.3), using formation porosity data, mineral molar volume and mass. For the Western Canada Sedimentary Basin samples an idealised porosity of 0.2 was chosen for the reservoir samples and 0.05 for the shale sample (Table 4.2). For the Surat Basin samples, porosity data were taken from Farquhar et al. (2014).

Table 4.2 Porosities used to calculate the mineral input in cm^3.

	Porosity
AF-01 - AF-05	0.2
AF-06	0.05
AF-07	0.161
AF-08	0.072
AF-09	0.095
AF-10	0.224

The actual reactive surface area of a mineral is generally accepted as being one to three orders of magnitude smaller than the measured or calculated surface area (Lasaga, 1995; White, 1995) due to factors like abundance of selective sites, grain to grain contacts, and channelling of fluid flow (Sonnenthal, 2000; Li et al., 2006; Zhu et al., 2006). To simulate reactions at reservoir scale, the reactive surface areas used to model the experiments in Chapter 3 were upscaled. The upscaling involved taking the mineral reactive surface areas of the Western Canada Sedimentary Basin and the Surat Basin samples and, for the framework grains, dividing by 100, and for the clay minerals, dividing by 1000 (Table 4.3). The reactive surface area of the framework minerals was decreased by two orders of magnitude to account for reduced fluid access in a reservoir system caused by factors like grain to grain contacts, surface coating, and channelling of brine flow. The reactive surface area of the clay minerals was decreased further due to their pore filling behaviour and their reactive surface area beeing largely controlled by selective sites consisting of grain edges. Two models were run for the Western Canada Sedimentary Basin samples using the upscaled reactive surface areas from the mortared and block simulation to evaluate the uncertainty of upscaling and to determine its effect on model outputs. Compared to literature values (Xu et al., 2005) the experiments already resulted in a significantly scaled carbonate reactive surface area input for the experimental simulations, hence, further upscaling of the carbonate reactive surface areas was deemed unnecessary. For hematite and pyrite a reactive surface area value of 10 was assigned on the basis of values described by Xu et al. (2005).

Table 4.3 Upscaled mineral reactive surface areas (cm^2/g) compared to values from Xu et al. (2005).

	Western Canada Sedimentary Basin samples		Surat Basin samples	Literature
	Mortared	Block	Block	Upscaled
Chalcedony; albite; K-feldspar;	8-80	1-10	20-50	9.8
Illite; muscovite; biotite*; chlorite; kaolinite	10-500	5-300	50-100	9.8-151.6
Calcite	0.05-2	0.003-0.1	0.01	9.8
Dolomite	5	0.2		9.8
Ankerite	0.1	0.1	0.007-0.02	9.8
Siderite	0.25-0.5	0.1-0.025	0.1	9.8
Hematite	10	10	10	12.9
Pyrite	10	10	10	12.9

*biotite was treated as a framework mineral for AF-10

Three storage scenarios (CO_2, CO_2-SO_2 and CO_2-SO_2-O_2) were modelled for the Surat Basin samples to determine the geochemical and physical impact of impurities. For the Western Canada Sedimentary Basin samples only CO_2-SO_2 injection was modelled since these simulations focused on issues of upscaling. The ion input was mostly based on the measured synthetic brine composition of the pH 1.5 (a) solution for the Western Canada Sedimentary Basin experiments, and the pH 1.5 (b) solution for the Surat Basin samples (Table 2.3). The concentration of SO_4^{2-} was set to the baseline value of 0.01 mmol/L.

To simulate CO_2 storage, CO_2 was swapped for H^+, $O_2(g)$ for $O_2(aq)$ and a charge balance was applied to HCO_3. At the injection depth, the proposed Surat Basin storage site has a pressure of 120 bar. Using the method of Duan and Sun (2003), the solubility of CO_2 was calculated at that pressure and 60°C and used to constrain the CO_2 fugacity in GWB. The supercritical CO_2 stream was incorporated at the calculated amount of dissolved CO_2 by fixing the CO_2 fugacity at a value of 80 (which produced the dissolved CO_2 content calculated according to Duan and Sun (2003)). By fixing the CO_2 fugacity, near well conditions were simulated, which are defined by the presence of supercritical CO_2. $O_2(g)$ was set and fixed to a log fugacity of -50 since the redox state at typical injection depth is dominated by reduction. CO_2-SO_2 storage was simulated by

modifying the CO_2 models to include SO_2(aq) instead of SO_4^{2-}. By choosing SO_2(aq) over SO_2(g) it was assumed that the injected SO_2 impurities were stripped out of the gas phase due to the higher solubility of SO_2. The concentration of SO_2(aq) was set to the input values used in Chapter 3, which were 31 mmol/L for the Western Canada Sedimentary Basin reactions and 37 mmol/L for the Surat Basin reaction. These values were chosen to achieve a very acidic pH (~1.5) to simulate near well conditions. To simulate CO_2-SO_2-O_2 storage, O_2 was implemented into the CO_2-SO_2 models by changing the O_2 fugacity to a fixed value of 0.8. The O_2 value was fixed to simulate near well conditions with abundant access to the supercritical CO_2 stream and O_2 impurities. All models were run at a simulation temperature of 60°C and for 100 y.

4.3. Results and Discussion

4.3.1. Upscaling

In order to investigate the impact of the chosen upscaling conditions, both the mortared and block modelled reactive surface areas of the Western Canada Sedimentary Basin samples were upscaled to reservoir values and run for 100 y. Table 4.3 lists the applied upscaled reactive surface areas and values used bu Xu et al. (2005). Xu et al. (2005) used reactive surface areas calculated by assuming that grains are an array of truncated spheres, which were upscaled by reducing them by one order of magnitude. Hence, the reactive surface area values used by Xu et al. (2005) were based on a theoretical calculation and not on measured values and might not represent an actual reservoir. For the silicate minerals in this study, the literature reactive surface areas fall within the range of applied reactive surface areas. The framework silicate reactive surface areas in the mortared model were equal to or higher than the literature values. The block model values on the other hand were equal to or lower than the literature values. The clay mineral reactive surface areas were generally in the range of the literature values or higher than the literature values. Only the block model of AF-03 used smaller clay mineral reactive surface areas than the literature. The fact that the theoretically calculated silicate reactive surface area values used by Xu et al. (2005) fall within the range of the applied reactive surface area values used in this study supports

the validity of the literature values. For the carbonate reactive surface areas both the mortared and block values are significantly smaller than the values from Xu et al. (2005), which is likely due to their pore filling habits. An inverse modelling approach by Scislewski et al. (2010) estimated calcite reactive surface area to vary between 0.00075 cm^2/g and 0.196 cm^2/g, which includes the values used here for both the mortared and the block simulations. The deviation between the carbonate reactive surface areas used in this study and the carbonate reactive surface areas used by Xu et al. (2005) demonstrates that carbonates require more upscaling than suggested by the literature. Since no experimental hematite and pyrite data existed, their reactive surface areas were based on the values used by Xu et al. (2005).

The upscaled mortared and block models resulted in the same mineral reactions. However, the calculated reaction extents were significantly different. This indicates that the method of upscaling has to be adjusted depending on the experimental set up. The mineral reactions calculated for the Western Canada Sedimentary Basin samples by the upscaled models are summarized for samples AF-01 to AF-06 in the following paragraphs.

AF-01

The upscaled models of AF-01 resulted in a similar change in pH (Figure 4.1), but different rates and amounts of minerals reacted depending on which sample particle size experiment they were based on (Figure 4.2). In both simulations, the pH was rapidly buffered through carbonate dissolution to a value of ~4.8 at which the pH is controlled by the abundant CO_2 gas and mineral precipitation. The mortared model predicted a continuous slow increase in pH subsequent to the carbonate buffering due to silicate dissolution. The block model on the other hand did not result in further pH buffering. The carbonate reaction rates in the block model were slightly lower than the rates of the mortared model. However, the total carbonate reaction extent was very similar in both models after about 10 y. In both simulations, calcite rapidly decreased by 0.16 vol%, but only in the upscaled mortared model did calcite subsequently precipitate 0.01 vol% (Figure 4.2a, b). Dolomite showed a similar pattern, in which it rapidly dissolved by almost 0.02 vol% in both simulations, but the subsequent precipitation extent was less in the block model (Figure 4.2c, d). Siderite reaction resulted in a loss of 0.08 vol% in the

mortared and in the block scenario, while ankerite precipitation was 0.01 vol% less in the block model. Gypsum initially precipitated about 0.035 vol% in both models. However, the reaction rate of gypsum was faster in the mortared model resulting in gypsum reaching equilibrium and starting to dissolve within the first year. In the block model, gypsum did not start to dissolve until the 28^{th} y after injection resulting in about 0.01 vol% more gypsum after the completion of the 100 y modelling period. The lower amount of gypsum resulted in a higher Ca availability in the mortared scenario, which explains the higher final amounts of calcite, dolomite and ankerite in this simulation.

The modelled silicate reaction extent was significantly higher in the upscaled mortared simulation than in the upscaled block simulation. Albite and K-feldspar dissolution were 7.5 and 3.5 times lower, respectively, in the block model. Chlorite reacted less as well, dissolving only about half the amount of the mortared simulation. The low chlorite reaction extent stands in contrast to the experimental models in Chapter 3 and is likely due to the reduced reactive surface area and the rapid pH buffering. Kaolinite, smectite and chalcedony were over-saturated throughout the modelling period and precipitated in both models. However, due to more silicate dissolution in the upscaled mortared model, more SiO_2 was available, resulting in a 6.5 times higher chalcedony and more than double the kaolinite and smectite precipitation compared to the upscaled block model. The higher SiO_2 availability in the mortared model resulted in muscovite saturation and precipitation of 0.045 vol% after about 10 y. The block model on the other hand reached muscovite saturation after approximately 50 y resulting in a total decrease in the amount of muscovite of ~$3x10^{-4}$ vol%.

The reaction extent of pyrite was very similar in both models, which was expected since both models used the same value for the pyrite reactive surface area. The total gain in porosity was reduced from 0.04 vol% in the mortared simulation to 0.02 vol% in the block simulation, mainly due to the reduced silicate reaction extents.

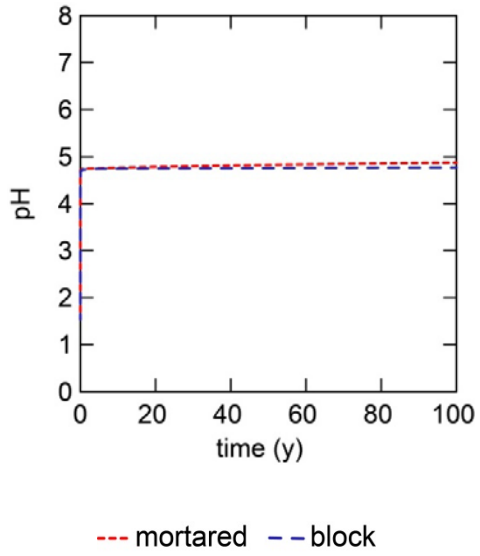

Figure 4.1 **Modelled change in pH for the upscaled mortared and block CO_2-SO_2 models of AF-01 over a 100 y modelling period.**

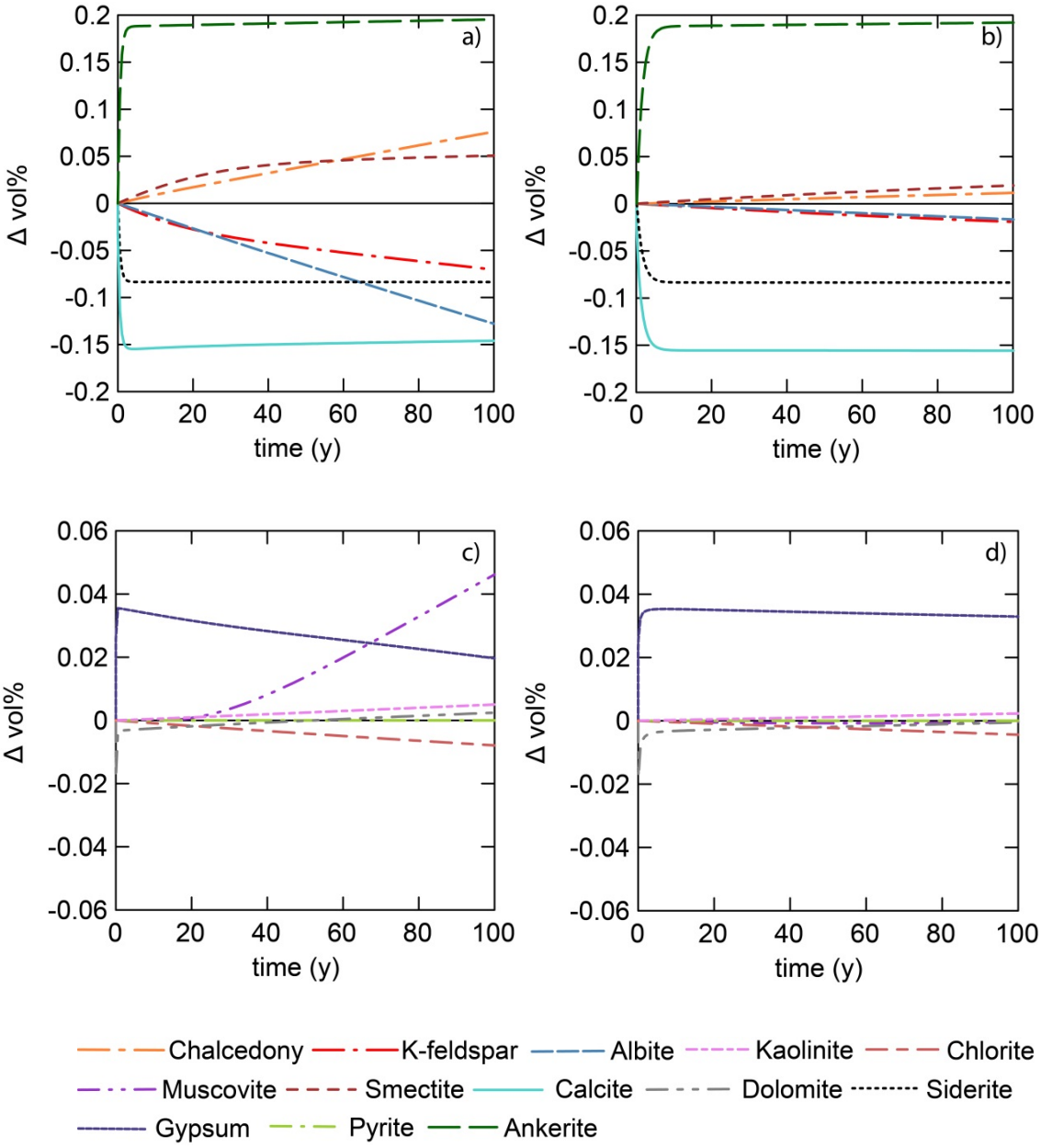

Figure 4.2 Modelled mineral reaction for the upscaled mortared (a+c) and block (b+d) CO_2-SO_2 models of AF-01 over a 100 y modelling period.

AF-02

The upscaled mortared and block model of AF-02 resulted in a different pH and different mineral reaction rates (Figure 4.3; Figure 4.4). The initial increase in pH was similar in both models (Figure 4.3). Rapid carbonate reactions resulted in an increase in pH to a value of 4.5, at which the pH was counter balanced by mineral precipitation. In

the mortared model, the carbonate minerals showed faster reaction rates. Calcite and siderite were reduced by 0.37 vol% and 0.26 vol%, respectively, within the first 8 y of the mortared model (Figure 4.4a, b). In the block simulation, the same amount of calcite and siderite dissolution was not reached until 80 y after injection. The slower calcite and siderite dissolution in the block model resulted in slower ankerite precipitation and delayed dolomite precipitation compared to the mortared model due to a lower availability of Ca, Mg and Fe. However, the precipitated amount of ankerite and dolomite was very similar in both simulations after completion of the 100 y modelling period (Figure 4.4a, b, c, d). Gypsum precipitated rapidly at the beginning of the mortared and block model, but its subsequent dissolution was faster in the mortared model resulting in it being used up after 26 y. In the block simulation on the other hand, 0.02 vol% of gypsum was still present after 100y. The faster gypsum dissolution resulted in additional pH buffering in the mortared model.

The smaller silicate reactive surface areas in the block model resulted in a significant reduction in silicate reaction rates, especially for the framework minerals. Hence, the block model predicted less pH buffering through silicate dissolution. Albite dissolution was seven times higher in the mortared model. About 0.017 vol% of K-feldspar dissolved within the first 6 y of the mortared model, while the same dissolution extent was not reached in the block model until 45 y after injection. The faster feldspar reaction rates resulted in a greater SiO_2 availability, which led to 6.5 times more chalcedony and 5.5 times more smectite precipitation. Further, muscovite and K-feldspar started to precipitate in the mortared model after dissolving initially. This was not observed for the block model. The reaction extent of chlorite, kaolinite and hematite reaction was similar in both models. The low chlorite reaction extent was likely due to the rapid pH buffering. The predicted porosity increase after 100 y was 0.04 vol% for the block model and 0.12 vol% for the mortared model.

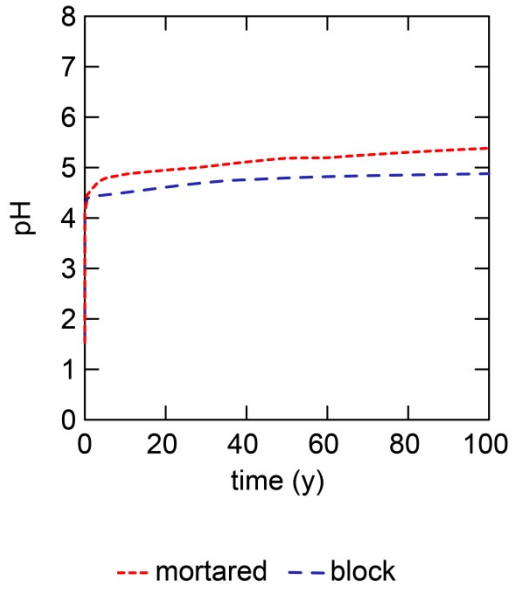

Figure 4.3 **Modelled change in pH for the upscaled mortared and block CO_2-SO_2 models of AF-02 over a 100 y modelling period.**

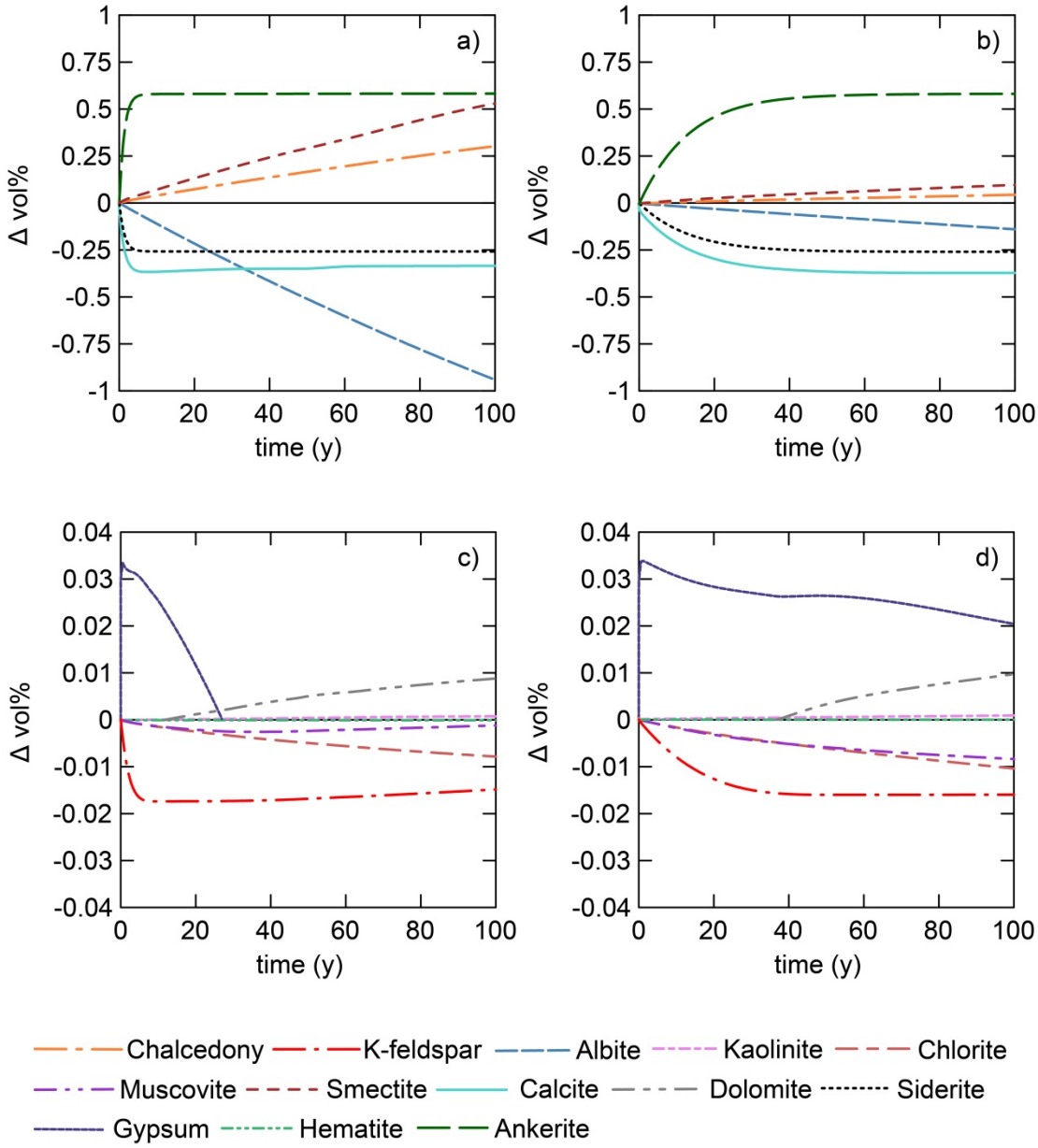

Figure 4.4 **Modelled mineral reaction for the upscaled mortared (a+c) and block (b+d) CO_2-SO_2 models of AF-02 over a 100 y modelling period.**

AF-03

The upscaled mortared and block model of AF-03 resulted in different reaction rates but very similar reaction extents after 100 y (Figure 4.6). The amount of calcite dissolution was the same in both models (Figure 4.6a, b), which was expected since the calcite reactive surface area was not scaled between the block and the mortared model.

The rapid calcite dissolution resulted in a pH increase to a value of 4, at which point the pH is controlled by the abundant CO_2 gas and mineral reactions (Figure 4.5). The reactive surface area of siderite on the other hand was reduced to one fifth, which resulted in a significantly slower siderite reaction rate in the block simulation (Figure 4.6c, d). This led to a slower precipitation rate of ankerite, due to the lower availability of Fe. However, both models resulted in a similar amount of siderite and ankerite reaction after 100 y. Gypsum precipitated early in both models, but dissolved again completely after ~3 y of the mortared simulation and ~30 y of the block simulation. Alunite precipitated in the mortared model, but started to dissolve again after about 20 y leaving it at a final value of 0.085 vol%. In the block model, alunite precipitated over the complete modelling period, but at a slower rate than in the mortared model, resulting in a total of 0.1 vol%.

The reaction extents of the framework silicate minerals were significantly different for the upscaled mortared and block model. Albite dissolution was 7.5 times higher in the mortared model. The K-feldspar and chalcedony reaction extent in the block model was reduced to 60% of the mortared model. The reduced silicate reaction in the block model resulted in less gradual pH buffering subsequent to the initial increase. Most of the clay minerals behaved very similar in both simulations. Only muscovite showed a significantly different reaction outcome in the block model compared to the mortared model. Due to more feldspar dissolution in the mortared model, large amounts of SiO_2 were released into the brine resulting in muscovite saturation and precipitation. In both simulations, a small amount of smectite precipitated at the beginning. However, smectite was not stable and dissolved again within the first year of the mortared and within the first 10 years of the block simulation. The reaction extent of hematite was similar in both models, which was expected since both models used the same hematite reactive surface area. The porosity decreased by 0.035 vol% in the mortared and by 0.05 vol% in the block simulation.

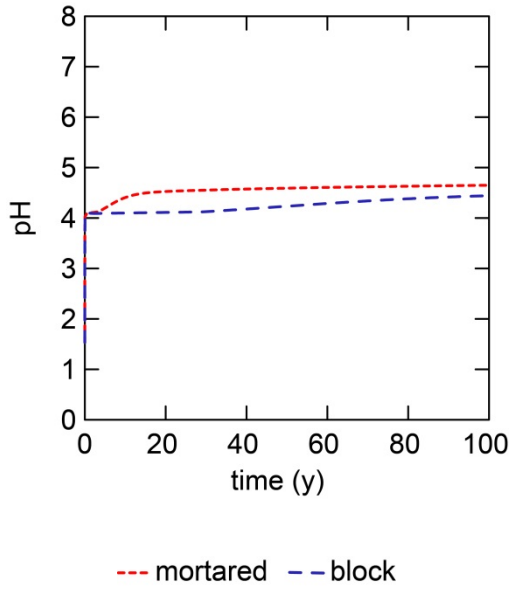

Figure 4.5 **Modelled change in pH for the upscaled mortared and block CO_2-SO_2 models of AF-03 over a 100 y modelling period.**

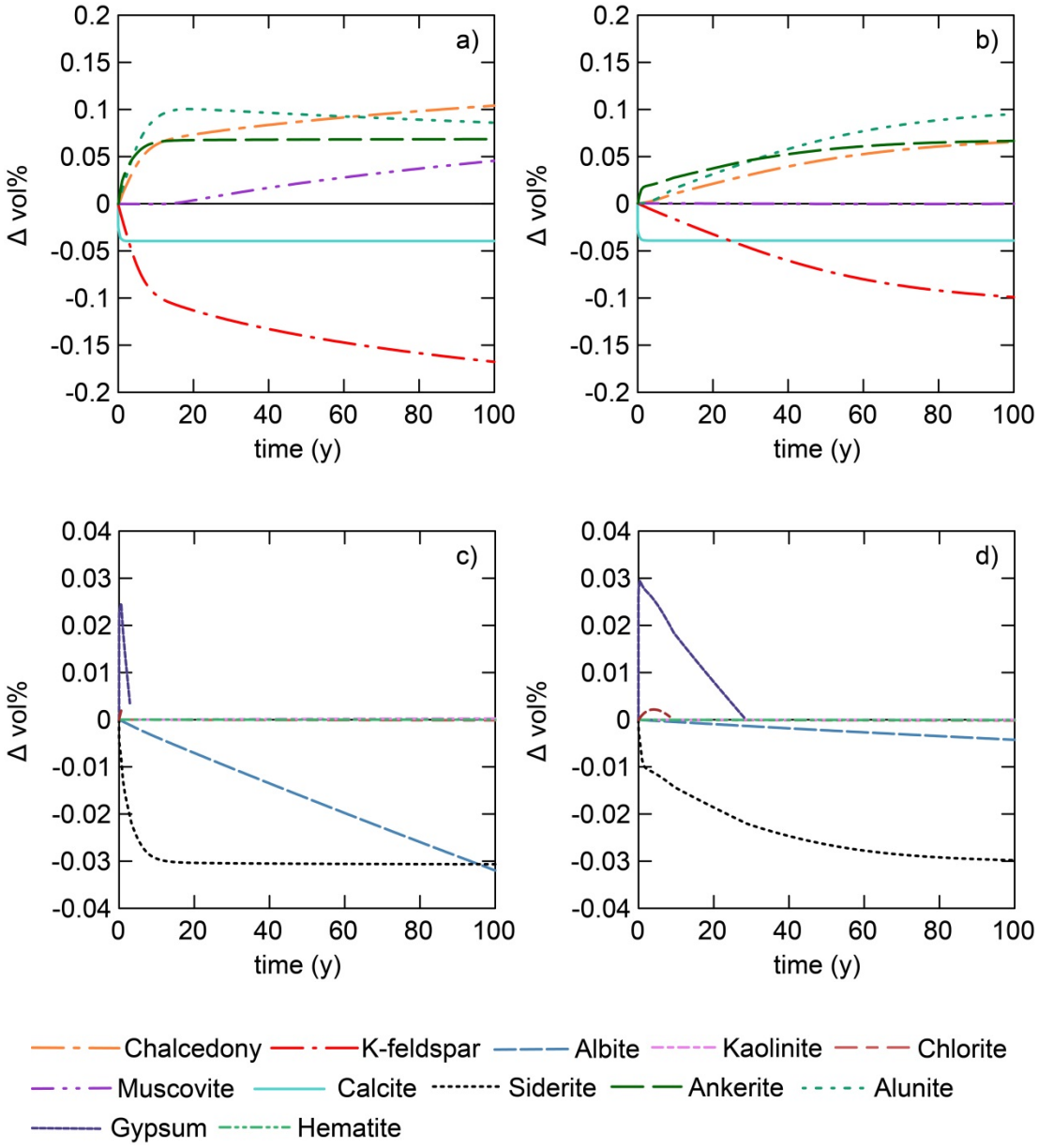

Figure 4.6 Modelled mineral reaction for the upscaled mortared (a+c) and block (b+d) CO_2-SO_2 models of AF-03 over a 100 y modelling period.

AF-04

The mineral reaction rates of the upscaled models of AF-04 were significantly different depending on which sample particle size experiment they were based on (Figure 4.8). In both models, calcite rapidly decreased by 0.05 vol% within the first year (Figure 4.8a, b) resulting in a rapid pH increase to about ~4.8 (Figure 4.7).

Subsequently, calcite dissolved faster in the mortared model resulting in 0.05 vol% less calcite in the mortared model compared to the block model after 100 y. This, combined with more silicate dissolution in the mortared model, resulted in a slightly higher final pH compared to the block model. Gypsum precipitated rapidly at the beginning of both simulations, but subsequently dissolved faster in the mortared reaction resulting in it being used up after approximately 95 y (Figure 4.8c, d).

The silicate reaction extents were significantly reduced from the mortared to the block model. Albite dissolution was 7.5 times higher, and chlorite and illite dissolution were 3 times higher in the mortared simulation releasing SiO_2, Al, Mg and Fe into the brine. The higher ion availability in the mortared model resulted in faster precipitation rates for chalcedony, smectite, ankerite and dolomite. Chalcedony precipitation was 8.5 times lower, smectite precipitation was 4 times lower, and ankerite and dolomite precipitation were 3 times lower in the block simulation compared to the model simulation. Kaolinite precipitation was slightly higher in the mortared model as well. The block model predicted a porosity increase of 0.02 vol% after 100y, while the mortared model resulted in a total porosity increase of 0.05 vol%.

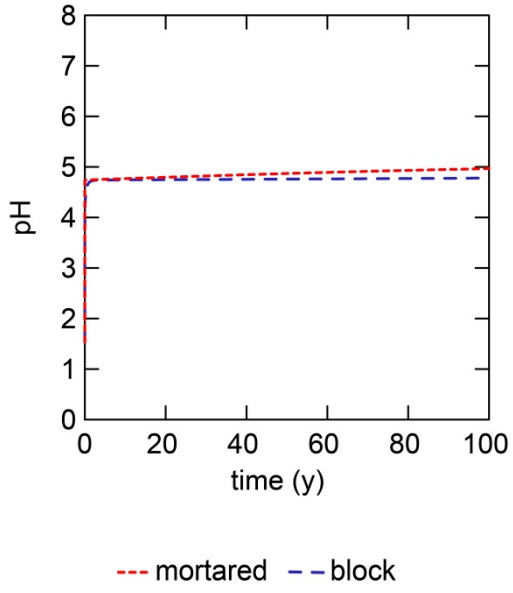

Figure 4.7 Modelled change in pH for the upscaled mortared and block CO_2-SO_2 models of AF-04 over a 100 y modelling period.

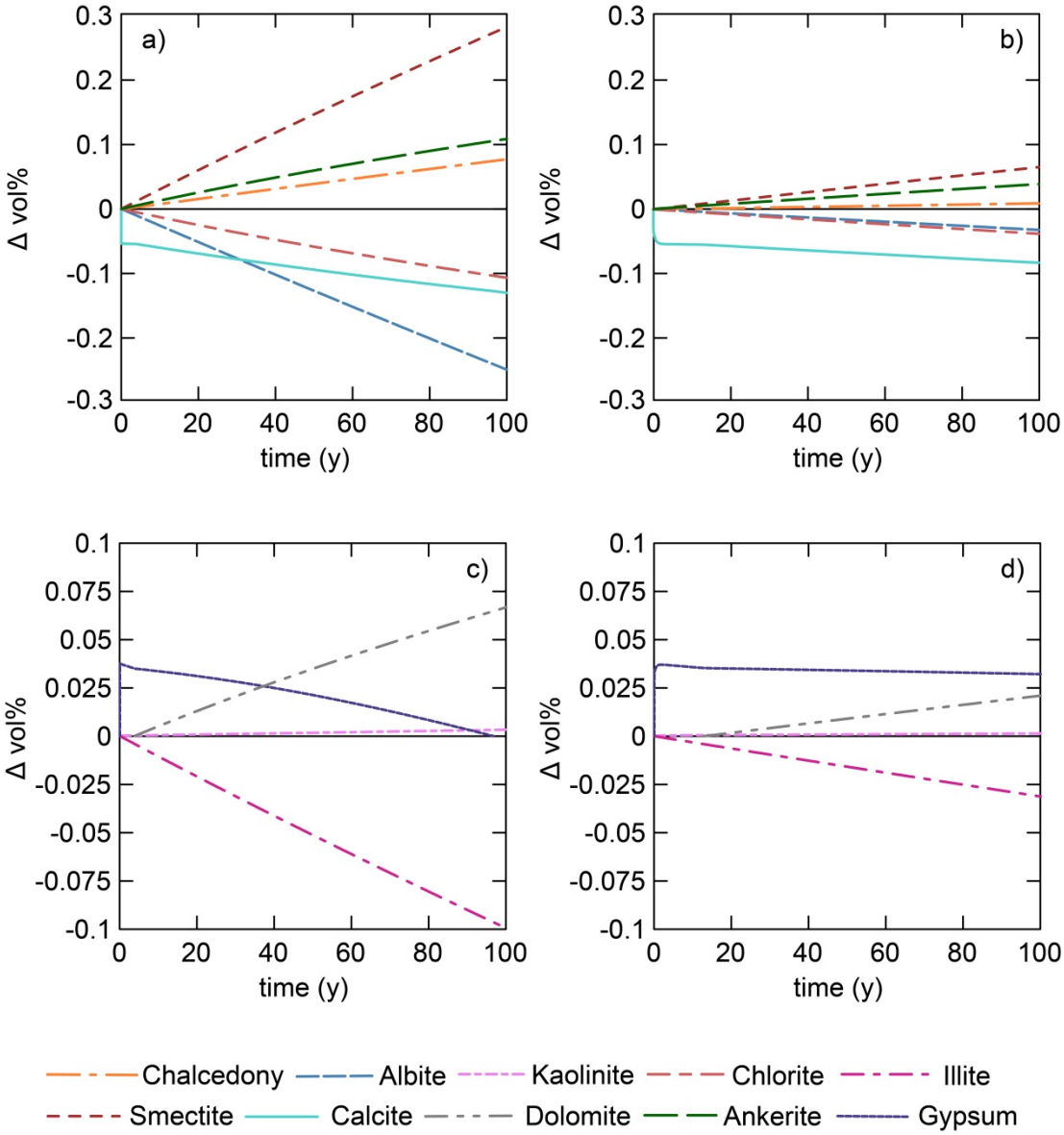

Figure 4.8 Modelled mineral reaction for the upscaled mortared (a+c) and block (b+d) CO_2-SO_2 models of AF-04 over a 100 y modelling period.

AF-05

Simulations of the block and mortared AF-05 mineral reactions were dominated by labradorite dissolution and smectite precipitation (Figure 4.10). Calcite dissolved rapidly at the beginning of both simulations (Figure 4.10a, b), resulting in a rapid pH increase (Figure 4.9). The subsequent precipitation rate of calcite was significantly greater in the mortared simulation resulting in a total gain in calcite of 0.06 vol%. In the

block model on the other hand, calcite was reduced by a total of 0.04 vol% after 100 y. Gypsum initially precipitated in both simulations and dissolved subsequently (Figure 4.10c, d). In the mortared model gypsum dissolved completely within the first 80 y of the modelling period, while gypsum was still present in the block model after the completion of the 100 y modelling period.

Silicate reaction was significantly higher in the mortared model compared to the block model, which resulted in a slightly greater final pH in the mortared model. Labradorite reaction was 6 times lower in the block model. K-feldspar, illite, chlorite and kaolinite dissolution were lower in the block model as well, resulting in lower amounts of SiO_2 and Al in the brine. Hence, the ion availability was higher in the mortared model resulting in more smectite, chalcedony, ankerite and dolomite precipitation. Further, K-feldspar reached saturation in the mortared model and stopped dissolving after 80 y. This was not observed for the block model. The pyrite dissolution extent was similar in both simulations, since they used the same pyrite reactive surface area. The different mineral reactions resulted in a reduction in porosity of 0.025 vol% for the mortared model. The block model on the other hand resulted in a slight porosity gain of 0.01 vol%.

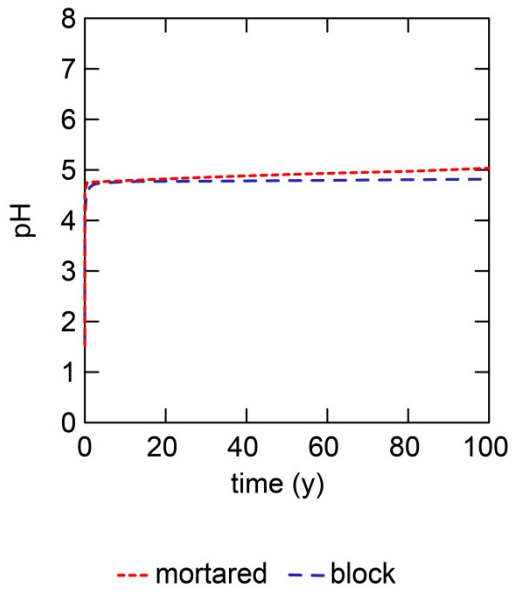

Figure 4.9 Modelled change in pH for the upscaled mortared and block CO_2-SO_2 models of AF-05 over a 100 y modelling period.

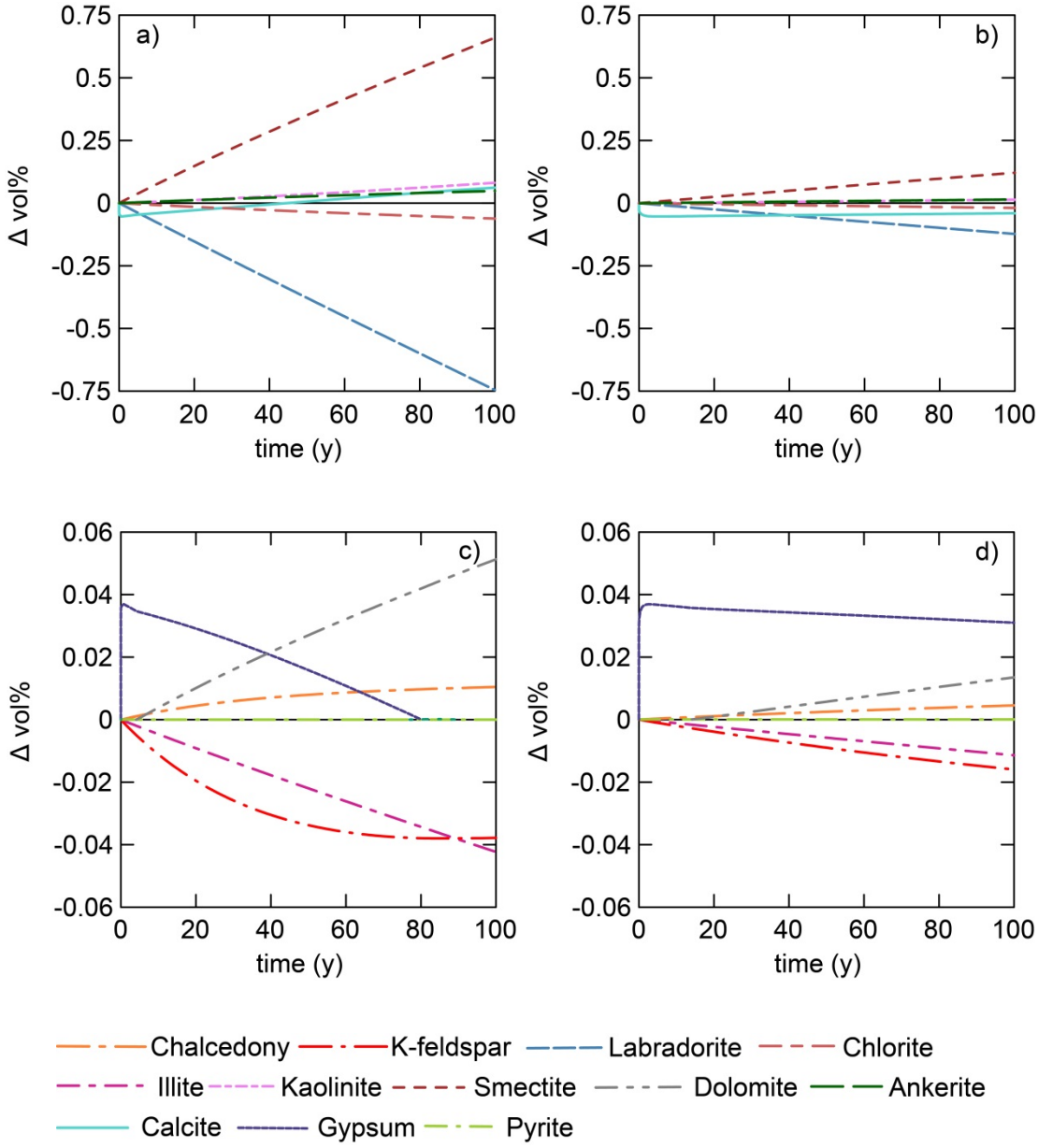

Figure 4.10 Modelled mineral reaction for the upscaled mortared (a+c) and block (b+d) CO_2-SO_2 models of AF-05 over a 100 y modelling period.

AF-06

The upscaled models of AF-06 resulted in a different final pH and different extent of reaction depending on which sample particle size experiment they were based on (Figure 4.11; Figure 4.12). The evolution of ankerite was similar in both models (Figure 4.12c, d). Ankerite rapidly decreased to ~0.01 vol% reflecting rapid pH buffering (Figure

4.11), but started to precipitate again as silicate mineral dissolution became more significant. This was reflected in the ankerite precipitation rate, whereby that of the block model was slightly slower than the mortared model despite having the same reactive surface area, indicating the rate of cation supply controlled the precipitation rate.

The modelled reaction rates for the framework silicates were significantly greater in the mortared model compared to the block model. Hence, the gradual pH increase induced by silicate dissolution was lower in the block model. Albite dissolution was 9.5 times higher and chalcedony precipitation was 6.5 times higher in the mortared model (Figure 4.12a, b). K-feldspar initially dissolved in both models and subsequently started to precipitate. However, the dissolution and precipitation extent of K-feldspar was significantly lower in the block simulation compared to the mortared simulation. The reaction rates of the clay minerals were mostly lower in the block model as well, resulting in less illite dissolution as well as less kaolinite and smectite precipitation. Chlorite on the other hand dissolved to a greater extent in the block model. The low chlorite reaction extent is likely due to the rapid pH buffering. This resulted in a greater Fe availability and more siderite precipitation in the block simulation. Magnesite precipitated in both simulations as well. However, magnesite started to form more than 20 y earlier in the mortared model than in the block model, resulting in slightly more magnesite after 100 y.

Gypsum and alunite precipitated early in both models, but dissolved again over the 100 y modelling period. In the mortared model, gypsum and alunite dissolved within the first 3 and 28 y of the modelling period, respectively. The block simulation on the other hand dissolved gypsum after 9 y and alunite after 70 y. Pyrite dissolved in both simulations to a similar extent, which was expected since both models used the same pyrite reactive surface area. All mineral reactions combined resulted in a porosity increase of 0.02 vol % in the mortared and 0.01 vol% in the block model after 100 y.

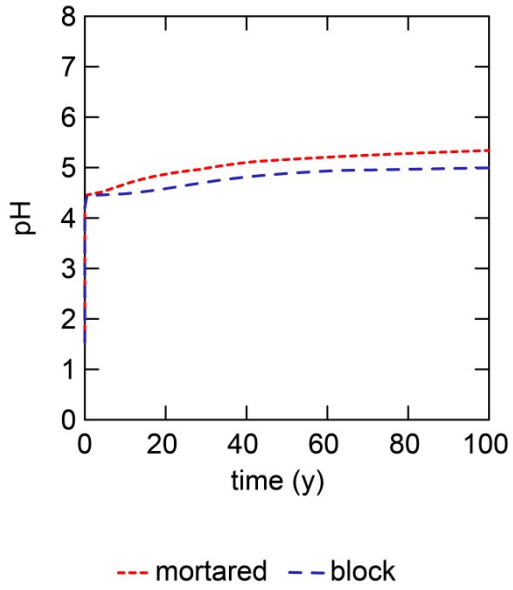

Figure 4.11 **Modelled change in pH for the upscaled mortared and block CO_2-SO_2 models of AF-06 over a 100 y modelling period.**

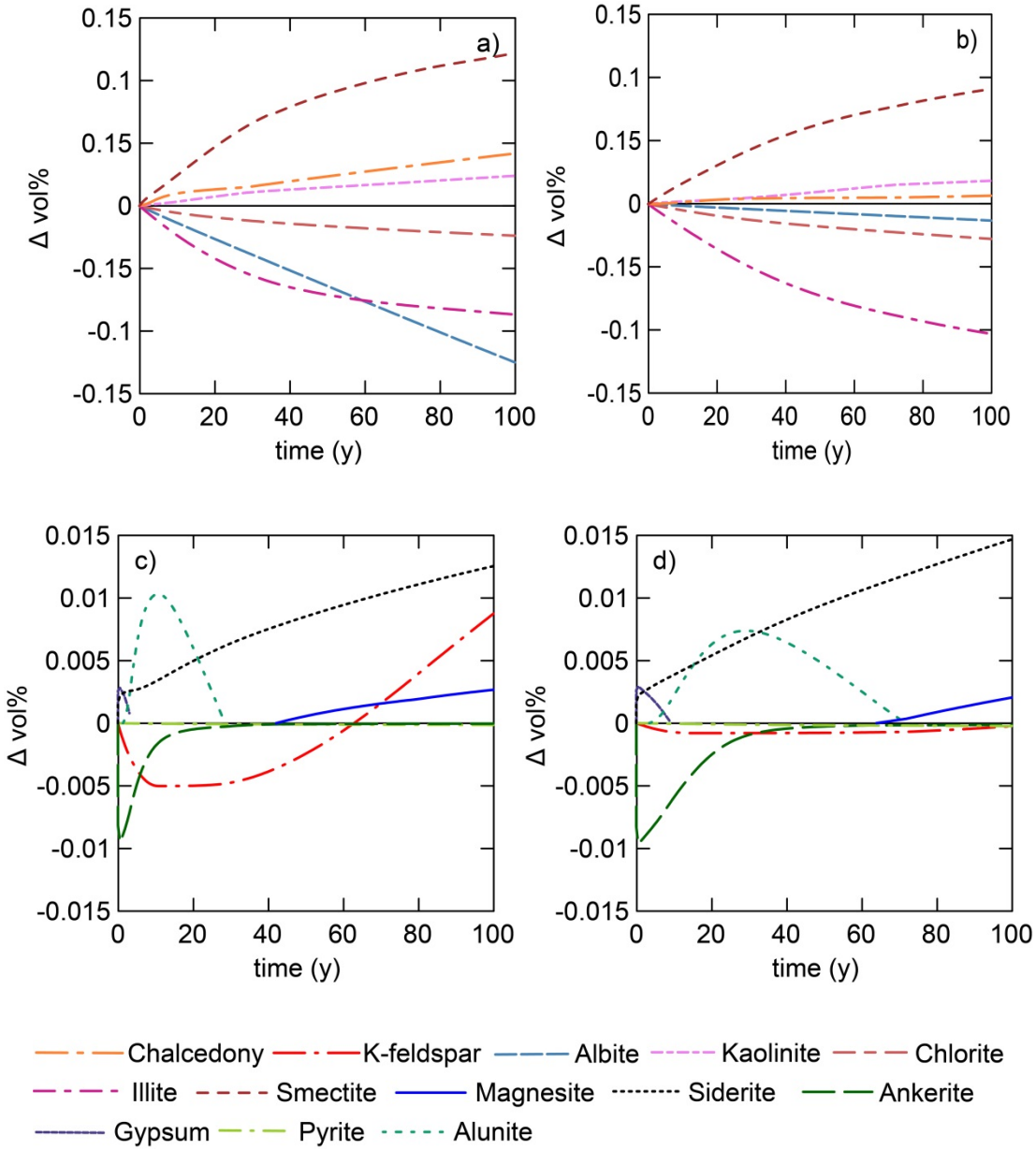

Figure 4.12 Modelled mineral reaction for the upscaled mortared (a+c) and block (b+d) CO_2-SO_2 models of AF-06 over a 100 y modelling period.

Discussion

The upscaling of the Western Canada Sedimentary Basin samples shifted the water-rock ratio of the simulated system from a water dominated experimental set up to rock dominated natural subsurface condition. The upscaled models accounted for the available pore space for reactive brine in reservoir and caprock/seal systems. The high

mineral to water ratio in the upscaled models resulted in greater amounts of minerals for pH buffering. Rapid carbonate dissolution buffered the pH to a value above 4 at which mineral precipitation and the abundant CO_2 gas counterbalanced the pH rise due to dissolution. In the experiments on the other hand, the amount of carbonate minerals in the different samples was commonly not sufficient to buffer the pH of the reactive brine to a value greater than 2.5, resulting in more acid induced mineral reaction. Chlorite in particular was more reactive in the experimental models than in the upscaled models. The mineral reactions predicted by the experimental models were controlled by the abundant SO_2. By incorporating CO_2 into the long term models, the system shifted from SO_2 dominated to CO_2 dominated. As mentioned above, the low pH induced through SO_2 was buffered rapidly to a value at which the pH and mineral reactions are controlled by CO_2. Hence, only the initial reactions where controlled by SO_2, subsequently the system was controlled by CO_2. This can be seen in the change from sulphate precipitation and carbonate dissolution at the beginning of the modelling period to sulphate dissolution and carbonate precipitation later on.

Mineral reaction rates are sensitive to the chosen reactive surface area (Hellevang and Aagaard, 2013b). However, reactive surface areas found in geologic formations are not quantitatively understood (Xu et al., 2004; Xu et al., 2005). Factors like grain coating, grain to grain contacts, and fluid flow channelling result in a reduction of available surface area (Sonnenthal et al., 2000; Li et al., 2006; Zhu et al., 2006). Most studies predicting long term carbon storage use calculated reactive surface areas. Hellevang and Aagaard (2013b) conducted a sensitivity analysis on reactive surface area and discovered that an increase of one order of magnitude in the fraction of active reactive surface area resulted in 3-4 times more CO_2 mineral storage. Xu et al. (2005) and Zerai et al. (2006) accounted for the uncertainties associated with reactive surface areas by reducing them by one and two orders of magnitude, respectively. This approach assumes that all mineral phases are affected equally by factors like grain to grain contacts or coating. However, due to their pore filling habit, calculated reactive surface areas of carbonates are likely to require more upscaling than framework silicates. The same goes for clay minerals, whose reactive surface areas are dependent on selective sites on grain edge faces (Metz et al., 2005; Marty et al., 2011). This study accounts for these factors by using upscaled reactive surface areas sourced from

experiments and by applying different scaling factors to framework silicates and clay minerals.

The differences in model outputs between the mortared and the block model point out the importance of accurate upscaling. The mortared model predicted faster reaction rates compared to the block model. By mortaring a rock sample, factors that limit reactive surface area, like grain to grain contacts and fluid channelling, were minimized. The reactive surface area values sourced from the mortared experiments are therefore likely close to the total mineral surface. The same applies for the freshly cut surfaces of the block sample. However, the mineral reactive surface area inside the block samples was constrained by grain coating, grain to grain contacts and other factors limiting reactive surface areas in a natural system. Hence, the block approach simulates actual reservoir conditions better, in particular for pore filling minerals, and minerals whose reactive surface area is dependent on selective sites on grain edge faces. By decreasing the reactive surface areas of the framework silicates and clay minerals by 100 and 1000, respectively, the upscaled block model accounted for the freshly cut outer surfaces of the block sample. The carbonate reactive surface areas are likely slightly overestimated due to some exposure on the outer block surface areas, which were not accounted for. However, due to the low abundance of carbonates in most of the samples this uncertainty is likely low. However, when looking at carbonate-rich block samples the importance of carbonate upscaling increases. The upscaled mortared simulations did not account for the pore filling habit of carbonates at all. Further, the applied scaling factors were likely not sufficient to account for the freshly exposed surface areas of the mortared grains. Hence, a different upscaling approach would be required to upscale mortared experiments to a reservoir scale.

The uncertainty associated with upscaling method used in this study was highly dependent on the mineral itself and the modelling period. The difference in calcite, siderite and dolomite reactive surface between the mortared and block upscaled models did not result in significantly different carbonate dissolution extents after 100 y, likely due to their high reactivity. However, over the course of the 100 y modelling period, the carbonate dissolution rate was usually lower in the block model compared to the mortared model, suggesting that when considering shorter time periods the uncertainty

associated with upscaled carbonate reactive surface areas increases. In most cases, the predicted carbonate precipitation extents of the mortared and block model were similar as well. AF-01 to AF-03 showed similar ankerite and dolomite precipitation extents after 100 y. This is due to the fact that these samples have low amounts of chlorite; hence ankerite and dolomite precipitation depended largely on ions released from carbonate dissolution. The models of AF-04 to AF-06 on the other hand showed a dependence of carbonate precipitation on chlorite dissolution, resulting in less ankerite in the AF-04 and AF-05 model and more siderite in the AF-06 model after 100 y. Hence, the uncertainty associated with the predicted amount of stored CO_2 in the mineral phase is likely not only associated with the error of carbonate upscaling, but also with the error of silicate upscaling.

The mortared and block models resulted in significantly different silicate dissolution rates and extents. In particular, the feldspars showed a significant reduction in dissolution extent from the mortared to the block model, resulting in less SiO_2 release, which in turn reduced the silicate precipitation rates. Hence, the uncertainty associated with upscaled framework silicate reactive surface areas over a 100 y period is quite high. Further, since albite dissolution, which was the dominating silicate reaction in most Western Canada Sedimentary Basin models, appears to be quite linear over the modelled time period, the error associated with incorrect upscaling of albite reactive surface areas increases with time.

The clay mineral dissolution extent was less affected by the difference in reactive surface area between the mortared and the block model. However, the slower chlorite dissolution rates in the AF-04 and AF-05 block models reduced ankerite and dolomite precipitation significantly compared to the mortared models, suggesting that the uncertainty associated with the clay mineral reaction rates affects not only the clay reaction rates, but also the precipitation of other minerals.

The greater reaction extent and ion availability predicted by the mortared models resulted in a quicker precipitation of sulphate minerals. However, it also resulted in faster sulphate dissolution rates, so that only in the mortared model of AF-01 SO_2 was still stored in the mineral phase after 100 y. In the block models on the other hand, only AF-

02 and AF-06 had no sulphate present after the completion of the modelling period. Hence, accurate upscaling is very important to predict how long and how much SO_2 will be stored in the mineral phase.

A very important factor to consider is how the use of different reactive surface areas affected the predicted porosity change. In most of the Western Canada Sedimentary Basin samples the mortared model predicted a greater porosity increase than the block model. All of the models predict both carbonate and silicate precipitation, but most of them not in a sufficient quantity to counterbalance the dissolution. Only for AF-03, was a decrease in porosity predicted by both models, which was greater in the block model. For AF-05, a decrease in porosity was predicted in the mortared model and an increase in porosity in the block model. This suggests that for AF-03 and AF-05, precipitation processes will dominate over the long term, reducing the formation porosity. For the other Western Canada Sedimentary Basin this is likely to happen as well, but the models give no information about the time frame. The initial porosity increase is beneficial for reservoir formations, since a greater pore space improves the injectivity and storage capacity of a reservoir. A long term porosity decrease is not of concern for a storage reservoir as long as the injection period is completed. For a seal formation on the other hand, the short term porosity increase is of great concern since it could affect the security of a caprock. A greater porosity often results in a higher permeability, which increases the probability of a leakage. Hence, the potential of a long term porosity decrease is desirable for seal formations since it can result in self-sealing and minimize leakage potential. Inaccurate upscaling could under- or overestimate porosity changes, which is of great concern when predicting the storage capacity and long term injectivity of a reservoir and the safety of a seal.

The upscaled Western Canada Sedimentary Basin models predicted the mineral reactions within the acidified zone close to the injector. At the injector, the pH induced by CO_2-SO_2 injection will be lower due to the high solubility of SO_2. Hence, more acid induced mineral dissolution will occur at the well than predicted in the models of the acidified zone close to the injector. Further, the mineral reactions at the well are likely controlled by SO_2 longer than further away due to most of the SO_2 being stripped out of the CO_2 gas proximal to the well. This results in more sulphate precipitation and less

carbonate precipitation. Only a small amount of SO_2 reaches the outside of the acidified zone, resulting in a pH value that is controlled by CO_2 beyond that zone. Therefore, carbonate precipitation will dominate over sulphate precipitation. The effect of CO_2-SO_2 injection can easily be modelled at any given point of a formation using models like the upscaled Western Canada Sedimentary Basin models by increasing or decreasing the amount of SO_2 depending on the distance to the injector.

4.3.2. CO_2, CO_2-SO_2 and CO_2-SO_2-O_2 storage

The geochemical reaction path models of the Surat Basin rocks were run under conditions of pure CO_2, CO_2-SO_2 and CO_2-SO_2-O_2 injection. The different injection stream contents resulted in significantly different model outputs. The biggest difference was in the initial pH of the simulations, and through that, the extent of reaction, although the presence of O_2 also introduced the potential for oxide mineral precipitation that was not likely in the other injection streams. In the following paragraphs, the results of the CO_2 and CO_2-SO_2-O_2 models of the Surat Basin formations are compared and summarized.

AF-07

The CO_2 and CO_2-SO_2-O_2 predictions of the Precipice Sandstone sample AF-07 resulted in significantly different outcomes (Table 4.4; Figure 4.13; Figure 4.14). All three storage scenarios predicted a similar final pH of about 4.67 (Table 4.4), at which the pH is controlled by the abundant CO_2 gas and carbonate mineral equilibrium. However, the addition of SO_2 resulted in a lower initial pH compared to pure CO_2 storage. The CO_2 and CO_2-SO_2-O_2 model predicted similar reaction extents for K-feldspar, albite and illite dissolution (Figure 4.14a, c, d), resulting in similar amounts of Na, K and SiO_2 (Figure 4.13 a, b, c, d). Chlorite dissolved in both models, but showed a more significant initial decrease in the CO_2-SO_2-O_2 prediction likely due to the lower pH. The precipitation extent of chalcedony and kaolinite decreased slightly with the addition of SO_2 and O_2. Smectite precipitation on the other hand was over 470 times greater in the CO_2-SO_2-O_2 simulation compared to the pure CO_2 simulation.

The model of pure CO_2 injection resulted in less carbonate reaction than the model of CO_2-SO_2-O_2 injection. About 0.03 vol% of ankerite dissolved, while approximately 0.01 vol% siderite and less than 0.001 vol% dolomite precipitated. The addition of SO_2 and O_2 resulted in 30 times more ankerite dissolution and 300 times more dolomite formation (Figure 4.14b), and consequently, more Ca and less Mg in the brine after 100 y. Further, it led to the precipitation of 0.26 vol% of calcite, 0.07 vol% of gypsum and 0.13 vol% of hematite. The formation of gypsum and hematite resulted in significantly lower amounts of SO_4 and Fe in the CO_2-SO_2-O_2 model compared to the CO_2 model. The pure CO_2 simulation resulted in a total porosity increase of 0.02 vol%, while the simulation including SO_2 and O_2 predicted a total porosity increase of 0.13 vol%.

Table 4.4 Initial and final pH for the 100 y CO_2, CO_2-SO_2 and CO_2-SO_2-O_2 storage simulations of AF-07 at reservoir scale.

	CO_2	CO_2-SO_2	CO_2-SO_2-O_2
pH_0	3.703	1.394	1.394
pH_{100}	4.665	4.595	4.745

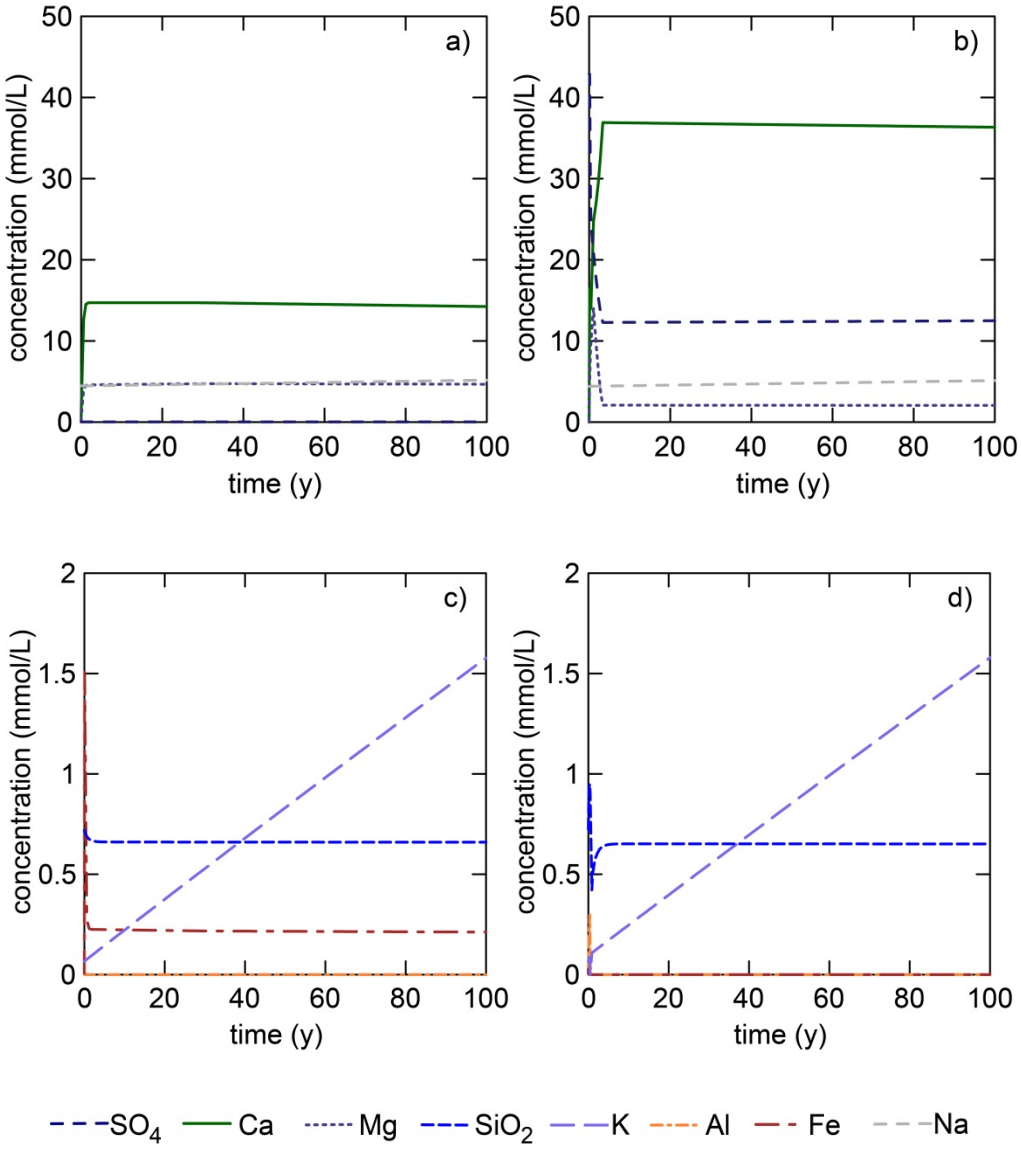

Figure 4.13 Modelled change in brine properties for the CO_2 (a+c) and CO_2-SO_2-O_2 (b+d) storage simulations of AF-07 over a 100 y modelling period.

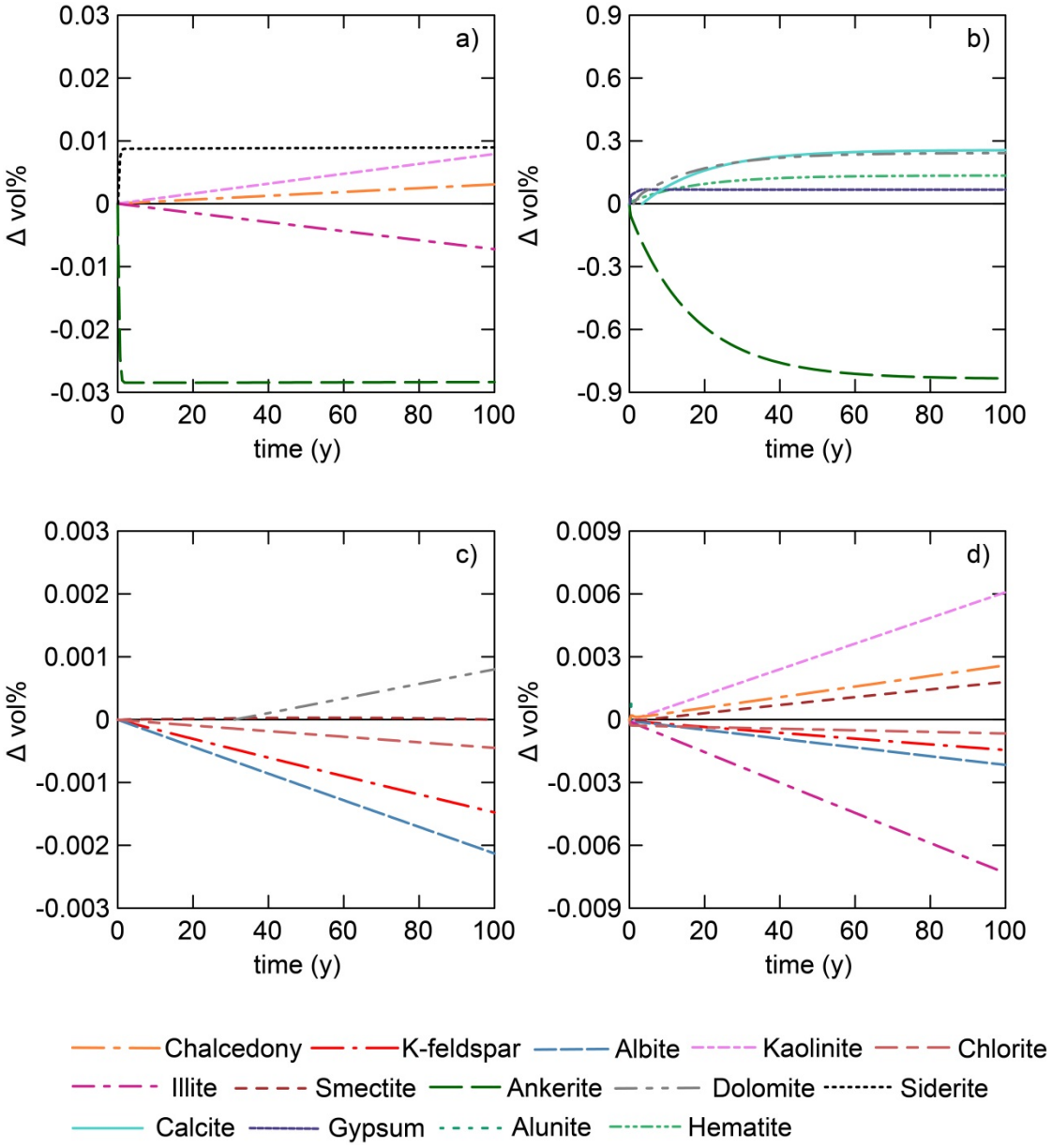

Figure 4.14 Modelled mineral reaction for the CO_2 (a+c) and CO_2-SO_2-O_2 (b+d) storage simulations of AF-07 over a 100 y modelling period.

AF-08

The CO_2 and CO_2-SO_2-O_2 storage models of the Evergreen Formation sample AF-08 resulted in some significant differences in the model outputs (Table 4.5; Figure 4.15; Figure 4.16). The different storage scenarios all resulted in a final pH value close to 5.35 (Table 4.5). However, the pure CO_2 model resulted in an initial pH of 3.7, while the

models including SO_2 resulted in an initial pH of 1.4. The CO_2 and CO_2-SO_2-O_2 storage models predicted very similar chalcedony, albite, illite, smectite, biotite and kaolinite reaction extents (Figure 4.16a, b, c, d). Hence, the evolution of SiO_2 was largely similar in both models over the 100 y modelling period (Figure 4.15c, d). Chlorite dissolution was slightly lower in the pure CO_2 model than in the model including SO_2 and O_2. K-feldspar reaction was lower in the pure CO_2 model as well. Further, K-feldspar reached saturation and started to precipitate slightly in the CO_2 model, which was not observed in the CO_2-SO_2-O_2 model. This resulted in a slightly lower K concentration in the CO_2 model after 100 y (Figure 4.15a, b).

The CO_2 and CO_2-SO_2-O_2 models predicted significant differences in carbonate reaction extent. Further, the predicted carbonate reaction rates of the CO_2-SO_2-O_2 simulation were significantly greater when compared to the CO_2 simulation. Pure CO_2 injection was predicted to result in a decrease in calcite of 0.01 vol%, and an increase in ankerite of 0.0047 vol% and dolomite of 0.0075 vol% after 100 y. The CO_2-SO_2-O_2 storage model on the other hand resulted in a decrease in ankerite of 10.75 vol% and an increase in dolomite of 3.18 vol% and calcite of 4.23 vol%. The pure CO_2 model predicted siderite formation at the beginning of the 100 y modelling period. However, siderite was not stable and dissolved again. The CO_2-SO_2-O_2 model resulted in gypsum and hematite precipitation. While gypsum completely dissolved again within the first 60 y of the modelling period, hematite reached a final value of about 1.75 vol%. Both models resulted in an increase in porosity after 100 y. However, the total porosity increase predicted by the CO_2-SO_2-O_2 model was 1.65 vol%, while the total porosity increase of the pure CO_2 model was only 0.04 vol%.

Table 4.5 Initial and final pH for the 100 y CO_2, CO_2-SO_2 and CO_2-SO_2-O_2 storage simulations of AF-08 at reservoir scale.

	CO_2	CO_2-SO_2	CO_2-SO_2-O_2
pH_0	3.703	1.394	1.394
pH_{100}	5.393	5.239	5.237

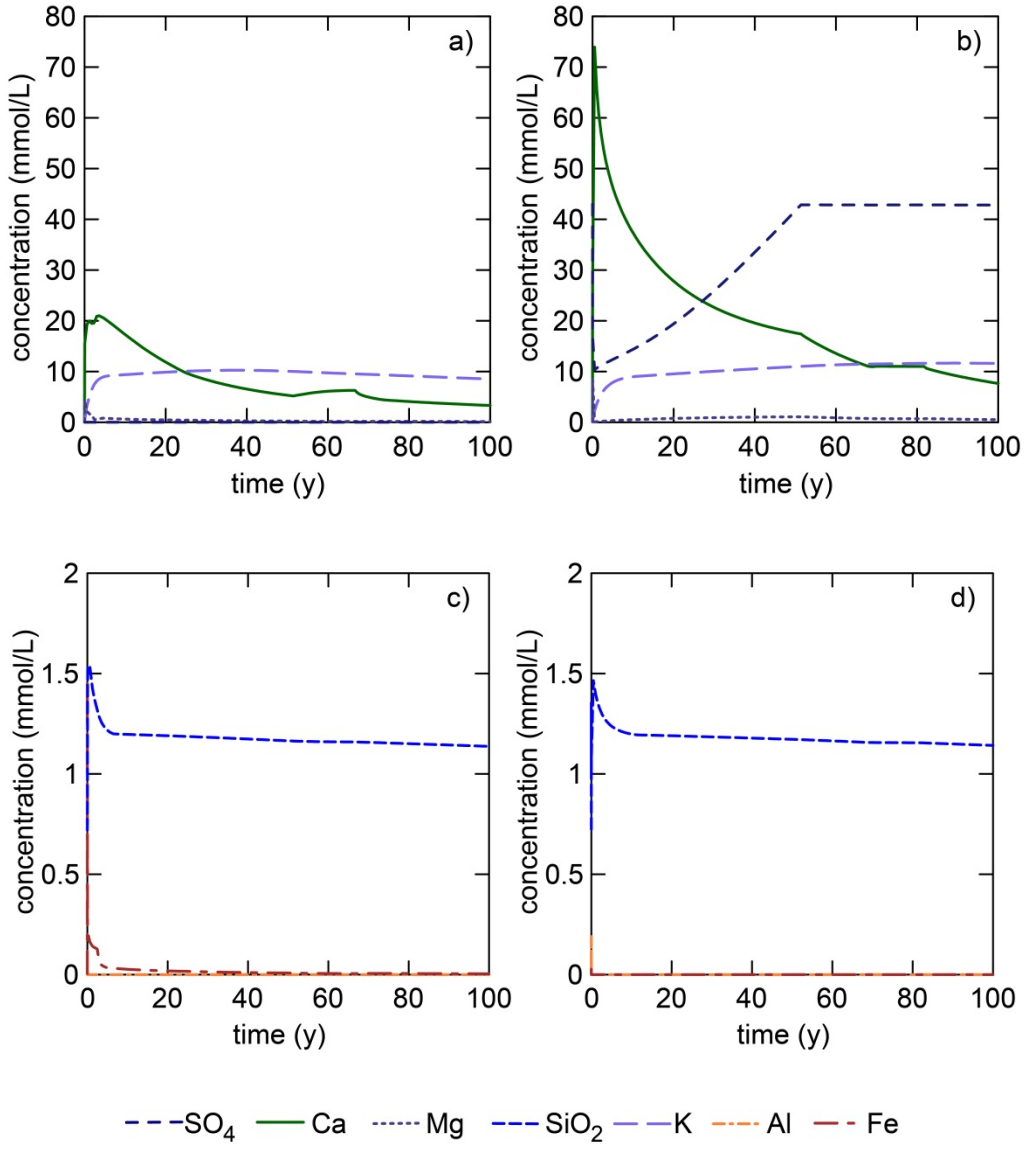

Figure 4.15 **Modelled change in brine properties for the CO_2 (a+c) and CO_2-SO_2-O_2 (b+d) storage simulations of AF-08 over a 100 y modelling period.**

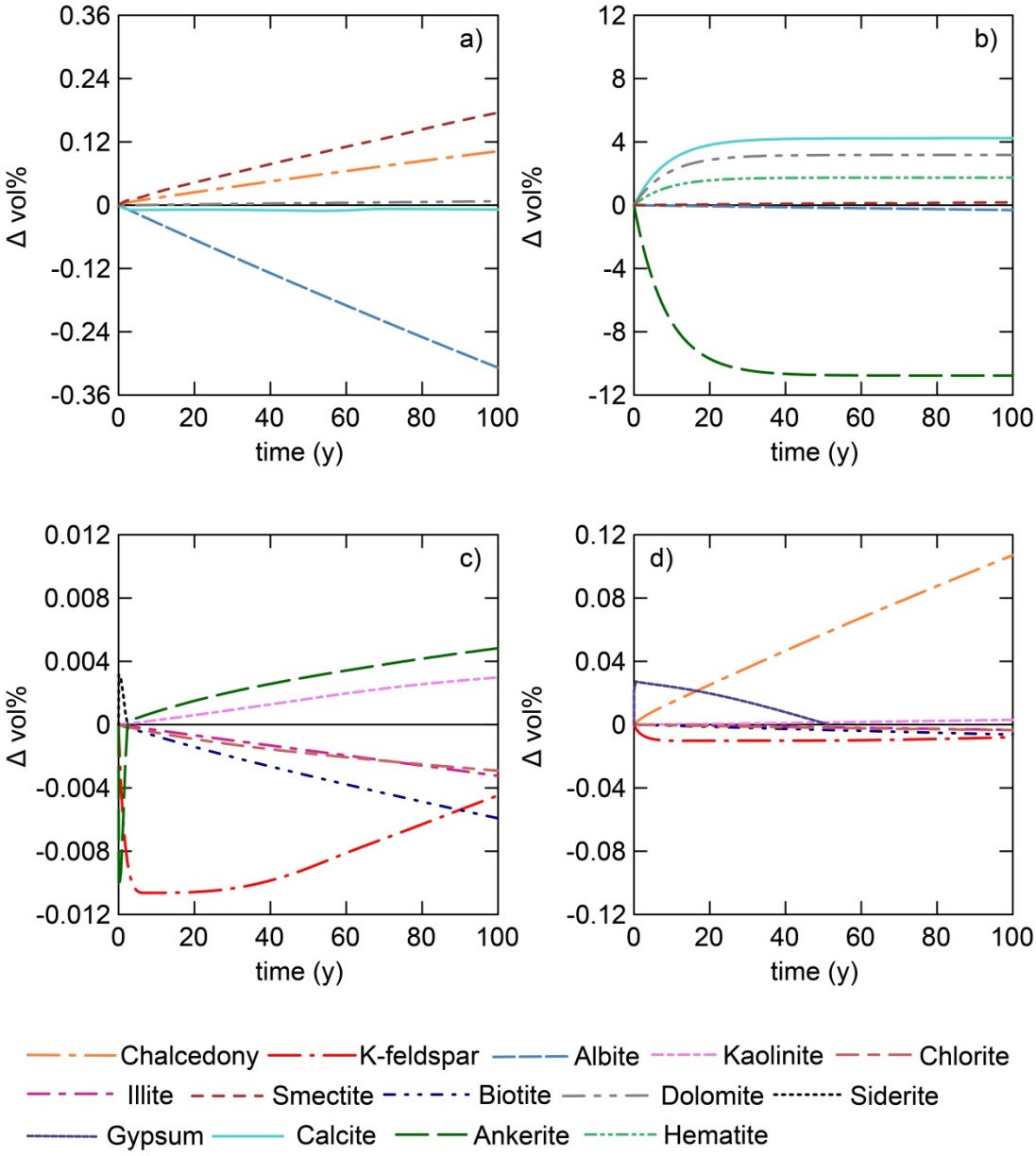

Figure 4.16 Modelled mineral reaction for the CO_2 (a+c) and CO_2-SO_2-O_2 (b+d) storage simulations of AF-08 over a 100 y modelling period.

AF-09

The models predicting CO_2 and CO_2-SO_2-O_2 storage for the Evergreen Formation sample AF-09 resulted in very similar results compared to the AF-08 model outputs (Table 4.6; Figure 4.17; Figure 4.18). The addition of SO_2 resulted in a significantly lower starting pH than the pure CO_2 model (Table 4.6). However, all models resulted in a

similar final pH of approximately 5.3 after 100 y. The CO_2 and CO_2-SO_2-O_2 storage simulations predicted similar silicate reaction extents. Albite decreased by 0.21 vol%, illite by 0.004 vol% and biotite by 0.027 vol% in both models (Figure 4.18a, b, c, d). Chalcedony, smectite and kaolinite precipitated at similar rates in both simulations as well, resulting in a similar final value for SiO_2 after 100 y (Figure 4.17c, d). The amount of chlorite dissolved was slightly higher in the CO_2-SO_2-O_2 model, likely due to the lower starting pH. K-feldspar dissolved at the beginning of both models, but reached saturation and started to precipitate after about 8 y. However, the K-feldspar precipitation rate was slightly higher in the pure CO_2 model, resulting in less K in the brine after 100 y (Figure 4.17a, b).

The extent of carbonate reactions predicted by the CO_2-SO_2-O_2 storage simulations was significantly greater than the amounts predicted by the CO_2 storage simulation, resulting in more Ca and Fe in the brine throughout the modelling period. The CO_2 model resulted in a decrease in ankerite by 0.06 vol% and increases in siderite by 0.02 vol % and dolomite by 0.05 vol%. The CO_2-SO_2-O_2 model predicted a decrease in ankerite 155 times higher than in the CO_2 model. Siderite decreased by a total of 2.8 vol%, while dolomite increased by approximately 2.6 vol%. Gypsum precipitated initially in the CO_2-SO_2-O_2 model, resulting in a decrease in SO_4. However, gypsum was not stable and dissolved again within the first 50 y of the modelling period, returning the amount of SO_4 to its original value. Hematite dissolved slightly in the CO_2 model. Through the addition of O_2, Fe released from mineral dissolution was oxidized and was removed from the brine through the precipitation of 0.01 vol% of hematite and 3.92 vol% of goethite (FeO(OH)) in the CO_2-SO_2-O_2. The predicted porosity increase of the CO_2 model was 0.02 vol% after 100y, while the CO_2-SO_2-O_2 model resulted in a total porosity increase of 1.62 vol%.

Table 4.6 Initial and final pH for the 100 y CO_2, CO_2-SO_2 and CO_2-SO_2-O_2 storage simulations of AF-09 at reservoir scale.

	CO_2	CO_2-SO_2	CO_2-SO_2-O_2
pH_0	3.703	1.394	1.394
pH_{100}	5.376	5.217	5.289

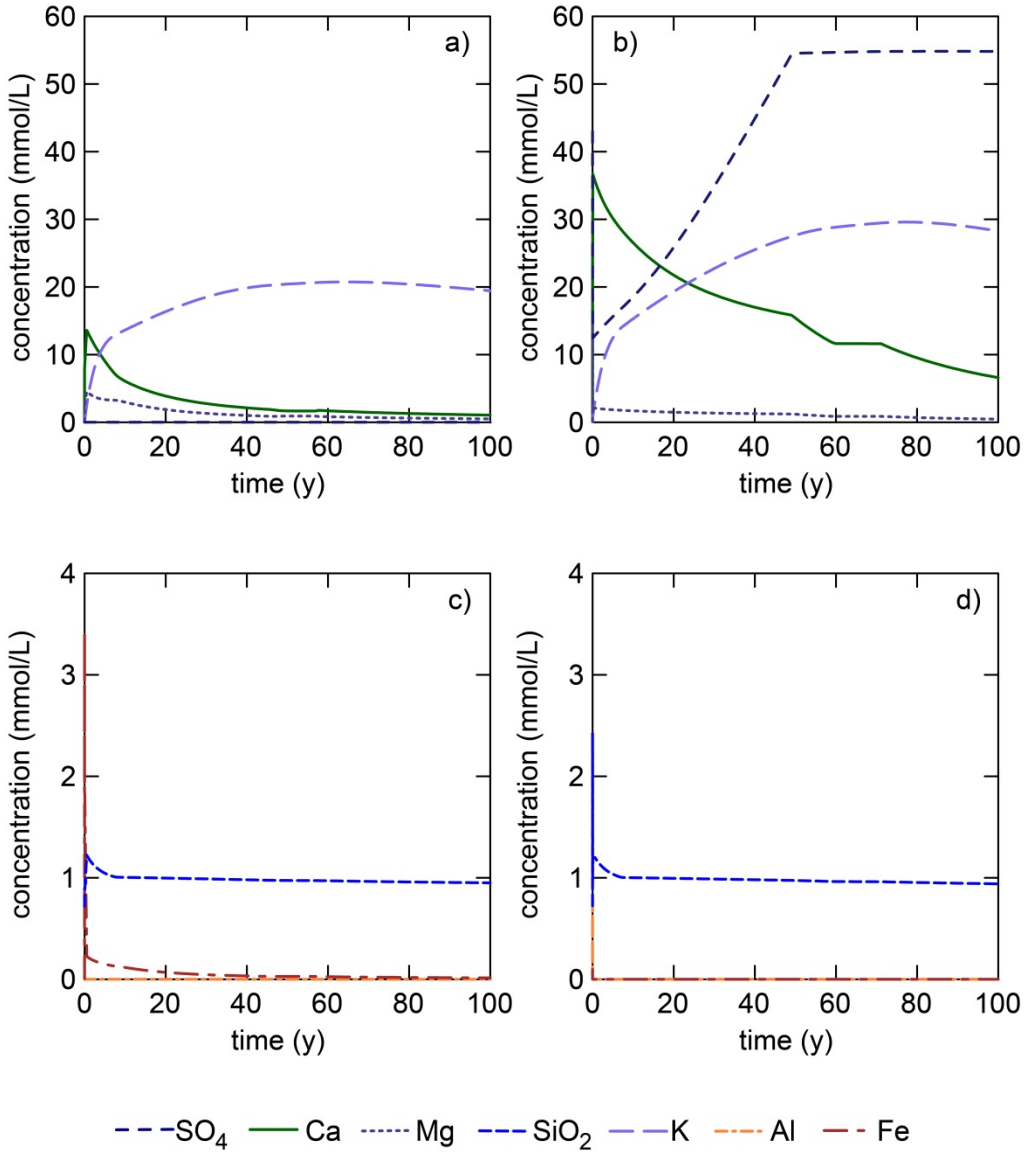

Figure 4.17 **Modelled change in brine properties for the CO_2 (a+c) and CO_2-SO_2-O_2 (b+d) storage simulations of AF-09 over a 100 y modelling period.**

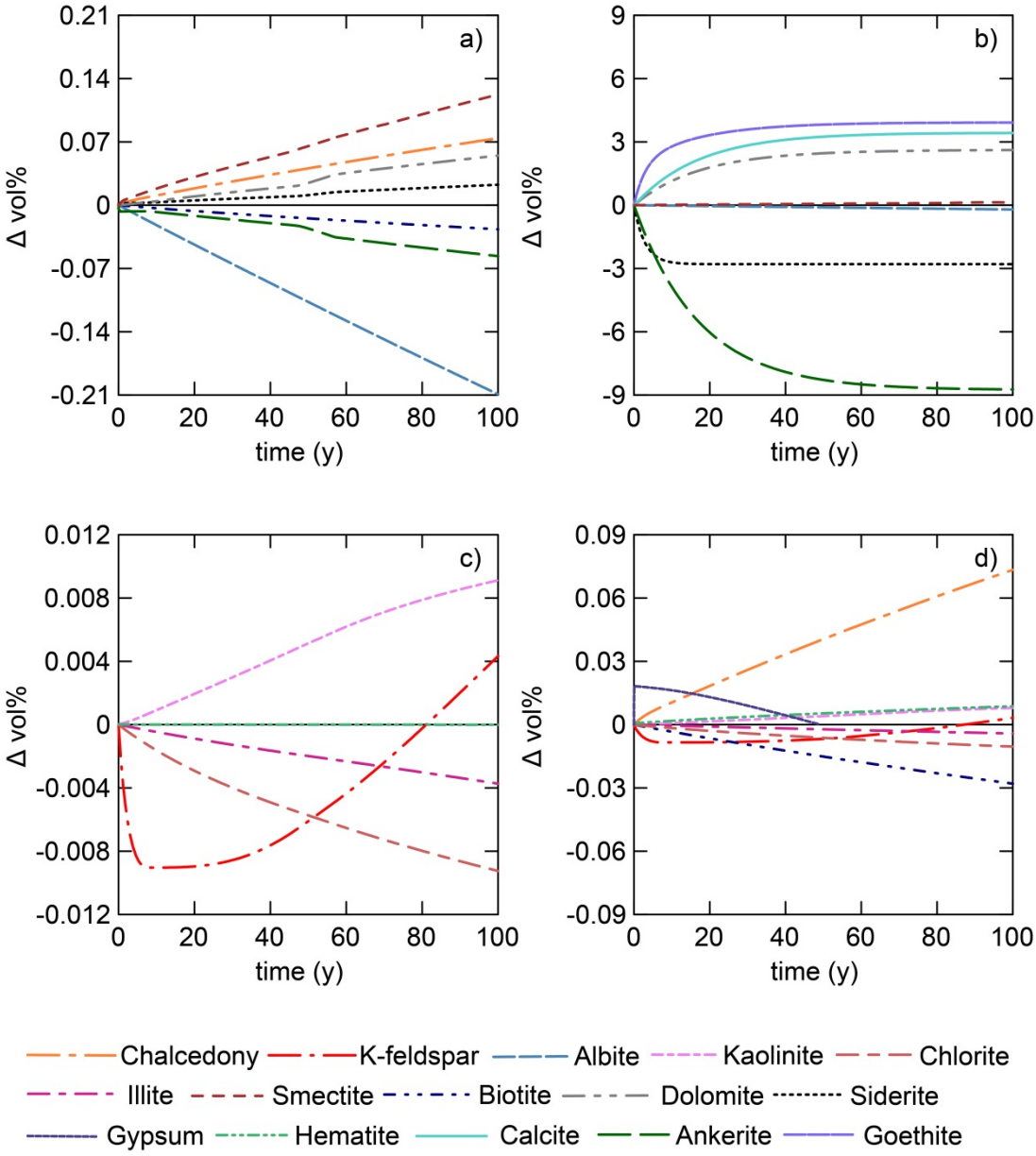

Figure 4.18 Modelled mineral reaction for the CO_2 (a+c) and CO_2-SO_2-O_2 (b+d) storage simulations of AF-09 over a 100 y modelling period.

AF-10

The CO_2 and CO_2-SO_2-O_2 storage models of the Hutton Sandstone sample AF-10 resulted in very different outcomes (Table 4.7; Figure 4.19; Figure 4.20). Like the other models, the addition of SO_2 led to a lower starting pH, but the final pH was similar

for all simulations (Table 4.7). The CO_2 and CO_2-SO_2-O_2 models predicted very different carbonate reaction extents. The dissolution of ankerite was almost 30 times greater in the CO_2-SO_2-O_2 model than in the CO_2 model (Figure 4.20a, b), resulting in significantly higher amounts of Ca in the brine (Figure 4.19a, b). Dolomite precipitation was about ten times greater in the CO_2-SO_2-O_2 storage simulation compared to the CO_2 simulation. Siderite on the other hand changed from precipitating in the CO_2 model to dissolving in the CO_2-SO_2-O_2 model (Figure 4.20b, c). This is due to the O_2 addition, which resulted in Fe oxidation and the precipitation of hematite and goethite (Figure 4.20c, d). In the pure CO_2 model hematite decreased slightly over the 100 y. The oxidation of SO_2 and ankerite dissolution led to rapid gypsum precipitation after injection. However, gypsum was not stable and dissolved completely shortly before the end of the modelling period.

The predicted silicate reaction extents of the CO_2 and CO_2-SO_2-O_2 storage simulation were similar for chalcedony, K-feldspar, albite and biotite. Muscovite and kaolinite precipitation were slightly decreased in the CO_2 model compared to the CO_2-SO_2-O_2 model. Smectite formation on the other hand was higher in the CO_2-SO_2-O_2 storage simulation. However, the total amount of silicate precipitation was similar in both models resulting in a final SiO_2 concentration of ~1.1 mmol/L after 100 y (Figure 4.19c, d). Chlorite dissolved in both models, but to a lesser extent in the CO_2 model. The porosity increased by a total of 0.03 vol% in the CO_2 model and by a total of 1.33 vol% in the CO_2-SO_2-O_2 model.

Table 4.7 Initial and final pH for the 100 y CO_2, CO_2-SO_2 and CO_2-SO_2-O_2 storage simulations of AF-10 at reservoir scale.

	CO_2	CO_2-SO_2	CO_2-SO_2-O_2
pH_0	3.703	1.394	1.394
pH_{100}	5.186	4.989	5.037

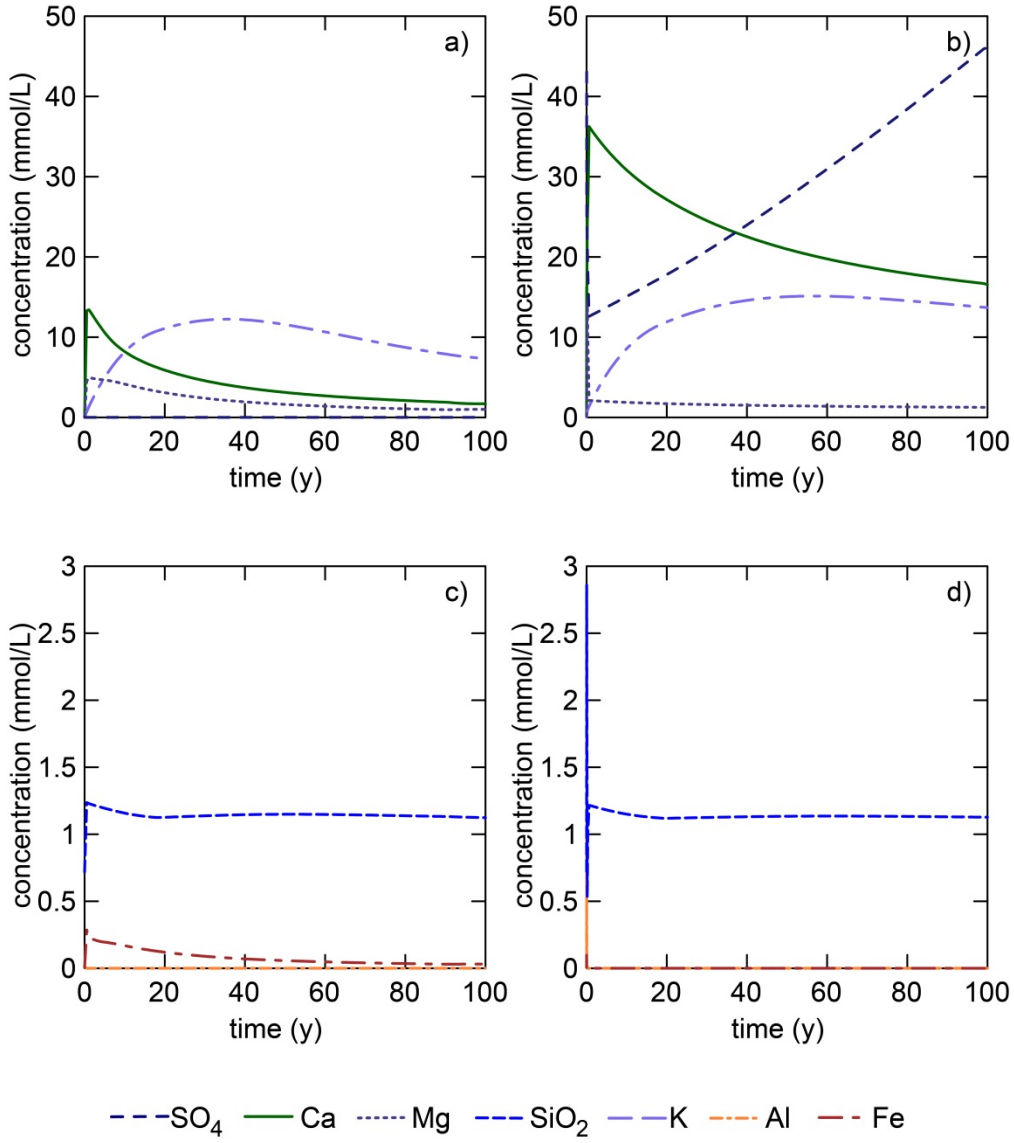

Figure 4.19 **Modelled change in brine properties for the CO_2 (a+c) and CO_2-SO_2-O_2 (b+d) storage simulations of AF-10 over a 100 y modelling period.**

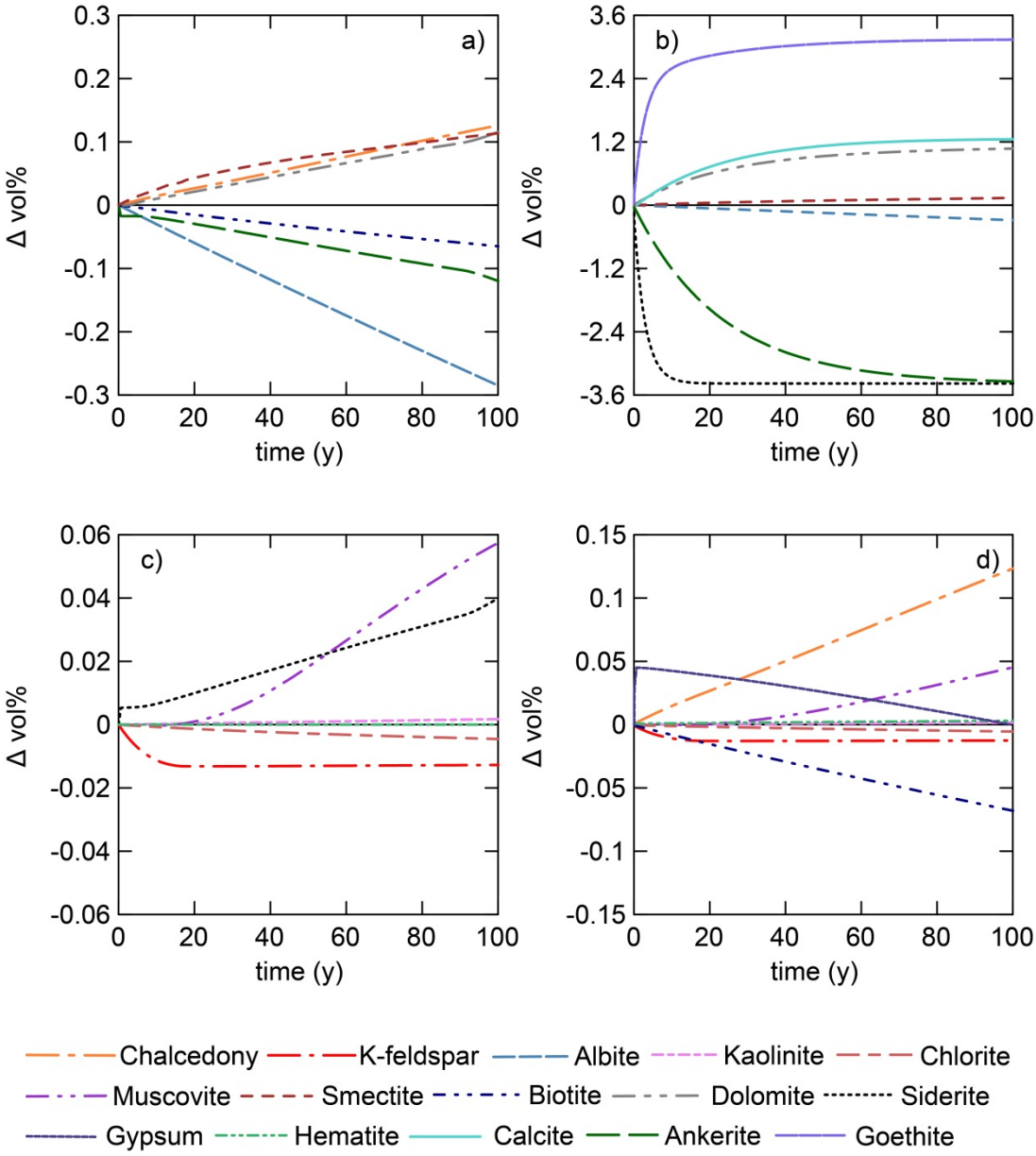

Figure 4.20 Modelled mineral reaction for the CO_2 (a+c) and CO_2-SO_2-O_2 (b+d) storage simulations of AF-10 over a 100 y modelling period.

Discussion

The comparison of pure CO_2, CO_2-SO_2 and CO_2-SO_2-O_2 storage showed significantly different geochemical and physical changes. The models simulated near injection well conditions at which the dissolution of CO_2 and SO_2 result in a strongly acidified zone. Xu et al. (2007) predicted that the addition of SO_2 would result in an

acidified zone extending to a radial distance of 200 m, compared to a radial distance of 50 m for pure CO_2 injection. The extent of the acidified zone is limited by SO_2 diffusion within the scCO_2 plume (Crandell et al., 2010; Ellis et al., 2010). The addition of SO_2 was predicted to lead to greater carbonate reaction extents and the precipitation of secondary sulphates within the acidified zone (Bacon et al., 2009, Knauss et al., 2005; Xu et al, 2007). The injection of CO_2-SO_2 was also predicted to result in a porosity increase within the acidified zone and a porosity decrease outside of the acidified one, due to carbonate precipitation (Xu et al, 2007). No data on CO_2-SO_2-O_2, which is addressed in this study, has been published.

The Surat Basin models predicted a lower starting pH for the models including SO_2. However, unlike the model by Xu et al. (2007), the pH was rapidly buffered to a value between 4.5 and 5.5, at which the acidity was controlled by the abundant CO_2 gas. Compared to pure CO_2 injection, the addition of SO_2 and O_2 did not result in significantly different amounts of silicate reaction for the Surat Basin Formations. Chlorite dissolution was affected the most by the addition of impurities, due to the lower starting pH. However, chlorite was less reactive than expected from the experimental modelling results due to the rapid initial pH buffering through carbonate dissolution. Since silicate mineral reaction rates are comparatively slow, they were affected little by the initial low pH, and since the buffered pH was at a value where it is controlled by CO_2, the CO_2 simulation had very similar amounts reacted for the silicate reactions as the CO_2-SO_2-O_2 simulation. Carbonate reaction was more affected by the added impurities. The simulation of CO_2-SO_2-O_2 storage resulted in extremely elevated carbonate reaction rates compared to pure CO_2 storage. The addition of SO_2 resulted in a lower initial pH, which was rapidly buffered by carbonate dissolution. Further, the addition of O_2 resulted in a change from reducing to oxidizing conditions. Therefore, the Fe(II) in ankerite and siderite was oxidized to Fe(III). The released Ca, Mg and HCO_3 were bound as calcite and dolomite, while Fe(III) precipitated in the form of hematite and goethite. This explains the increased carbonate reactions extent after the addition of O_2 as well as the precipitation of hematite and goethite. The latter were not observed in pure CO_2 storage simulations.

The addition of SO_2 resulted in sulphate (as gypsum) precipitation. Interestingly, it was in the Precipice Sandstone simulations where the highest amount of gypsum precipitated (~0.07 vol%), which likely reflects the higher availability of Ca because less pH buffering results in less carbonate precipitation. Therefore, it was only in the Precipice Sandstone Formation that long term SO_2 mineral trapping in form of gypsum persisted to after 100 y.

The predicted change in porosity was significantly greater in the simulations including the impurities, especially for the Evergreen and Hutton Sandstone Formations. This is of great concern for the Evergreen Formation, since it is likely to affect its sealing capacities. Hence, further studies on how much of the impure CO_2 gas reaches the Evergreen Formation are necessary to evaluate the safety of the seal. For the Precipice Sandstone and Hutton Sandstone Formation on the other hand, the porosity increase leads to an increase in potential storage volume and a higher injectivity, which are beneficial for carbon storage. Another issue emerging from O_2 injection is the potential of further acidification in pyrite-rich shales. Pyrite oxidation leads to the formation of sulphuric acid enhancing mineral reactions. Due to the lack of pyrite in the Surat Basin Formations this issue was not investigated in the current study, but should be pursued in the future.

4.4. Conclusions and Recommendations

4.4.1. Upscaling

The significant differences in model outcomes between the mortared and block upscaled models showed that the applied method of upscaling has to be specific to the available data on reactive surface area. While the upscaling method used in this study is considered sufficient to account for the freshly cut block surface areas, the upscaled mortared models need to be further adjusted to account for factors like grain coating and grain to grain contacts. Hence, the upscaled block models were deemed to simulate reservoir conditions better for the 100 y modelling period. Silicate minerals were especially sensitive to the applied reactive surface area. The smaller reactive surface areas used in the block models resulted in significantly reduced silicate dissolution and

precipitation rates. The error associated with inaccurate silicate reactive surface areas appeared to increase over time. Hence, it is important to choose an appropriate upscaling method for the data at hand and to account for uncertainties to predict long term silicate reactions. The simulated amounts of carbonate dissolution were not significantly influenced by the difference in applied reactive surface area over the long term modelling period due to the high reactivity of carbonates. However, when looking at short term predictions, the upscaling of carbonate reactive surface areas becomes more important. Carbonate precipitation rates can be limited by the dissolution of reactive silicate minerals, like chlorite. Therefore, careful upscaling of both carbonate and silicate reactive surface areas is crucial when predicting long term CO_2 mineral storage. Further, the changes in reaction extent affected the trapping of SO_2. Gypsum and alunite precipitation was slowed down in the block model, which used lower reactive surface areas. Moreover, both phases were stable over longer time periods in the block model compared to the mortared model. The mortared and block models of the Western Canada Sedimentary Basin predicted significantly different porosity changes after 100 y. This is especially important when predicting the safety of a seal, but influences the potential storage capacity of a storage reservoir as well.

The upscaled models of the Western Canada Sedimentary Basin samples, modelling CO_2-SO_2 storage, predicted geochemical and geophysical changes in the reservoir to 100 y after injection. The models enabled identification of dissolving and precipitating mineral phases and quantified their reaction extent. Further, the models clearly highlighted that the extent of upscaling of reactive surface area used in the literature provided a better simulation of reservoir conditions when compared to not including any upscaling. Further, one order of magnitude uncertainty in reactive surface area of carbonates was acceptable but had a more profound effect on silicate mineral reactions over long time periods. A reasonable scaling method was suggested, but further research is necessary to better solve the problem of upscaling.

4.4.2. CO_2, CO_2-SO_2 and CO_2-SO_2-O_2 storage

The comparison of CO_2, CO_2-SO_2 and CO_2-SO_2-O_2 storage scenarios revealed significant differences the predicted geochemical reactions and reaction extents. All three scenarios predicted similar silicate reaction extents. The addition of SO_2 resulted in

a lower starting pH, slightly higher carbonate reactions, and sulphate precipitation. The addition of O_2 besides SO_2 increased the carbonate dissolution and precipitation extents further and led to the precipitation of significant amounts of oxides. Additionally, the CO_2-SO_2-O_2 model predicted an increase in porosity up to 90 times greater than the CO_2 simulation. This is beneficial for the Hutton Sandstone and the Precipice Sandstone, since a greater porosity equals a greater storage capacity. However, the porosity increase predicted for the Evergreen Formation is a major safety concern, since it increases the possibility of leakage.

The upscaled models of the Surat Basin samples modelling carbon storage identified dissolving and precipitating mineral phases and quantified their reaction extents after 100 y. Through this, long term predictions on chemical and physical changes in the different formations were possible. Additionally, the models identified and quantified the effect of SO_2 and O_2 addition compared to the geochemical impact of pure CO_2 injection. The simulations evaluated the potential for safe and permanent storage in the Precipice and Hutton Sandstone, which are promising storage formations. For the Evergreen Formation, potential safety risks were identified, which intensified under the addition of O_2. Considering the abundance of O_2 in industrial gas streams, further research in this area is required to determine the exact impact of O_2 impurities. The reservoir models discussed in this study only give information on the geochemical impact of CO_2-SO_2 storage at a defined point of the reservoir. However, the movement of the gas and brine phase through the mineral phase will result in different geochemical impacts at different points of the reservoir. In order to investigate the spatial effect of CO_2-SO_2-O_2 storage reactive transport modelling needs to be done on this problematic.

Chapter 5. Conclusions and recommendations

Carbon capture and storage has been named by the ICPP (IPCC, 2007a) as a potential mitigation strategy for global warming. The effect of CO_2 injection on geochemical and physical properties of a seal-reservoir system as well as the safety of long-term CO_2 storage have been extensively investigated. However, captured gas streams from coal powered electric power plants contain some amounts of impurities, like O_2 and SO_x, which are expected to alter the effect and safety of CO_2 injection (Stanger and Wall, 2011). This aspect of CO_2 storage has not been the topic of many studies and needs to be further evaluated to ensure a safe use of carbon storage.

This research focused on the chemical and physical alterations in different reservoir and seal rocks caused by SO_2 impurities during geological storage. The co-injection of SO_2 is expected to intensify brine acidification through the formation of strong acids, like H_2SO_4, resulting in enhanced mineral dissolution and precipitation (Xu et al., 2007). Experiments and geochemical models on SO_2-brine-rock reactions were combined in this study to improve our understanding and modelling capability of CO_2-SO_2 storage. The experiments consisted of batch reactors containing synthetic brine acidified with H_2SO_4, an aqueous proxy of SO_2, with sedimentary rock samples from the Western Canada Sedimentary Basin, Canada, and the Surat Basin, Australia, reacted over 30 d. The Western Canada Sedimentary Basin samples were reacted at different temperatures, starting pH values and sample particle sizes to investigate the impact on reaction rates and to acquire information needed for upscaling to reservoir conditions. The Surat Basin sample experiments were used to investigate the effect of CO_2-SO_2 storage on rocks from a proposed storage site. In the final step, geochemical reaction path models of pure CO_2, CO_2-SO_2 and CO_2-SO_2-O_2 injection upscaled to reservoir scale were generated and run to 100 y. The Western Canada Sedimentary Basin sample models were used to evaluate the upscaling method used in this study. The Surat Basin

models were modified to include O_2, which is present in most industrial CO_2 streams, and compared to pure CO_2 simulations.

The Western Canada Sedimentary Basin experiments showed a strong dependence of rate and extent of H_2SO_4 induced reactions on sample mineralogy. In particular, a low pH, higher temperature and/or smaller particle size resulted in increased extent of reaction. To identify and quantify the H_2SO_4 induced mineral dissolution and precipitation, the experimental data were integrated into kinetically controlled reaction path models. Model fit was achieved by varying the reactive surface area of the individual mineral phases. The uncertainty in the reactive surface areas was determined to range from less than 5% to approximately 20%. The modelling results identified carbonate minerals as the most reactive minerals phases, in a decreasing order from calcite to dolomite to ankerite and siderite. The most reactive silicate phase was chlorite, followed by K-feldspar and illite/muscovite.

In order to fit the experimental data, the pH and temperature dependency kinetic data derived from the literature had to be adjusted for some mineral phases, in particular for chlorite and carbonates. The largest difference with the commonly used published values was for chlorite, and it is suspected that this is due to the fact that most available literature data are based on single mineral phase experiments with the chlorite sourced from igneous or metamorphic rocks, which at a minimum are morphologically different to the authigenic chlorite commonly found in sedimentary rocks. Minerals with a variable stoichiometry (e.g. chlorite; ankerite) showed a range in kinetic rate data, particularly for temperature dependence, depending on their composition, outlining the importance of accurate stoichiometric data when predicting the reaction of these minerals.

The modelling of the different sample particle size experiments required a reduction in reactive surface area as sample particle size increased. In comparison to upscaled literature values the experimentally derived values commonly overestimated silicate reactive surface areas and underestimated carbonate reactive surface areas. In a natural reservoir, mineral reactive surface areas are limited by factors like grain to grain contacts and fluid channelling. By mortaring the rock samples these factors were minimized such that high reaction rates were observed. This also applies to the outer

surfaces of the block samples. However, mineral reactive surface areas inside the block samples were limited by grain to grain contacts and other factors and better represent a natural reservoir. Therefore, reducing reactive surface areas is of importance when upscaling experimental outcomes to reservoir scale.

The upscaling of the experimental models changed the system from a water dominated experimental set up to a rock dominated natural reservoir. The shift in water-rock ratio resulted in a significantly greater pH buffering capacity of the system. The formation mineralogy, in particular the carbonate minerals, rapidly buffered the SO_2 induced acidification to a pH at which the system was controlled by CO_2. The comparison of the upscaled block and mortared model of the Western Canada Sedimentary Basin showed a significant reduction in reaction rate for silicate and carbonate minerals in the block model over the modelling period. However, the carbonate reaction extent after 100 y was similar in both simulations due to their high reactivity, while the silicate reaction extent was significantly greater in the upscaled mortared model which had a larger reactive surface area. Sulphate containing mineral precipitation was observed in both models, but the sulphate dissolution rates were significantly lower in the block model resulting in more long term SO_2 storage. The dissolution of initially precipitated sulphate phases and subsequent carbonate precipitation predicted by both models demonstrates a change from a SO_2 controlled system to a CO_2 controlled system. The predicted change in porosity was usually smaller in the block simulation, which is important when looking at seal safety and reservoir capacity. The upscaling method used in this study sufficiently accounts for the freshly cut surfaces of the block sample, but not for factors like grain to grain coating or fluid flow channelling. While the reactive surface areas sourced from the block experiments accounted for these factors, the mortared reactive surface areas would require further upscaling. Hence, the upscaled block models were deemed a better approach to simulate long term CO_2-SO_2 storage than the upscaled mortared models.

The Surat Basin experiments resulted in a significantly lower reaction extent for the Precipice Sandstone sample compared to the Evergreen Formation and the Hutton Sandstone samples. The experimental models identified calcite as the most reactive mineral phase, followed by ankerite and siderite. Chlorite showed the greatest reaction

extent of the silicate minerals. The Evergreen Formation, a potential seal, contains the highest amount of reactive mineral phases. The Hutton Sandstone, a potential storage reservoir, showed a similar reaction extent to the Evergreen Formation in the experimental models. For the Precipice Sandstone, the most promising storage reservoir, a significantly lower reaction extent was predicted.

The upscaled CO_2 models of the Surat Basin predicted a higher initial pH than the upscaled CO_2-SO_2-O_2 models. However, both models resulted in a rapid buffering of the pH to a value at which the pH is controlled by the abundant CO_2 gas. Hence, the greater acidification caused by SO_2 addition can be buffered by the rock mineralogies, in particular by the carbonate minerals. Both simulations predicted similar silicate reactions. Albite was commonly the most reactive silicate mineral. Unlike in the experimental simulations, chlorite reaction was comparatively low due to the rapid pH buffering. The addition of SO_2 and O_2 resulted in significantly greater carbonate reaction extents. The Fe in ankerite and siderite was oxidized through the added O_2 and precipitated as hematite and/or goethite, while the Ca, Mg and HCO_3 precipitated as calcite and/or dolomite. In the pure CO_2 model, on the other hand, calcite and ankerite were the main dissolving carbonate phases, while siderite and dolomite precipitated.

The addition of SO_2 resulted in the precipitation of gypsum, which was only stable in the Precipice Sandstone. The enhanced mineral reactions predicted by the CO_2-SO_2-O_2 simulations resulted in a significantly greater porosity increase after 100 y, especially for the Evergreen Formation and the Hutton Sandstone. This is of great concern for the Evergreen Formation since a porosity increase could affect its sealing properties. For the Precipice and Hutton Sandstones on the other hand the increase in porosity is advantageous for their storage capacity.

This study identified geochemical reactions induced by SO_2 impurities and the kinetic factors controlling the reaction rates. The use of adjusted kinetic rate data reduced the uncertainty associated with predicting geochemical reactions, especially for stoichiometric variable mineral phases. The results highlight the importance of the dependence of reactive surface area values, used to model experiments, on the experiment set up and that this can be used to determine appropriate upscaling.

Carbonate minerals in particular required significant scaling compared to literature values. A reasonable upscaling method was introduced to convert short term experimental data derived from block experiments into long term reservoir predictions. However, further research in this area is necessary to reduce the uncertainty associated with upscaling. Flow-through experiments incorporate the complexity of the porosity/permeability/reactive surface area relationship and could provide better insight on factors limiting reactive surface area than the batch experiments used in this study.

The low starting pH induced by SO_2 impurities was rapidly buffered in the long term CO_2-SO_2-O_2 models of the Surat Basin. The Precipice Sandstone and the Hutton Sandstone were identified as good reservoir formations for CO_2-SO_2-O_2 storage. For the Evergreen Formation, an increase in the leakage risk was predicted through the addition of SO_2 and O_2. The next step should be to investigate temporal and spatial changes in the Surat Basin Formations by using reactive transport modelling. This will give a better evaluation on the safety of the Evergreen Formation and the storage capacity of the Precipice and Hutton Sandstones.

Finally, this study focussed mainly on the effect of SO_2 impurities, but the models including O_2 predicted enhanced mineral reactions due to the change in redox conditions. Hence, the geochemical impact of O_2 impurities needs to be further evaluated. In addition, captured CO_2 gas containing SO_2 and O_2 is likely to include other impurities like NO_x and H_2, whose geochemical impacts also need to be investigated. A better understanding of the impact of the different impurities in the CO_2 gas streams will allow risk evaluations on CO_2 storage involving different CO_2 gas mixtures, ensuring a safe and permanent implementation of CO_2 storage.

References

Abercrombie, H.J., Hutcheon, I.E., Bloch, J.D., and de Caritat, P., 1994, Silica activity and the smectite-illite reaction: Geology, v. 22, p. 539-542.

Allen, D.E., Strazisar, B.R., Soong, Y., and Hedges, S.W., 2005, Modeling carbon dioxide sequestration in saline aquifers: Significance of elevated pressures and salinities: Fuel Processing Technology, v. 86, no. 14–15, p. 1569-1580.

André, L., Audigane, P., Azaroual, M., and Menjoz, A., 2007, Numerical modeling of fluid–rock chemical interactions at the supercritical CO_2–liquid interface during CO_2 injection into a carbonate reservoir, the Dogger aquifer (Paris Basin, France): Energy Conversion and Management, v. 48, no. 6, p. 1782-1797.

Arnorssen, S., and Stefansson, A., 1999, Assessment of feldspar solubility constants in water in the range 0° to 350°C at vapor saturation pressures: American Journal of Science , v. 299, p. 173-209.

Bachu, S., and Adams, J.J., 2003, Sequestration of CO_2 in geological media in response to climate change: Capacity of deep saline aquifers to sequester CO_2 in solution: Energy Conversion and Management, v. 44, no. 20, p. 3151-3175.

Bachu, S., 2008, CO_2 storage in geological media: Role, means, status and barriers to deployment: Progress in Energy and Combustion Science, v. 34, no. 2, p. 254-273.

Bacon, D.H., Sass, B.M., Bhargava, M., Sminchak, J., and Gupta, N., 2009, Reactive transport modeling of CO_2 and SO_2 injection into deep saline formations and their effect on the hydraulic properties of host rocks: Energy Procedia, v. 1, no. 1, p. 3283-3290.

Bateman, K., Turner, G., Pearce, J.M., Noy, D.J., Birchall, D., and Rochelle, C.A., 2005, Large-scale column experiment: Study of CO_2, porewater, rock reactions and model test case: Oil & Gas Science and Technology, v. 60, no. 1, p. 161-175.

Benson, S.M., and Cole, D.R., 2008, CO_2 sequestration in deep sedimentary formations: Elements, v. 4, no. 5, p. 325-331.

Bethke, C.M., and Yeakel, S., 2012b, The Geochemist's Workbench, Release 9.0, Reaction Modeling Guide: Champaign, Illinois, Aqueous Solutions, 96 pp.

Bethke, C.M., and Yeakel, S., 2012a, The Geochemist's Workbench, Release 9.0, Reference Manual: Champaign, Illinois, Aqueous Solutions, 369 pp.

Blum, A.E., and Stillings, L.L., 1995, Feldspar dissolution kinetics, *in* White, A.F. and Brantley, S.L. (eds.), Chemical weathering rates of silicate minerals: Washington, DC, Mineralogical Society of America, v. 31, p. 291-351.

Brantley, S.L., Kubicki, J.D., and White, A.F., editors, 2008, Kinetics of water-rock interaction: New York, Springer, 834 p.

Cadman, S.J., Pain, L., and Vuckovic, V., 1998, Bowen and Surat Basins, Clarence-Moreton Basin, Sydney Basin, Gunnedah Basin and other minor onshore basins, Qld, NSW and NT: Australian Petroleum Accumulations Report, Canberra, Bureau of Resource Sciences, v. 11.

Cantucci, B., Montegrossi, G., Vaselli, O., Tassi, F., Quattrocchi, F., and Perkins, E.H., 2009, Geochemical modeling of CO_2 storage in deep reservoirs: The Weyburn Project (Canada) case study: Chemical Geology, v. 265, no. 1-2, p. 181-197.

CEC, 2011, North American power plant air emissions: Commision for Environmental Cooperation, Montréal.

CGSS, 2010, An assessment of Queensland's CO_2 geological storage prospectivity - The Queensland CO_2 Geological Storage Atlas: CO_2 Geological Srorage Solutions Pty Ltd., Canberra.

CO2CRC, 2015, Images & Videos: Storage Images: Retrieved from http://www.co2crc.com.au/imagelibrary3/storage.php?screen=3, 7/6/2015.

Crandell, L.E., Ellis, B.R., and Peters, C.A., 2010, Dissolution potential of SO_2 co-injected with CO_2 in geologic sequestration: Environmental Science & Technology, v. 44, p. 349-355.

Czernichowski-Lauriol, I., Rochelle, C., Gaus, I., Azaroual, M., Pearce, J.M., and Durst, P., 2006, Geochemical interactions between CO_2, pore-waters and reservoir rocks; Advances in the geological storage of carbon dioxide; International approaches to reduce anthropogenic greenhouse gas emissions: NATO Science Series, Series IV, Earth and Environmental Sciences, v. 65, p. 157-174.

Davidson, P.M., 1994, Ternary irono magnesium, calcium carbonates: A thermodynamic model for dolomite as an ordered derivative of calcite-structure solutions: American Mineralogist , v. 79, p. 332-339.

De Caritat, P., Bloch, J., and Hutcheon, I., 1994, LPNORM: A linear programming normative analysis code: Computers & Geosciences, v. 20, no. 3, p. 313-347.

Delany, J.M., and Lundeen, S.R., 1989, The LLNL thermodynamic database: Report UCRL-21658, Livermore, California, Lawrence Livermore National Laboratory.

Duan, Z., and Sun, R., 2003, An improved model calculating CO_2 solubility in pure water and aqueous NaCl solutions from 273 to 533 K and from 0 to 2000 bar: Chemical Geology, v. 193, no. 3–4, p. 257-271.

Ellis, B.R., Crandell, L.E., and Peters, C.A., 2010, Limitations for brine acidification due to SO_2 co-injection in geologic carbon sequestration: International Journal of Greenhouse Gas Control, v. 4, no. 3, p. 575-582.

Ennis-King, J., and Paterson, L., 2005, Role of convective mixing in the long-term storage of carbon dioxide in deep saline formations: SPE Journal, v. 10, p. 349-356.

Exon, N.F., 1976, Geology of the Surat Basin in Queensland: Bulletin 166, Canberra, Bureau of Mineral Resources, Geology and Geophysics.

Farquhar, S.M., Pearce, J.K., Dawson, G.K.W., Golab, A., Sommacal, S., Kirste, D.M., Biddle D., Golding, S.D., 2015, A fresh approach to investigating CO_2 storage: Experimental CO_2–water–rock interactions in a low-salinity reservoir system: Chemical Geology, v. 399, p. 98-122.

Farquhar, S.M., Dawson, G.K.W., Esterle, J.S., and Golding, S.D., 2013, Mineralogical characterisation of a potential reservoir system for CO_2 sequestration in the Surat Basin: Australian Journal of Earth , v. 60, no. 1, p. 91-110.

Flaathen, T.K., Oelkers, E.H., Gislason, S.R., and Aagaard, P., 2011, The effect of dissolved sulphate on calcite precipitation kinetics and consequences for subsurface CO_2 storage: Energy Procedia, v. 4, no. 0, p. 5037-5043.

Flaathen, T.K., Gislason, S.R., and Oelkers, E.H., 2010, The effect of aqueous sulphate on basaltic glass dissolution rates: Chemical Geology, v. 277, no. 3–4, p. 345-354.

Garcia, S., Rosenbauer, R.J., Palandri, J., and Maroto-Valer, M.M., 2012, Sequestration of non-pure carbon dioxide streams in iron oxyhydroxide-containing saline repositories: International Journal of Greenhouse Gas Control, v. 7, no. 0, p. 89-97.

Garcia, S., Rosenbauer, R.J., Palandri, J., and Mercedes Maroto-Valer, M., 2011, Experimental and simulation studies of iron oxides for geochemical fixation of CO_2–SO_2 gas mixtures: Energy Procedia, v. 4, no. 0, p. 5108-5113.

Gaus, I., Audigane, P., André, L., et al., 2008, Geochemical and solute transport modelling for CO_2 storage, what to expect from it?: International Journal of Greenhouse Gas Control, v. 2, no. 4, p. 605-625.

Gaus, I., Azaroual, M., and Czernichowski-Lauriol, I., 2005, Reactive transport modelling of the impact of CO_2 injection on the clayey cap rock at Sleipner (North Sea): Chemical Geology, v. 217, no. 3–4, p. 319-337.

Geoscience Australia, 2015, Surat Basin: Retrieved from http://www.ga.gov.au/scientific-topics/energy/province-sedimentary-basin-geology/petroleum/onshore-australia/surat-basin#heading-1, 7/6/2015.

Gherardi, F., Xu, T., and Pruess, K., 2007, Numerical modeling of self-limiting and self-enhancing caprock alteration induced by CO_2 storage in a depleted gas reservoir: Chemical Geology, v. 244, no. 1-2, p. 103-129.

Glezakou, V., Peter McGrail, B., and Todd Schaef, H., 2012, Molecular interactions of SO_2 with carbonate minerals under co-sequestration conditions: A combined experimental and theoretical study: Geochimica et Cosmochimica Acta, v. 92, no. 0, p. 265-274.

Golubev, S.V., Bénézeth, P., Schott, J., Dandurand, J.L., and Castillo, A., 2009, Siderite dissolution kinetics in acidic aqueous solutions from 25 to 100 °C and 0 to 50 atm pCO_2: Chemical Geology, v. 265, no. 1–2, p. 13-19.

Gunter, W.D., Perkins, E.H., and Hutcheon, I., 2000, Aquifer disposal of acid gases: modelling of water–rock reactions for trapping of acid wastes: Applied Geochemistry, v. 15, no. 8, p. 1085-1095.

Hamer, M., Graham, R.C., Amrhein, C., and Bozhilov, K.N., 2003, Dissolution of Ripidolite (Mg, Fe-Chlorite) in Organic and Inorganic Acid Solutions: Soil Science Society of America Journal, v. 67, no. 2, p. 654-661.

Hellevang, H., and Aagaard, P., 2013b, Can the long-term potential for carbonatization and safe long-term CO_2 storage in sedimentary formations be predicted?: Applied Geochemistry, v. 39, p. 108-118.

Hellevang, H., Pham, V.T.H., and Aagaard, P., 2013a, Kinetic modelling of CO_2–water–rock interactions: International Journal of Greenhouse Gas Control, v. 15, p. 3-15.

Hodginkson, J., Preda, M., Hortle, A., McKillop, M., Dixon, O., and Foster, L., 2009, The potential impact of carbon dioxide injection on freshwater aquifers: The Surat and Eromanga Basins in Queensland: Queensland minerals and energy review series, Brisbane, Dept. of Employment, Economic Development and Innovation, v. 16, 133 pp.

Hoffmann, K.L., Totterdell, J.M., Dixon, O., Simpson, G.A., Brakel, A.T., Wells, A.T., and McKellar, J.L., 2009, Sequence stratigraphy of Jurassic strata in the lower Surat Basin succession, Queensland: Australian Journal of Earth Sciences, v. 56, p. 461-476.

Holland, T., Baker, J., and Powell, R., 1998, Mixing properties and activity-composition and relationships of chlorites in the system MgO-FeO-Al_2O_3-SiO_2-H_2O: European Journal of Mineralogy, v. 10, no. 3, p. 395-406.

IEAGHG, 2011, Effects of Impurities on Geological Storage of CO_2: Cheltenham, IEA Greenhouse Gas R&D Programme (IEAGHG).

IPCC, 2007b, Climate change 2007: Mitigation of climate change, *in* Metz, B., Davidson, O.R., Bosch, P.R., Dave, R. and Meyer, L.A. (eds.), Contribution of working group III to the fourth assessment report of the Intergovernmental Panel on Climate Change (IPCC): Cambridge, Cambridge University Press, 851 pp.

IPCC, 2007a, Climate change 2007: The physical science basis *in* Solomon, S., Qin, D., Manning, M., et al. (eds.), Contribution of working group I to the fourth assessment report of the Intergovernmental Panel on Climate Change (IPCC): Cambridge, Cambridge University Press, 996 pp.

IPCC, 2005, Metz, B., Davidson, O., de Coninck, H., Loos, M. and Meyer, L. (eds.), IPCC Special report on carbon dioxide capture and storage: Cambridge, Cambridge University Press, 440 pp.

Jenkins,C.R., Cook, P.J., Ennis-King, J., Undershultz, J., Boreham, C., Dance, T., de Caritat, P., Etheridge, D.M., Freifeld, B.M., Hortle, A., Kirste, D., Paterson, L., Pevzner, R., Schacht, U., Sharma, S., Stalker, L., Urosevic, M., 2012, Safe storage and effective monitoring of CO_2 in depleted gas fields: Proceedings of the National Academy of Sciences, v. 109, no. 2, p. E35-E41.

Kaldi, J.G., Gibson-Poole, C.M., and Payenberg, T.H.D., 2009, Geological input to selection and evaluation of CO_2 geosequestration sites. *in* Grobe, M., Pashin, J.C. and Dodge, R.L. (eds.), Carbon dioxide sequestration in geological media—State of the science: Tulsa, Oklahoma, AAPG Studies in Geology 59, p. 5-16.

Kaszuba, J.P., Janecky, D.R., and Snow, M.G., 2005, Experimental evaluation of mixed fluid reactions between supercritical carbon dioxide and NaCl brine: Relevance to the integrity of a geologic carbon repository: Chemical Geology, v. 217, no. 3-4, p. 277-293.

Kaszuba, J.P., Janecky, D.R., and Snow, M.G., 2003, Carbon dioxide reaction processes in a model brine aquifer at 200 °C and 200 bars: implications for geologic sequestration of carbon: Applied Geochemistry, v. 18, no. 7, p. 1065-1080.

Kather, A., Hermsdorf, C., and Klostermann, M., 2007, Der kohlebefeuerte Oxyfuel-Prozess—Grundlagen zur Dampferzeugergestaltung und Möglichkeiten zur Verminderung der Verunreinigungen im CO_2: VGB PowerTech, vol. 4, p. 84-91.

Kharaka, Y.K., Cole, D.R., Thordsen, J.J., Kakouros, E., and Nance, H.S., 2006b, Gas-water-rock interactions in sedimentary basins: CO_2 sequestration in the Frio Formation, Texas, USA: Journal of Geochemical Exploration, v. 89, p. 183-186.

Kharaka, Y.K., Cole, D.R., Hovorka, S.D., Gunter, W.D., Knauss, K.G., and Freifeld, B.M., 2006a, Gas-water-rock interactions in Frio Formation following CO_2 injection: Implications for the storage of greenhouse gases in sedimentary basins: Geology, v. 34, no. 7, p. 577-580.

Knauss, K.G., Johnson, J.W., and Steefel, C.I., 2005, Evaluation of the impact of CO_2, aqueous fluid, and reservoir rock interactions on the geologic sequestration of CO_2, with special emphasis on economic implications: Chemical Geology, v. 217, p. 339-350.

Kummerow, J., and Spangenberg, E., 2011, Experimental evaluation of the impact of CO_2-SO_2-brine-reservoir rock interactions on petrophysical properties: A case study from the Ketzin test site, Germany: Geochemistry Geophysics Geosystems (G3), v. 12, p. 1-10.

Lasaga, A.C., 1995, Fundamental approaches in describing mineral dissolution and precipitation rates: Reviews in Mineralogy and Geochemistry, v. 31, no. 1, p. 23-86.

Li, L., Peters, C.A., and Celia, M.A., 2006, Upscaling geochemical reaction rates using pore-scale network modeling: Advances in Water Resources: Advances in Water Resources, v. 29, no. 9, p. 1351-1370.

Liu, F., Lu, P., Griffith, C., Hedges, S.W., Soong, Y., Hellevang, H., and Zhu, C., 2012, CO_2–brine–caprock interaction: Reactivity experiments on Eau Claire shale and a review of relevant literature: International Journal of Greenhouse Gas Control, v. 7, no. 0, p. 153-167.

Lowson, R.T., Brown, P.L., Comarmond, M.C.J., and Rajaratnam, G., 2007, The kinetics of chlorite dissolution: Geochimica et Cosmochimica Acta, v. 71, no. 6, p. 1431-1447.

Lu, J., Kharaka, Y.K., Thordsen, J.J., Horita, J., Karamalidis, A., Griffith, C., Hakala, J.A., Ambats, G., Cole, D.R., Phelps, T.J., Manning, M.A., Cook, P.J., Hovorka, S.D., 2012, CO_2–rock–brine interactions in Lower Tuscaloosa Formation at Cranfield CO_2 sequestration site, Mississippi, U.S.A.: Chemical Geology, v. 291, no. 0, p. 269-277.

Martin, K.R., 1977, Sedimentology of the Precipice Sandstone, Surat Basin, Queensland: PhD thesis, Brisbane, The University of Queensland.

Marty, N.C.M., Cama, J., Sato, T., Chino, D., Villiéras, F., Razafitianamaharavo, A., Brendlé, J., Giffaut, E., Soler, J.M., Gaucher, E.C., Tournassat, C., 2011, Dissolution kinetics of synthetic Na-smectite. An integrated experimental approach: Geochimica et Cosmochimica Acta, v. 75, no. 20, p. 5849-5864.

Metz, V., Raanan, H., Pieper, H., Bosbach, D., and Ganor, J., 2005, Towards the establishment of a reliable proxy for the reactive surface area of smectite: Geochimica et Cosmochimica Acta, v. 69, no. 10, p. 2581-2591.

OECD/IEA, 2012, Energy Technology Perspecives 2012 - Pathways to a clean energy system: Paris, International Energy Agency, 690 pp.

OECD/IEA, 2006, IEA Energy Technology Essentials - CO_2 capture and storage: Paris, International Energy Agency.

Palandri, J.L., and Kharaka, Y.K., 2005b, Ferric iron-bearing sediments as a mineral trap for CO_2 sequestration: Iron reduction using sulfur-bearing waste gas: Chemical Geology, v. 217, p. 351-364.

Palandri, J.L., Rosenbauer, R.J., and Kharaka, Y.K., 2005a, Ferric iron in sediments as a novel CO_2 mineral trap: CO_2–SO_2 reaction with hematite: Applied Geochemistry, v. 20, no. 11, p. 2038-2048.

Palandri, J.L., and Kharaka, Y.K., 2004, A compilation of rate parameters of water-mineral interaction kinetics for application to geochemical modeling: USGS Open File Report 2004-1068, Menlo Park, California, National Energy Technology Laboratory – United States Department of Energy, 64 pp.

Pearce, J.K., Kirste, D.M., Dawson, G.K.W., Farquhar, S.M., Biddle, D., Golding, S.D., and Rudolph, V., 2015, SO_2 impurity impacts on experimental and simulated CO_2–water–reservoir rock reactions at carbon storage conditions: Chemical Geology, v. 399, p. 65-86.

Pham, V.T.H., Lu, P., Aagaard, P., Zhu, C., and Hellevang, H., 2011, On the potential of CO_2–water–rock interactions for CO_2 storage using a modified kinetic model: International Journal of Greenhouse Gas Control, v. 5, p. 1002-1015.

Plummer, L.N., Wigley, T.M.L., and Parkhurst, D.L., 1987, The kinetics of calcite dissolution in CO_2-water systems at 5-60 °C and 0. 0-1.0 atm CO_2: American Journal of Science, v. 278, p. 179-216.

Pruess, K, García, J., Kovscek, T., Oldenburg, Rutqvist, J., Steefel, C., Xu, T., 2004, Code intercomparison builds confidence in numerical models for geologic disposal of CO_2*:* 6th International Conference on Greenhouse Gas Control Technologies, v. 29, no. 9-10, p.1431-1444.

Rietveld, H.M., 1969, A profile refinement method for nuclear and magnetic structures: Journal of Applied Crystallography, v. 2, p. 65-71.

Sakurovs, R., Weir, S., French, D., and Day, S., 2011, Effect of impurity gases in carbon dioxide on sorption behavior and mineral matter in an Australian bituminous coal: International Journal of Coal Geology, v. 86, no. 4, p. 367-371.

Schoonen, M.A.A., Sklute, E.C., Dyar, M.D., and Strongin, D.R., 2012, Reactivity of sandstones under conditions relevant to geosequestration: 1. Hematite-bearing sandstone exposed to supercritical carbon dioxide commingled with aqueous sulfite or sulfide solutions: Chemical Geology, v. 296–297, no. 0, p. 96-102.

Scislewski, A., and Zuddas, P., 2010, Estimation of reactive mineral surface area during water–rock interaction using fluid chemical data: Geochimica et Cosmochimica Acta, v. 74, p. 6996-7007.

Smith, M.M., Wolery, T.J., and Carroll, S.A., 2013, Kinetics of chlorite dissolution at elevated temperatures and CO_2 conditions: Chemical Geology, v. 347, no. 0, p. 1-8.

Sonnenthal, E., and Spycher, N., 2000, Drift-scale coupled processes model: analysis and model report (AMR) N0120/U0110: Yucca Mountain Nuclear Waste Disposal Project, Berkeley, California, Lawrence Berkeley National Laboratory.

Soong, Y., Goodman, A.L., McCarthy-Jones, J.R., and Baltrus, J.P., 2004, Experimental and simulation studies on mineral trapping of CO_2 with brine: Energy Conversion and Management, v. 45, no. 11–12, p. 1845-1859.

Stanger, R., and Wall, T., 2011, Sulphur impacts during pulverised coal combustion in oxy-fuel technology for carbon capture and storage: Progress in Energy and Combustion Science, v. 37, no. 1, p. 69-88.

Summers, C.A., Dahlin, D.C., and Ochs, T.L., 2004 The effect of SO_2 on mineral carbonation in batch tests *in* 29th International Technical Conference on Coal Utilization & Fuel Systems, Clearwater, Florida, Coal Technology Association.

U.S. EPA, 2009, Acid Rain and Related Programs: 2007 Progress Report, Washington, DC, U.S. Environmental Protection Agency (EPA).

White, A.F., and Brantley, S.L., 2003, The effect of time on the weathering of silicate minerals: Why do weathering rates differ in the laboratory and field?: Chemical Geology, v. 202, no. 3-4, p. 479-506.

White, A.F., 1995, Chemical weathering rates of silicate minerals in soils: Reviews in Mineralogy and Geochemistry, v. 31, no. 1, p. 407-461.

Wilke, F.D.H., Vásquez, M., Wiersberg, T., Naumann, R., and Erzinger, J., 2012, On the interaction of pure and impure supercritical CO_2 with rock forming minerals in saline aquifers: An experimental geochemical approach: Applied Geochemistry, v. 27, no. 8, p. 1615-1622.

Xu, T., Apps, J.A., Pruess, K., and Yamamoto, H., 2007, Numerical modeling of injection and mineral trapping of CO_2 with H_2S and SO_2 in a sandstone formation: Chemical Geology, v. 242, no. 3–4, p. 319-346.

Xu, T., Apps, J.A., and Pruess, K., 2005, Mineral sequestration of carbon dioxide in a sandstone–shale system: Chemical Geology, v. 217, no. 3–4, p. 295-318.

Xu, T.F., Apps, J.A., and Pruess, K., 2004, Numerical simulation of CO_2 disposal by mineral trapping in deep aquifers: Applied Geochemistry, v. 19, no. 6, p. 917-936.

Xu, T., Apps, J.A., and Pruess, K., 2003, Reactive geochemical transport simulation to study mineral trapping for CO_2 disposal in deep arenaceous formations: Journal of Geophysical Research: Solid Earth, v. 108, p. 2156-2202.

Zerai, B., Saylor, B.Z., and Matisoff, G., 2006, Computer simulation of CO_2 trapped through mineral precipitation in the Rose Run Sandstone, Ohio: Applied Geochemistry, v. 21, no. 2, p. 223-240.

Zhu, C., and Lu, P., 2009, Alkali feldspar dissolution and secondary mineral precipitation in batch systems: 3. Saturation states of product minerals and reaction paths: Geochimica et Cosmochimica , v. 73, no. 11, p. 3171-3200.

Zhu, C., Veblen, D.R., Blum, A.E., and Chipera, S.J., 2006, Naturally weathered feldspar surfaces in the Navajo Sandstone aquifer, Black Mesa, Arizona: Electron microscopic characterization: Geochimica et Cosmochimica Acta, v. 70, no. 18, p. 4600-4616.

Appendix A.

Material characterization

Table A1 **XRD and XRF results of the Western Canada Sedimentary Basin sample mineralogies in comparison; results are given in wt%.**

	AF-01		AF-02		AF-03		AF-04		AF-05		AF-06	
	XRD	XRF	XRD	XRF	XRD	XRF	XRD	XRF	XRD	XRF	XRD	XRF
Quartz	71.34	67.92	38.79	37.27	67.95	65.81	48.67	45.11	60.27	63.41	53.11	50.00
K-Feldspar	1.33	3.25	16.23	21.22	12.35	19.68			3.64	3.60	2.18	2.20
Albite	1.67	1.52	25.51	25.72	0.40	0.42	33.03	30.00	16.60	14.22	2.17	2.20
Illite/muscovite	3.29	3.00	5.37	5.00	9.20	9.00	4.45	10.40	6.30	6.00	23.44	23.40
Kaolinite	2.87	4.02		6.17		2.20	5.93	7.46		9.92	3.05	7.01
Chlorite		1.86	1.93	1.93		1.20	3.57	5.47	3.64	4.90	2.22	4.50
Calcite	11.13	11.17	0.46	0.51		0.04	0.59	1.17		0.57		0.04
Dolomite	4.74	4.37										
Siderite	0.12	0.12		0.38		0.21						2.21
Hematite			1.02	0.80	0.75	0.58						
Pyrite	0.16	0.02	0.35							0.02	1.08	0.79
"Amorphous"	3.34		10.57		9.35		3.76		9.54		12.76	

Table A2 **Mineral phases detected in the Western Canada Sedimentary Basin samples using a scanning Microprobe; () indicate the mineral phase was detected only once.**

	AF-01	AF-02	AF-03	AF-04	AF-05	AF-06
K-feldspar	x	x	x		x	x
Albite		x		x	(x)	
Labradorite					x	
Illite				x	x	x
Muscovite		x	x	(x)		
Chlorite (Fe:Mg = 50:50)					x	
Chlorite (Fe:Mg = 60:40)	x			x		
Chlorite (Fe:Mg = 70:30)				x		
Calcite	x					
Siderite						x*

*minor amounts of Ca and Mg were detected in the siderite

Table A3 **XRD and QEMScan results of the Surat Basin sample mineralogies in comparison; results are given in wt%; no XRD data was available for AF-08.**

	AF-07		AF-08	AF-09		AF-10	
	XRD	QEMScan	QEMScan	XRD	QEMScan	XRD	QEMScan
Quartz	94.00	97.81	35.78	43.00	39.33	50.00	55.66
K-Feldspar	0.10	0.01	25.64	10.00	5.49	6.00	6.85
Albite	0.10	0.02	7.72	4.00	9.14	7.00	6.19
Illite/ muscovite	3.00	0.05	1.85	3.00	10.39	9.00	6.13
Biotite			0.39	2.00	1.21	8.00	0.53
Kaolinite	2.55	1.31	12.17	18.00	18.63	7.00	6.68
Chlorite	0.20	0.04	3.69	4.00	4.50	7.00	9.76
Calcite			0.16				
Ankerite				10.00		4.00	
Siderite				4.00			
Hematite				2.00		0.50	
Unclassified		0.76	12.60		11.30		8.22

Appendix B.

Experimental conditions

Table A4 Exact experimental conditions of batch experiment B-01 to B-40.

Experiment	Rock sample	Sample mass (g)	Sample particle size	Fluid Vol. (mL)	pH	Samples taken	T (˚C)
B-01	AF-01	3.004	mortared	150	9.49	10	60
B-02	AF-02	2.997	mortared	150	9.49	10	60
B-03	AF-03	3.000	mortared	150	9.49	10	60
B-04	AF-04	3.002	mortared	150	9.49	10	60
B-05	AF-05	3.003	mortared	150	9.49	10	60
B-06	AF-06	2.999	mortared	150	9.49	10	60
B-07	AF-01	3.002	mortared	150	1.54	15	60
B-08	AF-02	3.001	mortared	150	1.54	15	60
B-09	AF-03	3.002	mortared	150	1.54	15	60
B-10	AF-04	3.001	mortared	150	1.54	15	60
B-11	AF-05	2.999	mortared	150	1.54	15	60
B-12	AF-06	3.000	mortared	150	1.54	15	60
B-13	AF-01	3.001	crushed	150	1.54	15	60
B-14	AF-02	3.003	crushed	150	1.54	15	60
B-15	AF-03	3.002	crushed	150	1.54	15	60
B-16	AF-04	3.002	crushed	150	1.54	15	60
B-17	AF-05	3.003	crushed	150	1.54	15	60
B-18	AF-06	3.002	crushed	150	1.54	15	60
B-19	AF-01	4.001	block	150	1.54	15	60
B-20	AF-02	5.068	block	150	1.54	15	60
B-21	AF-03	6.329	block	150	1.54	15	60
B-22	AF-04	4.327	block	150	1.54	15	60
B-23	AF-05	5.329	block	150	1.54	15	60
B-24	AF-06	6.184	block	150	1.54	15	60
B-25	AF-01	3.002	mortared	150	3.02	10	60
B-26	AF-02	3.003	mortared	150	3.02	10	60
B-27	AF-03	3.001	mortared	150	3.02	10	60

Table A4 Exact experimental conditions of batch experiment B-01 to B-40 (continuation from p. 191).

Experiment	Rock sample	Sample mass (g)	Sample particle size	Fluid Vol. (mL)	pH	Samples taken	T (˚C)
B-28	AF-04	3.002	mortared	150	3.02	10	60
B-29	AF-05	3.000	mortared	150	3.02	10	60
B-30	AF-06	3.003	mortared	150	3.02	10	60
B-31	AF-01	3.004	mortared	150	1.40	15	22
B-32	AF-02	2.997	mortared	150	1.40	15	22
B-33	AF-03	3.001	mortared	150	1.40	15	22
B-34	AF-04	2.998	mortared	150	1.40	15	22
B-35	AF-05	3.002	mortared	150	1.40	15	22
B-36	AF-06	3.000	mortared	150	1.40	15	22
B-37	AF-07	1.618	block	100	1.40	15	60
B-38	AF-08	1.859	2 blocks	100	1.40	15	60
B-39	AF-09	1.320	2 blocks	100	1.40	15	60
B-40	AF-10	2.456	block	100	1.40	15	60

Appendix C.

Experimental water data

Table A5 **Temperature, pH, EC, elemental and ion concentrations measured for the ten brine samples of B-01; SP describes the initial brine composition before reaction.**

Sample Number	Time (h)	T (°C)	pH	EC (µS/cm)	Concentration (mmol/L)									
					Al	Ca	Fe	K	Mg	Na	HCO_3	SO_4^{2-}	Cl^-	SiO_2
SP	0	62	9.49	566	$2.76x10^{-3}$	0.02	$8.17x10^{-4}$	0.07	0.18	4.61	1.19	0.01	1.61	0.78
1	21	64	9.32	549	0.02	0.06	$7.56x10^{-3}$	0.13	0.12	4.62	1.17	0.03	1.63	0.76
2	32	63	9.31	551	0.02	0.06	$5.80x10^{-3}$	0.12	0.12	4.69	1.20	0.03	1.86	0.75
3	50	58	9.4	540	0.02	0.05	$5.29x10^{-3}$	0.13	0.11	4.47	1.19	0.02	1.41	0.72
4	98	61	8.98	552	0.02	0.06	$5.11x10^{-3}$	0.11	0.11	4.61		0.03	1.67	0.73
5	168	58	9.24	535	0.02	0.06	$4.89x10^{-3}$	0.13	0.08	4.19	1.19	0.03	1.76	0.69
6	240	63	9.3	549	0.02	0.05	$5.14x10^{-3}$	0.12	0.09	4.58	1.16	0.03	1.78	0.76
7	336	61	9.25	564	0.02	0.06	$5.60x10^{-3}$	0.12	0.08	4.10	1.18	0.02	1.54	0.77
8	456	60	9.2	556	0.02	0.06	$5.96x10^{-3}$	0.13	0.09	3.89	1.16	0.03	1.74	0.78
9	578	62	9.18	562	0.02	0.06	$4.50x10^{-3}$	0.12	0.09	4.05	1.16	0.02	1.45	0.82
10	695	61	9.13	581	0.02	0.06	$5.99x10^{-3}$	0.11	0.09	3.93	1.17	0.03	1.62	0.76

Table A6 **Temperature, pH, EC, elemental and ion concentrations measured for the ten brine samples of B-02; SP describes the initial brine composition before reaction.**

Sample Number	Time (h)	T (°C)	pH	EC (µS/cm)	Concentration (mmol/L)									
					Al	Ca	Fe	K	Mg	Na	HCO_3	SO_4^{2-}	Cl^-	SiO_2
SP	0	62	9.49	566	$2.76x10^{-3}$	0.02	$8.17x10^{-4}$	0.07	0.18	4.61	1.19	0.01	1.61	0.78
1	21	64	9.24	549	0.05	0.05	$3.77x10^{-3}$	0.11	0.15	4.48	1.06	0.08	1.74	0.87
2	32	63	9.2	552	0.05	0.05	$3.27x10^{-3}$	0.12	0.14	4.68	1.03	0.11	1.99	0.90
3	50	58	9.36	542	0.05	0.05	$3.17x10^{-3}$	0.15	0.13	4.75	1.01	0.07	1.52	0.87
4	98	61	9.26	547	0.05	0.05	$2.81x10^{-3}$	0.13	0.12	4.43	1.00	0.08	1.81	0.85
5	168	58	9.24	534	0.05	0.05	$3.04x10^{-3}$	0.14	0.12	4.52	1.22	0.10	2.46	0.89
6	240	63	9.22	552	0.06	0.05	$3.42x10^{-3}$	0.13	0.12	4.54	1.16	0.10	1.99	0.94
7	336	61	9.17	571	0.05	0.05	$3.32x10^{-3}$	0.12	0.13	4.11	1.11	0.10	1.69	0.99
8	456	60	9.24	553	0.05	0.04	$3.13x10^{-3}$	0.11	0.12	3.86	1.08	0.11	2.06	0.94
9	578	62	9.18	557	0.05	0.05	$3.23x10^{-3}$	0.13	0.12	3.73	1.14	0.10	1.69	0.94
10	695	61	9.07	566	0.05	0.05	$3.39x10^{-3}$	0.11	0.13	4.18	1.12	0.12	1.82	1.02

Table A7 **Temperature, pH, EC, elemental and ion concentrations measured for the ten brine samples of B-03; SP describes the initial brine composition before reaction.**

Sample Number	Time (h)	T (°C)	pH	EC (µS/cm)	Concentration (mmol/L)									
					Al	Ca	Fe	K	Mg	Na	HCO_3	SO_4^{2-}	Cl^-	SiO_2
SP	0	62	9.49	566	$2.76x10^{-3}$	0.02	$8.17x10^{-4}$	0.07	0.18	4.61	1.19	0.01	1.61	0.78
1	21	64	9.41	552	0.09	0.02	$6.56x10^{-3}$	0.19	0.15	4.48	1.06	0.02	1.64	0.89
2	32	63	9.41	549	0.10	0.02	$7.85x10^{-3}$	0.19	0.15	4.60	1.08	0.02	1.87	0.94
3	50	58	9.51	544	0.10	0.02	$7.56x10^{-3}$	0.20	0.14	4.51	1.03	0.02	1.31	0.91
4	98	61	9.36	550	0.10	0.02	$7.66x10^{-3}$	0.18	0.14	4.60	1.03	0.02	1.68	0.95
5	168	58	9.38	550	0.10	0.02	$7.45x10^{-3}$	0.18	0.13	4.39	1.06	0.02	1.83	0.93
6	240	63	9.41	553	0.11	0.02	$7.70x10^{-3}$	0.21	0.14	4.60	1.09	0.02	1.78	1.02
7	336	61	9.32	566	0.10	0.02	$7.28x10^{-3}$	0.17	0.14	3.84	1.09	0.02	1.62	1.05
8	456	60	9.24	564	0.11	0.02	$7.67x10^{-3}$	0.18	0.14	3.89	1.08	0.02	1.85	1.09
9	578	62	9.28	568	0.10	0.02	$7.88x10^{-3}$	0.16	0.14	3.82	1.06	0.02	1.23	1.08
10	695	61	9.22	568	0.10	0.02	$7.01x10^{-3}$	0.15	0.15	4.07	1.09	0.02	1.71	1.12

Table A8 **Temperature, pH, EC, elemental and ion concentrations measured for the ten brine samples of B-04; SP describes the initial brine composition before reaction.**

Sample Number	Time (h)	T (°C)	pH	EC (µS/cm)	Concentration (mmol/L)									
					Al	Ca	Fe	K	Mg	Na	HCO_3	SO_4^{2-}	Cl^-	SiO_2
SP	0	62	9.49	566	$2.76x10^{-3}$	0.02	$8.17x10^{-4}$	0.07	0.18	4.61	1.19	0.01	1.61	0.78
1	21	64	9.29	535	0.04	0.05	$9.30x10^{-3}$	0.08	0.11	4.38	1.11	0.05	1.65	0.74
2	32	63	9.34	532	0.04	0.06	$8.36x10^{-3}$	0.08	0.11	4.71	1.14	0.05	1.92	0.77
3	50	58	9.33	532	0.04	0.05	$8.50x10^{-3}$	0.08	0.10	4.53	1.08	0.05	1.64	0.75
4	98	61	9.3	534	0.03	0.05	$7.39x10^{-3}$	0.08	0.10	4.47	1.08	0.06	1.70	0.77
5	168	58	9.09	530	0.03	0.06	$6.93x10^{-3}$	0.09	0.09	4.41	1.09	0.07	2.37	0.75
6	240	63	9.27	537	0.03	0.05	$7.31x10^{-3}$	0.08	0.08	4.46	1.15	0.07	1.75	0.77
7	336	61	9.18	555	0.02	0.05	$6.37x10^{-3}$	0.09	0.08	3.88	1.08	0.07	1.61	0.77
8	456	60	9.24	541	0.03	0.06	$9.31x10^{-3}$	0.09	0.08	3.94	1.06	0.07	1.78	0.81
9	578	62	9.18	560	0.03	0.05	$6.81x10^{-3}$	0.08	0.06	3.80	1.12	0.06	1.26	0.80
10	695	61	9.07	541	0.02	0.04	$5.72x10^{-3}$	0.08	0.06	4.00	1.09	0.07	1.72	0.79

Table A9 **Temperature, pH, EC, elemental and ion concentrations measured for the ten brine samples of B-05; SP describes the initial brine composition before reaction.**

Sample Number	Time (h)	T (°C)	pH	EC (µS/cm)	Concentration (mmol/L)									
					Al	Ca	Fe	K	Mg	Na	HCO_3	SO_4^{2-}	Cl^-	SiO_2
SP	0	62	9.49	566	$2.76x10^{-3}$	0.02	$8.17x10^{-4}$	0.07	0.18	4.61	1.19	0.01	1.61	0.78
1	21	64	9.17	517	0.05	0.04	$1.08x10^{-2}$	0.10	0.12	4.31	1.11	0.03	1.72	0.87
2	32	63	9.14	522	0.05	0.05	$1.04x10^{-2}$	0.10	0.11	4.85	1.12	0.02	1.91	0.92
3	50	58	9.22	522	0.05	0.04	$1.10x10^{-2}$	0.09	0.11	4.19	1.16	0.01	1.61	0.85
4	98	61	8.94	531	0.05	0.04	$8.99x10^{-3}$	0.10	0.09	4.44	1.18	0.02	1.88	0.91
5	168	58	9.1	535	0.04	0.05	$9.23x10^{-3}$	0.10	0.08	4.36	1.14	0.02	1.64	0.91
6	240	63	9.08	538	0.04	0.04	$7.72x10^{-3}$	0.09	0.08	4.66	1.21	0.03	1.67	0.96
7	336	61	9.12	546	0.04	0.04	$9.46x10^{-3}$	0.10	0.08	3.79	1.14	0.02	1.65	0.96
8	456	60	9.12	532	0.03	0.05	$7.03x10^{-3}$	0.11	0.06	3.93	1.14	0.02	1.77	0.98
9	578	62	9.07	545	0.03	0.04	$8.49x10^{-3}$	0.09	0.06	3.53	1.13	0.02	1.48	0.93
10	695	61	8.81	539	0.03	0.05	$9.84x10^{-3}$	0.12	0.06	3.86	1.17	0.02	1.78	0.97

Table A10 **Temperature, pH, EC, elemental and ion concentrations measured for the ten brine samples of B-06; SP describes the initial brine composition before reaction.**

Sample Number	Time (h)	T (°C)	pH	EC (µS/cm)	Concentration (mmol/L)									
					Al	Ca	Fe	K	Mg	Na	HCO_3	SO_4^{2-}	Cl^-	SiO_2
SP	0	62	9.49	566	$2.76x10^{-3}$	0.02	$8.17x10^{-4}$	0.07	0.18	4.61	1.19	0.01	1.61	0.78
1	21	64	8.65	587	0.05	0.01	0.03	0.09	0.05	5.31	1.14	0.11	1.74	0.53
2	32	63	8.43	600	0.03	0.01	0.02	0.10	0.03	5.14	1.19	0.11	1.87	0.42
3	50	58	8.52	601	0.03	0.01	0.01	0.09	0.03	5.23	1.16	0.11	1.61	0.38
4	98	61	8.11	637	0.01	0.01	$8.53x10^{-3}$	0.12	0.02	5.60	1.15	0.17	1.94	0.34
5	168	58	7.92	659	0.01	0.01	$3.75x10^{-3}$	0.12	0.01	5.85	1.16	0.28	1.84	0.29
6	240	63	7.93	678	0.01	0.02	$4.16x10^{-3}$	0.12	0.02	5.82	1.18	0.34	1.92	0.29
7	336	61	8.06	709	0.02	0.03	$1.12x10^{-2}$	0.13	0.03	5.84	1.21	0.43	1.97	0.33
8	456	60	7.95	692	0.01	0.02	$5.61x10^{-3}$	0.11	0.02	5.05	1.14	0.55	1.88	0.28
9	578	62	8.15	705	0.01	0.03	$3.33x10^{-3}$	0.14	0.02	5.38	1.18	0.56	1.25	0.30
10	695	61	8.36	707	$3.32x10^{-3}$	0.01	$2.38x10^{-3}$	0.12	0.02	5.71	1.19	0.73	2.01	0.29

Table A11 Temperature, pH, EC, elemental and ion concentrations measured for the 15 brine samples of B-07; SP describes the initial brine composition before reaction.

Sample Number	Time (h)	T (°C)	pH	EC (µS/cm)	Concentration (mmol/L)									
					Al	Ca	Fe	K	Mg	Na	HCO_3	SO_4^{2-}	Cl^-	SiO_2
SP	0	60	1.54	14910	$3.83x10^{-3}$	0.05	$9.65x10^{-4}$	0.08	0.18	4.62		31.76	1.41	0.67
1	9	63	2.39	6590	0.20	16.37	0.13	0.17	3.40	5.17		25.89	1.40	0.97
2	21	62	2.81	5220	0.21	15.52	0.12	0.17	4.49	4.97		23.79	1.80	1.01
3	31	63	2.92	5270	0.21	15.23	0.11	0.25	4.98	5.44		22.17	1.62	1.11
4	43	60	3.64	4830	0.14	14.75	0.08	0.18	4.94	5.16		21.41	1.58	1.09
5	68	63	4.41	4650	0.04	13.70	0.04	0.18	4.99	5.02		23.80	1.78	1.09
6	92	58	5.06	4220	0.02	14.32	0.02	0.23	5.17	5.30		20.16	1.52	1.10
7	140	59	5.84	3970	0.01	13.26	0.01	0.23	4.78	5.02		20.09	1.54	1.08
8	188	61	6.00	3580	0.01	13.57	0.01	0.18	5.06	4.87		19.83	1.56	1.09
9	261	60	5.79	3068	0.01	13.99	0.01	0.19	5.19	4.94		20.16	1.62	1.09
10	333	62	5.71	3410	$4.14x10^{-3}$	12.78	$4.48x10^{-3}$	0.21	4.87	4.93		21.13	1.77	1.06
11	409	61	5.80	2830	$3.07x10^{-3}$	12.85	$2.08x10^{-3}$	0.19	4.92	4.89		19.80	1.81	1.04
12	479	59	5.84	2250	$1.92x10^{-3}$	13.08	$2.19x10^{-3}$	0.21	5.04	4.85		21.04	1.78	1.04
13	551	58	6.02	2160	$2.53x10^{-3}$	12.8	$2.38x10^{-3}$	0.25	4.86	5.17		24.94	1.87	1.04
14	623	62	5.99	2010	$3.42x10^{-3}$	12.81	$1.57x10^{-3}$	0.23	4.82	4.79		19.62	1.63	1.00
15	695	59	6.00	1890	$2.74x10^{-3}$	12.23	$2.19x10^{-3}$	0.24	4.67	4.73		18.89	1.90	0.97

Table A12 Temperature, pH, EC, elemental and ion concentrations measured for the 15 brine samples of B-08; SP describes the initial brine composition before reaction.

Sample Number	Time (h)	T (°C)	pH	EC (µS/cm)	Concentration (mmol/L)									
					Al	Ca	Fe	K	Mg	Na	HCO_3	SO_4^{2-}	Cl^-	SiO_2
SP	0	60	1.54	14910	3.83×10^{-3}	0.05	9.65×10^{-4}	0.08	0.18	4.62		31.76	1.41	0.67
1	9	63	1.68	12970	0.54	1.02	0.13	0.25	0.64	5.16		33.33	1.48	1.33
2	21	62	1.62	12260	1.09	1.05	0.30	0.39	1.04	5.12		33.89	1.81	2.12
3	31	63	1.62	12650	1.46	1.08	0.40	0.48	1.34	5.61		33.48	1.77	2.71
4	43	60	1.65	12560	1.70	1.05	0.47	0.47	1.45	5.31		33.02	1.65	3.03
5	68	63	1.62	12120	2.07	1.01	0.58	0.52	1.74	5.05		37.76	1.88	3.61
6	92	58	1.62	12860	2.39	1.21	0.67	0.61	1.87	5.51		33.51	1.61	4.07
7	140	59	1.68	12660	2.43	1.27	0.71	0.72	1.94	5.16		32.95	1.59	4.47
8	188	61	1.71	12540	2.72	1.21	0.75	0.62	2.14	4.98		33.21	1.66	4.88
9	261	60	1.76	12270	3.19	1.22	0.80	0.64	2.30	4.93		35.20	1.69	5.23
10	333	62	1.72	12820	3.39	1.22	0.83	0.78	2.40	5.52		35.84	1.82	5.64
11	409	61	1.74	12370	3.52	1.14	0.87	0.77	2.51	5.23		33.77	1.88	5.85
12	479	59	1.81	11100	3.57	1.13	0.89	0.76	2.61	5.23		35.96	1.70	6.00
13	551	58	1.85	9830	3.68	1.13	0.87	0.83	2.60	5.56		36.72	1.72	6.18
14	623	62	1.92	8890	3.78	1.18	0.86	0.78	2.66	5.19		32.14	1.60	6.20
15	695	59	1.84	8660	3.80	1.20	0.90	0.81	2.68	5.44		33.61	1.76	6.27

Table A13 Temperature, pH, EC, elemental and ion concentrations measured for the 15 brine samples of B-09; SP describes the initial brine composition before reaction.

Sample Number	Time (h)	T (°C)	pH	EC (µS/cm)	Concentration (mmol/L)									
					Al	Ca	Fe	K	Mg	Na	HCO_3	SO_4^{2-}	Cl^-	SiO_2
SP	0	60	1.54	14910	$3.83x10^{-3}$	0.05	$9.65x10^{-4}$	0.08	0.18	4.62		31.76	1.41	0.67
1	9	63	1.62	13180	0.28	0.14	0.05	0.27	0.21	5.01		35.99	1.51	0.94
2	21	62	1.63	13150	0.36	0.13	0.08	0.28	0.21	4.80		33.86	1.55	1.11
3	31	63	1.53	13150	0.44	0.14	0.10	0.36	0.22	5.19		27.77	1.61	1.30
4	43	60	1.59	13900	0.47	0.14	0.12	0.39	0.22	5.11		33.71	1.71	1.39
5	68	63	1.53	14070	0.54	0.13	0.15	0.41	0.22	4.86		40.00	1.80	1.57
6	92	58	1.53	14720	0.59	0.13	0.17	0.44	0.22	5.06		33.56	1.56	1.69
7	140	59	1.57	14410	0.65	0.14	0.20	0.50	0.22	4.98		34.17	1.51	1.87
8	188	61	1.57	14670	0.71	0.13	0.21	0.50	0.23	4.70		33.62	1.49	2.04
9	261	60	1.61	14760	0.78	0.15	0.23	0.57	0.22	4.71		35.40	1.80	2.27
10	333	62	1.59	15390	0.87	0.12	0.24	0.68	0.21	4.81		37.23	1.93	2.46
11	409	61	1.60	14900	0.96	0.14	0.26	0.71	0.22	4.64		34.22	1.73	2.67
12	479	59	1.57	13955	1.03	0.14	0.27	0.75	0.23	4.74		36.81	1.72	2.86
13	551	58	1.60	13010	1.11	0.13	0.27	0.84	0.22	4.98		37.53	1.75	3.01
14	623	62	1.62	12080	1.10	0.15	0.27	0.81	0.22	4.66		33.13	1.48	3.18
15	695	59	1.55	11880	1.16	0.14	0.27	0.87	0.22	4.78		34.05	1.60	3.20

Table A14 **Temperature, pH, EC, elemental and ion concentrations measured for the 15 brine samples of B-10; SP describes the initial brine composition before reaction; the IC measurement of sample 13 is missing because it was inconclusive.**

Sample Number	Time (h)	T (°C)	pH	EC (µS/cm)	Concentration (mmol/L)									
					Al	Ca	Fe	K	Mg	Na	HCO_3	SO_4^{2-}	Cl^-	SiO_2
SP	0	60	1.54	14910	$3.83x10^{-3}$	0.05	$9.65x10^{-4}$	0.08	0.18	4.62		31.76	1.41	0.67
1	9	63	1.79	11380	1.67	2.37	1.63	0.12	1.04	5.05		34.78	1.48	2.09
2	21	62	1.86	9560	3.65	2.34	3.35	0.12	1.98	4.84		33.63	1.58	3.57
3	31	63	1.86	9840	4.00	2.30	3.85	0.15	2.35	4.94		32.87	1.63	4.18
4	43	60	1.91	9890	4.20	2.24	4.27	0.21	2.50	5.06		32.77	1.57	4.49
5	68	63	1.90	9020	4.23	2.28	4.58	0.15	2.72	4.99		33.01	1.75	4.95
6	92	58	1.91	9830	4.96	2.56	4.99	0.00	2.86	5.15		33.97	1.53	5.22
7	140	59	1.97	9950	4.84	2.40	4.94	0.15	2.87	4.98		33.88	1.51	5.32
8	188	61	2.00	9710	4.84	2.47	4.97	0.17	3.09	4.79		33.45	1.94	5.48
9	261	60	2.03	9990	5.31	2.50	4.86	0.14	3.00	4.87		35.69	1.56	5.50
10	333	62	2.02	10360	5.26	2.33	4.99	0.19	3.07	5.02		36.87	1.78	5.47
11	409	61	2.04	9980	5.11	2.35	5.02	0.16	3.11	4.88		33.92	1.65	5.60
12	479	59	2.11	8535	5.22	2.34	5.15	0.17	3.19	4.97		36.93	1.74	5.68
13	551	58	2.13	7090	5.12	2.29	4.82	0.21	3.16	5.15				5.64
14	623	62	2.15	6550	4.98	2.16	4.50	0.29	2.96	4.56		34.00	1.53	5.34
15	695	59	2.03	6370	5.08	2.10	4.69	0.19	2.94	4.79		36.59	1.46	5.38

Table A15 **Temperature, pH, EC, elemental and ion concentrations measured for the 15 brine samples of B-11; SP describes the initial brine composition before reaction.**

Sample Number	Time (h)	T (°C)	pH	EC (µS/cm)	Concentration (mmol/L)									
					Al	Ca	Fe	K	Mg	Na	HCO_3	SO_4^{2-}	Cl^-	SiO_2
SP	0	60	1.54	14910	$3.83x10^{-3}$	0.05	$9.65x10^{-4}$	0.08	0.18	4.62		31.76	1.41	0.67
1	9	63	1.69	11610	1.55	1.10	1.03	0.17	1.37	5.02		33.01	1.42	2.15
2	21	62	1.76	10370	2.51	1.19	1.81	0.17	2.04	4.72		33.59	1.66	3.24
3	31	63	1.75	10960	2.91	1.26	2.12	0.29	2.47	5.19		32.65	1.61	3.95
4	43	60	1.80	10850	3.06	1.27	2.41	0.24	2.66	5.13		32.64	1.68	4.22
5	68	63	1.80	10760	3.50	1.34	2.63	0.24	2.89	5.14		37.03	1.71	4.72
6	92	58	1.80	10970	3.61	1.50	2.68	0.22	3.23	4.38		33.99	1.55	4.88
7	140	59	1.86	11090	3.77	1.56	2.83	0.35	3.25	4.58		33.78	1.52	4.85
8	188	61	1.89	10940	4.37	1.55	2.81	0.27	3.07	4.82		33.91	1.63	5.27
9	261	60	1.85	10940	4.25	1.62	2.87	0.24	3.27	4.95		34.98	1.68	5.45
10	333	62	1.86	11300	4.34	1.55	3.07	0.32	3.16	5.16		36.76	1.94	5.45
11	409	61	1.91	10940	4.49	1.51	3.00	0.30	3.35	4.95		33.84	1.69	5.54
12	479	59	1.95	9560	4.71	1.57	3.08	0.31	3.30	5.14		37.74	1.85	5.61
13	551	58	1.96	8180	4.97	1.55	2.87	0.35	3.29	5.29		37.82	1.78	5.52
14	623	62	2.00	7180	4.94	1.57	2.84	0.35	3.34	4.90		33.66	1.72	5.48
15	695	59	1.93	6970	5.06	1.54	2.97	0.37	3.30	5.20		32.21	1.33	5.50

Table A16 **Temperature, pH, EC, elemental and ion concentrations measured for the 15 brine samples of B-12; SP describes the initial brine composition before reaction.**

Sample Number	Time (h)	T (°C)	pH	EC (µS/cm)	Concentration (mmol/L)									
					Al	Ca	Fe	K	Mg	Na	HCO_3	SO_4^{2-}	Cl^-	SiO_2
SP	0	60	1.54	14910	$3.83x10^{-3}$	0.05	$9.65x10^{-4}$	0.08	0.18	4.62		31.76	1.41	0.67
1	9	63	1.81	10630	1.21	0.99	2.78	0.47	1.03	5.75		33.90	1.45	1.63
2	21	62	1.85	9660	2.90	1.07	4.46	0.33	1.84	6.51		33.86	1.61	2.90
3	31	63	1.82	10250	2.94	1.09	4.78	0.46	2.16	7.21		32.92	1.51	3.47
4	43	60	1.90	10170	2.95	1.06	5.06	0.42	2.25	7.06		32.46	1.52	3.70
5	68	63	1.83	9960	3.35	1.03	5.03	0.48	2.30	7.11		30.85	1.43	4.02
6	92	58	1.82	10570	3.52	1.27	5.46	0.38	2.75	6.29		31.96	1.45	4.45
7	140	59	1.90	10780	3.47	1.22	5.33	0.37	2.61	5.96		33.45	1.89	4.52
8	188	61	1.94	10680	3.92	1.17	5.13	0.46	2.39	6.36		33.24	1.56	4.58
9	261	60	1.95	10760	3.95	1.19	5.22	0.43	2.52	6.57		34.89	1.62	4.91
10	333	62	1.92	10920	4.16	1.17	5.76	0.52	2.48	6.85		35.94	1.86	5.18
11	409	61	1.96	10790	4.25	1.08	5.73	0.52	2.57	6.62		35.16	1.72	5.28
12	479	59	1.99	9415	4.14	1.05	5.82	0.52	2.55	6.62		35.31	1.70	5.31
13	551	58	2.01	8040	4.21	1.01	5.44	0.54	2.50	6.84		36.19	1.87	5.39
14	623	62	2.07	7380	4.30	1.04	5.64	0.54	2.66	6.84		34.94	1.62	5.51
15	695	59	1.98	7130	4.51	0.96	5.53	0.53	2.38	6.55		31.03	1.37	5.24

Table A17 Temperature, pH, EC, elemental and ion concentrations measured for the 15 brine samples of B-13; SP describes the initial brine composition before reaction.

Sample Number	Time (h)	T (°C)	pH	EC (µS/cm)	Concentration (mmol/L)									
					Al	Ca	Fe	K	Mg	Na	HCO_3	SO_4^{2-}	Cl^-	SiO_2
SP	0	60	1.54	14910	$3.83x10^{-3}$	0.05	$9.65x10^{-4}$	0.08	0.18	4.62		31.76	1.41	0.67
1	9	63	2.02	8010	0.18	12.16	0.15	0.17	2.77	4.99		29.15	1.67	0.94
2	21	62	2.24	6940	0.28	14.75	0.21	0.15	3.54	4.76		27.63	1.66	1.10
3	31	63	2.31	6960	0.33	14.71	0.22	0.19	3.92	5.19		26.44	1.43	1.23
4	43	60	2.44	6760	0.36	14.74	0.24	0.21	4.13	5.12		26.60	1.58	1.27
5	68	63	2.53	6370	0.37	14.54	0.22	0.17	4.20	5.14		24.04	1.78	1.34
6	92	58	2.67	6380	0.33	13.86	0.21	0.15	4.52	4.76		20.57	1.34	1.27
7	140	59	2.86	6240	0.32	13.87	0.18	0.12	4.90	4.18		22.92	1.53	1.35
8	188	61	2.99	5850	0.34	13.62	0.16	0.17	4.66	4.67		21.95	1.68	1.37
9	261	60	3.13	6150	0.33	13.47	0.15	0.15	4.72	5.03		22.34	1.63	1.40
10	333	62	3.21	6280	0.29	13.65	0.12	0.17	4.93	4.47		23.83	2.12	1.48
11	409	61	3.40	5670	0.27	12.82	0.10	0.19	4.81	4.80		21.25	1.76	1.36
12	479	59	3.51	4955	0.23	12.12	0.08	0.19	4.68	4.71		23.75	1.77	1.30
13	551	58	3.55	4240	0.23	12.85	0.07	0.22	4.98	5.11		21.65	1.85	1.41
14	623	62	3.70	4350	0.19	12.69	0.06	0.20	4.96	4.93		20.52	1.58	1.35
15	695	59	3.73	4290	0.17	11.76	0.05	0.20	4.59	4.83		18.16	1.38	1.29

Table A18 Temperature, pH, EC, elemental and ion concentrations measured for the 14 brine samples of B-14; SP describes the initial brine composition before reaction.

Sample Number	Time (h)	T (°C)	pH	EC (µS/cm)	Concentration (mmol/L)									
					Al	Ca	Fe	K	Mg	Na	HCO_3	SO_4^{2-}	Cl^-	SiO_2
SP	0	60	1.54	14910	$3.83x10^{-3}$	0.05	$9.65x10^{-4}$	0.08	0.18	4.62		31.76	1.41	0.67
1	9	63	1.56	12970	0.30	0.96	0.07	0.14	0.58	4.97		32.94	1.94	1.11
2	21	62	1.59	12320	0.73	0.99	0.20	0.20	0.93	4.66		32.09	1.57	1.66
3	31	63	1.60	12920	0.97	1.01	0.26	0.32	1.15	5.04		31.33	1.54	2.04
4	43	60	1.64	12810	1.28	1.03	0.35	0.33	1.36	5.19		33.49	1.72	2.46
5	68	63	1.60	12740	1.70	1.03	0.45	0.40	1.60	5.29		32.75	1.90	3.10
6	92	58	1.62	13250	1.65	1.22	0.52	0.46	1.87	5.02		30.06	1.51	3.05
7	140	59	1.67	13220	2.22	1.15	0.61	0.49	1.93	5.22		33.74	1.70	4.03
8	188	61	1.69	12730	2.54	1.21	0.64	0.49	2.12	4.91		33.85	1.68	4.48
9	261	60	1.70	13390	2.67	1.18	0.70	0.57	2.22	5.21		35.00	1.70	5.04
10	333	62	1.67	13680	3.16	1.19	0.77	0.62	2.37	5.17		35.17	1.94	5.43
11	409	61	1.75	12980	3.23	1.12	0.76	0.63	2.45	5.03		35.86	1.75	5.60
12	479	59	1.77	11720	3.54	1.17	0.79	0.66	2.58	5.17		35.20	1.72	5.85
13	551	58	1.67	10460	3.70	1.19	0.80	0.74	2.74	5.83		34.80	1.81	6.42
14	623	62	1.90	9180	3.72	1.16	0.79	0.65	2.51	5.19		34.63	1.92	6.11
15	695	59	1.73	8970	3.88	1.14	0.81	0.74	2.65	5.49		32.03	1.86	6.23

Table A19 Temperature, pH, EC, elemental and ion concentrations measured for the 15 brine samples of B-15; SP describes the initial brine composition before reaction.

Sample Number	Time (h)	T (°C)	pH	EC (µS/cm)	Concentration (mmol/L)									
					Al	Ca	Fe	K	Mg	Na	HCO_3	SO_4^{2-}	Cl^-	SiO_2
SP	0	60	1.54	14910	$3.83x10^{-3}$	0.05	$9.65x10^{-4}$	0.08	0.18	4.62		31.76	1.41	0.67
1	9	63	1.53	13240	0.03	0.11	0.02	0.12	0.20	4.93		33.20	1.57	0.77
2	21	62	1.56	12850	0.05	0.12	0.03	0.10	0.20	4.76		28.86	1.37	0.84
3	31	63	1.53	13890	0.06	0.12	0.04	0.14	0.21	5.19		32.90	1.51	0.91
4	43	60	1.57	14080	0.08	0.12	0.05	0.16	0.21	5.20		33.30	1.63	0.95
5	68	63	1.50	14040	0.11	0.12	0.07	0.17	0.20	5.02		37.90	1.86	1.00
6	92	58	1.50	15030	0.12	0.11	0.09	0.17	0.20	4.61		30.80	1.41	1.04
7	140	59	1.56	15220	0.16	0.12	0.10	0.19	0.20	4.86		33.52	1.49	1.18
8	188	61	1.56	15160	0.19	0.11	0.11	0.24	0.20	4.44		33.91	1.50	1.22
9	261	60	1.50	15230	0.27	0.11	0.14	0.30	0.21	4.94		35.48	1.81	1.48
10	333	62	1.47	15780	0.34	0.11	0.15	0.36	0.21	4.93		36.68	1.76	1.66
11	409	61	1.54	15450	0.39	0.12	0.15	0.41	0.20	4.60		35.36	1.94	1.76
12	479	59	1.52	15430	0.47	0.13	0.17	0.46	0.21	4.72		36.46	1.93	2.01
13	551	58	1.56	14410	0.51	0.13	0.16	0.59	0.20	4.95		35.34	1.70	2.10
14	623	62	1.65	12880	0.53	0.13	0.17	0.63	0.20	4.74		35.02	1.94	2.18
15	695	59	1.61	12500	0.58	0.12	0.18	0.73	0.19	4.85		32.78	1.82	2.25

Table A20 **Temperature, pH, EC, elemental and ion concentrations measured for the 15 brine samples of B-16; SP describes the initial brine composition before reaction; no ICP data is available for sample 1 due to a pump malfunction.**

Sample Number	Time (h)	T (°C)	pH	EC (µS/cm)	Concentration (mmol/L)									
					Al	Ca	Fe	K	Mg	Na	HCO_3	SO_4^{2-}	Cl^-	SiO_2
SP	0	60	1.54	14910	$3.83x10^{-3}$	0.05	$9.65x10^{-4}$	0.08	0.18	4.62		31.76	1.41	0.67
1	9	63	1.65	11600								32.90	1.60	
2	21	62	1.74	10230	2.47	2.14	2.51	0.10	1.50	4.85		30.27	1.41	2.72
3	31	63	1.79	10260	3.30	2.22	3.25	0.19	1.91	5.19		31.06	1.48	3.34
4	43	60	1.86	10270	3.80	2.25	3.63	0.13	2.15	5.14		31.70	1.57	3.63
5	68	63	1.86	9930	3.88	2.25	4.10	0.13	2.42	5.05		36.40	1.76	4.13
6	92	58	1.89	10050	4.41	2.71	4.74	0.13	2.97	4.78		30.92	1.40	4.77
7	140	59	1.95	10150	4.61	2.53	4.96	0.13	2.94	5.03		33.50	1.45	4.86
8	188	61	1.98	10030	4.99	2.42	4.74	0.16	2.86	4.59		33.79	1.53	4.84
9	261	60	1.97	10470	4.81	2.42	5.13	0.14	3.08	4.98		34.80	1.65	5.29
10	333	62	1.96	10500	4.91	2.41	5.13	0.14	3.10	4.87		35.36	1.90	5.30
11	409	61	2.03	10180	5.09	2.28	4.88	0.12	3.07	4.68		34.99	1.77	5.25
12	479	59	2.02	8830	5.07	2.25	4.98	0.14	3.10	4.57		37.46	1.83	5.26
13	551	58	1.96	7480	5.08	2.34	4.91	0.17	3.11	5.06		34.98	1.92	5.53
14	623	62	2.12	6540	5.22	2.26	4.73	0.14	3.06	4.76		33.67	1.54	5.34
15	695	59	2.02	6350	5.30	2.15	4.82	0.18	3.03	5.01		31.86	1.46	5.40

Table A21 Temperature, pH, EC, elemental and ion concentrations measured for the 15 brine samples of B-17; SP describes the initial brine composition before reaction.

Sample Number	Time (h)	T (°C)	pH	EC (µS/cm)	Concentration (mmol/L)									
					Al	Ca	Fe	K	Mg	Na	HCO_3	SO_4^{2-}	Cl^-	SiO_2
SP	0	60	1.54	14910	$3.83Ex10^{-3}$	0.05	$9.65x10^{-4}$	0.08	0.18	4.62		31.76	1.41	0.67
1	9	63	1.63	11740	1.27	0.99	0.89	0.14	1.21	5.08		33.43	1.57	1.90
2	21	62	1.70	10790	2.21	1.17	1.63	0.17	1.98	5.22		32.64	1.64	3.01
3	31	63	1.72	10750	2.62	1.13	1.95	0.20	2.28	5.32		32.80	1.53	3.49
4	43	60	1.78	10960	2.64	1.19	2.11	0.23	2.49	5.20		33.58	1.69	3.85
5	68	63	1.76	10880	3.16	1.25	2.43	0.23	2.72	5.26		35.53	1.84	4.38
6	92	58	1.76	11320	3.61	1.45	2.51	0.22	2.98	5.08		31.32	1.53	4.81
7	140	59	1.83	11370	3.87	1.48	2.83	0.21	3.03	5.04		32.37	1.46	5.02
8	188	61	1.86	10840	4.11	1.54	2.88	0.24	3.11	4.84		33.03	1.47	5.18
9	261	60	1.88	11350	3.98	1.51	2.94	0.25	3.19	5.10		34.94	1.80	5.43
10	333	62	1.84	11700	4.40	1.56	3.02	0.26	3.31	5.11		34.71	1.73	5.62
11	409	61	1.95	10760	4.63	1.46	2.85	0.25	3.18	4.87		35.32	1.86	5.39
12	479	59	1.94	9550	4.59	1.54	3.04	0.26	3.37	4.87		34.71	1.81	5.58
13	551	58	1.88	8340	4.60	1.56	2.97	0.29	3.33	5.32		36.17	1.88	5.76
14	623	62	2.05	7250	4.65	1.55	2.90	0.27	3.37	5.03		33.68	1.70	5.61
15	695	59	1.93	7090	4.73	1.54	2.96	0.30	3.33	5.34		32.45	1.48	5.68

Table A22 Temperature, pH, EC, elemental and ion concentrations measured for the 15 brine samples of B-18; SP describes the initial brine composition before reaction.

Sample Number	Time (h)	T (°C)	pH	EC (µS/cm)	Concentration (mmol/L)									
					Al	Ca	Fe	K	Mg	Na	HCO_3	SO_4^{2-}	Cl^-	SiO_2
SP	0	60	1.54	14910	$3.83x10^{-3}$	0.05	$9.65x10^{-4}$	0.08	0.18	4.62		31.76	1.41	0.67
1	9	63	1.72	10630	1.19	1.03	3.34	0.27	1.26	6.97		33.65	1.57	1.71
2	21	62	1.80	9830	2.17	1.14	4.25	0.27	1.81	6.84		32.58	1.57	2.53
3	31	63	1.84	10280	2.57	1.14	4.62	0.33	2.07	7.32		31.22	1.46	2.98
4	43	60	1.88	10170	2.79	1.12	4.65	0.39	2.18	7.07		34.42	1.65	3.15
5	68	63	1.81	10170	2.96	1.12	4.78	0.37	2.28	7.07		36.75	2.06	3.63
6	92	58	1.87	10550	2.77	1.26	4.88	0.36	2.46	6.68		31.77	1.48	3.73
7	140	59	1.87	11130	3.44	1.30	5.17	0.39	2.46	6.89		33.58	1.93	4.28
8	188	61	1.87	10750	3.24	1.22	4.90	0.51	2.39	6.41		32.40	1.47	4.31
9	261	60	1.92	11230	3.68	1.22	5.08	0.51	2.45	6.86		34.88	1.63	4.77
10	333	62	1.90	11460	3.96	1.19	5.26	0.47	2.50	6.80		38.00	1.78	5.05
11	409	61	2.01	10890	3.90	1.10	5.15	0.48	2.56	6.67		35.50	1.77	5.24
12	479	59	1.97	9725	4.04	1.16	5.42	0.47	2.60	6.50		35.04	1.88	5.33
13	551	58	1.91	8560	4.02	1.10	5.08	0.48	2.55	6.90		34.85	1.79	5.43
14	623	62	2.08	7490	4.22	1.16	5.21	0.48	2.68	6.93		32.05	1.77	5.53
15	695	59	1.92	7360	4.28	1.10	5.20	0.66	2.57	7.10		33.15	1.85	5.52

Table A23 Temperature, pH, EC, elemental and ion concentrations measured for the 15 brine samples of B-19; SP describes the initial brine composition before reaction.

Sample Number	Time (h)	T (°C)	pH	EC (µS/cm)	Concentration (mmol/L)									
					Al	Ca	Fe	K	Mg	Na	HCO_3	SO_4^{2-}	Cl^-	SiO_2
SP	0	60	1.54	14910	$3.83x10^{-3}$	0.05	$9.65x10^{-4}$	0.08	0.18	4.62		31.76	1.41	0.67
1	9	63	1.68	11560	0.08	3.90	0.07	0.22	1.05	4.96		32.76	1.61	0.82
2	21	62	1.76	10390	0.18	6.45	0.15	0.23	1.71	5.32		31.51	1.55	0.98
3	31	63	1.79	10700	0.22	7.68	0.19	0.25	1.93	5.23		28.76	1.70	1.07
4	43	60	1.86	10290	0.26	8.59	0.22	0.27	2.18	5.21		31.79	1.63	1.15
5	68	63	1.89	9780	0.31	10.11	0.25	0.23	2.53	5.09		29.62	1.75	1.23
6	92	58	1.95	9740	0.31	11.49	0.28	0.22	2.94	4.73		29.00	1.54	1.30
7	140	59	2.07	9420	0.38	12.38	0.31	0.24	3.02	4.79		30.25	1.61	1.41
8	188	61	2.15	7770	0.42	13.22	0.31	0.24	3.23	4.76		28.56	1.61	1.49
9	261	60	2.24	8840	0.44	13.40	0.32	0.31	3.58	4.91		29.42	1.62	1.59
10	333	62	2.29	8590	0.46	14.44	0.32	0.29	3.85	4.95		31.32	2.14	1.66
11	409	61	2.46	7760	0.44	13.63	0.29	0.27	3.85	4.78		28.38	1.94	1.61
12	479	59	2.49	6390	0.47	14.23	0.28	0.31	4.04	5.28		31.36	2.17	1.73
13	551	58	2.50	5020	0.47	14.48	0.27	0.30	4.21	5.22		28.77	1.80	1.76
14	623	62	2.68	4390	0.42	13.45	0.23	0.29	3.98	4.83		29.23	1.45	1.65
15	695	59	2.64	4010	0.41	13.18	0.23	0.32	4.03	5.01		29.62	1.70	1.67

Table A24 **Temperature, pH, EC, elemental and ion concentrations measured for the 15 brine samples of B-20; SP describes the initial brine composition before reaction; the IC measurement of sample 14 is missing because it was inconclusive.**

Sample Number	Time (h)	T (°C)	pH	EC (µS/cm)	Concentration (mmol/L)									
					Al	Ca	Fe	K	Mg	Na	HCO_3	SO_4^{2-}	Cl^-	SiO_2
SP	0	60	1.54	14910	$3.83x10^{-3}$	0.05	$9.65x10^{-4}$	0.08	0.18	4.62		31.76	1.41	0.67
1	9	63	1.59	12950	0.15	0.64	0.03	0.10	0.43	4.91		33.35	1.71	0.85
2	21	62	1.58	12360	0.39	0.96	0.09	0.26	0.75	5.39		33.33	1.74	1.15
3	31	63	1.58	12700	0.55	1.04	0.14	0.21	0.95	5.30		33.18	1.64	1.32
4	43	60	1.65	12910	0.69	1.13	0.18	0.22	1.08	4.95		34.99	1.91	1.42
5	68	63	1.60	13040	1.01	1.34	0.27	0.24	1.39	5.18		35.03	1.84	1.81
6	92	58	1.58	13350	1.16	1.68	0.35	0.28	1.83	4.82		31.71	1.62	2.09
7	140	59	1.65	13760	1.43	1.62	0.39	0.31	1.79	4.65		33.57	1.73	2.21
8	188	61	1.68	13040	1.85	1.80	0.51	0.35	2.23	5.02		33.64	1.95	2.73
9	261	60	1.68	13690	2.23	1.84	0.61	0.45	2.51	5.30		35.62	1.80	3.18
10	333	62	1.66	13720	2.54	1.86	0.69	0.49	2.73	5.12		34.44	1.86	3.50
11	409	61	1.80	12640	2.67	1.72	0.71	0.46	2.86	5.02		36.44	2.03	3.71
12	479	59	1.72	11525	3.08	1.71	0.74	0.53	3.00	5.29		35.36	1.92	4.04
13	551	58	1.72	10410	3.09	1.78	0.81	0.59	3.21	5.16		33.43	1.76	4.27
14	623	62	1.86	9040	3.23	1.84	0.84	0.54	3.31	5.21				4.45
15	695	59	1.79	8630	3.41	1.75	0.86	0.59	3.40	5.20		33.59	1.68	4.49

Table A25 **Temperature, pH, EC, elemental and ion concentrations measured for the 15 brine samples of B-21; SP describes the initial brine composition before reaction; the SO_4^{2-} measurement for sample 3 is missing because because it was inconclusive.**

Sample Number	Time (h)	T (°C)	pH	EC (µS/cm)	Concentration (mmol/L)									
					Al	Ca	Fe	K	Mg	Na	HCO_3	SO_4^{2-}	Cl^-	SiO_2
SP	0	60	1.54	14910	$3.83x10^{-3}$	0.05	$9.65x10^{-4}$	0.08	0.18	4.62		31.76	1.41	0.67
1	9	63	1.59	13000	0.01	0.10	0.00	0.08	0.19	4.60		33.55	1.56	0.72
2	21	62	1.56	12770	0.03	0.15	0.01	0.12	0.21	5.13		31.70	1.45	0.80
3	31	63	1.54	13910	0.03	0.13	0.01	0.10	0.18	4.45			1.69	0.72
4	43	60	1.61	13530	0.04	0.17	0.02	0.13	0.21	5.02		33.74	1.53	0.84
5	68	63	1.52	14180	0.05	0.19	0.02	0.15	0.20	5.00		37.08	1.71	0.88
6	92	58	1.50	14690	0.06	0.20	0.04	0.13	0.23	4.37		31.63	1.49	0.95
7	140	59	1.55	14930	0.09	0.20	0.04	0.15	0.21	4.60		33.65	1.46	0.95
8	188	61	1.57	15300	0.11	0.22	0.05	0.15	0.21	4.56		34.57	1.61	1.00
9	261	60	1.53	15900	0.14	0.24	0.06	0.19	0.20	4.61		35.21	1.85	1.09
10	333	62	1.46	15500	0.19	0.25	0.07	0.26	0.21	4.78		34.64	1.86	1.23
11	409	61	1.66	14840	0.23	0.24	0.08	0.30	0.21	4.68		35.34	1.85	1.31
12	479	59	1.55	14650	0.27	0.25	0.08	0.30	0.21	5.01		35.35	1.78	1.41
13	551	58	1.46	14460	0.31	0.25	0.09	0.36	0.22	4.99		33.71	1.93	1.50
14	623	62	1.66	12810	0.33	0.26	0.10	0.35	0.21	4.81		34.08	1.48	1.58
15	695	59	1.52	12550	0.35	0.25	0.11	0.39	0.21	4.87		34.07	1.85	1.65

Table A26 Temperature, pH, EC, elemental and ion concentrations measured for the 15 brine samples of B-22; SP describes the initial brine composition before reaction.

Sample Number	Time (h)	T (°C)	pH	EC (µS/cm)	Concentration (mmol/L)									
					Al	Ca	Fe	K	Mg	Na	HCO_3	SO_4^{2-}	Cl^-	SiO_2
SP	0	60	1.54	14910	$3.83x10^{-3}$	0.05	$9.65x10^{-4}$	0.08	0.18	4.62		31.76	1.41	0.67
1	9	63	1.63	12390	0.43	0.83	0.41	0.12	0.45	5.07		33.43	1.56	1.04
2	21	62	1.65	11340	1.02	1.24	1.01	0.15	0.81	5.36		32.56	1.52	1.53
3	31	63	1.67	12080	1.36	1.44	1.38	0.13	1.00	5.18		32.29	1.44	1.80
4	43	60	1.72	10950	1.58	1.48	1.61	0.13	1.12	4.86		33.16	1.59	1.89
5	68	63	1.69	11650	2.15	1.87	2.14	0.15	1.42	5.04		34.03	1.84	2.34
6	92	58	1.71	11530	2.44	2.14	2.52	0.15	1.63	5.01		32.09	1.47	2.56
7	140	59	1.81	11490	2.80	2.45	3.03	0.15	1.94	4.67		33.93	1.58	2.90
8	188	61	1.85	11090	3.18	2.74	3.56	0.14	2.26	4.80		33.84	1.55	3.25
9	261	60	1.91	10940	3.68	2.88	4.05	0.16	2.58	4.94		34.75	1.72	3.57
10	333	62	1.91	11110	4.20	3.05	4.46	0.16	2.76	4.96		34.50	1.74	3.87
11	409	61	2.06	9910	4.21	3.27	4.91	0.16	3.09	5.07		36.30	1.65	4.16
12	479	59	2.03	8595	4.41	3.17	4.77	0.17	3.07	5.29		35.16	1.66	4.30
13	551	58	2.01	7280	4.33	3.30	4.99	0.18	3.20	5.24		31.65	1.92	4.49
14	623	62	2.17	6270	4.72	3.28	4.96	0.16	3.18	4.84		34.51	1.95	4.33
15	695	59	2.04	6040	4.82	3.06	4.99	0.18	3.13	4.92		34.58	1.71	4.30

Table A27 **Temperature, pH, EC, elemental and ion concentrations measured for the 15 brine samples of B-23; SP describes the initial brine composition before reaction; the IC measurement of sample 12 and the Cl^- measurement for sample 5 are missing because because they were inconclusive.**

Sample Number	Time (h)	T (°C)	pH	EC (µS/cm)	Concentration (mmol/L)									
					Al	Ca	Fe	K	Mg	Na	HCO_3	SO_4^{2-}	Cl^-	SiO_2
SP	0	60	1.54	14910	$3.83x10^{-3}$	0.05	$9.65x10^{-4}$	0.08	0.18	4.62		31.76	1.41	0.67
1	9	63	1.63	12370	0.41	0.59	0.25	0.13	0.56	4.92		33.49	1.58	1.06
2	21	62	1.64	11740	0.84	0.82	0.55	0.15	0.96	5.16		30.02	1.40	1.49
3	31	63	1.61	12190	1.13	0.94	0.77	0.16	1.17	5.16		32.67	1.52	1.81
4	43	60	1.70	12090	1.43	1.07	0.97	0.22	1.39	5.24		32.03	1.60	2.02
5	68	63	1.67	11960	1.87	1.26	1.31	0.19	1.75	5.07		31.70		2.45
6	92	58	1.67	11990	2.24	1.50	1.61	0.18	2.05	5.14		29.55	1.40	2.82
7	140	59	1.75	11800	2.71	1.68	1.93	0.23	2.45	4.74		33.80	1.58	3.23
8	188	61	1.82	11680	2.90	1.72	2.09	0.28	2.66	4.68		33.93	1.61	3.41
9	261	60	1.82	11920	3.45	1.85	2.60	0.23	3.13	5.05		35.34	1.73	3.99
10	333	62	1.82	11890	4.31	2.00	2.92	0.27	3.50	5.10		35.11	1.93	4.44
11	409	61	1.97	10680	4.31	1.92	3.02	0.25	3.74	4.88		36.03	1.94	4.53
12	479	59	1.96	9300	4.63	1.94	3.11	0.30	3.89	5.39				4.89
13	551	58	1.90	7920	4.57	2.21	3.47	0.31	4.53	5.83		30.89	1.49	5.44
14	623	62	2.06	6830	4.70	2.01	3.26	0.28	4.13	5.17		34.88	1.53	5.01
15	695	59	1.98	6540	4.90	1.96	3.27	0.27	4.14	5.12		35.20	1.55	5.04

Table A28 **Temperature, pH, EC, elemental and ion concentrations measured for the 15 brine samples of B-24; SP describes the initial brine composition before reaction; the IC measurement of sample 12 is missing because it was inconclusive.**

Sample Number	Time (h)	T (°C)	pH	EC (µS/cm)	Concentration (mmol/L)									
					Al	Ca	Fe	K	Mg	Na	HCO_3	SO_4^{2-}	Cl^-	SiO_2
SP	0	60	1.54	14910	$3.83x10^{-3}$	0.05	$9.65x10^{-4}$	0.08	0.18	4.62		31.76	1.41	0.67
1	9	63	1.84	9780	1.38	1.39	4.47	0.35	1.61	9.42		33.06	1.58	2.09
2	21	62	1.96	8460	2.18	1.69	6.24	0.45	2.50	10.05		32.60	1.61	3.12
3	31	63	2.02	8700	2.95	1.87	7.62	0.53	3.07	10.59		31.28	1.57	3.87
4	43	60	2.08	8520	2.92	1.70	7.55	0.45	2.86	8.99		32.93	1.54	3.70
5	68	63	2.08	8630	3.91	1.94	7.82	0.49	3.42	9.80		34.03	1.82	4.44
6	92	58	2.14	8360	4.00	1.94	8.00	0.44	3.31	8.99		32.48	1.57	4.41
7	140	59	2.21	8740	4.06	2.03	8.65	0.46	3.59	8.83		34.04	1.58	4.67
8	188	61	2.23	8450	4.15	2.08	8.55	0.45	3.79	8.84		34.18	1.53	4.86
9	261	60	2.27	8910	4.50	1.95	9.18	0.51	3.85	9.39		35.91	1.64	5.03
10	333	62	2.28	8980	4.42	2.05	9.39	0.52	4.04	9.18		38.42	2.14	5.12
11	409	61	2.35	8770	4.58	1.97	9.40	0.49	4.03	8.99		37.16	1.87	5.15
12	479	59	2.33	7600	4.61	1.92	9.66	0.51	4.03	9.67				5.23
13	551	58	2.26	6430	4.66	1.97	9.56	0.53	4.22	9.57		34.95	1.91	5.32
14	623	62	2.39	5660	5.01	1.89	9.04	0.47	3.94	9.03		35.77	1.66	5.01
15	695	59	2.26	5440	5.01	1.92	9.03	0.53	4.06	9.48		35.79	1.67	5.12

Table A29 **Temperature, pH, EC, elemental and ion concentrations measured for the ten brine samples of B-25; SP describes the initial brine composition before reaction.**

Sample Number	Time (h)	T (°C)	pH	EC (µS/cm)	Concentration (mmol/L)									
					Al	Ca	Fe	K	Mg	Na	HCO_3	SO_4^{2-}	Cl^-	SiO_2
SP	0	62	3.02	944	$1.52x10^{-3}$	0.02	$1.09x10^{-3}$	0.07	0.19	4.71		2.98	1.65	0.81
1	21	64	7.81	819	$6.17x10^{-3}$	0.87	$2.91x10^{-3}$	0.12	0.17	4.52		3.05	1.71	0.76
2	32	63	7.89	816	$2.85x10^{-3}$	0.87	$1.14x10^{-3}$	0.15	0.17	4.67		2.46	1.40	0.78
3	50	58	8.07	813	$2.23x10^{-3}$	0.83	$4.53x10^{-4}$	0.17	0.17	4.44		2.43	1.57	0.73
4	98	61	7.83	823	$3.32x10^{-3}$	0.92	$9.86x10^{-4}$	0.15	0.17	4.56		2.78	1.84	0.78
5	168	58	7.86	827	$3.14x10^{-3}$	0.88	$5.89x10^{-4}$	0.15	0.16	4.53		2.53	1.57	0.75
6	240	63	7.86	824	$3.17x10^{-3}$	0.89	$9.33x10^{-4}$	0.15	0.17	4.45		2.60	1.88	0.76
7	336	61	7.82	827	$1.15x10^{-3}$	0.86	$4.05x10^{-4}$	0.17	0.16	4.48		2.78	1.71	0.76
8	456	60	8.07	828	$1.19x10^{-3}$	0.86	$9.38x10^{-4}$	0.17	0.15	4.29		2.46	1.27	0.73
9	578	62	8.05	835	$1.01x10^{-3}$	0.80	$2.40x10^{-4}$	0.16	0.13	4.14		2.37	1.30	0.69
10	695	61	8.11	836	$4.87x10^{-4}$	0.87	0.00	0.17	0.14	4.79		2.78	1.78	0.75

Table A30 **Temperature, pH, EC, elemental and ion concentrations measured for the ten brine samples of B-26; SP describes the initial brine composition before reaction.**

Sample Number	Time (h)	T (°C)	pH	EC (µS/cm)	Concentration (mmol/L)									
					Al	Ca	Fe	K	Mg	Na	HCO_3	SO_4^{2-}	Cl^-	SiO_2
SP	0	62	3.02	944	$1.52x10^{-3}$	0.02	$1.09x10^{-3}$	0.07	0.19	4.71		2.98	1.65	0.81
1	21	64	4.14	786	$1.21x10^{-2}$	0.46	$4.88x10^{-3}$	0.16	0.27	4.84		3.18	1.90	0.94
2	32	63	4.38	794	$8.41x10^{-3}$	0.46	$4.16x10^{-3}$	0.15	0.26	4.80		2.58	1.39	0.93
3	50	58	4.58	787	$5.97x10^{-3}$	0.45	$3.91x10^{-3}$	0.17	0.25	4.69		2.55	1.46	0.91
4	98	61	4.89	792	$7.30x10^{-3}$	0.48	$3.71x10^{-3}$	0.21	0.26	4.67		2.85	1.67	0.98
5	168	58	4.69	788	$7.50x10^{-3}$	0.49	$4.32x10^{-3}$	0.17	0.27	4.61		2.67	1.71	1.03
6	240	63	4.36	808	$4.19x10^{-3}$	0.45	$2.36x10^{-3}$	0.17	0.24	4.56		2.94	1.94	1.01
7	336	61	4.32	803	$4.77x10^{-3}$	0.48	$1.93x10^{-3}$	0.20	0.25	4.69		2.89	1.84	1.05
8	456	60	4.79	812	$7.36x10^{-3}$	0.44	$1.47x10^{-2}$	0.18	0.24	4.44		2.56	1.40	1.01
9	578	62	4.55	817	$4.63x10^{-3}$	0.45	$1.73x10^{-3}$	0.19	0.25	4.56		2.59	1.36	1.06
10	695	61	4.69	814	$3.06x10^{-3}$	0.46	$9.08x10^{-4}$	0.20	0.24	4.72		2.86	1.71	1.04

Table A31 **Temperature, pH, EC, elemental and ion concentrations measured for the ten brine samples of B-27; SP describes the initial brine composition before reaction.**

Sample Number	Time (h)	T (°C)	pH	EC (µS/cm)	Concentration (mmol/L)									
					Al	Ca	Fe	K	Mg	Na	HCO_3	SO_4^{2-}	Cl^-	SiO_2
SP	0	62	3.02	944	$1.52x10^{-3}$	0.02	$1.09x10^{-3}$	0.07	0.19	4.71		2.98	1.65	0.81
1	21	64	3.31	831	0.08	0.06	0.03	0.20	0.18	4.46		3.14	1.73	0.89
2	32	63	3.36	829	0.09	0.07	0.03	0.21	0.19	4.81		2.56	1.32	0.95
3	50	58	3.42	818	0.09	0.06	0.03	0.22	0.19	4.70		2.55	1.32	0.96
4	98	61	3.46	825	0.10	0.07	0.04	0.21	0.19	4.53		2.87	1.86	1.01
5	168	58	3.36	830	0.10	0.08	0.04	0.24	0.19	4.38		2.63	1.86	1.02
6	240	63	3.39	829	0.09	0.07	0.04	0.27	0.19	4.75		2.91	1.81	1.05
7	336	61	3.49	821	0.10	0.08	0.04	0.27	0.19	4.57		2.84	1.70	1.07
8	456	60	3.49	833	0.08	0.07	0.03	0.23	0.18	4.32		2.51	1.24	1.03
9	578	62	3.53	833	0.09	0.07	0.03	0.24	0.17	4.30		2.49	1.30	1.02
10	695	61	3.48	818	0.09	0.07	0.03	0.24	0.19	4.73		2.89	1.79	1.09

Table A32 Temperature, pH, EC, elemental and ion concentrations measured for the ten brine samples of B-28; SP describes the initial brine composition before reaction.

Sample Number	Time (h)	T (°C)	pH	EC (µS/cm)	Concentration (mmol/L)									
					Al	Ca	Fe	K	Mg	Na	HCO_3	SO_4^{2-}	Cl^-	SiO_2
SP	0	62	3.02	944	$1.52x10^{-3}$	0.02	$1.09x10^{-3}$	0.07	0.19	4.71		2.98	1.65	0.81
1	21	64	7.22	794	$5.38x10^{-3}$	0.86	$8.93x10^{-4}$	0.10	0.16	4.60		3.17	1.76	0.77
2	32	63	7.17	803	$3.93x10^{-3}$	0.86	$1.11x10^{-3}$	0.13	0.15	4.56		2.52	1.32	0.74
3	50	58	7.58	809	$2.65x10^{-3}$	0.88	$6.34x10^{-4}$	0.12	0.15	4.77		2.59	1.34	0.75
4	98	61	7.66	810	$4.23x10^{-3}$	0.93	$4.33x10^{-4}$	0.12	0.13	4.50		2.85	1.83	0.75
5	168	58	7.56	813	$2.44x10^{-3}$	0.97	$1.38x10^{-3}$	0.13	0.12	4.56		2.70	1.69	0.77
6	240	63	7.65	820	$2.47x10^{-3}$	0.98	$3.11x10^{-4}$	0.17	0.10	4.67		2.91	1.80	0.76
7	336	61	7.53	815	$1.85x10^{-3}$	0.94	$6.36x10^{-4}$	0.14	0.11	4.52		2.91	1.94	0.75
8	456	60	7.61	831	$2.21x10^{-3}$	0.95	$2.90x10^{-4}$	0.16	0.09	4.54		2.50	1.25	0.76
9	578	62	7.71	829	$1.19x10^{-3}$	1.02	$2.47x10^{-4}$	0.18	0.09	4.73		2.56	1.31	0.77
10	695	61	7.78	823	$1.22x10^{-3}$	0.94	$4.17x10^{-6}$	0.16	0.08	4.68		2.89	1.83	0.73

Table A33 Temperature, pH, EC, elemental and ion concentrations measured for the ten brine samples of B-29; SP describes the initial brine composition before reaction.

Sample Number	Time (h)	T (°C)	pH	EC (µS/cm)	Concentration (mmol/L)									
					Al	Ca	Fe	K	Mg	Na	HCO_3	SO_4^{2-}	Cl^-	SiO_2
SP	0	62	3.02	944	$1.52x10^{-3}$	0.02	$1.09x10^{-3}$	0.07	0.19	4.71		2.98	1.65	0.81
1	21	64	4.21	760	$1.24x10^{-2}$	0.33	$2.69x10^{-3}$	0.14	0.19	4.49		3.17	1.79	0.92
2	32	63	4.56	771	$1.29x10^{-2}$	0.34	$2.57x10^{-3}$	0.15	0.21	5.07		2.54	1.32	1.04
3	50	58	4.91	762	$1.24x10^{-2}$	0.35	$2.76x10^{-3}$	0.15	0.21	4.88		2.65	1.40	1.03
4	98	61	4.75	779	$8.17x10^{-3}$	0.34	$1.41x10^{-3}$	0.16	0.21	4.59		2.87	1.79	1.05
5	168	58	4.69	783	$9.01x10^{-3}$	0.35	$1.24x10^{-3}$	0.16	0.20	4.40		2.74	1.70	1.08
6	240	63	4.65	784	$6.44x10^{-3}$	0.35	$9.95x10^{-4}$	0.16	0.20	4.50		2.88	1.78	1.09
7	336	61	4.68	782	$5.55x10^{-3}$	0.35	$4.87x10^{-4}$	0.17	0.21	4.54		2.94	1.73	1.13
8	456	60	4.78	792	$5.40x10^{-3}$	0.33	$4.21x10^{-4}$	0.17	0.19	4.19		2.41	1.21	1.06
9	578	62	4.93	785	$6.45x10^{-3}$	0.35	$9.25x10^{-4}$	0.20	0.21	4.52		2.56	1.31	1.11
10	695	61	4.76	794	$4.04x10^{-3}$	0.35	$2.52x10^{-4}$	0.25	0.20	4.77		2.86	1.84	1.12

Table A34 Temperature, pH, EC, elemental and ion concentrations measured for the ten brine samples of B-30; SP describes the initial brine composition before reaction.

Sample Number	Time (h)	T (°C)	pH	EC (µS/cm)	Concentration (mmol/L)									
					Al	Ca	Fe	K	Mg	Na	HCO_3	SO_4^{2-}	Cl^-	SiO_2
SP	0	62	3.02	944	$1.52x10^{-3}$	0.02	$1.09x10^{-3}$	0.07	0.19	4.71		2.98	1.65	0.81
1	21	64	6.07	821	$2.89x10^{-3}$	0.05	$1.40x10^{-3}$	0.16	0.05	5.55		3.28	1.91	0.73
2	32	63	6.49	847	$3.56x10^{-3}$	0.05	$1.23x10^{-3}$	0.19	0.06	6.31		2.57	1.35	0.77
3	50	58	7.04	847	$3.36x10^{-3}$	0.07	$7.88x10^{-4}$	0.17	0.07	6.21		2.68	1.89	0.74
4	98	61	6.88	863	$4.65x10^{-3}$	0.09	$2.86x10^{-3}$	0.20	0.10	6.16		3.03	1.91	0.61
5	168	58	6.68	909	$1.93x10^{-3}$	0.10	$9.25x10^{-4}$	0.20	0.12	6.06		2.87	1.76	0.52
6	240	63	6.8	883	$1.88x10^{-3}$	0.12	$1.31x10^{-3}$	0.21	0.13	6.33		3.19	1.81	0.49
7	336	61	6.93	906	$1.43x10^{-3}$	0.13	$7.69x10^{-4}$	0.23	0.14	6.17		3.19	1.73	0.44
8	456	60	5.86	930	$1.58x10^{-3}$	0.16	$1.05x10^{-3}$	0.25	0.19	6.23		3.02	1.31	0.45
9	578	62	5.82	944	$1.95x10^{-3}$	0.19	$6.48x10^{-4}$	0.26	0.22	6.42		3.08	1.27	0.48
10	695	61	5.4	967	$9.05x10^{-4}$	0.23	$1.54x10^{-4}$	0.29	0.25	6.78		3.22	1.85	0.50

Table A35 Temperature, pH, EC, elemental and ion concentrations measured for the 15 brine samples of B-31; SP describes the initial brine composition before reaction.

Sample Number	Time (h)	T (°C)	pH	EC (µS/cm)	Concentration (mmol/L)									
					Al	Ca	Fe	K	Mg	Na	HCO_3	SO_4^{2-}	Cl^-	SiO_2
SP	0	22.3	1.40	17120	$1.14x10^{-2}$	0.05	$6.05x10^{-3}$	0.07	0.17	4.45		31.45	1.41	0.72
1	8	22.8	1.87	9210	0.06	10.10	0.04	0.18	0.80	4.93		29.50	1.58	0.78
2	19	22.5	2.07	7140	0.07	13.12	0.05	0.16	1.61	5.01		26.56	1.41	0.78
3	28	22	2.30	5310	0.08	15.37	0.06	0.16	2.60	5.15		27.04	1.26	0.79
4	52	22.7	2.59	4430	0.08	17.04	0.06	0.16	3.55	5.01		26.09	1.70	0.81
5	77	22.2	3.08	3800	0.09	17.24	0.07	0.15	4.42	4.64		27.60	1.79	0.82
6	101	22.8	3.99	3420	0.05	18.49	0.07	0.21	5.26	4.31		21.89	1.78	0.86
7	141	22.3	4.80	3390	0.04	16.15	0.04	0.22	4.66	4.69		20.15	1.39	0.82
8	189	22.8	5.35	3350	0.03	16.12	0.03	0.22	4.70	4.68		21.31	1.38	0.82
9	263	22	5.31	3330	$7.28x10^{-3}$	15.70	$5.48x10^{-3}$	0.21	4.96	4.87		18.35	1.27	0.84
10	331	21.9	5.32	3260	$1.08x10^{-2}$	16.14	$4.86x10^{-3}$	0.23	5.06	4.77		20.51	1.70	0.86
11	433	21.6	5.08	3220	$6.64x10^{-3}$	15.32	$2.92x10^{-3}$	0.22	4.93	4.41		19.82	1.46	0.81
12	505	21.6	4.97	3210	$6.94x10^{-3}$	15.49	$3.05x10^{-3}$	0.22	5.11	4.53		21.86	1.69	0.83
13	581	23.2	5.34	3160	$9.74x10^{-3}$	14.95	$4.27x10^{-3}$	0.22	5.46	3.98		21.09	1.95	0.83
14	644	22.2	5.37	3160	$4.43x10^{-3}$	12.90	$1.90x10^{-3}$	0.25	4.54	4.77		19.75	1.79	0.77
15	695	22.6	5.34	3140	$1.12x10^{-2}$	13.12	$4.17x10^{-3}$	0.26	4.59	4.62		19.45	1.70	0.80

Table A36 Temperature, pH, EC, elemental and ion concentrations measured for the 15 brine samples of B-32; SP describes the initial brine composition before reaction.

Sample Number	Time (h)	T (°C)	pH	EC (µS/cm)	Concentration (mmol/L)									
					Al	Ca	Fe	K	Mg	Na	HCO_3	SO_4^{2-}	Cl^-	SiO_2
SP	0	22.3	1.40	17120	$1.14x10^{-2}$	0.05	$6.05x10^{-3}$	0.07	0.17	4.45		31.45	1.41	0.72
1	8	22.8	1.45	16100	0.08	0.66	0.01	0.16	0.31	4.15		31.91	1.68	0.72
2	19	22.5	1.43	15880	0.19	0.97	0.03	0.19	0.43	5.09		30.52	1.35	0.94
3	28	22	1.44	15810	0.22	1.00	0.04	0.18	0.43	5.03		33.94	1.52	1.00
4	52	22.7	1.44	15030	0.26	0.95	0.05	0.17	0.44	4.81		33.90	1.75	1.02
5	77	22.2	1.44	15390	0.32	1.02	0.07	0.22	0.49	4.77		36.91	1.79	1.14
6	101	22.8	1.44	15190	0.26	1.10	0.09	0.19	0.56	4.23		32.00	1.47	1.24
7	141	22.3	1.44	15500	0.42	0.98	0.10	0.23	0.55	4.71		30.46	1.52	1.25
8	189	22.8	1.43	16320	0.48	1.09	0.14	0.23	0.61	4.56		32.57	1.36	1.33
9	263	22	1.45	16390	0.63	1.07	0.18	0.26	0.70	4.97		30.38	1.61	1.60
10	331	21.9	1.47	16120	0.70	1.07	0.21	0.29	0.79	4.61		32.81	1.68	1.71
11	433	21.6	1.49	16100	0.80	1.10	0.26	0.35	0.87	4.63		29.09	1.68	1.85
12	505	21.6	1.49	16060	0.84	1.13	0.28	0.31	0.94	4.61		36.02	1.81	2.00
13	581	23.2	1.49	15490	0.87	1.12	0.31	0.31	1.04	4.59		34.41	1.78	2.13
14	644	22.2	1.49	15640	1.03	1.01	0.33	0.40	1.01	4.97		33.20	1.52	2.17
15	695	22.6	1.50	15410	1.04	1.01	0.34	0.41	1.01	4.65		33.80	1.51	2.16

Table A37 Temperature, pH, EC, elemental and ion concentrations measured for the 15 brine samples of B-33; SP describes the initial brine composition before reaction.

Sample Number	Time (h)	T (°C)	pH	EC (µS/cm)	Concentration (mmol/L)									
					Al	Ca	Fe	K	Mg	Na	HCO_3	SO_4^{2-}	Cl^-	SiO_2
SP	0	22.3	1.40	17120	$1.14x10^{-2}$	0.05	$6.05x10^{-3}$	0.07	0.17	4.45		31.45	1.41	0.72
1	8	22.8	1.41	16410	0.14	0.11	0.05	0.23	0.19	4.62		31.57	1.55	0.82
2	19	22.5	1.42	16270	0.18	0.13	0.07	0.22	0.20	4.87		30.60	1.31	0.86
3	28	22	1.42	15640	0.18	0.13	0.07	0.23	0.19	4.73		33.12	1.59	0.85
4	52	22.7	1.43	15420	0.19	0.13	0.07	0.21	0.19	4.77		34.15	1.84	0.87
5	77	22.2	1.39	15800	0.20	0.14	0.08	0.21	0.19	4.52		37.11	1.82	0.89
6	101	22.8	1.43	15500	0.14	0.14	0.08	0.21	0.20	3.85		31.45	1.34	0.88
7	141	22.3	1.44	16310	0.23	0.13	0.09	0.25	0.19	4.63		30.52	1.33	0.91
8	189	22.8	1.43	16910	0.23	0.13	0.09	0.24	0.19	4.40		32.29	1.26	0.91
9	263	22	1.44	17060	0.26	0.14	0.09	0.24	0.20	4.69		30.56	1.31	1.00
10	331	21.9	1.47	17130	0.27	0.14	0.10	0.24	0.21	4.53		33.13	1.52	1.02
11	433	21.6	1.47	17190	0.26	0.14	0.10	0.27	0.20	4.23		32.14	1.58	1.02
12	505	21.6	1.49	17280	0.26	0.15	0.10	0.26	0.21	4.24		34.62	1.68	1.05
13	581	23.2	1.48	16740	0.29	0.14	0.10	0.31	0.19	4.72		35.06	1.52	1.06
14	644	22.2	1.47	16980	0.31	0.13	0.11	0.31	0.20	4.89		33.44	1.46	1.12
15	695	22.6	1.46	16750	0.31	0.13	0.11	0.31	0.20	4.64		33.15	1.35	1.11

Table A38 **Temperature, pH, EC, elemental and ion concentrations measured for the 15 brine samples of B-34; SP describes the initial brine composition before reaction; no ICP data is available for sample 5 due to a pump malfunction.**

Sample Number	Time (h)	T (°C)	pH	EC (µS/cm)	Concentration (mmol/L)									
					Al	Ca	Fe	K	Mg	Na	HCO_3	SO_4^{2-}	Cl^-	SiO_2
SP	0	22.3	1.40	17120	$1.14x10^{-2}$	0.05	$6.05x10^{-3}$	0.07	0.17	4.45		31.45	1.41	0.72
1	8	22.8	1.47	15380	0.13	1.70	0.08	0.12	0.25	4.52		31.81	1.32	0.81
2	19	22.5	1.47	15070	0.38	2.41	0.26	0.11	0.36	5.04		30.94	1.20	1.03
3	28	22	1.47	14180	0.49	2.37	0.41	0.12	0.41	4.94		29.21	1.33	1.13
4	52	22.7	1.50	13880	0.67	2.45	0.65	0.12	0.53	5.06		34.59	1.74	1.39
5	77	22.2	1.49	13710										
6	101	22.8	1.52	13190	0.78	2.65	1.03	0.12	0.90	4.33		31.77	1.35	1.93
7	141	22.3	1.55	13130	1.55	2.36	1.58	0.13	0.97	4.62		30.27	1.28	2.09
8	189	22.8	1.58	13280	2.06	2.52	2.15	0.12	1.36	4.49		32.15	1.23	2.56
9	263	22	1.63	12260	2.57	2.48	2.66	0.12	1.56	4.78		30.80	1.30	2.97
10	331	21.9	1.68	11700	2.91	2.50	3.10	0.12	1.85	4.40		30.93	1.26	3.34
11	433	21.6	1.69	11230	4.08	2.47	3.56	0.13	1.99	4.36		32.68	1.45	3.57
12	505	21.6	1.69	10770	4.10	2.62	3.93	0.13	2.25	4.39		35.09	1.71	3.89
13	581	23.2	1.73	10150	4.16	2.44	4.11	0.15	2.35	5.02		35.33	1.67	4.07
14	644	22.2	1.74	10100	4.15	2.18	3.92	0.15	2.23	4.56		33.56	1.36	3.85
15	695	22.6	1.74	9770	4.24	2.36	4.26	0.15	2.45	4.59		33.81	1.33	4.14

Table A39 Temperature, pH, EC, elemental and ion concentrations measured for the 15 brine samples of B-35; SP describes the initial brine composition before reaction.

Sample Number	Time (h)	T (°C)	pH	EC (µS/cm)	Concentration (mmol/L)									
					Al	Ca	Fe	K	Mg	Na	HCO_3	SO_4^{2-}	Cl^-	SiO_2
SP	0	22.3	1.40	17120	$1.14x10^{-2}$	0.05	$6.05x10^{-3}$	0.07	0.17	4.45		31.45	1.41	0.72
1	8	22.8	1.46	15610	0.29	0.77	0.11	0.14	0.36	4.72		31.49	1.34	0.90
2	19	22.5	1.46	15080	0.72	1.05	0.38	0.15	0.68	4.93		31.33	1.56	1.21
3	28	22	1.47	14170	0.87	1.07	0.51	0.17	0.75	4.90		31.25	1.30	1.35
4	52	22.7	1.50	13990	1.00	1.09	0.64	0.16	0.90	5.02		35.10	1.43	1.58
5	77	22.2	1.49	13940	1.23	1.12	0.83	0.14	1.09	4.59		35.18	1.70	1.80
6	101	22.8	1.50	13330	0.83	1.15	0.81	0.15	1.34	3.96		32.25	1.57	2.03
7	141	22.3	1.52	13350	1.86	1.10	1.41	0.17	1.55	4.60		30.80	1.31	2.37
8	189	22.8	1.55	13320	2.06	1.15	1.63	0.17	1.79	4.76		32.35	1.23	2.62
9	263	22	1.60	12910	2.47	1.17	1.99	0.17	2.06	4.68		31.61	1.32	2.97
10	331	21.9	1.64	12590	2.49	1.22	2.21	0.17	2.42	4.40		31.47	1.32	3.25
11	433	21.6	1.65	12200	2.70	1.22	2.41	0.17	2.53	4.39		32.37	1.32	3.38
12	505	21.6	1.66	12040	2.88	1.32	2.66	0.18	2.77	4.36		33.68	1.74	3.66
13	581	23.2	1.64	11440	3.23	1.19	2.66	0.20	2.67	4.92		34.22	1.65	3.65
14	644	22.2	1.67	11540	3.37	1.13	2.67	0.20	2.74	4.84		33.74	1.36	3.72
15	695	22.6	1.67	11310	3.45	1.22	2.74	0.23	2.83	4.66		34.51	1.40	3.91

Table A40 Temperature, pH, EC, elemental and ion concentrations measured for the 15 brine samples of B-36; SP describes the initial brine composition before reaction.

Sample Number	Time (h)	T (°C)	pH	EC (µS/cm)	Concentration (mmol/L)									
					Al	Ca	Fe	K	Mg	Na	HCO_3	SO_4^{2-}	Cl^-	SiO_2
SP	0	22.3	1.40	17120	$1.14x10^{-2}$	0.05	$6.05x10^{-3}$	0.07	0.17	4.45		31.45	1.41	0.72
1	8	22.8	1.47	15320	0.13	0.36	0.15	0.23	0.23	6.34		30.10	1.28	0.91
2	19	22.5	1.50	14440	0.41	0.92	1.27	0.29	0.60	7.04		30.70	1.21	1.22
3	28	22	1.51	14370	0.58	1.00	2.01	0.34	0.76	6.88		30.93	1.35	1.36
4	52	22.7	1.53	13140	0.78	1.07	2.51	0.32	0.91	7.12		35.27	1.57	1.68
5	77	22.2	1.53	13030	1.03	1.11	2.93	0.33	1.10	6.79		31.34	1.58	1.91
6	101	22.8	1.53	12450	1.33	1.02	3.22	0.31	1.17	6.56		32.19	1.40	2.10
7	141	22.3	1.54	12600	1.59	1.05	3.57	0.34	1.30	6.59		31.41	1.36	2.31
8	189	22.8	1.56	12570	1.80	1.03	3.62	0.31	1.33	6.34		32.24	1.23	2.42
9	263	22	1.60	12400	2.09	1.05	3.95	0.32	1.54	6.25		31.76	1.39	2.71
10	331	21.9	1.66	12110	2.12	1.09	4.39	0.33	1.79	6.39		31.54	1.33	3.06
11	433	21.6	1.69	11840	2.44	1.08	4.37	0.32	1.81	6.15		32.17	1.33	3.10
12	505	21.6	1.69	11740	2.48	1.11	4.45	0.33	2.05	5.51		34.27	1.68	3.24
13	581	23.2	1.70	11240	2.62	1.01	4.65	0.38	1.90	6.94		33.59	1.74	3.32
14	644	22.2	1.70	11340	2.76	0.98	4.42	0.40	1.84	6.40		31.41	1.44	3.22
15	695	22.6	1.70	11020	2.77	0.99	4.43	0.35	1.91	6.22		34.36	1.48	3.28

Table A41 Temperature, pH, EC, elemental and ion concentrations measured for the 15 brine samples of B-37; SP describes the initial brine composition before reaction.

Sample Number	Time (h)	T (°C)	pH	EC (µS/cm)	Concentration (mmol/L)									
					Al	Ca	Fe	K	Mg	Na	HCO_3	SO_4^{2-}	Cl^-	SiO_2
SP	0	61	1.40	13030	$1.14x10^{-2}$	0.05	$6.05x10^{-3}$	0.07	0.17	4.45		31.45	1.41	0.72
1	8	61	1.39	11780	0.03	0.08	0.06	0.08	0.19	4.64		33.32	1.40	0.78
2	19	61	1.38	11600	0.05	0.08	0.10	0.10	0.20	5.04		31.97	1.25	0.83
3	28	59	1.37	11430	0.06	0.08	0.11	0.12	0.20	4.86		32.40	1.74	0.82
4	52	60	1.39	10910	0.07	0.08	0.12	0.14	0.20	4.76		34.07	2.27	0.83
5	77	63	1.37	11670	0.08	0.08	0.13	0.15	0.21	4.46		35.29	2.20	0.89
6	101	58	1.40	11810	0.10	0.08	0.15	0.17	0.21	5.07		33.05	2.06	0.94
7	141	60	1.39	12060	0.12	0.09	0.14	0.16	0.21	4.74		31.83	1.70	0.94
8	189	58	1.37	12680	0.14	0.09	0.14	0.18	0.20	4.53		33.13	1.49	0.97
9	263	58	1.36	13160	0.17	0.09	0.16	0.17	0.22	4.72		33.23	1.65	1.07
10	331	61	1.39	13230	0.17	0.10	0.17	0.18	0.23	4.71		33.30	1.72	1.16
11	433	62	1.39	13200	0.24	0.10	0.17	0.18	0.23	4.72		34.11	1.75	1.24
12	505	60	1.39	13670	0.26	0.10	0.18	0.19	0.26	4.40		34.47	2.16	1.35
13	581	61	1.40	14440	0.29	0.09	0.18	0.21	0.22	5.00		32.90	2.27	1.29
14	644	62	1.40	14460	0.32	0.10	0.19	0.21	0.22	5.13		33.19	1.62	1.38
15	695	61	1.37	14420	0.31	0.10	0.18	0.20	0.22	4.65		36.39	2.14	1.34

Table A42 Temperature, pH, EC, elemental and ion concentrations measured for the 15 brine samples of B-38; SP describes the initial brine composition before reaction.

Sample Number	Time (h)	T (°C)	pH	EC (µS/cm)	Concentration (mmol/L)									
					Al	Ca	Fe	K	Mg	Na	HCO_3	SO_4^{2-}	Cl^-	SiO_2
SP	0	61	1.40	13030	$1.14x10^{-2}$	0.05	$6.05x10^{-3}$	0.07	0.17	4.45		31.45	1.41	0.72
1	8	61	1.48	10120	0.76	1.79	1.10	0.23	0.68	5.76		32.05	1.41	1.31
2	19	61	1.56	8880	1.57	2.33	2.04	0.22	1.01	5.36		31.36	2.47	1.80
3	28	59	1.60	7950	2.26	2.98	2.79	0.32	1.34	5.97		32.22	1.81	2.42
4	52	60	1.72	7350	3.10	3.54	3.49	0.36	1.69	6.02		32.83	2.38	3.26
5	77	63	1.68	7410	3.19	3.69	3.62	0.38	1.84	5.32		33.58	2.05	3.61
6	101	58	1.73	7720	3.35	3.64	3.97	0.44	1.88	5.89		31.54	1.15	3.87
7	141	60	1.75	7970	3.34	3.63	4.04	0.47	1.92	5.88		32.43	1.46	4.12
8	189	58	1.75	7410	3.43	3.55	3.94	0.46	1.91	5.52		33.45	1.35	4.21
9	263	58	1.75	7500	3.82	3.86	4.13	0.51	2.06	5.77		33.38	1.50	4.62
10	331	61	1.77	7780	3.86	3.86	4.24	0.58	2.08	5.54		33.73	1.58	4.84
11	433	62	1.77	7740	3.88	3.95	4.15	0.60	2.09	5.65		33.49	1.66	4.91
12	505	60	1.76	7720	4.06	4.00	4.15	0.56	2.32	5.04		33.64	2.08	4.97
13	581	61	1.77	7830	4.22	3.63	4.06	0.69	2.00	6.08		33.19	2.06	4.96
14	644	62	1.76	7730	4.56	3.70	4.07	0.74	2.00	6.21		33.66	1.51	5.12
15	695	61	1.76	7610	4.44	3.70	3.90	0.72	1.99	5.80		34.64	1.77	5.02

Table A43 Temperature, pH, EC, elemental and ion concentrations measured for the 15 brine samples of B-39; SP describes the initial brine composition before reaction.

Sample Number	Time (h)	T (°C)	pH	EC (µS/cm)	Concentration (mmol/L)									
					Al	Ca	Fe	K	Mg	Na	HCO_3	SO_4^{2-}	Cl^-	SiO_2
SP	0	61	1.40	13030	$1.14x10^{-2}$	0.05	$6.05x10^{-3}$	0.07	0.17	4.45		31.45	1.41	0.72
1	8	61	1.43	10880	0.48	0.20	1.22	0.13	0.37	4.86		31.85	1.30	1.10
2	19	61	1.45	10010	0.98	0.23	2.01	0.21	0.51	6.14		31.75	1.73	1.35
3	28	59	1.45	10200	1.20	0.24	2.28	0.22	0.57	5.84		32.31	1.29	1.46
4	52	60	1.52	9250	1.48	0.27	2.67	0.25	0.75	5.72		34.09	1.69	1.71
5	77	63	1.49	9450	1.75	0.32	3.29	0.30	1.00	5.62		33.59	1.41	2.12
6	101	58	1.54	9400	2.18	0.28	3.44	0.33	1.00	5.79		31.39	1.25	2.20
7	141	60	1.55	10050	2.55	0.30	3.79	0.37	1.17	5.97		32.63	1.52	2.58
8	189	58	1.56	9430	2.49	0.28	3.63	0.38	1.16	5.44		33.54	1.34	2.65
9	263	58	1.58	9150	2.88	0.31	3.96	0.45	1.31	5.64		33.68	1.53	3.09
10	331	61	1.61	9580	3.18	0.35	4.13	0.52	1.47	5.74		33.20	1.54	3.51
11	433	62	1.62	9660	3.28	0.33	4.05	0.53	1.43	5.49		34.33	2.05	3.71
12	505	60	1.60	9790	3.34	0.35	4.23	0.55	1.69	5.23		34.27	2.01	4.18
13	581	61	1.61	9780	3.69	0.33	4.28	0.71	1.52	6.50		33.31	2.16	4.39
14	644	62	1.62	9750	3.87	0.30	3.88	0.69	1.38	5.82		33.40	1.53	4.06
15	695	61	1.61	9680	3.88	0.31	3.81	0.68	1.44	5.61		34.17	2.80	4.19

Table A44 Temperature, pH, EC, elemental and ion concentrations measured for the 15 brine samples of B-40; SP describes the initial brine composition before reaction.

Sample Number	Time (h)	T (°C)	pH	EC (µS/cm)	Concentration (mmol/L)									
					Al	Ca	Fe	K	Mg	Na	HCO_3	SO_4^{2-}	Cl^-	SiO_2
SP	0	61	1.40	13030	$1.14x10^{-2}$	0.05	$6.05x10^{-3}$	0.07	0.17	4.45		31.45	1.41	0.72
1	8	61	1.45	10980	0.76	0.12	1.24	0.12	0.35	5.28		31.49	1.57	1.25
2	19	61	1.50	9630	1.71	0.17	2.71	0.12	0.58	5.43		32.73	1.70	1.89
3	28	59	1.53	9300	2.18	0.17	3.43	0.18	0.68	5.33		32.31	1.34	2.18
4	52	60	1.65	7770	3.48	0.20	5.55	0.16	0.96	5.10		33.68	1.94	2.84
5	77	63	1.64	8010	3.92	0.23	6.10	0.19	1.19	4.66		33.91	2.06	3.25
6	101	58	1.72	7640	4.15	0.22	6.37	0.19	1.26	5.24		31.50	2.12	3.47
7	141	60	1.77	7320	4.87	0.24	7.23	0.23	1.46	5.65		32.88	1.46	4.06
8	189	58	1.82	6770	5.26	0.22	7.65	0.20	1.41	4.93		30.80	1.47	3.89
9	263	58	1.87	6200	5.84	0.25	8.17	0.27	1.68	5.23		33.90	1.59	4.48
10	331	61	1.91	6530	5.74	0.25	8.44	0.29	1.80	4.96		34.23	1.65	4.64
11	433	62	1.95	6280	5.92	0.27	8.62	0.31	1.84	5.04		34.80	1.71	4.82
12	505	60	1.91	6340	6.02	0.25	8.95	0.27	1.94	4.40		31.71	2.06	4.84
13	581	61	1.94	6260	6.10	0.23	8.96	0.38	1.79	5.78		33.87	2.17	4.90
14	644	62	1.91	5750	5.88	0.22	8.91	0.35	1.70	5.13		34.03	1.56	4.56
15	695	61	1.93	5490	5.87	0.25	8.82	0.38	1.81	5.26		34.87	1.85	4.85

Appendix D.

Kinetic rate data

Table A45 Kinetic rate data used to model chlorite at different compositions.

	Western Canada Sedimentary Basin samples						Surat Basin samples
	AF-01	AF-02	AF-03	AF-04	AF-05	AF-06	AF-07 - AF-10
Fe:Mg	60:40	25:75	10:90	65:35	50:50	75:25	75:25
$E_{a(H)}$ (kJ/mol)	36	31	15	36	34	40	40
$n_{(H)}$	0.7	0.7	0.75	0.7	0.7	0.8	0.8

Table A46 Kinetic rate data used to model ankerite at different compositions.

	Western Canada Sedimentary Basin samples	Surat Basin samples
	AF-06	AF-07 - AF-10
Ca:Fe:Mg	50:25:25	50:35:15
$E_{a(H)}$ (kJ/mol)	32	48
$n_{(H)}$	0.8	0.75

Appendix E.

Reactive surface areas

Table A47 Reactive surface areas (cm^2/g) applied to model the reaction of AF-01 at different sample particle sizes.

	Mortared	Crushed	Block
Chalcedony; albite; K-feldspar;	8000	8000	1000
Illite; muscovite; chlorite; kaolinite	$1x10^5$	$1x10^5$	$0.5x10^5$
Calcite	0.1	0.05	0.005
Dolomite	5	1	0.2
Ankerite	0.5	0.5	0.2

Table A48 Reactive surface areas (cm^2/g) applied to model the reaction of AF-02 at different sample particle sizes.

	Mortared	Crushed	Block
Chalcedony; albite; K-feldspar;	4000	3000	500
Illite; muscovite; chlorite; kaolinite	$2x10^5$	$2x10^5$	$1.5x10^5$
Calcite	0.05	0.05	0.005
Siderite	0.25	0.25	0.025

Table A49 Reactive surface areas (cm^2/g) applied to model the reaction of AF-03 at different sample particle sizes.

	Mortared	Crushed	Block
Chalcedony; albite; K-feldspar;	7000	3000	800
Illite; muscovite; chlorite; kaolinite	1x104	1x104	5000
Calcite	0.1	0.1	0.1
Siderite	0.5	0.25	0.1

Table A50 Reactive surface areas (cm^2/g) applied to model the reaction of AF-04 at different sample particle sizes.

	Mortared	Crushed	Block
Chalcedony; albite; K-feldspar;	800	500	100
Illite; muscovite; chlorite; kaolinite	$5x10^5$	$5x10^5$	$1.5x10^5$
Calcite	2	1	0.03

Table A51 Reactive surface areas (cm^2/g) applied to model the reaction of AF-05 at different sample particle sizes.

	Mortared	Crushed	Block
Chalcedony; albite; K-feldspar;	5000	1500	800
Illite; muscovite; chlorite; kaolinite	$4x10^5$	$3x10^5$	$1x10^5$
Calcite	0.1	0.1	0.0035

Table A52 Reactive surface areas (cm^2/g) applied to model the reaction of AF-06 at different sample particle sizes.

	Mortared	Crushed	Block
Chalcedony; albite; K-feldspar;	5000	1000	500
Illite; muscovite; chlorite; kaolinite	$4x10^5$	$4x10^5$	$3x10^5$
Ankerite	0.1	0.1	0.1

Table A53 Reactive surface areas (cm^2/g) applied to model the reaction of the Surat Basin samples.

	AF-07	AF-08	AF-09	AF-10
Chalcedony; albite; K-feldspar;	2000	4000	5000	4000
Illite; muscovite; biotite*; chlorite; kaolinite	$1x10^5$	$8x10^4$	$7x10^4$	$5x10^4$
Calcite		0.01		
Ankerite	0.01	0.02	0.01	0.007
Siderite			0.1	0.1

*biotite was treated like a framework mineral for AF-10

Appendix F.

Figure copyright

Creative commons declarations from the CO2CRC and Commenwealth of Australia (Geoscience Australia) can be found under the following links, respectively:

http://www.co2crc.com.au/imagelibrary2/conditions.html (7/6/2015)

http://www.ga.gov.au/copyright (7/6/2015)